

**FORMULATION AND PRODUCTION OF AN ADDITIVELY MANUFACTURED  
Ti6Al4V (ELI) COMPOSITE WITH ENHANCED MECHANICAL PROPERTIES**

MASENATE SELESO THAMAE

Dissertation submitted in fulfillment of the requirements for the degree

**MASTER OF ENGINEERING**

in

**MECHANICAL ENGINEERING**

in the

Department of Mechanical and Mechatronics Engineering

at

Central University of Technology, Free State

Supervisor: Prof. M Maringa

Co-supervisor: Prof W B du Preez

BLOEMFONTEIN, 2024

## DECLARATION OF INDEPENDENT WORK

### DECLARATION CONCERNING INDEPENDENT WORK

I, Masenate Seleso Thamae, identity number ##### and student number #####, do hereby declare that this research project submitted to Central University of Technology, Free State for the degree MASTER OF ENGINEERING IN MECHANICAL ENGINEERING, is my independent work; and complies with the Code of Academic Integrity, as well as other relevant policies, procedures, rules and regulations of Central University of Technology, Free State; and has not been submitted before to any institution by myself or any other person in fulfillment (or partial fulfillment) of the requirements for the attainment of any qualification.

---

**SIGNATURE OF STUDENT**

**DATE**

## ACKNOWLEDGEMENTS

Firstly, all thanks to Almighty God for his blessings. I would like to extend my deepest gratitude to my supervisors, Prof. Maina Maringa, and Prof Willie du Preez for guiding me through the long journey of research, their patience, excellent suggestion, and outstanding efforts throughout this study are appreciated. They both have been there for me for these three years, motivating me whenever I felt weak, lacking energy, and struggling during the research. Prof. Maringa would give good motivational examples of other students he taught who succeeded in their research. He pushed me to work harder and gave me the spirit to complete my master's degree within the expected number of years. My supervisors put in extra hours to mark or correct the many documents submitted to them, which enabled me to finish in time, and I wouldn't be successful in this research without their guidance. They helped me to understand the principles related to this work.

To all my colleagues who I engaged with in this research and socially at CUT, you are all appreciated because of your suggestions and ideas, which all contributed to my research.

I cannot begin to express my deep-felt gratitude to my husband, who has been with me, supporting and encouraging me throughout the research. Without him, I would not be where I am in this research today. Whenever I felt everything was difficult for me, he would volunteer to spend sleepless nights trying to help me understand and face the problems upon me. I owe it all to you, Mr. Sekake Thamae. All thanks to the whole family for their support in this journey.

Lastly, I would like to thank the Collaborative Program in Additive Manufacturing sincerely for their financial support, which made it possible for me to undertake this work.

## ABSTRACT

This research focused on the production of additively manufactured SiC/Ti6Al4V(ELI) composites with enhanced mechanical properties over those of the Ti6Al4V(ELI) alloy to increase the application of the alloy in the aircraft and automotive industries. The titanium alloy Ti6Al4V is mostly used in engineering applications due to its excellent combination of high specific strength, good fatigue properties and outstanding corrosion resistance. A limitation of titanium alloys is their poor abrasion resistance. This and other properties of these alloys were expected to be improved in this work by the addition of a strengthening phase consisting of silicon carbide (SiC) particles. These particles were used as reinforcement in the Ti6Al4V(ELI) matrix because of their excellent resistance to wear, high sublimation temperature relative to the melting temperature of Ti6Al4V(ELI), specific stiffness, specific strength, hardness, and fracture toughness that are higher than those of the Ti6Al4V(ELI) matrix.

Because SiC particles have a lower density ( $3.21 \text{ g/cm}^3$ ) than Ti6Al4V(ELI) (density:  $4.45 \text{ g/cm}^3$ ) and a coefficient of thermal expansion (CTE) of  $4.6 \times 10^{-6}/\text{K}$ , that is lower than the CTE of Ti6Al4V(ELI) of  $8.6 \times 10^{-6}/\text{K}$ , the addition of SiC particles was expected to reduce the overall density and CTE of an SiC/Ti6Al4V(ELI) composite. When applied to the joints of aircraft structures, an SiC/Ti6Al4V(ELI) composite with a CTE closer to that of carbon fibre/epoxy resin composites ( $2.1 \times 10^{-6}/\text{K}$ ) would minimize thermal-related buckling or separation at the interfaces. Furthermore, SiC particles with higher wear resistance than Ti6Al4V(ELI) would increase the wear resistance of an SiC/Ti6Al4V(ELI) composite.

After mixing different volume fractions of Ti6Al4V(ELI) and SiC powder particles, single tracks were built from the mixtures to determine the optimum process parameters of laser power, scanning speed and energy density, all of which are known to influence the quality of built parts. Single tracks were built with different process parameter settings for each volume fraction of SiC (5 %, 10 %, 15 %, 20 %, 25 %, and 30 %) studied here. Top surface analysis of the tracks was done to identify the presence or absence of the keyhole and balling effects and to determine the degree of irregularity and discontinuity of the printed tracks. Thereafter, cross-sections of the tracks were prepared and examined in optical and/or scanning electron microscopes to determine

the geometrical characteristics of single tracks of width, height, and depth of penetration into the substrate.

The presence of continuous tracks with no balling, a lack of porosity, proper penetration, and dimensional stability in the generated tracks advised the selection of the best process parameters for each volume fraction. The best process parameters chosen for each SiC volume fraction were then utilized to create single layers at 50  $\mu\text{m}$ , 60  $\mu\text{m}$ , 70  $\mu\text{m}$ , 80  $\mu\text{m}$ , 90  $\mu\text{m}$ , 100  $\mu\text{m}$ , and 110  $\mu\text{m}$  hatch distances. Top surface examination of the layers was performed to investigate the continuity of tracks, balling or humping effect, surface roughness, and insufficient melting of the tracks. This was followed by cutting and preparation of cross-sections to investigate the degree of overlapping of tracks and the presence or absence of interior pores. Based on this analysis, the best hatch distances for each SiC volume fraction were selected for future use in the building of 3D specimens.

Best single tracks were found at SiC volume fractions lying between 5 % and 25 %, inclusive, based on measured depth-to-width ratios of 0.5. At a SiC volume fraction of 30 %, the built tracks were observed to have poor penetration with depth-to-width ratios less than the optimum value of 0.5. The process parameters for these best single tracks were further used to build single layers where the hatch distances were varied from 50  $\mu\text{m}$ , 60  $\mu\text{m}$ , 70  $\mu\text{m}$ , 80  $\mu\text{m}$ , 90  $\mu\text{m}$ , 100  $\mu\text{m}$ , to 110  $\mu\text{m}$  for each SiC volume fraction from 5 % to 25 %, inclusive, while keeping all other process parameters, such as laser power, scanning speed and layer thickness constant, with the first two at the best-determined values. The best hatch distance for each volume fraction was then identified as the one that led to a printed layer with good overlapping, smooth surface topography and acceptable depth of penetration.

It was recommended in this study that the mechanical properties of SiC/Ti6Al4V(ELI) composites might be increased at SiC volume fractions from 5 % to 25 %, inclusive, due to the fact that the best single tracks and single layers were obtained. Furthermore, the specimens to be built at the highest SiC volume fraction of 30 % might lead to decreased mechanical properties due to poor characteristics of produced tracks and single layers.

## PUBLICATIONS EMANATING FROM THIS RESEARCH

### Journal Articles

1. **Thamae, M., Maringa, M., and du Preez, W.B.**, A comparative analysis of low and high SiC volume fraction additively manufactured SiC/Ti6Al4V(ELI) composites based on the best process parameters of laser power, scanning speed and hatch distance, *Materials Journal*, 2024, Vol.17, No,11.2606. <https://www.mdpi.com/1996-1944/17/11/2606>.
2. **Thamae, M., Maringa, M., and du Preez, W.B.**, Determining the best hatch distances for selective laser melted SiC/Ti6Al4V(ELI) composites of different volume fractions of SiC, submitted to *Results in Materials Journal* on 28<sup>th</sup> May 2024. <https://www.sciencedirect.com/journal/results-in-materials>.

### Conference Proceedings

1. **Seleso, M., Maringa, M., and du Preez, W.B.**, 2020. Designing a ceramic particulate composite to enhance selected mechanical properties of Ti6Al4V. Rapid Product Development Association of South Africa (RAPDASA) 21<sup>st</sup> Annual International Conference, Japie van Lill Auditorium, Central University of Technology, Free State, South Africa, 3<sup>rd</sup> November 2020, pp. 41-55. <https://site.rapdasa.org/past-proceedings-2020/>
2. **Seleso, M., Maringa, M., and du Preez, W.B.**, 2021. Parameters Affecting the Mixing of Powders and the Results of Mixing SiC and Ti6Al4V(ELI) powders. RAPDASA-RobMech-PRASA Conference – 22<sup>nd</sup> Annual International RAPDASA Conference, CSIR International Conference Centre, Pretoria, South Africa, 3<sup>rd</sup>-5<sup>th</sup> November 2021, pp. 73-75. <https://site.rapdasa.org/past-proceedings-2021/>
3. **Thamae, M<sup>1</sup>., Maringa, M., and du Preez, W.B.**, 2022. Influence of selective laser melting process parameters on the characteristics of SiC/Ti6Al4V(ELI) single tracks. RAPDASA-RobMech-PRASA-CoSAAMI Conference – Digital Technology in Product Development – 23<sup>rd</sup> Annual International RAPDASA Conference, Somerset West, South Africa, 9<sup>th</sup>-11<sup>th</sup> November 2022, pp. 1-15. <https://doi.org/10.1051/mateconf/202237001003>

---

<sup>1</sup> Seleso, M., and Thamae, M. is the same person

## TABLE OF CONTENTS

<b>DECLARATION OF INDEPENDENT WORK .....</b>	<b>II</b>
<b>ACKNOWLEDGEMENTS.....</b>	<b>III</b>
<b>ABSTRACT .....</b>	<b>IV</b>
<b>PUBLICATIONS EMANATING FROM THIS RESEARCH .....</b>	<b>VI</b>
<b>TABLE OF CONTENTS .....</b>	<b>VII</b>
<b>TABLE OF FIGURES.....</b>	<b>XIV</b>
<b>LIST OF TABLES.....</b>	<b>XXV</b>
<b>ABBREVIATIONS AND ACRONYMS .....</b>	<b>XXVIII</b>
<b>CHAPTER 1: INTRODUCTION .....</b>	<b>1</b>
1.1. BACKGROUND.....	1
1.2. PROBLEM STATEMENT.....	4
1.3. AIM OF THE PROJECT .....	5
1.3.1. Research Objectives .....	5
1.4. OVERVIEW OF THE DISSERTATION .....	7
1.5. REFERENCES .....	8
<b>CHAPTER 2: LITERATURE REVIEW .....</b>	<b>10</b>
2.0. INTRODUCTION .....	10
2.1. COMPOSITE MATERIALS.....	10
2.1.1. Historical Background of Composites .....	11
2.1.2. Types of Composites .....	12
2.2. DESIGNING Ti6Al4V METAL MATRIX COMPOSITES .....	15
2.2.1. Metallic bases of metal matrix composites .....	16
2.2.2. Theoretical Limitations of Particulate Reinforcement .....	17
2.2.3. Particle Size and Shape .....	22
2.3. THE Ti6Al4V(ELI) ALLOY.....	24
2.3.1. Microstructure and Mechanical Properties of Ti6Al4V Alloy.....	25

2.4.	ADDITIVE MANUFACTURING .....	27
2.4.1.	Direct Metal Laser Sintering (DMLS).....	27
2.4.2.	Powder Mixing Technologies .....	39
2.5.	REFERENCES .....	43
<b>CHAPTER 3:</b>	<b>MATERIALS AND METHODS .....</b>	<b>52</b>
3.1.	SIEVING OF Ti6Al4V(ELI) POWDERS .....	53
3.2.	WEIGHING OF SiC AND Ti6Al4V(ELI) POWDERS FOR MIXING .....	53
3.3.	MIXING OF POWDER.....	56
3.4.	BUILDING OF DMLS SiC/Ti6Al4V(ELI) SINGLE TRACKS .....	57
3.5.	BUILDING SINGLE LAYERS AT DIFFERENT SiC MASS FRACTIONS .....	58
3.6.	PREPARATION OF SPECIMENS FOR ANALYSES USING A SEM AND AN OPTICAL MICROSCOPE.....	61
3.7.	CHARACTERIZATION OF POWDER AND SPECIMENS.....	62
3.7.1.	Scanning Electron Microscopy .....	62
3.7.2.	Optical Microscopy.....	63
3.7.3.	Inductively Coupled Plasma-Optical Emission Spectrometry .....	64
3.8.	REFERENCES .....	65
<b>CHAPTER 4:</b>	<b>ANALYTICAL MODELLING OF THE PROPERTIES OF SiC/Ti6Al4V(ELI) COMPOSITES.....</b>	<b>66</b>
4.0.	INTRODUCTION .....	66
4.1.	MODELLING THE PROPERTIES OF SiC/Ti6Al4V(ELI) PARTICULATE COMPOSITES .....	66
4.2.	REFERENCES .....	74
<b>CHAPTER 5:</b>	<b>CHARACTERIZATION OF SiC, Ti6Al4V(ELI) AND MIXED SiC AND Ti6Al4V(ELI) POWDERS .....</b>	<b>75</b>
5.0.	INTRODUCTION .....	75
5.1.	MORPHOLOGY OF Ti6Al4V(ELI) POWDER BEFORE AND AFTER MIXING .....	75
5.2.	REFERENCES .....	80

<b>CHAPTER 6:</b>	<b>ANALYSIS OF SiC/Ti6Al4V(ELI) SINGLE TRACKS.....</b>	<b>81</b>
6.0.	INTRODUCTION .....	81
6.1.	ANALYSIS OF SINGLE TRACKS AT A 5 % SiC VOLUME FRACTION IN AN SiC/Ti6Al4V(ELI) COMPOSITE.....	81
6.1.1.	Comparative analysis of the best single tracks at a 5% SiC volume fraction in an SiC/Ti6Al4V(ELI) composite.....	87
6.1.2	Analysis of single tracks at different scanning speeds and constant laser power of 200 W.....	88
6.1.3.	Analysis of single tracks at constant scanning speeds with different values of laser power .....	92
6.2.	ANALYSIS OF SINGLE TRACKS OF A 10 % SiC VOLUME FRACTION IN AN SiC/Ti6Al4V(ELI) COMPOSITE.....	94
6.2.1.	Comparative analysis of the best single tracks at a 10% SiC volume fraction of an SiC/Ti6Al4V(ELI) composite .....	96
6.3.	ANALYSIS OF SINGLE TRACKS OF A 15 % SiC VOLUME FRACTION IN AN SiC/Ti6Al4V(ELI) COMPOSITE.....	98
6.3.1.	Comparative analysis of the best single tracks at a 15% SiC volume fraction in an SiC/Ti6Al4V(ELI) composite.....	100
6.4.	ANALYSIS OF SINGLE TRACKS AT A 20 % SiC VOLUME FRACTION IN AN SiC/Ti6Al4V(ELI) COMPOSITE.....	101
6.4.1.	Comparative analysis of the best single tracks at a 20% SiC volume fraction in an SiC/Ti6Al4V(ELI) composite.....	103
6.5.	ANALYSIS OF SINGLE TRACKS AT A 25 % SiC VOLUME FRACTION IN AN SiC/Ti6Al4V(ELI)COMPOSITE .....	105
6.5.1.	Comparative analysis of the best single tracks at a 25% SiC volume fraction in an SiC/Ti6Al4V(ELI) composite.....	108

6.6.	ANALYSIS OF SINGLE TRACKS AT A 30 % SIC VOLUME FRACTION IN AN SIC/TI6AL4V(ELI) COMPOSITE .....	110
6.7.	DISCUSSIONS AND SUMMARY .....	113
6.8.	REFERENCES .....	118
<b>CHAPTER 7:</b>	<b>TOP SURFACE AND CROSS-SECTIONAL ANALYSIS OF SINGLE LAYERS OF SIC/TI6AL4V(ELI) COMPOSITES .....</b>	<b>122</b>
7.0.	INTRODUCTION .....	122
7.1.	CROSS-SECTION AND TOP SURFACE ANALYSIS OF SINGLE LAYERS BUILT WITH A 5% SIC VOLUME FRACTION OF AN SIC/TI6AL4V(ELI) COMPOSITE .....	122
7.2.	CROSS-SECTION AND TOP SURFACE ANALYSIS OF SINGLE LAYERS BUILT WITH A 10 % SIC VOLUME FRACTION OF AN SIC/TI6AL4V(ELI) COMPOSITE .....	129
7.3.	CROSS-SECTION AND TOP SURFACE ANALYSIS OF SINGLE LAYERS BUILT WITH A 15 % SIC VOLUME FRACTION OF AN SIC/TI6AL4V(ELI) COMPOSITE .....	134
7.4.	CROSS-SECTION AND TOP SURFACE ANALYSIS OF SINGLE LAYERS BUILT WITH A 20 % SIC VOLUME FRACTION OF AN SIC/TI6AL4V(ELI) COMPOSITE .....	139
7.5.	CROSS-SECTION AND TOP SURFACE ANALYSIS OF SINGLE LAYERS BUILT WITH A 25% SIC VOLUME FRACTION IN AN SIC/TI6AL4V(ELI) COMPOSITE.....	144
7.6.	CROSS-SECTION AND TOP SURFACE ANALYSIS OF SINGLE LAYERS BUILT WITH 30% SIC VOLUME FRACTION IN AN SIC/TI6AL4V(ELI) COMPOSITE.....	148
7.7.	REFERENCES .....	152
<b>CHAPTER 8:</b>	<b>CONCLUSIONS AND RECOMMENDATIONS .....</b>	<b>155</b>
8.0	INTRODUCTION .....	155
8.1.	CONCLUSIONS.....	155
8.2.	RECOMMENDATIONS.....	157
<b>APPENDIX A:</b>	<b>ANALYSIS OF SINGLE TRACKS BUILT WITH A 5% VOLUME FRACTION OF SIC IN AN SIC/TI6AL4V(ELI) COMPOSITE .....</b>	<b>158</b>
A1.	THE EFFECTS OF SCANNING SPEED AT A CONSTANT LASER POWER OF 100 W.....	158
A2.	THE EFFECTS OF SCANNING SPEEDS AT A LASER POWER OF 150 W .....	161
A3.	THE EFFECTS OF SCANNING SPEED AT A LASER POWER OF 250 W .....	164
A4.	THE EFFECTS OF SCANNING SPEED AT A LASER POWER OF 300 W .....	167

A5.	THE EFFECTS OF SCANNING SPEED AT THE HIGHEST LASER POWER OF 350 W .....	169
A6.	ANALYSIS OF SINGLE TRACKS AT CONSTANT SCANNING SPEED WITH DIFFERENT VALUES OF LASER POWER .....	170
A7.	THE EFFECTS OF DIFFERENT LASER SCANNING SPEEDS AND POWER AT A CONSTANT LINEAR ENERGY DENSITY .....	171
<b>APPENDIX B. ANALYSIS OF SINGLE TRACKS BUILT AT A VOLUME FRACTION OF 10 % SIC IN AN SIC/TI6AL4V(ELI) COMPOSITE .....</b>		<b>174</b>
B1.	THE EFFECTS OF DIFFERENT LASER SCANNING SPEEDS AT A LASER POWER OF 100 W .....	174
B2.	THE EFFECTS OF DIFFERENT LASER SCANNING SPEEDS AT A LASER POWER OF 150 W .....	177
B3.	THE EFFECTS OF DIFFERENT LASER SCANNING SPEEDS AT A LASER POWER OF 200 W .....	179
B4.	THE EFFECTS OF DIFFERENT LASER SCANNING SPEEDS AT A LASER POWER OF 250 W .....	182
B5.	THE EFFECTS OF DIFFERENT LASER SCANNING SPEEDS AT A LASER POWER OF 300 W .....	183
B6.	THE EFFECTS OF DIFFERENT LASER SCANNING SPEEDS AT A LASER POWER OF 350 W .....	185
B7.	The Effects of Constant Scanning Speed at Different Values of Laser Power .....	186
<b>APPENDIX C. ANALYSIS OF SINGLE TRACKS BUILT AT A VOLUME FRACTION OF SIC OF 15 % IN AN SIC/TI6AL4V(ELI) COMPOSITE .....</b>		<b>188</b>
C1.	THE EFFECTS OF DIFFERENT LASER SCANNING SPEEDS AT A LASER POWER OF 100 W .....	188
C2.	THE EFFECTS OF DIFFERENT LASER SCANNING SPEEDS AT A LASER POWER OF 150 W .....	190
C3.	THE EFFECTS OF DIFFERENT LASER SCANNING SPEEDS AT A LASER POWER OF 200 W .....	193
C4.	THE EFFECTS OF DIFFERENT LASER SCANNING SPEEDS AT A LASER POWER OF	

	250 W .....	195
C5.	THE EFFECTS OF DIFFERENT LASER SCANNING SPEEDS AT A LASER POWER OF 300 W .....	197
C6.	THE EFFECTS OF DIFFERENT LASER SCANNING SPEEDS AT A LASER POWER OF 350 W .....	199
C7.	THE EFFECTS OF A CONSTANT SCANNING SPEED AT DIFFERENT VALUES OF LASER POWER .....	201
<b>APPENDIX D: ANALYSIS OF SINGLE TRACKS BUILT AT A 20 % VOLUME</b>		
	<b>FRACTION OF SIC IN AN SIC/TI6AL4V(ELI) COMPOSITE .....</b>	<b>203</b>
D1.	THE EFFECTS OF DIFFERENT LASER SCANNING SPEEDS AT A LASER POWER OF 100 W .....	203
D2.	THE EFFECTS OF DIFFERENT VARYING LASER SCANNING SPEEDS AT A LASER POWER OF 150 W .....	205
D3.	THE EFFECTS OF DIFFERENT LASER SCANNING SPEEDS AT A LASER POWER OF 200 W .....	207
D4.	THE EFFECT OF DIFFERENT LASER SCANNING SPEEDS AT A LASER POWER OF 250 W .....	209
D5.	THE EFFECT OF DIFFERENT LASER SCANNING SPEEDS AT A LASER POWER OF 300 W .....	211
D6.	THE EFFECT OF DIFFERENT LASER SCANNING SPEEDS AT A LASER POWER OF 350 W .....	213
<b>APPENDIX E. ANALYSIS OF SINGLE TRACKS BUILT AT A 25 % VOLUME</b>		
	<b>FRACTION OF SIC IN AN SIC/TI6AL4V(ELI) COMPOSITE .....</b>	<b>216</b>
E1.	THE EFFECT OF DIFFERENT LASER SCANNING SPEEDS AT A LASER POWER OF 100 W .....	216
E2.	THE EFFECT OF DIFFERENT LASER SCANNING SPEEDS AT A LASER POWER OF 150 W .....	218
E3.	THE EFFECTS OF DIFFERENT LASER SCANNING SPEEDS AT LASER POWER OF 200 W .....	220
E4.	THE EFFECTS OF DIFFERENT LASER SCANNING SPEEDS AT A LASER POWER OF	

	250 W .....	222
E5.	THE EFFECT OF DIFFERENT LASER SCANNING SPEEDS AT A LASER POWER OF 300 W .....	225
E6.	THE EFFECT OF DIFFERENT LASER SCANNING SPEEDS AT A LASER POWER OF 350 W .....	227
E7.	THE INFLUENCE OF DIFFERENT VALUES OF LASER POWER AT A CONSTANT LASER SCANNING SPEED .....	230
<b>APPENDIX F. ANALYSIS OF SINGLE TRACKS BUILT AT A 30 % VOLUME</b>		
	<b>FRACTION OF SIC IN AN SIC/TI6AL4V(ELI) COMPOSITE .....</b>	<b>231</b>
F1.	THE EFFECT OF DIFFERENT LASER SCANNING SPEEDS AT A LASER POWER OF 100 W .....	231
F2.	THE EFFECT OF DIFFERENT LASER SCANNING SPEEDS AT A LASER POWER OF 150 W .....	233
F3.	THE EFFECT OF DIFFERENT LASER SCANNING SPEEDS AT A LASER POWER OF 200 W .....	236
F4.	THE EFFECT OF DIFFERENT LASER SCANNING SPEEDS AT A LASER POWER OF 250 W .....	238
F5.	THE EFFECT OF DIFFERENT LASER SCANNING SPEEDS AT A LASER POWER OF 300 W .....	240
F6.	THE EFFECT OF DIFFERENT LASER SCANNING SPEEDS AT A LASER POWER OF 350 W .....	242
F7.	THE EFFECT OF DIFFERENT LASER POWERS AT A CONSTANT LASER SCANNING SPEED OF 0.8 M/S.....	244
F8.	REFERENCES FOR ALL APPENDICES .....	246

## Table of Figures

FIGURE 2.1:	LAYOUT OF THE LITERATURE REVIEW .....	10
FIGURE 2.2:	THE STACKING OF SUCCESSIVE ORIENTED, FIBRE-REINFORCED LAYERS FOR A LAMINAR COMPOSITE (GIBSON, 2016) .....	13
FIGURE 2.3:	A COMPOSITE SANDWICH STRUCTURE INDICATING THE FACING SHEETS AND CENTRAL THICK CORE BONDING THE TWO FACES TOGETHER (GIBSON, 2016).....	13
FIGURE 2.4:	PLOTS OF RoM AND IRoM CURVES SHOWING THE CALCULATED VARIATION OF THE ELASTIC MODULUS OF SiC/Ti6Al4V(ELI) COMPOSITES WITH VOLUME FRACTION OF SiC (SELESO ET AL., 2020) .....	19
FIGURE 2.5:	PLOT OF THE STIFFNESS VERSUS REINFORCEMENT VOLUME FRACTION FOR SiC/Ti6Al4V(ELI) COMPOSITES BASED ON THE HALPIN-TSAI SEMI-EMPIRICAL EQUATIONS, TOGETHER WITH THE UPPER AND LOWER BOUND CURVES .....	21
FIGURE 2.6:	EQUIAXED MICROSTRUCTURE OF Ti6Al4V (SEFER ET AL., 2016) .....	26
FIGURE 2.7:	LAMELLAR MICROSTRUCTURE OF Ti6Al4V (A), (B) CHARACTERISTIC DIMENSIONS OF A LAMELLAR MICROSTRUCTURE (SIENIAWSKI ET AL., 2013) .....	26
FIGURE 2.8:	IMAGES OF THE EOSINT M270 (LEFT) AND M280 (RIGHT) MACHINES (DZOGBEWU ET AL., 2017).....	29
FIGURE 2.9:	SCHEMATIC VIEW OF THE DMLS PROCESS (MANFREDI ET AL., 2013).....	30
FIGURE 2.10:	THE FOUR MOST CRITICAL PROCESS PARAMETERS FOR DMLS (BINELI ET AL., 2011) .....	32
FIGURE 2.11:	OVERLAPPING RATE BETWEEN ADJACENT TRACKS FOR VARIOUS HATCH DISTANCES: (A) 75 $\mu$ M, (B) 100 $\mu$ M, (C) 150 $\mu$ M, AND (D) 200 $\mu$ M (DONG ET AL., 2018).....	33
FIGURE 2.12:	DEPTH OF PENETRATION OF SINGLE TRACKS AT DIFFERENT SCANNING SPEEDS, (A) 250 MM/S, (B) 500 MM/S, AND (C) 750 MM/S (MUGWAGWA ET AL., 2018) .....	35
FIGURE 2.13:	SCANNING DIRECTIONS OF THE UNIDIRECTIONAL AND BI-DIRECTIONAL SCAN PATTERNS (JIA ET AL., 2021).....	37
FIGURE 2.14:	SCHEMATIC OF A STRIPE SCAN PATTERN SHOWING SCAN VECTORS AS ARROWS WITHIN EACH STRIPE (YU ET AL., 2005) .....	37
FIGURE 2.15:	ALTERNATING BLOCK PATTERNS AT ROTATION-ANGLES OF 45° (A), AND 90° (B) (ALI, 2018).....	38
FIGURE 2.16:	DIAGRAM OF CHESSBOARD SCANNING STRATEGY (ALI, 2018).....	38

FIGURE 2.17:	A SCHEMATIC DIAGRAM OF A CONTINUOUS POWDER MIXER (YEOW ET AL., 2011) .....	41
FIGURE 2.18:	A SCHEMATIC OF A V-BLENDER MACHINE (BAUMAN ET AL., 2008) .....	42
FIGURE 3.1:	RESEARCH FLOW DIAGRAM .....	52
FIGURE 3.2:	MANUAL SIEVE USED TO SIEVE Ti6Al4V(ELI) POWDER AT CRPM.....	53
FIGURE 3.3:	PLASTIC CONTAINERS USED FOR STORING MIXED POWDER .....	56
FIGURE 3.4:	AN IMAGE OF THE MULTI-BATCH MIXER USED IN THIS STUDY .....	57
FIGURE 3.5:	SCHEMATIC VIEW OF THE LAYOUT ON THE SUBSTRATE OF THE SINGLE LAYERS BUILT .....	60
FIGURE 3.6:	IMAGES OF (A) THE STRUERS CITO PRESS-1 MACHINE AND (B) THE STRUERS TEGRAMIN-25 POLISHING MACHINE.....	61
FIGURE 3.7:	AN IMAGE OF A JSM-6610 SCANNING MICROSCOPE .....	63
FIGURE 3.8:	AN IMAGE OF THE ZEISS AXIO SCOPE.A1 OPTICAL MICROSCOPE (OM).....	64
FIGURE 4.1:	CURVES OF THE STRENGTH OF SiC/Ti6Al4V(ELI) COMPOSITES VERSUS VOLUME FRACTION OF SiC PARTICLES BASED ON THE VOIGT RULE FOR HIGH AND LOW STRENGTH OF SiC PARTICLES .....	67
FIGURE 4.2:	VARIATION OF THE ELASTIC MODULUS OF SiC/Ti6Al4V(ELI) COMPOSITES WITH VARYING VOLUME FRACTIONS OF SiC PARTICLES .....	68
FIGURE 4.3:	CURVES OF ELASTIC MODULUS BASED ON THE REUSS AND VOIGT RULES, AS WELL AS THE HALPIN-TSAI SEMI-EMPIRICAL EQUATIONS FOR DIFFERENT VOLUME FRACTIONS OF SiC .....	69
FIGURE 4.4:	PLOTS OF HALPIN-TSAI SEMI-EMPIRICAL CURVES OF ELASTIC MODULUS VERSUS SiC VOLUME FRACTION WITH DIFFERENT MAGNITUDES OF THE SHAPE PARAMETERS.....	70
FIGURE 4.5:	PLOTS OF THE VOIGT, REUSS, AS WELL AS HASHIN AND STRICKMAN, MODELS FOR PREDICTING THE CTES OF SiC/Ti6Al4V(ELI) COMPOSITES FOR DIFFERENT VOLUME FRACTIONS OF SiC PARTICLES .....	71
FIGURE 4.6:	THEORETICAL VALUES OF THE HARDNESS OF THE SiC/Ti6Al4V(ELI) COMPOSITE FOR DIFFERENT SiC VOLUME FRACTIONS, BASED ON THE REUSS AND VOIGT RULES .....	73

FIGURE 5.1:	SEM (A) SE MICROGRAPH OF Ti6Al4V(ELI) PARTICLES, AND (B) BE IMAGES OF SiC PARTICLES BEFORE MIXING .....	75
FIGURE 5.2:	SEM SE MICROGRAPHS OF (A) Ti6Al4V(ELI) PARTICLES, (B) SMALL SiC PARTICLES AND SATELLITES ADHERING TO Ti6Al4V(ELI) PARTICLES AFTER MIXING.....	76
FIGURE 5.3:	SEM SE MICROGRAPHS OF SiC/Ti6Al4V(ELI) MIXTURES AT DIFFERENT SiC VOLUME FRACTIONS, AT MAGNIFICATIONS OF $\times 300$ (IMAGES IN THE LEFT COLUMN) AND $\times 500$ (IMAGES IN THE RIGHT COLUMN), (A) AND (B) 5% SiC VOL. FRACTION, (C) AND (D) 10% SiC VOL. FRACTION, (E) AND (F) 15% SiC VOL. FRACTION .....	77
FIGURE 5.4:	SEM SE MICROGRAPHS OF SiC/Ti6Al4V(ELI) MIXTURES AT DIFFERENT SiC VOLUME FRACTIONS, AT MAGNIFICATIONS OF $\times 300$ (IMAGES IN THE LEFT COLUMN) AND $\times 500$ (IMAGES IN THE RIGHT COLUMN) (A) AND (B) 20% VOL. FRACTION, (C) AND (D) 25% VOL. FRACTION, (E), AND (F) 30% VOL. FRACTION .....	78
FIGURE 6.1:	TOP VIEW OF SINGLE TRACKS INDICATING THE SURFACE CHARACTERISTICS OF TRACK CONTINUITY, SPATTER PARTICLES, NECKING AND BALLING FOR A 5 % SiC VOLUME FRACTION OF AN SiC/Ti6Al4V(ELI) COMPOSITE .....	83
FIGURE 6.2:	CROSS-SECTIONS OBTAINED AT A 5 % SiC VOLUME FRACTION OF AN SiC/Ti6Al4V(ELI) COMPOSITE SHOWING THE DIMENSIONS OF THEIR CRITICAL GEOMETRICAL FEATURES.....	86
FIGURE 6.3:	TOP VIEWS AND CROSS-SECTIONS OF THE BEST SINGLE TRACKS PRODUCED AT A 5% SiC VOLUME FRACTION IN AN SiC/Ti6Al4V(ELI) COMPOSITE .....	87
FIGURE 6.4:	MICROGRAPHS OF SINGLE TRACKS BUILT AT A LASER POWER OF 200 W AND DIFFERENT LASER SCANNING SPEEDS FROM 0.8 M/S TO 1.6 M/S .....	89
FIGURE 6.5:	CROSS-SECTIONAL IMAGES OF SINGLE TRACKS PRODUCED AT A LASER POWER OF 200 W AT DIFFERENT SCANNING SPEEDS FROM 0.8 M/S TO 1.5 M/S .....	90
FIGURE 6.6:	TOP SURFACE (A) SEM MICROGRAPH, (B) MAGNIFIED SEM MICROGRAPH, BOTH OF SINGLE TRACKS BUILT AT 200 W, 1 M/S (200 J/M) SHOWING PARTICLES OF SiC AND SPATTER Ti6Al4V(ELI) .....	92

FIGURE 6.7:	TOP SURFACE SCANS AND CROSS-SECTIONS OF SINGLE TRACKS BUILT AT A SCANNING SPEED OF 0.8 M/S AND DIFFERENT LASER POWERS OF 100 W, 150 W, AND 200 W .....	92
FIGURE 6.8:	TOP VIEWS AND CROSS-SECTIONS OF THE BEST SINGLE TRACKS PRODUCED AT A 10% SiC VOLUME FRACTION IN AN SiC/Ti6Al4V(ELI) COMPOSITE .....	97
FIGURE 6.9:	TOP VIEW IMAGES AND CROSS-SECTIONS OF THE BEST SINGLE TRACKS PRODUCED AT A 15% SiC VOLUME FRACTION IN AN SiC/Ti6Al4V(ELI) COMPOSITE .....	100
FIGURE 6.10:	TOP VIEW AND CROSS-SECTIONS OF THE BEST SINGLE TRACKS PRODUCED AT 20% SiC VOLUME FRACTION IN AN SiC/Ti6Al4V(ELI) COMPOSITE .....	104
FIGURE 6.11:	TOP VIEWS AND CROSS-SECTIONS OF THE BEST SINGLE TRACKS AT LASER POWERS OF 100 W AND 200 W PRODUCED AT A 25% SiC VOLUME FRACTION IN AN SiC/Ti6Al4V(ELI) COMPOSITE .....	109
FIGURE 6.12:	GRAPHS OF THE VARIATION OF BEST PROCESS PARAMETERS SET VALUES OF LASER POWER, LINEAR ENERGY DENSITY AND LASER SCANNING SPEED WITH SiC VOLUME FRACTION .....	114
FIGURE 6.13:	GRAPHS OF WIDTH AND HEIGHT ABOVE THE SUBSTRATE AND DEPTH OF PENETRATION OF SiC/Ti6Al4V(ELI) SINGLE TRACKS BUILT AT DIFFERENT VOLUME FRACTIONS OF SiC .....	116
FIGURE 7.1:	GRAPH OF THEORETICAL OVERLAP RATES VERSUS HATCH DISTANCES OF AN SiC/Ti6Al4V(ELI) COMPOSITE AT 5% SiC VOLUME FRACTION AT DIFFERENT HATCH DISTANCES FROM 50 μM TO 110 μM .....	124
FIGURE 7.2:	SEM SE IMAGES OF THE CROSS-SECTIONS OF SINGLE LAYERS AT DIFFERENT HATCH DISTANCES OF (A) 50 μM, (B) 60 μM, (C) 70 μM, (D) 80 μM, (E) 90 μM, (F) 100 μM, AND (G) 110 μM .....	125
FIGURE 7.3:	A SCHEMATIC VIEW OF SINGLE RE-MELTING OF THE TRACKS IN A LAYER BASED ON THE RELATIONSHIP BETWEEN HATCH DISTANCES AND THE WIDTHS OF TRACK .....	126
FIGURE 7.4:	A SCHEMATIC VIEW OF DOUBLE RE-MELTING OF THE TRACKS IN A LAYER BASED ON THE RELATIONSHIP BETWEEN HATCH DISTANCES AND THE WIDTHS OF TRACK .....	126
FIGURE 7.5:	THE SEM SE IMAGES OF SINGLE LAYERS AT HATCH DISTANCES OF 50 μM, (B) 60 μM, (C) 70 μM, (D) 80 μM, AND (E) 90 μM.....	128

FIGURE 7.6:	GRAPH OF THEORETICAL OVERLAP RATE VERSUS HATCH DISTANCE, AT 10% SiC VOLUME FRACTION IN AN SiC/Ti6Al4V(ELI) COMPOSITE AT DIFFERENT HATCH DISTANCES FROM 50 $\mu\text{M}$ TO 110 $\mu\text{M}$ .....	130
FIGURE 7.7:	SEM SE IMAGES OF CROSS-SECTIONS OF SINGLE LAYERS AT DIFFERENT HATCH DISTANCES OF (A) 50 $\mu\text{M}$ , (B) 60 $\mu\text{M}$ , (C) 70 $\mu\text{M}$ , (D) 80 $\mu\text{M}$ , (E) 90 $\mu\text{M}$ , (F) 100 $\mu\text{M}$ , AND (G) 110 $\mu\text{M}$ .....	131
FIGURE 7.8:	SEM SE IMAGES OF THE TOP SURFACES OF SINGLE LAYERS BUILT AT HATCH DISTANCES OF 70 $\mu\text{M}$ (LEFT), AND 80 $\mu\text{M}$ (RIGHT) .....	133
FIGURE 7.9:	GRAPH OF THEORETICAL OVERLAP RATES VERSUS HATCH DISTANCES OF AN SiC/Ti6Al4V(ELI) COMPOSITE AT 15% SiC VOLUME FRACTION AT DIFFERENT HATCH DISTANCES FROM 50 $\mu\text{M}$ TO 110 $\mu\text{M}$ .....	135
FIGURE 7.10:	SEM SE IMAGES OF CROSS-SECTIONS OF SINGLE LAYERS BUILT AT DIFFERENT HATCH DISTANCES OF (A) 50 $\mu\text{M}$ , (B) 60 $\mu\text{M}$ , (C) 70 $\mu\text{M}$ , (D) 80 $\mu\text{M}$ , (E) 90 $\mu\text{M}$ , (F) 100 $\mu\text{M}$ , AND (G) 110 $\mu\text{M}$ .....	136
FIGURE 7.11:	SEM SE IMAGES OF THE TOP VIEW OF SINGLE LAYERS BUILT AT HATCH DISTANCES OF (A) 50 $\mu\text{M}$ , (B) 60 $\mu\text{M}$ , AND (B) 70 $\mu\text{M}$ .....	138
FIGURE 7.12:	GRAPH OF THEORETICAL OVERLAP RATES VERSUS HATCH DISTANCES AT 20% SiC VOLUME FRACTION IN AN SiC/Ti6Al4V(ELI) COMPOSITE AT DIFFERENT HATCH DISTANCES FROM 50 $\mu\text{M}$ TO 110 $\mu\text{M}$ .....	140
FIGURE 7.13:	SEM SE IMAGES OF CROSS-SECTIONS OF SINGLE LAYERS PRODUCED AT CONSTANT LASER POWER, SCANNING SPEED, AND ENERGY DENSITY OF 200 W, 0.9 M/S, AND 222 J/M, RESPECTIVELY, WITH DIFFERENT HATCH DISTANCES OF (A) 50 $\mu\text{M}$ , (B) 60 $\mu\text{M}$ , (C) 70 $\mu\text{M}$ , (D) 80 $\mu\text{M}$ , (E) 90 $\mu\text{M}$ , (F) 100 $\mu\text{M}$ , AND (G) 110 $\mu\text{M}$ .....	141
FIGURE 7.14:	SEM SE MICROGRAPHS OF THE TOP SURFACES OF SINGLE LAYERS BUILT AT HATCH DISTANCES OF (A) 50 $\mu\text{M}$ , (B) 60 $\mu\text{M}$ , (C) 70 $\mu\text{M}$ , AND (D) 80 $\mu\text{M}$ .....	143
FIGURE 7.15:	GRAPH OF THEORETICAL OVERLAP RATES VERSUS HATCH DISTANCES AT 25 % SiC VOLUME FRACTION IN AN SiC/Ti6Al4V(ELI) COMPOSITE AT DIFFERENT HATCH DISTANCES FROM 50 $\mu\text{M}$ TO 110 $\mu\text{M}$ .....	145
FIGURE 7.16:	SEM SE IMAGES OF CROSS-SECTIONS OF SINGLE LAYERS PRODUCED AT A CONSTANT LASER POWER, SCANNING SPEED, AND ENERGY DENSITY OF 200 W,	

	1.2 M/s, AND 167 J/M, RESPECTIVELY, WITH DIFFERENT HATCH DISTANCES (A) 50 μM, (B) 60 μM, (C) 70 μM, (D) 80 μM, (E) 90 μM, (F) 100 μM, AND (G) 110 μM .....	146
FIGURE 7.17:	GRAPH OF THEORETICAL OVERLAP RATE VERSUS HATCH DISTANCE OF SiC/Ti6Al4V(ELI) AT 30 % VOLUME FRACTION OF SiC IN SiC/Ti6Al4V(ELI) COMPOSITE AT DIFFERENT HATCH DISTANCES FROM 50 μM TO 110 μM.....	149
FIGURE 7.18:	SEM SE IMAGES OF CROSS-SECTIONS OF SINGLE LAYERS PRODUCED AT A CONSTANT LASER POWER, SPEED, AND ENERGY DENSITY OF 350 W, 1.7 M/s, AND 206 J/M, RESPECTIVELY, WITH DIFFERENT HATCH DISTANCES (A) 50 μM, (B) 60 μM, (C) 70 μM, (D) 80 μM, (E) 90 μM, (F) 100 μM, AND (G) 110 μM .....	150
FIGURE 7.19:	SEM SE MICROGRAPHS OF TOP SURFACES OF SINGLE LAYERS PRODUCED AT DIFFERENT HATCH DISTANCES OF 50 μM.....	151
FIGURE A1:	SINGLE TRACKS BUILT AT A POWER OF 100 W AND DIFFERENT LASER SCANNING SPEEDS FROM 0.3 M/s TO 0.9 M/s.....	158
FIGURE A2:	CROSS-SECTIONAL IMAGES OF SINGLE TRACKS PRODUCED AT A LASER POWER OF 100 W, WITH LASER SCANNING SPEEDS FROM 0.3 M/s TO 0.9 M/s.....	160
FIGURE A3:	SINGLE TRACKS BUILT AT A LASER POWER OF 150 W AND DIFFERENT SCANNING SPEEDS FROM 0.6 M/s TO 1.2 M/s.....	161
FIGURE A4:	CROSS-SECTIONAL IMAGES OF SINGLE TRACKS BUILT AT SCANNING SPEEDS FROM 0.6 M/s TO 1.2 M/s AT A LASER POWER OF 150 W.....	163
FIGURE A5:	SINGLE TRACKS BUILT AT LASER SCANNING SPEEDS FROM 1.1 M/s TO 1.9 M/s AT A CONSTANT POWER OF 250 W .....	164
FIGURE A6:	CROSS-SECTIONS OF TRACKS BUILT AT A LASER POWER OF 250 W WITH DIFFERENT SCANNING SPEEDS FROM 1.1 M/s TO 1.9 M/s.....	166
FIGURE A7:	SINGLE TRACKS BUILT AT A CONSTANT POWER OF 300 W WITH SCANNING SPEEDS FROM 1.2 M/s TO 2.4 M/s.....	167
FIGURE A8:	CROSS-SECTIONAL IMAGES OF THE TRACKS BUILT AT A LASER POWER OF 300 W WITH DIFFERENT LASER SCANNING SPEEDS FROM 1.2 M/s TO 2.4 M/s .....	168
FIGURE A9:	SINGLE TRACKS BUILT AT A LASER POWER OF 350 W AND DIFFERENT SCANNING SPEEDS FROM 1.5 M/s TO 2.7 M/s.....	169

FIGURE A10:	TOP SURFACE SCANS AND CROSS-SECTIONS OF SINGLE TRACKS BUILT AT A SCANNING SPEED OF 0.8 M/S AND DIFFERENT LASER POWERS OF 100 W, 150 W, AND 200 W .....	170
FIGURE A11:	SINGLE TRACKS PRINTED AT A LINEAR ENERGY DENSITY OF 167 J/M AND DIFFERENT LASER SCANNING SPEEDS AND POWER.....	172
FIGURE A12:	CROSS-SECTIONS OF SINGLE TRACKS PRINTED AT A LINEAR ENERGY DENSITY OF 167 J/M AND DIFFERENT LASER SCANNING SPEEDS AND POWER .....	173
FIGURE B1:	SINGLE TRACK IMAGES AT A CONSTANT POWER OF 100 W AND DIFFERENT LASER SCANNING SPEEDS FROM 0.3 M/S TO 0.7 M/S .....	174
FIGURE B2:	CROSS-SECTIONAL VIEWS OF TRACKS BUILT AT LASER SCANNING SPEEDS FROM 0.3 M/S TO 0.7 M/S WITH A CONSTANT POWER OF 100 W.....	175
FIGURE B3:	SINGLE-TRACK SEM IMAGES AT A LASER POWER OF 150 W AND DIFFERENT SCANNING SPEEDS FROM 0.6 M/S TO 0.9 M/S.....	177
FIGURE B4:	CROSS-SECTIONS OF TRACKS BUILT AT DIFFERENT LASER SCANNING SPEEDS FROM 0.6 M/S TO 1.2 M/S AT A CONSTANT LASER POWER OF 150 W.....	178
FIGURE B5:	MICROGRAPHS OF SINGLE TRACKS BUILT AT A CONSTANT LASER POWER OF 200 W AND DIFFERENT LASER SCANNING SPEEDS FROM 0.8 M/S TO 1.6 M/S .....	180
FIGURE B6:	CROSS-SECTIONAL IMAGES OF TRACKS BUILT AT LASER SCANNING SPEEDS FROM 0.8 M/S TO 1.6 M/S .....	181
FIGURE B7:	SINGLE TRACKS BUILT AT A CONSTANT LASER POWER OF 250 W AND DIFFERENT LASER SCANNING SPEEDS FROM 1.1 M/S TO 1.7 M/S .....	182
FIGURE B8:	SINGLE TRACKS BUILT AT A CONSTANT POWER OF 300 W WITH DIFFERENT LASER SCANNING SPEEDS FROM 1.2 M/S TO 2.4 M/S .....	183
FIGURE B9:	CROSS-SECTIONS OF THE SINGLE TRACKS PRINTED AT THE LASER POWER OF 300 W WITH DIFFERENT LASER SCANNING SPEEDS FROM 1.2 M/S TO 2.4 M/S.....	184
FIGURE B10:	SINGLE TRACKS BUILT AT THE HIGHEST LASER POWER OF 350 W AND DIFFERENT SCANNING SPEEDS .....	185
FIGURE B11:	CROSS-SECTIONS OF SINGLE TRACKS PRINTED AT A LASER POWER OF 350 W WITH DIFFERENT LASER SCANNING SPEEDS FROM 1.5 M/S TO 2.7 M/S .....	186
FIGURE B12:	SINGLE TRACKS BUILT AT A CONSTANT SCANNING SPEED OF 0.8 M/S WITH DIFFERENT POWERS OF 150 W AND 200W.....	187

FIGURE C1:	SINGLE TRACKS AT A CONSTANT LASER POWER OF 100 W WITH DIFFERENT LASER SCANNING SPEEDS FROM 0.4 M/S TO 0.9 M/S .....	188
FIGURE C2:	CROSS-SECTIONAL VIEWS OF SINGLE TRACKS PRODUCED AT A CONSTANT LASER POWER OF 100 W WITH DIFFERENT SCANNING SPEEDS FROM 0.4 M/S TO 0.9 M/S.....	189
FIGURE C3:	SINGLE TRACKS AT A CONSTANT LASER POWER OF 150 W WITH DIFFERENT LASER SCANNING SPEEDS FROM 0.7 M/S TO 1.2 M/S .....	191
FIGURE C4:	CROSS-SECTIONAL VIEWS OF SINGLE TRACKS PRODUCED AT A CONSTANT LASER POWER OF 150 W, WITH DIFFERENT SCANNING SPEEDS FROM 0.7 M/S TO 1.2 M/S.....	192
FIGURE C5:	SINGLE TRACKS AT A CONSTANT LASER POWER OF 200 W WITH DIFFERENT LASER SCANNING SPEEDS FROM 0.8 M/S TO 1.4 M/S .....	193
FIGURE C6:	CROSS-SECTIONAL VIEWS OF TRACKS PRODUCED AT A CONSTANT LASER POWER OF 200 W WITH DIFFERENT LASER SCANNING SPEEDS FROM 1 M/S TO 1.6 M/S.....	194
FIGURE C7:	TOP VIEW OF SINGLE TRACKS PRODUCED AT A CONSTANT LASER POWER OF 250 W WITH DIFFERENT SCANNING SPEEDS FROM 1.1 M/S TO 1.9 M/s .....	195
FIGURE C8:	CROSS-SECTIONAL VIEWS OF TRACKS PRODUCED AT A CONSTANT LASER POWER OF 250 W AND DIFFERENT LASER SCANNING SPEEDS .....	196
FIGURE C9:	TOP SURFACE VIEW OF THE TRACKS BUILT WITH A 300 W LASER POWER AT DIFFERENT SCANNING RATES RANGING FROM 1.2 M/S TO 2.4 M/S.....	197
FIGURE C10:	CROSS-SECTIONAL VIEWS OF TRACKS PRODUCED AT A CONSTANT LASER POWER OF 300 W AND DIFFERENT LASER SCANNING SPEEDS FROM 1.2 M/S TO 2.4 M/S.....	198
FIGURE C11:	THE TOP VIEW OF THE SURFACE SCANS PRODUCED AT A LASER POWER OF 350 W AT DIFFERENT SCANNING SPEEDS FROM 1.5 M/S TO 2.5 M/S.....	199
FIGURE C12:	CROSS-SECTIONAL VIEWS OF TRACKS PRODUCED AT A CONSTANT LASER POWER OF 350 W AND DIFFERENT LASER SCANNING SPEED FROM 1.5 M/S TO 2.5 M/S .....	200
FIGURE C13:	CROSS-SECTIONAL VIEWS OF TRACKS BUILT AT (A AND B) A CONSTANT SPEED OF 0.8 M/S, WITH DIFFERENT MAGNITUDES OF LASER POWER FROM 100 W TO 150 W, AND (C AND D) A CONSTANT SPEED OF 1.5 M/S AND MAGNITUDES OF LASER POWER OF 250 W AND 350 W .....	201

FIGURE D1:	TOP SURFACE VIEWS OF SINGLE TRACKS PRODUCED AT A CONSTANT LASER POWER OF 100 W, WITH DIFFERENT LASER SCANNING SPEEDS FROM 0.3 M/S TO 0.9 M/S.....	203
FIGURE D2:	TOP SURFACE VIEW OF SINGLE TRACKS PRODUCED AT A CONSTANT LASER POWER OF 100 W, WITH DIFFERENT LASER SCANNING SPEEDS FROM 0.3 M/S TO 0.9 M/S.....	204
FIGURE D3:	TOP SURFACE VIEWS OF SINGLE TRACKS PRODUCED AT A CONSTANT LASER POWER OF 150 W, WITH DIFFERENT LASER SCANNING SPEEDS FROM 0.6 M/S TO 1.2 M/S.....	205
FIGURE D4:	TOP SURFACE VIEW OF SINGLE TRACKS PRODUCED AT A CONSTANT LASER POWER OF 100 W, WITH DIFFERENT LASER SCANNING SPEEDS FROM 0.3 M/S TO 0.9 M/S.....	206
FIGURE D5:	TOP VIEWS OF SINGLE TRACKS PRODUCED AT A CONSTANT POWER OF 200 W AND DIFFERENT LASER SCANNING SPEEDS FROM 0.8 M/S TO 1.6 M/S.....	207
FIGURE D6:	CROSS-SECTIONAL VIEWS OF THE SINGLE TRACKS BUILT AT A CONSTANT LASER POWER OF 200 W, WITH DIFFERENT LASER SCANNING SPEEDS FROM 0.8 M/S TO 1.6 M/S.....	208
FIGURE D7:	TOP VIEW IMAGES OF TRACKS BUILT AT A LASER POWER OF 250 W WITH DIFFERENT LASER SCAN SPEEDS FROM 1.2 M/S TO 1.9 M/S.....	209
FIGURE D8:	CROSS-SECTIONAL VIEWS OF SINGLE TRACKS BUILT AT A CONSTANT LASER POWER OF 250 W, WITH DIFFERENT LASER SCANNING SPEEDS FROM 1.1 M/S TO 1.9 M/S.....	210
FIGURE D9:	TOP VIEW MICROGRAPHS OF TRACKS BUILT AT DIFFERENT LASER SCANNING SPEEDS AND A LASER POWER OF 300 W.....	211
FIGURE D10:	IMAGES OF THE CROSS-SECTIONS OF SINGLE TRACKS BUILT AT A LASER POWER OF 300 W, WITH DIFFERENT LASER SCANNING SPEEDS FROM 1.2 M/S TO 2 M/S.....	212
FIGURE D11:	TOP VIEW IMAGES OF SINGLE TRACKS BUILT AT A CONSTANT POWER OF 350 W WITH DIFFERENT LASER SCANNING SPEEDS FROM 1.5 M/S TO 2.5 M/S.....	213
FIGURE D12:	CROSS-SECTIONAL VIEW OF SINGLE TRACKS BUILT AT A LASER POWER OF 350 W, WITH DIFFERENT LASER SCANNING SPEEDS FROM 1.5 M/S TO 2.5 M/S.....	214

FIGURE E1:	TOP VIEWS OF SINGLE TRACKS BUILT AT DIFFERENT LASER SCANNING SPEEDS FROM 0.3 M/S TO 0.9 M/S AT A CONSTANT POWER OF 100 W .....	216
FIGURE E2:	CROSS-SECTIONAL VIEWS OF SINGLE TRACKS PRODUCED AT A LASER POWER OF 100 W, WITH DIFFERENT LASER SCANNING SPEEDS FROM 0.3 M/S TO 0.9 M/S .....	217
FIGURE E3:	SINGLE TRACKS BUILT AT A CONSTANT LASER POWER OF 150 W WITH DIFFERENT LASER SCANNING SPEEDS FROM 0.6 M/S TO 1.2 M/S .....	218
FIGURE E4:	CROSS-SECTIONS OF TRACKS PRODUCED AT A LASER POWER OF 150 W, WITH LASER SCANNING SPEEDS RANGING FROM 0.6 M/S TO 1.2 M/S .....	219
FIGURE E5:	TOP VIEW OF THE TRACKS BUILT AT LASER SCANNING SPEEDS FROM 0.9 M/S TO 1.6 M/S AT A CONSTANT LASER POWER OF 200 W .....	220
FIGURE E6:	CROSS-SECTIONAL IMAGES OF SINGLE TRACKS PRODUCED AT A LASER POWER OF 200 W AND DIFFERENT SCANNING SPEEDS .....	221
FIGURE E7:	TOP SURFACE MICROGRAPHS OF TRACKS, BUILT AT A CONSTANT POWER OF 250 W AND DIFFERENT LASER SCANNING SPEEDS FROM 1.1. M/S TO 1.9 M/S.....	223
FIGURE E8:	CROSS-SECTIONAL VIEWS OF SINGLE TRACKS BUILT AT A LASER POWER OF 250 W .....	224
FIGURE E9:	TOP SURFACE MICROGRAPHS OF TRACKS, BUILT AT A CONSTANT POWER OF 300 W AND DIFFERENT LASER SCANNING SPEEDS FROM 1.2. M/S TO 2.4 M/S .....	225
FIGURE E10:	CROSS-SECTIONAL VIEWS OF THE TRACKS BUILT AT A LASER POWER OF 300 W .....	226
FIGURE E11:	TOP SURFACE SEM MICROGRAPHS OF TRACKS, BUILT AT A CONSTANT POWER OF 350 W AND DIFFERENT LASER SCANNING SPEEDS FROM 1.5 M/S TO 2.7 M/S .....	228
FIGURE E12:	CROSS-SECTIONS OF TRACKS BUILT AT A CONSTANT LASER POWER OF 350 W AND DIFFERENT LASER SCANNING SPEEDS FROM 1.5 M/S TO 2.7 M/S.....	229
FIGURE E13:	CROSS-SECTIONS BUILT AT A LASER SCANNING SPEED OF 0.8 M/S AND DIFFERENT VALUES OF LASER POWER FROM 100 W TO 200 W .....	230
FIGURE F1:	TOP SURFACE SEM IMAGES OF SINGLE TRACKS PRODUCED AT A CONSTANT LASER POWER OF 100 W WITH DIFFERENT LASER SCANNING SPEEDS .....	231
FIGURE F2:	CROSS-SECTIONAL VIEWS OF SINGLE TRACKS BUILT AT A CONSTANT LASER POWER OF 100 W.....	232
FIGURE F3:	SINGLE TRACKS BUILT AT A LASER POWER OF 150 W, WITH DIFFERENT LASER SCANNING SPEEDS FROM 0.6 M/S TO 1.2 M/S.....	234

FIGURE F4:	CROSS-SECTIONS OF TRACKS PRODUCED AT A CONSTANT LASER POWER OF 150 W, WITH DIFFERENT LASER SCANNING SPEEDS FROM 0.6 M/S TO 1.2 M/S.....	235
FIGURE F5:	TOP VIEW IMAGES OF SINGLE TRACKS PRODUCED AT A CONSTANT LASER POWER OF 200 W AND DIFFERENT LASER SCANNING SPEEDS .....	236
FIGURE F6:	CROSS-SECTIONAL IMAGES OF SINGLE TRACKS PRODUCED AT A CONSTANT LASER POWER OF 200 W.....	237
FIGURE F7:	SINGLE TRACKS BUILT AT A LASER POWER OF 250 W, WITH DIFFERENT LASER SCANNING SPEEDS .....	238
FIGURE F8:	CROSS-SECTIONS OF SINGLE TRACKS BUILT AT A CONSTANT LASER POWER OF 250 W AND DIFFERENT LASER SCANNING SPEEDS FROM 1.2 M/S TO 1.9 M/S.....	239
FIGURE F9:	SINGLE TRACKS BUILT AT A LASER POWER OF 300 W, WITH DIFFERENT LASER SCANNING SPEEDS FROM 1.2 M/S TO 2.4 M/S.....	241
FIGURE F10:	CROSS-SECTIONS OF SINGLE TRACKS BUILT AT A LASER POWER OF 300 W, WITH DIFFERENT LASER SCANNING SPEEDS FROM 1.4 M/S TO 2.4 M/S.....	242
FIGURE F11:	SINGLE TRACKS BUILT AT A LASER POWER OF 350 W, WITH DIFFERENT LASER SCANNING SPEEDS FROM 1.5 M/S TO 2.7 M/S.....	243
FIGURE F12:	CROSS-SECTIONS OF SINGLE TRACKS PRODUCED AT A CONSTANT LASER POWER OF 350 W AT DIFFERENT SCANNING SPEEDS FROM 1,5 M/S TO 2.7 M/s .....	244
FIGURE F13:	CROSS-SECTIONS OF SINGLE TRACKS PRODUCED AT A CONSTANT LASER SCANNING SPEED WITH DIFFERENT LASER POWERS FROM 100 W TO 200 W .....	245

## List of Tables

TABLE 2.1:	FUNCTIONS OF MATRICES AND REINFORCEMENTS IN A COMPOSITE (CAMPBELL, 2010; THORI ET AL., 2013; MACKIE ET AL., 2012).....	11
TABLE 2.2:	SOME MECHANICAL AND PHYSICAL PROPERTIES OF VARIOUS PARTICLE REINFORCEMENTS AND THE Ti6Al4V MATRIX (SERIN, 2018; ABHIJITH, 2016; JUSTIN ET AL., 2011; RABINKIN, 2013; WALKER, 1991; JANKOWIAK, 2011).....	15
TABLE 2.3:	SOME MECHANICAL AND PHYSICAL PROPERTIES OF THREE METALLIC BASES FOR METAL MATRIX COMPOSITES (LAUREL, 2017; NAGAVALLY, 2017; JUSTIN ET AL., 2011). .....	17
TABLE 2.4:	THE SHAPE AND SIZE OF SiC AND Ti6Al4V PARTICLES USED IN THE PRESENT WORK.....	24
TABLE 2.5:	DIFFERENCE IN COMPOSITION OF Ti6Al4V AND Ti6Al4V(ELI) .....	24
TABLE 2.6:	TECHNICAL DATA OF EOSINT M270 AND M280 MACHINES (ELS ET AL., 2016) .....	29
TABLE 3.1:	THE TOTAL MASS OF SiC, Ti6Al4V(ELI) AND MIXED POWDERS REQUIRED FOR TWO TYPES OF TEST SPECIMENS FOR EACH VOLUME FRACTION OF SiC .....	55
TABLE 3.2:	PROCESS PARAMETERS USED FOR BUILDING SiC/Ti6Al4V(ELI) SINGLE TRACKS.....	58
TABLE 3.3:	PROCESS PARAMETERS USED AT EACH VOLUME FRACTION TO BUILD SINGLE LAYERS .....	59
TABLE 3.4:	DETAILS OF THE GRINDING AND POLISHING STEPS RECOMMENDED BY STRUERS (DZOGBEWU ET AL., 2017).....	62
TABLE 6.1:	CATEGORISATION OF SINGLE TRACKS BASED ON THE CONTINUITY AND DISCONTINUITY TRACKS, PRE-BALLING/NECKING AND BALLING .....	82
TABLE 6.2:	CATEGORISATION OF THE CROSS-SECTIONS OF SINGLE TRACKS BASED ON DEPTH-TO-WIDTH RATIOS .....	85
TABLE 6.3:	CATEGORISATION OF SINGLE TRACKS BASED ON CONTINUITY AND DISCONTINUITY TRACKS, PRE-BALLING/NECKING AND BALLING.....	94
TABLE 6.4:	CATEGORISATION OF THE CROSS-SECTIONS OF SINGLE TRACKS BASED ON DEPTH-TO-WIDTH RATIOS .....	95
TABLE 6.5:	CATEGORISATION OF SINGLE TRACKS BASED ON CONTINUITY AND DISCONTINUITY TRACKS, PRE-BALLING/NECKING AND BALLING .....	98

TABLE 6.6:	CATEGORISATION OF THE CROSS-SECTIONS OF SINGLE TRACKS BASED ON DEPTH-TO-WIDTH RATIOS.....	99
TABLE 6.7:	CATEGORISATION OF SINGLE TRACKS BASED ON TRACK CONTINUITY, DISCONTINUITY, PRE-BALLING/NECKING AND BALLING .....	102
TABLE 6.8:	CATEGORISATION OF THE CROSS-SECTIONS OF SINGLE TRACKS BASED ON DEPTH-TO-WIDTH RATIOS.....	103
TABLE 6.9:	CATEGORISATION OF SINGLE TRACKS BASED ON CONTINUITY AND DISCONTINUITY TRACKS, PRE-BALLING/NECKING AND BALLING .....	105
TABLE 6.10:	CATEGORISATION OF THE CROSS-SECTIONS OF SINGLE TRACKS BASED ON DEPTH-TO-WIDTH RATIOS.....	107
TABLE 6.11:	CATEGORISATION OF SINGLE TRACKS BASED ON CONTINUITY AND DISCONTINUITY TRACKS, PRE-BALLING/NECKING AND BALLING .....	111
TABLE 6.12:	CATEGORISATION OF THE CROSS-SECTIONS OF SINGLE TRACKS BASED ON DEPTH-TO-WIDTH RATIOS.....	112
TABLE 6.13:	SUMMARY OF THE BEST PROCESS PARAMETERS FROM 5 % TO 30 % SiC VOLUME FRACTIONS OF SiC IN SiC/Ti6Al4V(ELI) COMPOSITES DETERMINED IN THIS CHAPTER.....	113
TABLE 6.14:	SUMMARY OF THE GEOMETRICAL CHARACTERISTICS OF WIDTH, DEPTH AND HEIGHT OF TRACKS PRINTED WITH THE BEST PROCESS PARAMETERS FOR 5% TO 30% SiC VOLUME FRACTIONS OF SiC IN SiC/Ti6Al4V(ELI) COMPOSITES .....	115
TABLE 7.1:	THEORETICAL, CALCULATED OVERLAP RATES AT DIFFERENT HATCH DISTANCES FROM 50 $\mu\text{m}$ TO 110 $\mu\text{m}$ , FOR A 5% SiC VOLUME FRACTION OF AN SiC/Ti6Al4V(ELI) COMPOSITE, BUILT AT A LASER POWER AND SCANNING SPEED OF 200 W AND 1.2 M/S, RESPECTIVELY.....	123
TABLE 7.2:	THEORETICAL, CALCULATED VALUES OF OVERLAP RATES AT DIFFERENT HATCH DISTANCES FROM 50 $\mu\text{m}$ TO 110 $\mu\text{m}$ FOR A 10 % SiC VOLUME FRACTION OF AN SiC/Ti6Al4V(ELI) COMPOSITE BUILT AT A LASER POWER AND SCANNING SPEED OF 150 W, 0.8 M/S, RESPECTIVELY .....	130
TABLE 7.3:	THEORETICAL, CALCULATED VALUES OF OVERLAP RATES AT DIFFERENT HATCH DISTANCES FROM 50 $\mu\text{m}$ TO 110 $\mu\text{m}$ FOR A 15 % SiC VOLUME FRACTION OF	

AN SiC/Ti6Al4V(ELI) COMPOSITE BUILT AT A LASER POWER AND SCANNING SPEED OF 100 W, 0.4 M/S, RESPECTIVELY .....	134
TABLE 7.4: THEORETICAL, CALCULATED VALUES OF OVERLAP RATES AT DIFFERENT HATCH DISTANCES FROM 50 $\mu\text{M}$ TO 110 $\mu\text{M}$ FOR A 20% SiC VOLUME FRACTION OF AN SiC/Ti6Al4V(ELI) COMPOSITE BUILT AT A LASER POWER AND SCANNING SPEED OF 200 W, 0.9 M/S, RESPECTIVELY .....	139
TABLE 7.5: THEORETICAL, CALCULATED VALUES OF OVERLAP RATES AT DIFFERENT HATCH DISTANCES FROM 50 $\mu\text{M}$ TO 110 $\mu\text{M}$ FOR A 25% SiC VOLUME FRACTION OF AN SiC/Ti6Al4V(ELI) COMPOSITE BUILT AT A RESPECTIVE LASER POWER AND SCANNING SPEED OF 200 W, 1.2 M/S .....	144
TABLE 7.6: THEORETICAL, CALCULATED VALUES OF OVERLAP RATES AT DIFFERENT HATCH DISTANCES FROM 50 $\mu\text{M}$ TO 110 $\mu\text{M}$ FOR A 30 % SiC VOLUME FRACTION OF AN SiC/Ti6Al4V(ELI) COMPOSITE BUILT AT A LASER POWER AND SCANNING SPEED OF 350 W, 1.7 M/S, RESPECTIVELY .....	148

## ABBREVIATIONS AND ACRONYMS

3D	Three-Dimensions
AM	Additive Manufacturing
ASTM	American Society for Testing and Materials
CAD	Computer-Aided Design
CRPM	Centre for Rapid Prototyping and Manufacturing
CTE	Coefficient of Thermal Expansion
DMLS	Direct Metal Laser Sintering
ELI	Extra Low Interstitial
K	Kelvin
LPBF	Laser Powder Bed Fusion
MMC	Metal Matrix Composite
OM	Optical Microscope
SEM	Scanning Electron Microscope
SLM	Selective Laser Melting
$\mu\text{m}$	Micrometre

## CHAPTER 1: INTRODUCTION

### 1.1. Background

Additive manufacturing (AM) is a technique that uses 3D model data to build parts in a layer-by-layer fashion until a complete component is produced. The benefits of AM include the production of parts with complex geometries, like hollow structures and undercuts that are not possible to produce with normal subtractive methods, less waste of materials and a reduction in the number of parts for components with complex geometries (Gospondinov et al., 2016).

The direct metal laser sintering (DMLS) technique has traditionally been applied to pre-alloyed metallic powder but is also gaining use for metallic composite powders (Gospondinov, et al., 2016). The Ti6Al4V alloy is already used in aircraft but cannot be applied at temperatures higher than 500 °C (Veiga et al., 2012). Therefore, applications of this alloy in parts such as rocket nozzles, leading edges of wings, and nose tips are excluded (Veiga et al., 2012). Aircraft fly at high velocities and require materials that are lightweight and can withstand high temperatures for long periods. To this end, the thermal properties of Ti6Al4V are improved by reinforcing the alloy with ultra-high temperature ceramics, because they are stable at temperatures above 500 °C (Serin et al., 2016).

Titanium and its alloys are widely used due to their good mechanical and physical properties. Titanium is more corrosion-resistant in seawater and air than stainless steel. It is highly reactive with oxygen and forms an oxide layer (TiO<sub>2</sub>) between 5–6 nm thick on its surface (Megson et al., 2016; Veiga et al., 2012). This very adherent oxide layer prevents further corrosion because corrosive agents cannot diffuse through it to reach the metal. Due to the high corrosion resistance of titanium, it is widely used for biomedical implants and marine applications like outboard motors, hulls of ships, propeller shafts and other structures exposed to seawater (Veiga et al., 2012).

The most widely used alloy of titanium is Ti6Al4V, which is stronger (ultimate tensile stress (UTS) = 950 MPa) than most steels (UTS = 400–1000 MPa) and aluminium (UTS = 45–60 MPa). It has a density of 4.45 g/cm<sup>3</sup> that is lower than that of structural steel (7.4 g/cm<sup>3</sup>) and higher than that of aluminium (2.5 g/cm<sup>3</sup>) (Rosso et al., 2003; Megson et al., 2016; Veiga et al., 2012). The specific strength of Ti6Al4V (211 kNm/kg)

is much higher than that of steel (54–139 kNm/kg) and aluminium (18–24 kNm/kg), which gives it an advantage over aluminium and steel in the manufacture of lightweight structures in the aircraft industry (Donachie, 2000). SiC particles have values of strength and hardness within the ranges of (240-1625 MPa), and (600-3800 GPa), respectively. Consequently, the values of strength of SiC/Ti6Al4V(ELI) composites are expected to vary with increasing volume fraction of SiC particles. Thus, according to the Reuss rule (which from the elastic theory of composites gives more accurate predictions for particulate composites than the Voigt rule), the strength of SiC/Ti6Al4V(ELI) is expected to lie within the range 808 MPa-1085 MPa at a volume fraction of 20% and 680 MPa-1200 MPa at a volume fraction of 40%, for the two extreme values of strength of SiC mentioned here, respectively. The volume fraction of SiC filler likewise impacts the hardness of SiC/Ti6Al4V(ELI) composites. According to the Reuss rule, the hardness of the composite is expected to lie within the range 440-850 MPa at a 20% SiC volume fraction and 557-1338 MPa at a 40% SiC volume fraction, for the two extreme values of hardness of SiC mentioned here, respectively.

At a volume fraction of reinforcing SiC particles of 20%, the elastic modulus of the SiC/Ti6Al4V (ELI) composite is expected from the Reuss rule to be 130 GPa. This is higher than that of Ti6Al4V (110 GPa) and lower than that of the SiC particles (410 GPa). This is an 18% increase in modulus over that of Ti6Al4V. At a volume fraction of the reinforcing SiC particles of 40%, the elastic modulus of the composite is expected from the Reuss rule to increase further to 156 GPa. This represent an increase of 42% over that of Ti6Al4V(ELI). However, in practice, the final values of strength, hardness and stiffness obtained will depend on the quality of the interface between the two constituent components of the composite, which is subject to various factors such as roughness of the bonding surfaces, CTE of the two constituents, and their bonding surface area.

A composite material is a combination of two or more elements that results in better properties than the individual components alone. Composites are made up of two phases: reinforcement and matrix (Walker, 1991; Baker, 2004). Matrices are often tough and ductile, whereas reinforcing elements are strong with high stiffness and low density. The properties of composites are primarily influenced by the matrix and reinforcement properties, as well as the interface created between the two, with the

interface having a key role in composite performance (Walker,1991). Metal matrix composites (MMCs) are composites that have metals and their alloys as matrices and are reinforced with other metals or non-metallic materials like ceramics in the form of whiskers, particles, or fibres. The most common MMCs are classified in three different types, namely particle-reinforced MMCs, short-fibre- or whisker-reinforced MMCs, and continuous fibre-reinforced MMCs (Peasby, 2001).

Particles usually reinforce a composite equally in all directions and, therefore, are said to provide isotropic reinforcement (Rosso, 2003). The addition of particles in a matrix increases the modulus of the matrix, reduces the percentage elongation, and increases the tensile strength. Ceramic particles have low coefficients of thermal expansion and will, therefore, give rise to Ti6Al4V composites with lower coefficients of thermal expansion than the Ti6Al4V matrix. This minimizes expansion and contraction during the heating or cooling of the composites (Rosso, 2003).

Particulate reinforcements that are generally used in MMCs include ceramics such as nitrides, oxides, and carbides. Examples of these are silicon carbide, tungsten carbide, titanium carbide, boron nitride, boron carbide, alumina, and aluminosilicates (Nagavally, 2017). Silicon carbide has a sublimation temperature of 2730 °C, which is higher than the melting point of Ti6Al4V (1604-1660 °C) (Rehman et al., 2022). The higher temperature for SiC ensures that its particles do not melt to form an alloy with the Ti6Al4V matrix during AM. Silicon carbide has a higher specific stiffness of 132 MNm/kg than Ti6Al4V (26 MNm/kg) and a density of 3.1 g/cm<sup>3</sup> which is lower than that of Ti6Al4V (4.45 g/cm<sup>3</sup>) (Li et al., 2014; Mukerji, 1993).

Silicon carbide has a thermal expansion coefficient of  $4.6 \times 10^{-6}$  /K which is lower than the value of  $8.6 \times 10^{-6}$  /K for Ti6Al4V (ELI). Therefore, when integrated into the latter to form a composite, SiC reduces the mismatch due to temperature changes at interfaces with carbon fibre/epoxy resin composites (Rosso et al., 2003). **Of these three materials, silicon carbide has the highest thermal conductivity (120 W/m.K) followed by Ti6Al4V(ELI) (6.70 W/m.K) and finally, carbon fibre/epoxy resin composites (2.13 W/m.K). Their specific heat capacities are 750 J/kg.K, 526.3 J/kg.K and 100.0 J/kg.K, in the same order, respectively (Mukerji, 1993). High thermal conductivity implies faster equilibration of temperature in a material and, therefore, minimization of hot spots in it. Higher heat capacity, on the other hand, implies better capacity to**

store heat and lower material temperatures for the same amount of supplied heat. As a result, both these properties are desirable outcomes for heat shields that make SiC a good candidate for the reinforcement of Ti6Al4V(ELI) with respect to its use as a heat shield in engines of high-speed planes to increase turbine efficiency (Yi et al., 2014).

However, it is important to note that, depending on the specific type of the constituents of carbon-epoxy resin composites, their values of thermal conductivity and specific heat go up to 400 W/m.K and 1.20 J/kg.K respectively. Nevertheless, this does not negate the value of SiC as a reinforcement material for Ti6Al4V(ELI) in applications of the resulting composite as a heat shield.

Ramah et al. (2014) found that with a maximum SiC volume fraction of 20 % in an aluminium matrix, cracking around the filler particles could be avoided. However, as the volume fraction increased above this value the hardness of the composite increased, and the initiation of cracks at the interfaces, which led to the failure of the composites, increased.

Mohanavel et al. (2021) varied the SiC weight fraction from 0 % to 20 % to investigate the influence of SiC particles on the properties of AA6351 aluminium matrix composites. They reported that the mechanical properties of the composite improved with increasing SiC content. The maximum value of hardness was achieved at 20 % volume fraction, which was considered the optimum value.

Dash et al. (2016), while investigating the behaviour of aluminium matrix composites under thermal stresses, observed that ceramic reinforcements have a large difference in CTE compared to the matrix. They observed that this induced large residual stresses near the interfaces of the composite constituents when they were cooled from fabrication temperatures. They then noted that the induced residual stresses at the interfaces affected the physical and mechanical properties of built parts.

From the foregoing overview, it is clear that the overall behaviour of composites, including their response to heating as it occurs in AM, depends on the volume fraction of the reinforcement. This creates a need to carry out tests and, in the case of AM, build specimens at different volume fractions of fillers to establish any volume fraction-related trends that may exist.

## 1.2. Problem Statement

The traditional materials used in aircraft structures were required to have a combination of good mechanical properties such as strength, stiffness and hardness and low physical property of density, as well as low thermo-physical properties such as CTE and thermal conductivity. However, these traditional materials (aluminium, steel, and carbon fibre composites) do have some limitations. Steels have high strength and high stiffness but also high density, which reduce the efficiency of aircraft due to their weight. Aluminium is the lightest of the traditional materials used but has relatively low strength. **The specific strength of Ti6Al4V (211 kNm/kg) is much higher than that of steel (54–139 kNm/kg) and aluminium (18–24 kNm/kg), which gives it an advantage over aluminium and steel in the manufacture of lightweight structures in the aircraft industry (Donachie, 2000).**

Silicon carbide has the high thermal conductivity (120 W/m.K) that is higher than Ti6Al4V(ELI) (6.70 W/m.K) and carbon fibre/epoxy resin composites (2.13 W/m.K). Their specific heat capacities are 750 J/kg.K, 526.3 J/kg.K and 100.0 J/kg.K, in the same order, respectively (Mukerji, 1993). High thermal conductivity implies faster equilibration of temperature in a material and, therefore, minimization of hot spots in it. Higher heat capacity, on the other hand, implies better capacity to store heat and lower material temperatures for the same amount of supplied heat. As a result, both these properties are desirable outcomes for heat shields that make SiC a good candidate for the reinforcement of Ti6Al4V(ELI) with respect to its use as a heat shield in engines of high-speed planes to increase turbine efficiency (Yi et al., 2014).

Ti6Al4V has a CTE of ( $8.6 \times 10^{-6}$  /K) that is lower than that of aluminium ( $24 \times 10^{-6}$ /K), steel  $12.5 \times 10^{-6}$ /K (Serin et al., 2018; Aradhya et al., 2015). Carbon fibre/epoxy resin composites sheets have a lower CTE of  $2.1 \times 10^{-6}$ /K while carbon fibre tubes have a CTE of  $0.1 \times 10^{-6}$ /K (Aradhya et al., 2015). **The CTE of SiC/Ti6Al4V(ELI) composite is dependent on the volume fraction of filler and is seen to decrease with increasing volume fraction of SiC particles. At 20 % and 40 % volume fraction, the values of the CTE that are predicted from the Reuss model are  $7.71 \times 10^{-6}$ /K and  $6.06 \times 10^{-6}$ /K, both of which are much closer to the value for carbon fibre epoxy resin composites compared to those of the other metals and alloys mentioned here.**

A mismatch of CTE between connected components induces thermal stresses because of the differences in expansion during cooling and heating of adjoining materials. When carbon fibre/epoxy composites are joined with aluminium or steel, the mismatch of the CTE may cause buckling at joints during contraction or separation of the materials during expansion (Aradhya et al., 2015). Because SiC particles have a lower density ( $3.21 \text{ g/cm}^3$ ) than Ti6Al4V(ELI) (density:  $4.45 \text{ g/cm}^3$ ) and a coefficient of thermal expansion (CTE) of  $4.6 \times 10^{-6}/\text{K}$ , that is lower than that of Ti6Al4V(ELI) of  $8.6 \times 10^{-6}/\text{K}$ , the addition of SiC particles into Ti6Al4V(ELI) is expected to reduce the overall density and CTE of an SiC/Ti6Al4V(ELI) composite. The use of SiC/Ti6Al4V(ELI) composites which from the foregoing analysis will have values of CTE that are much closer to that of carbon fibre/epoxy resin composites than aluminium and steel and is preferred at joints as this reduces the mismatch due to changes of temperature at the joints (Rosso et al., 2003).

Aluminium and low alloy steels are the two groups of aircraft materials most likely to be influenced by galvanic corrosion. Carbon fibre/epoxy composites are often put in close contact with metal alloys such as aluminium alloys, and the electrical conductivity of carbon fibre/epoxy composites induces galvanic corrosion at their interface (Rosso et al., 2003). Galvanic corrosion will therefore occur at joints, rivets, and fasteners in an aircraft where these materials are in contact. Therefore, Ti6Al4V is preferable to steel and aluminium alloys as the alloy does not exhibit this shortcoming (Aradhya et al., 2015).

Conventional methods of manufacturing are unable to produce parts with highly complex geometries, are wasteful since material must be removed to create required shapes and consume a lot of time in machining and assembly of multi-component parts (Gospondinov et al., 2016). Therefore, AM is attractive because parts with complex geometries can be manufactured as monoliths, there is less waste of material as it uses only the amount necessary to build the parts, and there are no requirements for the assembly of multi-component parts (Gospondinov et al., 2016).

### 1.3. Aim of the Project

The aim of the project was to formulate and design a particulate Ti6Al4V(ELI) composite reinforced with a selected ceramic and produce it using DMLS, targeting

specific strength, stiffness and hardness that are higher than those of the Ti6Al4V(ELI) matrix. The resultant composite must have a coefficient of thermal expansion that is closer to that of carbon fibre/epoxy resin composite than is the case for Ti6Al4V(ELI) to minimise thermal-related buckling or separation at the interfaces of composite constituent materials in aircraft structures.

### 1.3.1. Research Objectives

- To model or predict the elastic behaviour of various compositions of the SiC/Ti6Al4V(ELI) composite.
- To study different methods of mixing powder and select the most appropriate one to use in the present work.
- To build Ti6Al4V(ELI) single tracks and single layers from the designed MMC by DMLS.
- To study the top surface morphology of the printed single tracks and the geometrical characteristics of width, height, and depth of penetration of their cross-sections, for each SiC volume fraction.
- To investigate the top surfaces morphology of single layers and cross-sections of different overlapping tracks to select the best hatch distance to be used for building of 3D specimens.

### 1.4. Limitations of the study

Quantitative analysis of the surface roughness of single layers was not done but rather qualitative analysis, which is discussed in Chapter 7. The composition of SiC particles was not determined because the composition of the SiC powder specified by the supplier was accepted, based on experience of the reliability of the supplier. There was no attempt to study the particle size distribution of Ti6Al4V(ELI) powder, as this has been studied widely and is readily available for the Ti6Al4V(ELI) powder used in this work, neither of SiC powder with its very irregular shapes. Selection of the optimal SiC volume fraction for reinforcement of Ti6Al4V(ELI) was not carried out in this study

as so building and mechanical testing of three-dimensional specimens due to a limitation of time. This is expected to form part of future continuing research on this composite. The study of the mechanical properties of SiC/Ti6Al4V(ELI) composites in the present work was thus limited to theoretical modelling, whose details are contained in Chapter 4 of this dissertation.

### **1.5. Overview of the Dissertation**

The dissertation begins with an introduction that contains a background to the study, problem statement, project goal, and research objectives. Chapter 2 provides an overview of composite materials and their classification, properties of the Ti6Al4V(ELI) alloy, and the DMLS process and parameters. Chapter 3 of the dissertation addresses the materials and methods employed in the present investigation. The findings and discussion of this work are separated into four chapters: Chapter 4, Chapter 5, Chapter 6, and Chapter 7. Analytical modelling of the characteristics of SiC/Ti6Al4V(ELI) particulate composites is discussed in Chapter 4, and the characterization of SiC, Ti6Al4V(ELI), and mixed powders is presented in Chapter 5. The top view and cross-sectional analyses of single tracks are contained in Chapter 6, while top view and cross-sectional analyses of single layers are covered in Chapter 7. Finally, the findings and recommendations of this work are presented in Chapter 8.

## 1.6. REFERENCES

- [1]. **Ali, K.S.A., Mohanavel, V., Vendan, S.A., Ravichandran, M., Yadav, A., Gucwa, M., and Winczek, J.,** 2021. Mechanical and microstructural characterization of friction stir welded SiC and B4C reinforced aluminium alloy AA6061 metal matrix composites. *Materials*, 14(11), p.p. 3110.
- [2]. **Aradhya, K.S. and Doddamani, M.R.,** 2015. Characterization of mechanical properties of SiC/Ti-6Al-4V metal matrix composite (MMC) using finite element method. *American Journal of Material Science*, Vol.5, pp. 7-11.
- [3]. **Baker, A.A.,** 2004. Composite materials for aircraft structures, *2<sup>nd</sup> Edition*, © 2004, *American Institute of Astronautics and Astronautics*, Virginia. <http://dx.doi.org/10.2514/4.861680>.
- [4]. **Dash, K., Sukumaran, S., and Ray, B.C.,** 2016. The behaviour of aluminium matrix composites under thermal stresses. *Science and Engineering of Composite Materials*, 23(1), pp.1-20.
- [5]. **Donachie, J. Jr,** 2001. Heat treating titanium and its alloys. Chapter 8 in *Titanium: A Technical Guide*, 2<sup>nd</sup> Edition, © 2000, *ASM International*, Materials Park, Ohio, p.381 **ISBN: 978-0-87170-686-7**.
- [6]. **Gospodinov, D., Ferdinandov, N., and Dimitrov, S.,** 2016. Classification, properties and application of titanium and its alloys. *Proceedings of University of Ruse*, 55(2), pp. 27-37.
- [7]. **Hangshenas, M.,** 2016. Metal matrix composites. Module in *Material Science and Material Engineering*, vol. 5, pp. 1-10.
- [8]. **Li, J., Xu, Y., Xiao, W., Ma, C., and Huang, X.,** 2022. Development of Ti-Al-Ta-Nb-(Re) near- $\alpha$  high temperature titanium alloy: Microstructure, thermal stability, and mechanical properties. *Journal of Materials Science and Technology*, 109, pp. 1-11.
- [9]. **Megson, T.H.G.,** 2016. Aircraft structures for engineering students. 6<sup>th</sup> edition, © 2017, 2013, 2007, 1999, *Elsevier Ltd*, Cambridge, United States., **ISBN: 978-0-08-100914-7**.

- [10]. **Mukerji, J.**, 1993. Ceramic matrix composites. *Defence Science Journal*, 43(4), p. 385.
- [11]. **Nagavally, R.R.**, 2016. Composite materials-history, types, fabrication techniques, advantages, and applications. Proceedings of *29th IRF International Conference*, 24th July, Bengaluru, India, pp. 25-30.
- [12]. **Rahman, M.H., and Mamun, H.M.R.**, 2014. Characterization of silicon carbide reinforced aluminum composites, *Procedia Engineering*, 90, pp. 103-109.
- [13]. **Rosso, M.**, 2006. Ceramic and metal matrix composites: Routes and properties. *Journal of Materials Processing Technology*, 175(1-3), pp. 364-375.
- [14]. **Serin, G., Kahya, M., Unver, H.O., Gulec, Y., Durlu, N., and Eroglu, O.**, 2016. A review of additive manufacturing technologies. The 17th International Conference on Machine Design and Production July 12 – July 15 2016, Bursa, Turkiye.
- [15]. **Sheasby, P.G., Pinner, R. and Wernick, S.**, 2001. *The surface treatment and finishing of aluminium and its alloys*, Materials Park, OH: ASM international, Vol. 1, p. 231. ISBN: 0-904477-21-5, 0-904477-22-3, 0-904477-23-1.
- [16]. **Ur Rehman, A., Saleem, M.A., Liu, T., Zhang, K., Pitir, F., and Salamci, M.U.**, 2022. Influence of silicon carbide on direct powder bed selective laser process (sintering/melting) of alumina. *Materials*, 15(2), p.p. 637.
- [17]. **Veiga, C., Davim, J.P. and Loureiro, A.J.R.**, 2012. Properties and applications of titanium alloys: a brief review. *Reviews on advanced Materials Science*, 32(2), pp.133-148.
- [18]. **Walker, W.P.**, 1991. Handbook of metal etchants, © 1991 by CRC Press LLC. Washington, USA.  
[https://vector.umd.edu/images/links/Handbook\\_of\\_Metal\\_Etchants.pdf](https://vector.umd.edu/images/links/Handbook_of_Metal_Etchants.pdf)
- [19]. **Yi, K.J., Baek, S.W., Kim, M.Y., Lee, S.N., and Kim, W.C.**, 2014. The effects of heat shielding in jet engine exhaust systems on aircraft survivability. *Numerical Heat Transfer, Part A: Applications*, 66(1), pp. 89-106.

## CHAPTER 2: LITERATURE REVIEW

Some of the material contained in this chapter has been published in peer-reviewed conference proceedings as detailed below:

1. **Seleso, M., Maringa, M., and du Preez, W.**, 2020. "Designing a ceramic particulate composite to enhance selected mechanical properties of Ti6Al4V". Rapid Product Development Association of South African (RAPDASA) 21<sup>st</sup> Annual International Conference, Japie van Lill Auditorium, Central University of Technology, Free State, South Africa, 3<sup>rd</sup> November 2020, pp. 41-55. <https://site.rapdasa.org/past-proceedings-2020/>
2. **Seleso, M., Maringa, M., and du Preez, W.**, 2021. "Parameters affecting the mixing of powders and the results of mixing SiC and Ti6Al4V(ELI) Powders". RAPDASA-RobMech-PRASA Conference – 22<sup>nd</sup> Annual International RAPDASA Conference, International Conference Centre CSIR, Pretoria, South Africa, 3<sup>rd</sup>–5<sup>th</sup> November 2021, pp.73-75. <https://site.rapdasa.org/past-proceedings-2021/>

### 2.1. Introduction

This chapter presents a review of composite materials, their background and classification. A review is also presented in the chapter on titanium alloys, their properties and microstructure after exposure to different heat treatments, powder mixing technologies, the DMLS process and optimum process parameters. The layout of the literature review is shown in Figure 2.1.

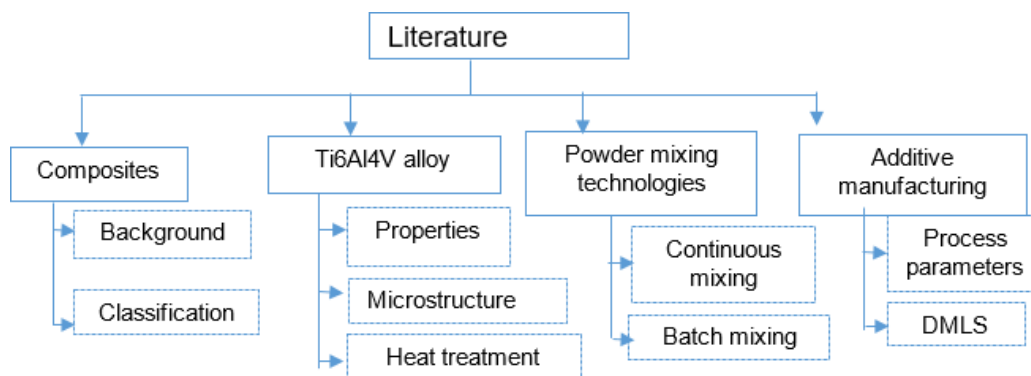


**Figure 2.1:** *Layout of the literature review*

### 2.2. Composite Materials

A composite material can be defined as a combination of two or more materials that results in better properties than those of the individual components alone (Gibbons.,1988; Thori et al., 2013; Wang et al., 2023). Composites are comprised of natural and synthetic constituents in any order. The two forms of constituents in a composite are the reinforcement and the matrix. Matrices are usually tough and ductile while reinforcing materials are strong, they have high values of strength,

stiffness, and low density. In a composite, the toughness and ductility of the matrix are combined with the strength, stiffness and density of the reinforcement to achieve a combination of desirable properties (Campbell, 2010). Table 2.1 gives a summary of the functions of matrices and reinforcements in a composite.

**Table 2.1: Functions of matrices and reinforcements in a composite (Campbell, 2010; Thori et al., 2013; Mackie et al., 2012)**

Matrices	Reinforcements
<ul style="list-style-type: none"> <li>• Hold the reinforcing phase together</li> <li>• Protect the reinforcing phase from environmental damage</li> <li>• Help to distribute applied loads to the reinforcing phase</li> </ul>	<ul style="list-style-type: none"> <li>• Increase strength</li> <li>• Increase stiffness</li> </ul>

Typically, composites have a high strength-to-weight and stiffness-to-weight ratios, which lead to fuel savings when used in in automotive and aircraft applications. They also offer design flexibility, because they can be easily moulded into complex shapes, and corrosion resistance, which makes them good choices where chemicals are handled and stored (Mackie et al., 2012; Thori et al., 2013). When compared to metallics, composites have higher material costs, lower reusability and are more difficult to repair (Thori et al., 2013; Campbell et al., 2010).

### 2.2.1. Historical Background of Composites

The first uses of composites date back to the 1500s BC when early Egyptians used a mixture of mud and straw to create strong and durable buildings (Nagavally, 2017). The mud was used as a binder or matrix, and the straw was used as a reinforcing fibre to provide stiffness and strength so that the properties of the two constituents when combined could create strong and durable buildings. Later, in the 1200s AD, the Mongols invented the first composite bow, using a combination of wood, bone, and animal glue (Campbell, 2010). The modern era of composites began when scientists developed plastics. Before then, natural resins derived from plants and animals were the only source of glue and binders. In the early 1900s, plastics such as vinyl, polystyrene, polyester, and phenolic were developed. The plastics alone could not provide enough strength and stiffness for some structural applications; therefore, reinforcement was needed to provide strength and rigidity (Nagavally, 2017).

## 2.2.2 Types of Composites

Composites are classified, based on the structure of reinforcements, as fibre-reinforced composites, particle-reinforced composites, and structural composites.

### **Fibre-reinforced composites**

Fibre-reinforced composites are composed of a variety of short or continuous fibres bound together by a matrix. Fibres typically have high specific strength and specific stiffness (Maringa, 2002; Campbell, 2010). In fibre-reinforced composites, the fibres reinforce along the direction of their lengths. Reinforcement may be mainly 1-dimensional (1D), 2-dimensional (2D), or 3-dimensional (3D). The 1D- reinforcement gives maximum strength in one direction, while 2D-reinforcement gives maximum strength in two mutually orthogonal directions. On the other hand, 3D-reinforcement gives maximum strength in three mutually orthogonal directions (Gibsons, 2016). Fibre reinforcement occurs in the form of continuous aligned fibres, as well as short, discontinuous aligned and randomly oriented fibres.

### **Particle-reinforced composite**

Particles usually reinforce a composite equally in all directions and, therefore, are said to provide isotropic reinforcement (Campbell, 2010). Particles used to strengthen matrices are normally spread randomly throughout the matrices (Campbell, 2010). The addition of particles into a matrix gives rise to a composite with a stiffness that is higher than that of the matrix and a coefficient of thermal expansion that is lower than that of the matrix when particles have a higher stiffness and lower coefficient of thermal expansion (CTE) than that of the matrix, respectively. Moreover, the reinforcement particles also support higher tensile, compressive, and shear stresses, in cases where the respective values of strength of the particles are higher than those of the matrix. An example of a particle-reinforced composite is concrete, where the aggregates (sand and gravel) are the particles and cement is the matrix (Johnes, 1990).

### **Structural composites**

The term is mainly used to refer to large components that are prevalent in civil and mechanical structures. It is also applied to cases of load-bearing small composite

structures in the field of mechanical engineering. Large composite structures are of two types: laminar composites and sandwich panels. Laminar composites are composed of 2D sheets or panels that have a preferred high-strength direction such as is found in wood and continuous and aligned fibre-reinforced composites. The layers are stacked and subsequently cemented together such that the orientation of the direction of high strength varies with each successive layer (Gibson, 2016). Figure 2.2 shows an example of a laminar composite structure.

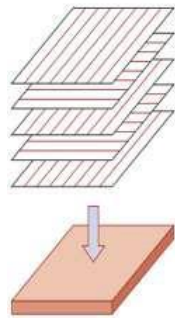


**Figure 2.1:** *The stacking of successive oriented, fibre-reinforced layers for a laminar composite (Gibson, 2016)*

Sandwich panels consist of a relatively thick core of low-density foam bound on both faces to thin sheets of a different material. The facing sheets have high strength and stiffness-to-weight ratios and are widely used in aerospace structures (Gibson, 2016). Figure 2.2 shows a sandwich panel structure.

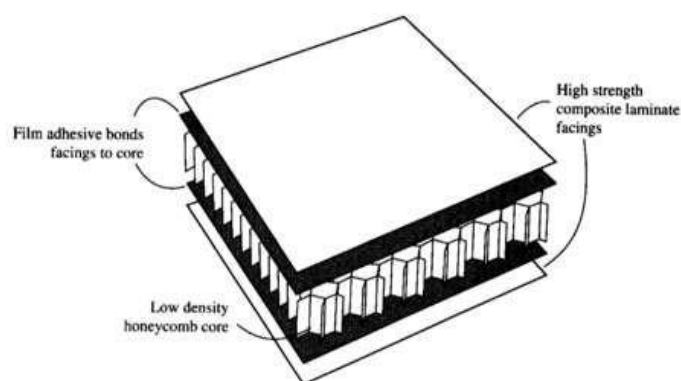


**Figure 2.2:** *A composite sandwich structure indicating the facing sheets and central thick core bonding the two faces together (Gibson, 2016)*

Composites are also classified based on the nature of the matrices as metal matrix composites, polymer matrix composites, and ceramic matrix composites.

### **Polymer matrix composites (PMCs)**

This type of composite uses polymers or plastic resin as a matrix and a variety of fibres such as glass, carbon, and aramid as the reinforcement. Polymeric matrices are classified into thermosets, thermoplastics, and elastomers (Akay, 2015).

### **Ceramic matrix composites (CMCs)**

Ceramic matrix composites have matrices such as alumina ( $\text{Al}_2\text{O}_3$ ), silicon nitrate ( $\text{Si}_3\text{N}_4$ ) calcium aluminosilicate ( $\text{CaAl}_2\text{Si}_2\text{O}_8$ ) reinforced by fibres or particles such as carbon, silicon carbide ( $\text{SiC}$ ), boron ( $\text{B}_2\text{O}_3$ ) and aluminium oxides ( $\text{Al}_2\text{O}_3$ ) (Mukerji, 1993; Sun et al., 2023). They are used in applications where resistance to high temperatures and corrosive environments is desired. Ceramic composites find applications in jet engines, automobile engines, deep-sea mining, cutting tools, dies and pressure vessels (Rosso, 2006; Shrivastava et al., 2024, Sun et al., 2023). The advantages of ceramic composites include high stiffness, high oxidation and corrosion resistance, high melting points, high strength-to-weight ratios, and very long service life (Mukerji, 1993). Ceramic composites suffer the disadvantage of being very brittle, with low tensile strain to failure.

### **Metal matrix composites (MMCs)**

The matrices in this category of composites include metals like aluminium, titanium, magnesium, and their respective alloys that are generally reinforced with non-metallic materials like ceramics in the form of whiskers, particles, or fibres, to form metal matrix composites. Aluminium and titanium are commonly used due to their high strength-to-weight ratio, high thermal and electrical conductivity, high toughness, and resistance to corrosion (Rosso, 2006). The non-metallic part in such composites provides strength, stiffness, and hardness, while the metallic part provides toughness, which prevents early failure and propagation of cracks (Rosso, 2006; Harris, 1999).

MMCs find applications in the manufacture of cutting tools (tungsten carbide), automotive brake pads (alumina-based MMCs), power electronics (dymalloy) and gas

turbine blades (silicon carbide/titanium/aluminium, tungsten/niobium, tungsten/copper) (Sarmah et al., 2014). MMCs have the advantages of higher operating temperatures, non-flammability, creep resistance, high stiffness, and strength. They suffer the disadvantages of being expensive and more difficult to repair and process than traditional materials (Gonzalez, 1985).

Aluminium alloys are commonly used due to their favourable strength-to-weight ratios but are susceptible to various failure mechanisms, including corrosion fatigue and stress corrosion cracking. These issues become critical in operational environments where aircraft are repeatedly subjected to fluctuating loads and corrosive atmospheres. Tavares and Castro et al., (2017) provide an overview of fatigue in aircraft structures, emphasizing the need for ongoing research into the performance of materials under various conditions. Moreover, the poor wear resistance of conventional aluminum alloys significantly limits their potential application in the aerospace and automotive fields for components such as pistons and cylinder heads, where wear resistance is critical (Li et al., 2020).

### 2.3. Designing Ti6Al4V Metal Matrix Composites

Table 2.2 is used in the design of MMCs to compare **some** of the mechanical and physical properties of various ceramic particle reinforcements used in MMCs, to choose the best reinforcement for Ti6Al4V (ELI). **Specific strength is also known as the strength-to-weight ratio and is a measure of the strength of a material relative to its weight.**

**Table 2.2: Some mechanical and physical properties of various particle reinforcements and the Ti6Al4V matrix (Serin, 2018; Abhijith, 2016; Justin et al., 2011; Rabinkin, 2013; Walker, 1991; Jankowiak, 2011)**

Mechanical Properties	Particle Reinforcements					Matrix
	Silicon nitride (SiN)	Silicon carbide (SiC)	Tungsten carbide (WC)	Boron nitride (BN)	Aluminium oxide (Al <sub>2</sub> O <sub>3</sub> )	
Tensile strength (MPa)	60–525	240–1 271	370–530	27–83.3	282	950
Specific strength (kNm/kg)	25–160	75–490	23–34	13–37	75	211
Young's modulus (GPa)	166–297	410	600–686	20–103	300	110

Specific stiffness (MNm/kg)	69–90	132	38–43	9.5–45	79	24
Knoop hardness (kg.mm-1/GPa)	8 000–30 500	600–3 800	17 000–36 000	660–3 000	1 175	363
Physical and thermo-physical properties						
Melting point (°C)	1 900	2 730	3 000–3 193	3 000–3 140	2 000	1 604–1 660
Boiling point (°C)	2 830*	>2 000	6 000	2 250	2 977	3 260–3 287
Density (g/cm <sup>3</sup> )	2.4–3.3	3.1	15.8	2.1–2.3	3.8	4.5
Specific heat capacity (J/kg.K)	673–1 100	750	184–292	770–1 150	451	526.3
Thermal conductivity (W/m.K)	10–43	120	28–88	19–52	18	6.7
Coefficient of thermal expansion (10 <sup>-6</sup> /K)	1.4–3.7	4.6	5.4	3.8	8.1	8.6

\*It cannot be heated above 1850 °C due to dissociation into its components, silicon and nitrogen.

It is evident from Table 2.2 that the melting point of silicon carbide particles (2730°C) is higher than that of Ti6Al4V (1604–1660 °C) and lower than those of tungsten carbide (3000–3193°C) and boron nitride (3000 –3140°C) Such high temperatures ensure that the particulates do not melt to form an alloy with the Ti6Al4V matrix during AM. The lowest value in the range of specific strength of silicon carbide (75 kNm/kg) is still higher than those of silicon nitride, boron nitride, and tungsten carbide and is the same as that of alumina, while its upper value (490 kNm/kg) is higher than that of Ti6Al4V (211 kNm/kg) (Krenkel, 2008). **The limiting lower and higher values of strength and hardness of SiC particles given in Table 2.2, are expected to cause divergence of predicted curves of strength and hardness of SiC/Ti6Al4V(ELI) based on the elastic theories of composites.**

The specific stiffness of silicon carbide particles of 132 MNm/kg is the highest of all the particles in Table 2.2. Silicon carbide has a low density of 3.1 g/cm<sup>3</sup> which is lower than that of Ti6Al4V (4.5 g/cm<sup>3</sup>), tungsten carbide, and alumina but higher than those of boron nitride and silicon nitride. Silicon carbide has a low CTE, which creates a problem of mismatch at interfaces with Ti6Al4V but is an advantage at interfaces with carbon fibre-reinforced epoxy resin composites with their lower values of CTE for carbon nanotube sheets of 2.1×10<sup>-6</sup>/K and for carbon nanotubes of 0.1×10<sup>-6</sup>/K (Lule et al., 2020). **Aluminum has a higher thermal expansion coefficient (8.1×10<sup>-6</sup>/K)**

compared to carbon fiber and epoxy resin. This means that when subjected to changes of temperature, aluminum will expand and contract more than carbon fiber and epoxy resin. This mismatch of CTEs at the interfaces of the carbon fibre/epoxy resin composite leads interlaminar buckling and debonding at interfaces (Azimpour-Shishevan et al., 2019).

The coefficient of thermal expansion of CuSiC and AlSiC metal matrix composites was investigated by Arif et al. (2019). Their findings demonstrated that CuSiC and AlSiC composites had excellent inter-particle bonding because the particles of SiC particles in them limited the expansion of copper and aluminium matrices due to their value of CTE that is lower than those of copper and aluminium. Most metal matrix composites that have a mismatch in the CTE of two joining materials in thermal applications experience degradation in the performance of their products that ultimately results in operational failure (Arif et al. 2019).

Galvanic corrosion usually occurs in composites when dissimilar metals are in direct electrical contact in a corrosive environment (Findley et al., 2002). This type of corrosion occurs at the joints of two dissimilar metals. It is generally a result of poor design and material selection. Findley et al., 2002 studied an upper surface wing panel made of stainless steel and aluminium. They reported that the barrier originally occurring between the two dissimilar metals had broken down thus allowing their direct contact. This led to the formation of a galvanic cell in which the more noble metal (stainless steel) accelerated the corrosion of aluminium (Findley et al., 2002).

Silicon carbide has a high thermal conductivity 120 W/m.K and specific heat capacity (750 J/kg.K) (Krenkel, 2008). As noted earlier in Section 1.1, high thermal conductivity implies faster equilibration of temperature in a material and, therefore, minimization of hot spots in it. Higher heat capacity, on the other hand, implies better capacity to store heat and lower material temperature for the same amount of supplied heat. As a result, both these properties are desirable outcomes for heat shields that make SiC a good candidate for the reinforcement of Ti6Al4V (ELI) for use as a heat shield (Nagavally, 2017; Lule et al., 2020).

### 2.3.1. Metallic bases of metal matrix composites

Ti6Al4V is a preferred alloy in aerospace applications for airframes and engine components, since it has an excellent strength-to-weight ratio (211 kNm/kg) compared to steel (54–139 kNm/Kg) and aluminium (18–24 kNm/Kg). It is as strong as high-strength steel but about 45 % lighter, while aluminium is the lightest metal among the three but with lower strength. The high specific strength of Ti6Al4V allows for the manufacture of lightweight components and, therefore, provides a reduction in fuel consumption. This makes Ti6Al4V applicable to the aerospace industry, where speed, power and strength are required (Kutz, 2006; Akay, 2015). The alloy is used in the manufacture of landing gear, wing panels, turbine inlet guide vanes, fire walls, and hydraulic tubing. It can also be used in the manufacture of engine parts like bolts, compressor disks, fan blades and fan disks since it provides additional strength and durability without increasing weight (Akay, 2015). Table 2.2 compares some mechanical and physical properties of Ti6Al4V with those of aluminium 7075 and stainless steel.

**Table 2.3: Some mechanical and physical properties of three metallic bases for metal matrix composites (Laurel, 2017; Nagavally, 2017; Justin et al., 2011).**

Properties	Metallic Bases		
	Ti6Al4V	Aluminium 7075 alloy	Stainless steel
<b><i>Mechanical properties</i></b>			
Tensile strength (MPa)	950	572	400–1 000
Specific tensile strength (kNm/kg)	211	18–24	54–139
Specific stiffness (MNm/kg)	24	27.6	28
Hardness (Knoop hardness) (MPa)	363	191	140
Percentage elongation (%)	14	11	10–15
<b><i>Physical and thermo-physical properties</i></b>			
Melting point (°C)	1 604–1 660	475–635	1 837
Boiling point (°C)	3 260–3 287	2 470	2 860
Density (g/cm <sup>3</sup> )	4.4–4.5	2.8	7.4
Specific heat capacity (J/kg.K)	526.3	960	420

### 2.3.2. Theoretical Limitations of Particulate Reinforcement

There are several analytical models used to predict the elastic behaviour of composite materials, including the Rule of Mixtures (RoM), Inverse Rule of Mixtures (IRoM), equations of Guth and, separately, Smallwood, Mooney equation, Halpin-Tsai semi-empirical equations, Hashin and Strickman bounds, Kerner equations and the equations of McGee and McCullough (Messiry, 2013; Maringa, 2002). The Hashin and Strickman equations are widely used to predict the properties of particulate composites and fall between the upper and lower bounds (Ahmed,1990). Kerner equations are some of the most elaborate equations for composite materials consisting of spherical particles in a matrix. The assumption is made in these equations of perfect adhesion of the matrix and filler (particles). The Kerner equations are useful for composites reinforced with randomly dispersed spherical particles in polymer and metal matrices (Ahmed, 1990; Nielsen, 1967). For the reasons detailed in the next session, the Halpin- Tsai equations, the Rule of Mixtures, and the Inverse Rule of Mixtures were preferred for use in this study.

#### The Rule of Mixtures

The RoM, also known as the Voigt or iso-strain rule, and the IRoM, also known as the Reuss or iso-stress rule, define the upper and lower bounds of the properties of composite materials, respectively. The assumptions are made in the rules that the constituent components of the composite are perfectly bonded together and that they deform together (Ahmed, 1990; Hull, 1990). The upper and lower bounds are represented by the Voigt and Reuss rules shown as equations (2.1), (2.2), and (2.3), respectively (Messiry, 2013; Hull, 1990; Hu, 2012):

$$E_c = E_m V_m + E_p V_p \quad (2.1)$$

$$\sigma_c = \sigma_m V_m + \sigma_p V_p \quad (2.2)$$

$$E_c = \frac{E_m E_p}{E_m V_p + E_p V_m} \quad (2.3)$$

In these equations, the symbols  $E$ ,  $V$ ,  $\sigma$ ,  $c$ ,  $m$ ,  $p$  denote elastic modulus, volume

fraction, strength, as well as composite, matrix, and particulate phase, respectively (Ahmed, 1990; Hull, 1990; Harris, 1999). The Reuss and Voigt rules are also used to predict the CTE of composites. The Reuss Rule leads to the following expression for the CTE (Harris, 1999).

$$\alpha_c = \frac{V_m E_m \alpha_m + V_p E_p \alpha_p}{V_m E_m + V_p E_p} \quad (2.4)$$

where the symbols  $\alpha_c$ ,  $\alpha_m$ , and  $\alpha_p$  represent the CTEs of the composite, matrix, and particles, respectively. The Voigt model, which assumes uniform strain in a composite arising from a uniform change of temperature, leads to an expression for effective CTE as follows:

$$\alpha_c = V_m \alpha_m + V_p \alpha_p \quad (2.5)$$

The RoM is not useful for making predictions in the transverse direction of reinforcing fibres and often overestimates the properties of unidirectional fibre-reinforced composites (Ahmed, 1990; Nelson, 1997; Hu, 2012). The RoM does not consider the aspect ratios of reinforcing particles and is inexact in estimating the effective modulus of particulate MMCs. However, it is more exact in the longitudinal direction of continuous fibre reinforcement with high aspect ratios. It is for this reason that the IRoM is used to predict the values of elastic modulus for composites in the transverse direction. Figure 2.3 shows the graphs of the elastic modulus versus reinforcement volume fraction for SiC/Ti6Al4V composites based on the RoM and IRoM.

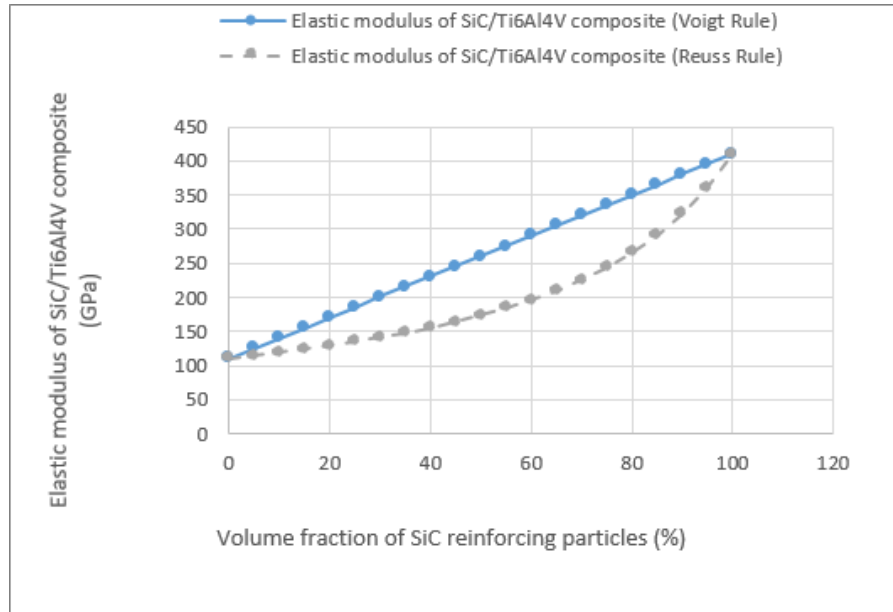


**Figure 2.3:** *Plots of RoM and IRoM curves showing the calculated variation of the elastic modulus of SiC/Ti6Al4V (ELI) composites with volume fraction of SiC (Seleso et al., 2020)*

### The Halpin-Tsai Semi-Empirical Equations

The Halpin-Tsai semi-empirical model is the most widely used model to predict the elastic moduli of composites, though it suffers the drawback of being dependent on parameters that need to be determined experimentally. The Halpin-Tsai semi-empirical model predicts both the transverse and longitudinal Young's modulus and shear modulus of composite materials (Osoka, 2018; Gibson, 1994). For composites with aligned fibres, the Halpin-Tsai semi-empirical model defines Young's modulus as follows:

$$E = \frac{E_m(1+\eta\xi V_f)}{(1-\eta V_f)} \quad (2.6)$$

$$\eta = \frac{\frac{E_f}{E_m} - 1}{\frac{E_f}{E_m} + \xi} \quad (2.7)$$

In this equation, the parameters  $E_f$  and  $E_m$  denote the elastic modulus of fibre and matrix, respectively,  $V_f$  the volume fraction of fibre,  $\eta$  a stress partitioning factor and  $\xi$  a shape factor which measures the reinforcing efficiency and depends upon the

geometry and distribution or packing arrangement of the reinforcing fibres and the direction of loading (Ahmed,1990; Harris, 1999). When the value of  $\xi$  becomes very small ( $\xi \rightarrow 0$ ) the Halpin-Tsai semi-empirical model reduces to the IRoM or Reuss rule. For composites with large values of  $\xi$  ( $\xi \rightarrow \infty$ ), the Halpin-Tsai semi-empirical model reduces to the RoM or Voigt rule. For composites reinforced with randomly oriented fibres, the Halpin-Tsai semi-empirical model is more elaborate and takes the form (Osoka, 2018; Ahmed,1990):

$$E_c = E_m \left[ \frac{3}{8} \left( \frac{1 + \xi \eta_l V_f}{1 + \eta_l V_f} \right) + \frac{5}{8} \left( \frac{1 + 2 \eta_T V_f}{1 - \eta_T V_f} \right) \right] \quad (2.8)$$

In Equation 8, the symbols ( $\eta_l$  and  $\eta_T$ ) stand for:

$$\eta_l = \frac{\frac{E_f}{E_m} - 1}{\frac{E_f}{E_m} + \frac{2l}{d}} \quad (2.9)$$

$$\eta_T = \frac{\frac{E_f}{E_m} - 1}{\frac{E_f}{E_m} + 2} \quad (2.10)$$

where the symbols  $\eta_l$ , and  $\eta_T$  represent stress partitioning factors in longitudinal and transverse directions while  $l$  and  $d$  represent length and diameter of the fibres. The Halpin-Tsai semi-empirical equations are good for predicting properties at low-volume fractions of the reinforcing phase but underestimate the properties at high-volume fractions. The Halpin-Tsai equations allow sensible interpolations to be made between the upper and lower bounds of composite properties. They offer the advantage of being simple and easy to use in design and give good predictions, though they suffer the setback of being dependent on parameters that need to be determined experimentally (Gibson, 1994; Harris, 1990). In addition, the Halpin-Tsai equations are also useful in determining the properties of composites that contain discontinuous fibres oriented in the loading direction. Therefore, the Halpin-Tsai equations are seen to be flexible and adaptable to model any type of composite, thus their preference here over other models (Luo, 2018; Gibson, 1994). Figure 2.4 shows a plot of the stiffness versus reinforcement volume fraction for SiC/Ti6Al4V(ELI) composites based on the Halpin-

Tsai semi-empirical equations with the upper and lower bound curves shown too.

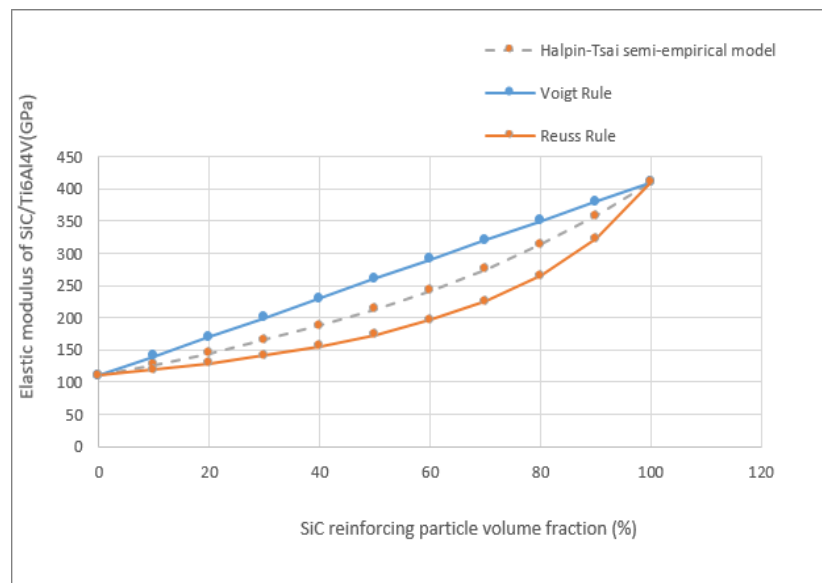


**Figure 2.4:** Plot of the stiffness versus reinforcement volume fraction for SiC/Ti6Al4V (ELI) composites based on the Halpin-Tsai semi-empirical equations, together with the upper and lower bound curves.

### Hashin and Strickman Model

The Hashin and Strickman equations are widely used to predict the properties of particulate composites and fall between the above-mentioned lower and upper bounds (Calvo-Jurado, 2015). They are described by the following equations:

**The lower bound equation** (Ahmed, 1990)

$$E_c = \frac{9 \left[ K_p + \frac{V_m}{\frac{1}{K_m - K_p} + 3K_p + 4G_p} \right] \left[ G_p + \frac{V_m}{\frac{1}{G_m - G_p} + 5G_p(3K_m + 4G_m)} \right]}{3 \left[ K_p + \frac{V_m}{\frac{1}{K_m - K_p} + 3K_p + 4G_p} \right] + \left[ G_p + \frac{V_m}{\frac{1}{G_m - G_p} + 5G_p(3K_p + 4G_p)} \right]} \quad (2.11)$$

In Equation 2.11, the symbols  $K$  and  $G$  represent the bulk and shear moduli, respectively, while the other symbols correspond with those used in previous equations. The Poisson's ratio  $\nu_c$  of composites in this model is given by the expression:

$$\nu_c = \frac{3K_c - 2G_c}{2(G_c + 3K_c)} \quad (2.12)$$

### The upper bound equation (Ahmed,1990)

$$E_c = \frac{9 \left[ K_m + \frac{V_p}{\frac{1}{K_p - K_m} + \frac{3V_m}{3K_m + 4G_m}} \right] \left[ G_m + \frac{V_p}{\frac{1}{G_p - G_m} + \frac{6V_m(K_m + 2G_m)}{5G_m(3K_m + 4G_m)}} \right]}{3 \left[ K_m + \frac{V_p}{\frac{1}{K_p - K_m} + \frac{3V_m}{3K_m + 4G_m}} \right] + \left[ G_m + \frac{V_m}{\frac{1}{G_p - G_m} + \frac{6V_m(K_m + 2G_m)}{5G_m(3K_m + 4G_m)}} \right]} \quad (2.13)$$

The Hashin and Strickman equations are also used to predict the CTE of composites since the mixture rules do not give accurate results for it. The Hashin and Strickman expression for the CTE of composites is as follows:

$$\alpha_c = \alpha_m + \frac{\alpha_p - \alpha_m}{1/E_p - 1/E_m} (1/E_c - 1/E_m) \quad (2.14)$$

#### 2.3.4. Particle Size and Shape

The size and shape of particles affect the mechanical properties of particulate composites such as stiffness and strength. The modulus of a composite is insensitive to the size of particles for sizes above 20–30 nm up to the micrometre scale (1–5  $\mu\text{m}$ ), below which there is a significant increase of elastic modulus of composites with decreasing particle size (Ahmed, 1990; Fu et al., 2008). For particles above 5  $\mu\text{m}$ , there is also an increase in modulus of elasticity as the volume fraction of particles increases. The strength of reinforced composites depends on the effective stress transfer between the matrix and the reinforcement. A higher amount of nanomaterial reinforcement loading causes particle agglomeration, which reduces load transfer between the matrix and the reinforcement due to the lower available surface area for bonding. Therefore, the strength of composite materials is better at lower loadings of reinforcement (Jordan et al., 2005; Fu et al., 2008).

The interfacial bond strength of nano filler particles does not affect the magnitude of the elastic modulus of particulate composites since the levels of loading are typically too low to cause expansion large enough to initiate interfacial separation. Moreover, the surfaces of nano particles are too small to facilitate stress transfer to the full strength of the reinforcing fillers (Ahmed, 1990; Fu et al., 2008). However, the

interfacial bond strength does support a continuous increase in the strength of particulate composites with increasing size of the reinforcing particles due to stress transfer through the interface (Jordan et al., 2005). Increasing the volume fraction of nano filler particles was noted to lead to an increase in the stiffness of the resulting composite. In MMCs, stress is transferred from the matrix to the reinforcing phase through the interfacial bond. A strong interfacial bond is important to ensure strengthening occurs because of reinforcement, otherwise, the addition of filler will lead to a reduction of strength (Hull, 1990).

Thermosetting resins have the drawback of poor resistance to crack growth and the addition of reinforcing particles improves their toughness by acting as crack arrestors. Where the matrix is brittle, as in the case of thermosets, during cracking, the matrix becomes unloaded at the crack and the load formerly carried by the matrix is then transferred to the filler particles. When the matrix is ductile, and well bonded to reinforcing filler particles, cracks are attracted to the poles of particles and then propagate through the matrix above or below the respective particles (Fu, 2008). When the reinforcing particles are untreated and have poor adhesion to the matrix, the strength of the resulting composite decreases with the increase in particle content.

However, when particles are dispersed well within the matrix and interfacial adhesion is good, the strength of the composite initially increases as the filler content increases up to 5 % for polymer composites. Above this value, strength decreases due to particle agglomeration (Adams, 1993) and the attendant reduction of reinforcing surface area. The foregoing reasoning is not a preserve of polymer matrices but applies to all types of matrices, including metal matrices.

An increase of volume fraction of SiC particles till 40 vol % in SiC/Ti6Al4V composite was observed to lead to values of strength and hardness that were higher than those of the matrix and which increased with increasing volume fraction of SiC. However, it encouraged the initiation of cracks at the SiC/Ti6Al4V interfaces that were likely to lead to failure of the composite (Zang et al., 2023). This sets an upper limit for the reinforcement of Ti6Al4V with SiC particles to avoid failure of the composite. However, the CTE of SiC/Ti6Al4V composites was observed to decrease with increasing volume fraction of SiC particles (Fu, 2008). The foregoing review shows that the size of reinforcing particles affects various mechanical properties of composites differently, as

was observed by Maringa (2018).

Particles with sharp corners lower the strength of composites, due to the effects of stress concentration, while spherical particles give rise to composites with higher values of Young's modulus (Ahmed et al., 1990). The foregoing material demands that morphological studies of particulate composites be carried out for constituent powders before and after mixing, as well as after the building of the final products (Fu, 2008; Jordan et al., 2018). Table 2.4 gives a summary of the shape and size of the particles used in the present work.

**Table 2.4: The shape and size of SiC and Ti6Al4V particles used in the present work**

Morphology of Particles	SiC	Ti6AL4V
Shape	Irregular	Spherical
Size	<45 $\mu\text{m}$	45-50 $\mu\text{m}$

## 2.4. The Ti6Al4V(ELI) Alloy

The Ti6Al4V alloy is the most common alpha-beta titanium alloy and consists of 6% aluminium, 4% vanadium, about 0.25 % iron and 0.2% oxygen with the remainder being titanium (Gospodinov et al., 2016). In Ti6Al4V(ELI) the abbreviation (ELI) stands for Extra Low Interstitials, which in this case are oxygen, nitrogen, and carbon. Table 2.5 shows the difference in composition of Ti6Al4V and Ti6Al4V(ELI)

**Table 2.5: Difference in composition of Ti6Al4V and Ti6Al4V (ELI)**

Alloy	Aluminium	Vanadium	Iron	Oxygen	Titanium	Nitrogen	Carbon
Ti6Al4V	6%	4%	0.25%	0.2%	89.4%	0.05%	0.08%
Ti6Al4V (ELI)	6%	4%	0.25%	0.13%	89.8%	0.03%	0.08%

Ti6Al4V(ELI) alloy is commonly referred to as surgical titanium or medical titanium grade because it can resist corrosion from body fluids, is compatible with body tissue, and hence is a metal of choice within the medical industry (Gospodinov et al., 2016).

Ti6Al4V(ELI) is used to make medical implants that are used in complex surgical procedures like installation of bone fracture devices, hip and knee joint replacements, surgical staples, finger and toe replacements, installation of bone plates and screws (Schulz et. al., 2018). It also finds application in the dental industry to produce titanium

surgical devices like scissors and surgical tweezers. The alloy is also used in aerospace applications where fracture toughness and fatigue strength are important (Pang et al., 2025).

The advantages of Ti6Al4V (ELI) include high specific strength, high toughness, and high corrosion resistance (Donachie, 1988). It can be moulded easily, cut into small strands, coils, and wires, and is durable. Moreover, it has high specific strength, which is an advantage in the construction of lightweight structures. Ti6Al4V(ELI) has good fracture resistance (fracture toughness), which is good for dental implants, and its non-magnetic property allows patients with titanium implants to be safely examined with magnetic resonance imaging (MRI) (Froes, 2018).

#### 2.4.1. Microstructure and Mechanical Properties of Ti6Al4V Alloy

The mechanical properties of the alloy depend mainly on the arrangement and combination of  $\alpha$  and  $\beta$  phases as well as the grain size or average grain diameter (Fan et. al., 2016). There are four types of microstructures of this alloy, namely lamellar, equiaxed, bimodal, and martensitic. The equiaxed microstructure is formed from the beta phase that exists above the beta transus temperature upon cooling below this temperature. This cooling leads to recrystallization and globulization to form equiaxed grains. Therefore, the equiaxed microstructure of Ti6Al4V consists of globular primary alpha-phase grains dispersed in a matrix comprised of transformed beta grains, as shown in Figure 2.5.

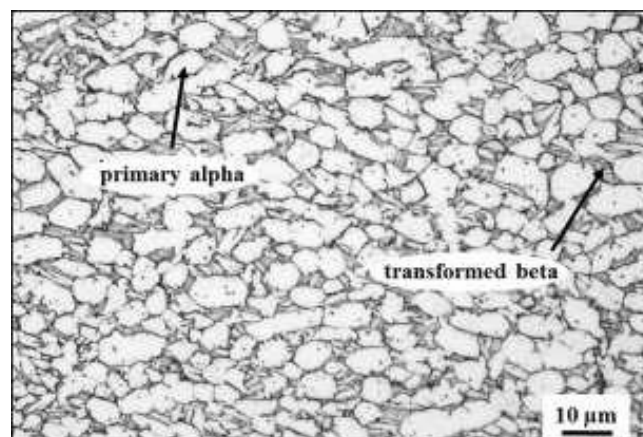


**Figure 2.5:** Equiaxed microstructure of Ti6Al4V (Sefer et al., 2016)

A lamellar microstructure is formed in the two-phase ( $\alpha + \beta$ ) field below the beta transus temperature. It consists of colonies of alternate alpha and beta phases forming lamellae within a primary beta grain (Sieniawski et al., 2013). The bimodal microstructure is a combination of lamellar and equiaxed microstructures and combines the advantages of both lamellar and equiaxed microstructures. The bimodal microstructure possesses the best combination of strength and ductility as well as good fatigue properties (Lütjering, 1998).

The lamellar microstructure is characterized by low tensile ductility, better resistance to crack propagation and poorer resistance to fatigue crack initiation, while the equiaxed microstructure has better strength and ductility at room temperature, better resistance to fatigue crack initiation and poorer resistance to fatigue crack propagation (Sieniawski et al., 2013). Figure 2.6 shows micrographs of Ti6Al4V lamellar microstructure.

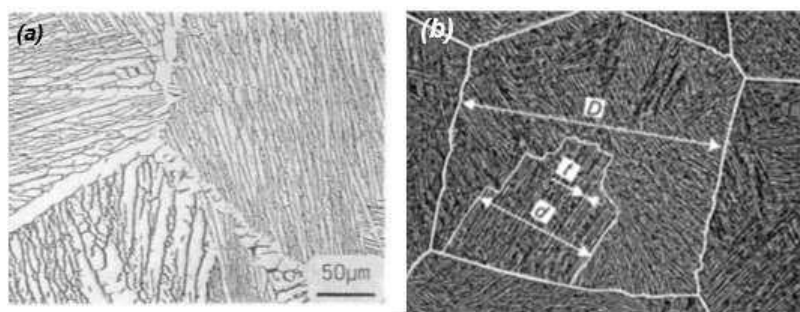


**Figure 2.6:** *Lamellar microstructure of Ti6Al4V (a), (b) characteristic dimensions of a lamellar microstructure (Sieniawski et al., 2013)*

In Figure 2.6 (b) the characteristic dimensions of the lamellar microstructure are shown. Here, the symbol  $D$  represents the grain size of the primary beta phase,  $d$  size of the colonies of alpha lamellae, and  $t$  thickness of the alpha lamellae (Sieniawski et al., 2013). In the case of the lamellar microstructure, the thickness of the alpha lamellae and the diameter of their colonies have the strongest influence on the mechanical properties of the microstructure.

## **2.5. Additive Manufacturing**

AM or 3D printing, which was originally known as rapid prototyping, generally refers to techniques that produce three-dimensional parts by adding material in a layer-by-layer fashion (Olmos et al., 2017). The main purpose of AM is to produce complex net-shaped metals or non-metal parts in a single-build process (Olmos et al., 2017; Li et al., 2024; Jaswin et al., 2024). In AM, there is no need for tooling design and manufacturing, and separate machines to remove material, thus resulting in less waste of materials (Serin et al., 2018). AM is grouped into different categories that include binder jetting, directed energy deposition, material extrusion, material jetting, powder bed fusion, and sheet lamination. Laser powder-based fusion (LPBF) is the category applicable to the present research and it includes the techniques, selective laser sintering (SLS), selective laser melting (SLM), and direct metal laser sintering (DMLS) (Serin et al., 2018; Gokuldoss et al., 2017).

### **2.5.1. Direct Metal Laser Sintering (DMLS)**

This is the brand name of the metal-based PBF systems of EOS GmbH (Electro Optical Systems) that produce metal parts directly from 3D computer-aided design (CAD) models. It is an SLM technology because it involves the complete melting of the powder (Kar et al., 2024). The technology uses a laser beam to melt and fuse fine metal powder particles in a layer-upon-layer process (Binelli et al., 2011). It finds applications in the aerospace and medical industries in which the most widely used alloy is the titanium alloy Ti6Al4V. The benefits of DMLS include significant time and cost savings in the production of parts because it can produce complex parts directly and avoids lengthy machining times (Jaswin et al., 2024). It can create geometries that are impossible to machine, such as sharp internal angles, it has high dimensional accuracy of parts and supports shorter time-to-market manufacturing (Manfredi et al., 2013).

#### **2.5.1.1. History of Direct Metal Laser Sintering**

The first generation of DMLS technology was introduced in the years 1994–1995. Teamwork between EOS GmbH and Electrolux Rapid Development resulted in the development of the EOSINT M250 machine. This machine was equipped with a CO<sub>2</sub>

laser and, at the time, the DMLS sintering process worked similarly to selective laser sintering for plastics, in the sense that metal powder was partially melted and fused to create metal parts. Therefore, the metal parts created by this machine were not fully dense (Shellabear et al., 2004).

Over the years it became obvious that the company needed another machine to improve and fully utilize the manufacturing methods. The EOSINT M270 machine was launched in 2004, which was the first commercial DMLS machine with a fibre laser. This machine enabled faster processing with higher resolution than the previous generation machine. Moreover, the M270 machine provided a more efficient platform for current DMLS materials and especially for the ongoing development of new powders and processes for a wider spectrum of future applications (Shellabear et al., 2004). During the year 2007, EOS introduced EOS Titanium Ti64, the first commercial DMLS process for titanium. This resulted in the EOSINT M280 machine, which is an updated and improved version of the M270. An EOSINT M280 machine of the Centre for Rapid Prototyping and Manufacturing (CRPM) at Central University of Technology, Free State (CUT) was used in the current study.

The most significant feature that sets the M280 machine apart from the M270 is the laminar flow of inert argon gas across the building platform, compared to the turbulent gas flow of the M270. The improved gas flow from turbulent to laminar is important in lieu of the fact that the high laser intensity vaporizes powder, which condenses thereafter to produce spatter particles. Improved gas flow reduces the spatter of particles onto the solidified melt, since they are sucked away and are not sintered onto the surface of the solidified melt (Els et al., 2016; Weilhammer, 2011). This change improves the quality of parts by producing parts with smoother surfaces. The 400 W high-power laser in the M280 machine can melt more metal powder per second, thus achieving shorter build times and higher productivity of parts than the EOSINT M270 (Els et al., 2016).

The M280 machine with its 400 W ytterbium-fibre laser provides excellent beam power stability to ensure the manufacturing of quality parts (Dzogbewu et al., 2017). The inert operating atmosphere of argon gas permits the processing of reactive metal powders, such as titanium and aluminium. The laser scanner can scan at a speed of 7 m/s and covers an exposure area of 250 mm×250 mm on the build platform (Dzogbewu et al.,

2017). The M280 machine has a higher build volume height (+110 mm) and a Z stroke, allowing it to manufacture larger and taller parts than was previously achievable (Weilhammer, 2011). Images of the EOSINT M270 and M280 machines are shown in Figure 2.7 and the technical data for the two machines are summarized in Table 2.6.



**Figure 2.7:** Images of the EOSINT M270 (left) and M280 (right) machines (Dzogbewu et al., 2017)

**Table 2.6:** Technical data of EOSINT M270 and M280 machines (Els et al., 2016)

	EOSINT M270	EOSINT M280
Maximum scanning speed (m/s)	7	7
Laser type	Ytterbium-fibre laser	Ytterbium-fibre laser
Building volume (x, y, z) (mm)	250×250×215	250×250×325
Layer thickness (µm)	20–100	20–80
Laser power (W)	200	200 or 400

### 2.5.1.2. Direct Metal Laser Sintering Process

To obtain optimum results when using a DLMS machine, a systematic procedure must be followed. There should be careful consideration given to each step as any step that is not performed accurately will affect the final product. The first step is pre-processing, in which a 3D digital model is created, using 3D CAD software, which is thereafter converted to the STL file format (Els et al., 2016). Subsequently, support structures

are generated to provide the following functions: hold unsupported geometries in place, anchor the part to help prevent thermal distortion during fabrication, fix the part to the building platform and conduct excess heat away from the manufactured part (Manfredi et al., 2013; Dzogbewu et al., 2017; Wang et al., 2021). The complete build file, including parts and supports, is then sliced digitally into 2D layers of appropriate thickness. Layers of thickness between 20  $\mu\text{m}$  and 40  $\mu\text{m}$  are especially suitable regarding accuracy and speed of production. Thinner layers provide greater accuracy but lead to increased production time (Manfredi et al., 2013; Song et al., 2023). Before building commences, the powder is sieved to remove large particles and ensure reliable consistency. Figure 2.8 shows a schematic view of the DMLS process.

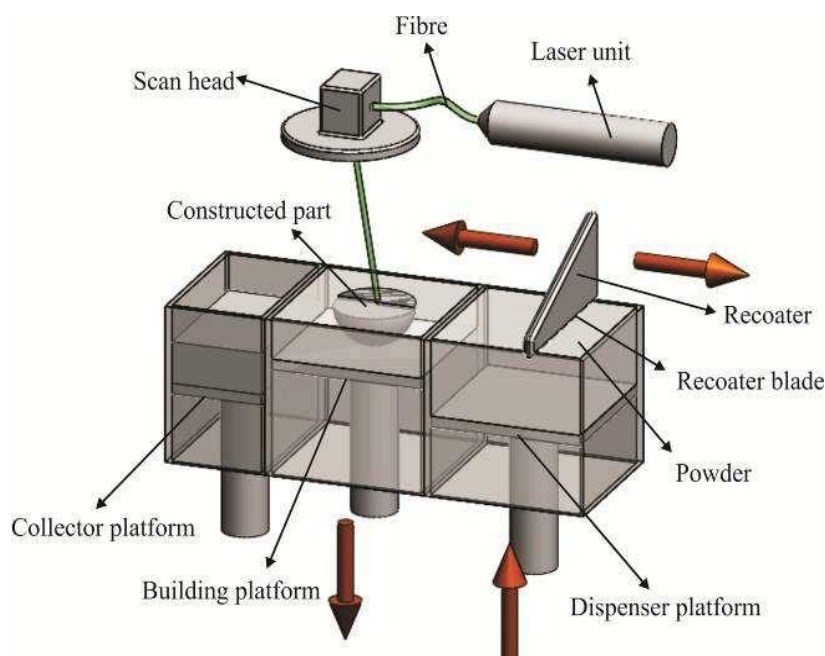


**Figure 2.8:** Schematic view of the DMLS process (Manfredi et al., 2013)

The DMLS process is the next step. Figure 2.9 shows a dispenser platform into which powder is charged before it is transferred onto the building platform, as well as a collector platform for collecting excess powder. A stainless steel recoater blade spreads powder from the dispenser platform to the build platform, ensuring uniform layer thickness (Manfredi et al., 2013; Bineli et al., 2011). A computer numerical controlled (CNC) machine program then controls the laser beam variables to selectively fuse powder particles in the X and Y planes in accordance with the data in the 2D build.stl file.

When a layer is completed, the building platform moves down by the distance of one-layer thickness and the powder dispenser platform moves up by the same distance, allowing the recoater blade to spread and level a fresh layer of powder onto the powder bed and the previously solidified layer. The particles in the fresh layer of powder are then selectively fused and the layer is also fused onto the previous layer. By repeating this process, a fully functional prototype is eventually generated (Manfredi et al, 2013; Spears et al., 2016).

### 2.5.1.3. DMLS Process Parameters

Over 50 different process parameters influence the quality of manufactured parts. These parameters are classified into four categories: laser parameters, scanning parameters, powder material properties, and build environment parameters (Spears et al., 2016; Mani et al., 2015). Scanning speed, laser power, layer thickness, and hatch distance are the four most important parameters (Dzogbewu et al., 2017). Because each of these process parameters has a range of values and each set of values has a different influence on built parts, it is crucial to find their optimum values for use in producing continuous single tracks, multiple tracks, and, eventually, 3D objects (Bineli et al., 2011). The four most critical process parameters for DMLS mentioned above are shown in Figure 2.9 and discussed in the following sections.

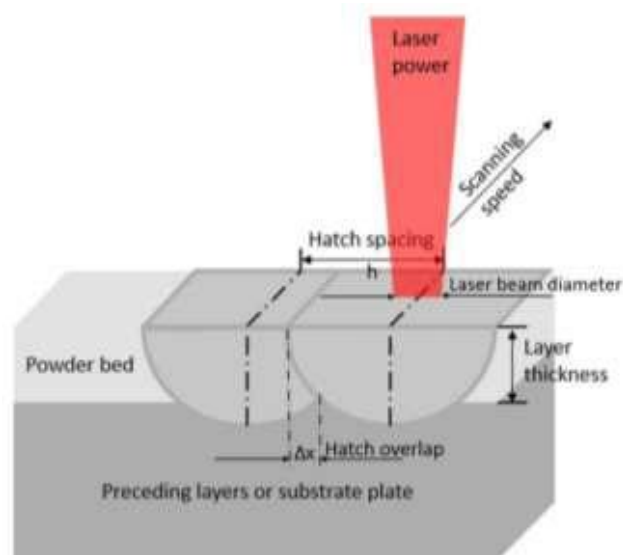


**Figure 2.9:** The four most critical process parameters for DMLS (Bineli et al., 2011)

## Hatch Distance

This parameter also referred to as hatch spacing, is defined as the distance between the centres of two laser scan lines produced upon melting and solidification of the powder (Dajene et al., 2025). Increasing or decreasing the hatch distance between tracks leads to particles of the exposed region not being fused or over-fused, respectively (Bineli et al., 2011). When the hatch spacing is reduced, the rate of overlapping increases, thus leading to a reduction in the formation of pores between the adjacent overlapping tracks (Dong et al., 2018). When the hatch distance is increased beyond the optimum value, the rate of overlapping decreases, and in cases where no overlapping occurs, unmelted powder exists between neighbouring tracks. Non- overlapping tracks result in insufficient metallurgical bonding, and a lowering of the mechanical characteristics of the produced parts (Dong et al., 2024). Figure 2.10 shows different overlapping rates for different hatch distances where the average track width is 200  $\mu\text{m}$ .

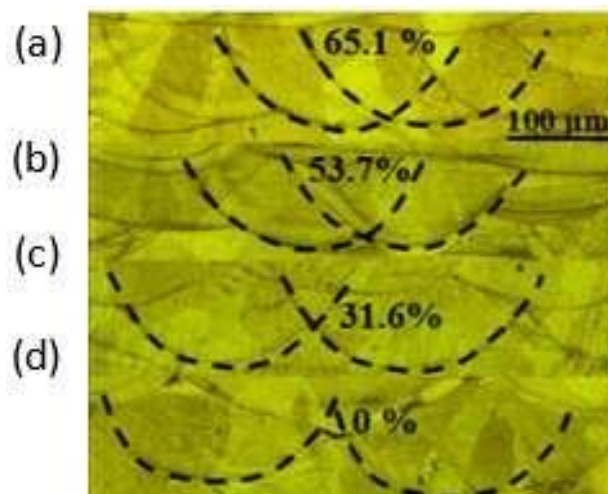


**Figure 2.10:** Overlapping rate between adjacent tracks for various hatch distances: (a) 75  $\mu\text{m}$ , (b) 100  $\mu\text{m}$ , (c) 150  $\mu\text{m}$ , and (d) 200  $\mu\text{m}$  (Dong et al., 2018)

Dong et al. (2018), in their study of the influence of hatch spacing on the microstructure and as-built quality of 316L stainless steel samples fabricated by SLM, found over-fusion of the layers at a low hatch distance of 75  $\mu\text{m}$ . They discovered that an overlap rate of 53.7 % at a hatch distance of 100  $\mu\text{m}$  resulted, in satisfactory metallurgical bonding between the tracks. As the hatch distance was raised to 150  $\mu\text{m}$ , some of the powder between the tracks failed to melt. They also observed that there was no

overlapping at a hatch distance of 200  $\mu\text{m}$ , as is evident in Figure 2.10 (d), and that there was no repetitive melting region between the tracks (Dong et al., 2018). As a result, it was determined that a 53.7% overlap rate is acceptable.

### **Laser Power, Scanning Speed and Linear Energy Density**

The laser power of an AM machine is defined as the amount of power in its laser beam. Lasers produce heat upon contact with materials. A Yb-fibre laser is normally used rather than a CO<sub>2</sub> laser, due to its shorter wavelength (1060–1100 nm) compared to 9–11  $\mu\text{m}$  for the latter and generates up to 400 W of power (Weilhammer, 2011). Scanning speed is defined as the speed at which a laser beam runs over the powder. Linear energy density is defined as the ratio of power to scanning speed of a laser beam. The formula for linear energy density defines the intensity of laser energy input to a layer of powder being melted and is given by Equation 2.15.

$$LED = \frac{P}{V} \quad (2.15)$$

where the symbol *LED* stands for linear energy density, *P* laser power, and *V* scanning speed (Bineli et al., 2011). The amount of LED received by the powder is primarily influenced by two parameters: laser scanning speed and laser power (Anam et al., 2014). To ensure there is strong fusion between the layers, the LED must be enough to melt the current layer of powder and previously fused layers. It is evident from Equation 2.15 that the LED decreases with increasing scanning speed and vice versa. Volumetric energy density (*VED*) is defined as the ratio between laser power and the product of scanning speed (*V*), hatch distance (*h*) and powder layer thickness (*t*). It expresses the amount of energy delivered per unit volume of powder deposited on the powder bed (Ciurana et al., 2011) and is defined as:

$$VED = \frac{P}{Vht} \quad (2.16)$$

As the powder absorbs energy from the laser beam, its temperature rises dramatically during fusion. The laser beam loses some heat to the environment of the build chamber as it travels to the powder bed and some of the heat in the powder at the surface is transferred through the powder bed via convection and radiation (Anam et al., 2014).

The most important process parameter is laser power, which determines the depth of

penetration of the laser beam, while scanning speed is an important parameter that determines the width of the heat-affected zone (HAZ) and melt pool (Dzogbewu et al., 2017). When the LED is high (high laser power at low scanning speed), the powder is exposed to laser irradiation for a longer duration. This results in high melt pool temperature, low melt pool viscosity and low surface tension, leading to the formation of continuous single tracks with deep penetration (Dzogbewu et al., 2017). When the energy density is extremely high, evaporation from the melt pool occurs. Furthermore, the high energy density causes deep penetration into the powder, resulting in the formation of keyholes (Shrestha et al., 2019). Low LED results in insufficient melting of metal powder particles which leads to increased porosity (Kusuma, 2016).

With reference to Equation 2.15, as the scanning speed increases at the same power, the melt pool temperature decreases resulting in an increase in both surface tension and viscosity of the melt pool. This results in the production of discontinuous tracks with irregular widths and the phenomenon known as balling. Balling commonly happens at high scanning speeds, which decreases the energy transferred to the powder and the substrate and results in a decreased depth of penetration. **Reduced depth of penetration causes poor bonding between the track and the substrate** (Aboulkhair et al., 2019). As the scanning speed increases, the height of the track above the substrate or surface increases but the depth of penetration of the laser beam also decreases, as shown in Figure 2.11, which in both cases is due to lower dwell time of the laser beam and the attendant lower values of surface tension and viscosity of the melt.

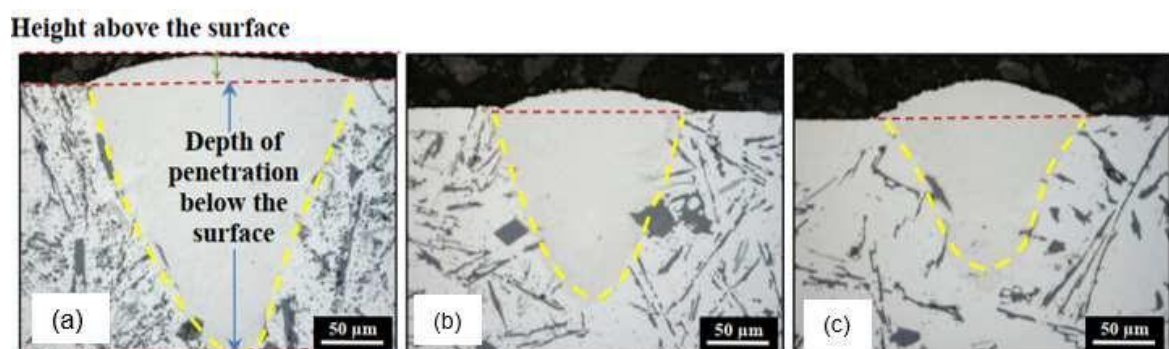


**Figure 2.11:** Depth of penetration of single tracks at different scanning speeds, (a) 250 mm/s, (b) 500 mm/s, and (c) 750 mm/s (Mugwagwa et al., 2018)

Single tracks with constant widths and smooth molten surfaces are produced when

laser power and scanning speed are optimized (Dong et al., 2024). Ramosena et al., 2019 and Bineli et al., 2011, revealed the best process parameters for laser power and scanning speed for producing single tracks of Ti6Al4V as 200 W and 1.2 m/s.

### **Layer Thickness**

The thickness of each layer of powder spread during recoating corresponds to the distance travelled by the lowered platform after each layer is built. If the layer thickness is too large the heat from the laser does not fully penetrate the layer thus resulting in incomplete melting of the particles of powder and the occurrence of porosity (Ramosena et al., 2019). *When the layer thickness is optimum for a particular set of process parameters, heat fully penetrates the top layer, and some of the previous layers are re-melted to ensure good bonding between the layers. Lack of fusion between the track and the substrate or between the track and the previous layer would result in lack of cohesion. Such lack of full cohesion of layers in 3D parts causes a decrease of the tensile strength of built parts in a direction parallel to the build direction (Dzogbewu et al., 2022).*

According to Qiu et al., (2015), raising the layer thickness of Ti6Al4V powder above 60  $\mu\text{m}$  leads to the formation of a porous surface structure. The staircase effect is primarily determined by the inclination angle and layer thickness. Due to the layer-by-layer process of building, the increase in layer thickness causes the staircase effect to increase especially on non-flat edges when producing curved parts. This increases the surface roughness of the final built part. Reducing the thickness of the layer can reduce the staircase effect but at the expense of increased production time (Aboulkhair et al., 2023). The low layer thickness can ensure the production of titanium alloy samples with high density and low porosity (Yao et al., 2024). The vertical inclined surfaces also result in an increase in surface roughness because of the partially melted surrounding powder particles during contour scanning (Yasa et al., 2011; Bottini et al., 2023).

Mugwagwa et al., (2018), in their work on the influence of process parameters on related distortions in SLM, produced samples using two different powder layer thicknesses of 30  $\mu\text{m}$  and 45  $\mu\text{m}$ . They found that increasing the layer thickness above 30  $\mu\text{m}$  increased porosity and resulted in a poor surface finish at the low scanning speeds of 0.4 m/s to 0.6 m/s and low power 80–120 W, which were insufficient to

effectively melt the layer of powder. This shows that when the layer thickness is large the power should also be increased to have enough energy to melt the particles of powder (Mugwagwa et al., 2018).

### Scanning Strategies

Scanning strategies are defined as 2D moving patterns of the laser beam over the powder during melting of powder. Scanning strategies are known to have a great influence on the microstructure and mechanical properties of built parts (Jia et al., 2021; Newby et al., 2018). Scanning strategies include rotated stripe, alternating block patterns, chessboard, bi-directional, also known as parallel scan pattern or zig-zag pattern, and unidirectional scan pattern (zheng et al., 2024), with the rotated stripe pattern, bi-directional, and unidirectional scan pattern being the most used in DMLS. Scanning strategies differ by the scanning vector length, scanning time, scanning direction, scanning sequence, and hatch distance (Jia et al., 2021). The two most common strategies are unidirectional and bi-directional/zigzag scanning strategies. They both have the same longitudinal vector-length but differ in scanning directions.

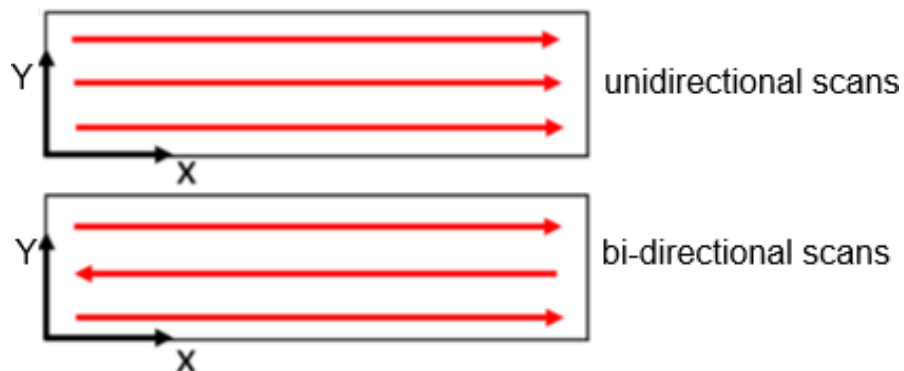


**Figure 2.12: Scanning directions of the unidirectional and bi-directional scan patterns**  
(Jia et al., 2021)

Kruth et al. (2010) investigated the effect of scanning strategies on the relative density of Ti6Al4V manufactured by SLM. They found that a zigzag alternating pattern produced parts with high relative density since the risk of having unmelted zones between adjacent scan tracks is low due to the rotation of scan lines through 90° for each new layer. Similar results were reported by (Thijis et al., 2010).

## Rotated Stripe Pattern

A rotated stripe pattern uses the scan vectors or arrows within each stripe to define the relationship between subsequent layers. Each layer is divided into a series of parallel lines, shown with red dashes in Figure 2.13 that form the boundaries of the stripes. From one layer to the next, the stripes rotate anticlockwise through an angle of  $67^\circ$ , thus forming a crosshatch pattern (Yu et al., 2005).

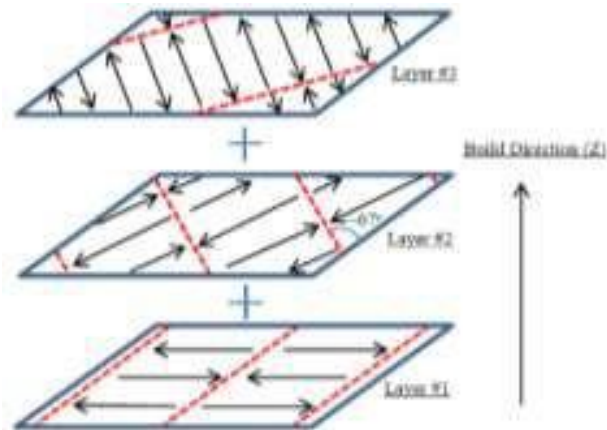


**Figure 2.13:** Schematic of a stripe scan pattern showing scan vectors as arrows within each stripe (Yu et al., 2005)

## Alternating Block Pattern

The scan vectors in this case rotate at an angle of  $90^\circ$  or  $45^\circ$  between adjacent layers. Figure 2.15 (a) indicates the rotation of scan vectors by an angle of  $45^\circ$  and Figure 2.14 (b) indicates the rotation of scan vectors by an angle of  $90^\circ$ .

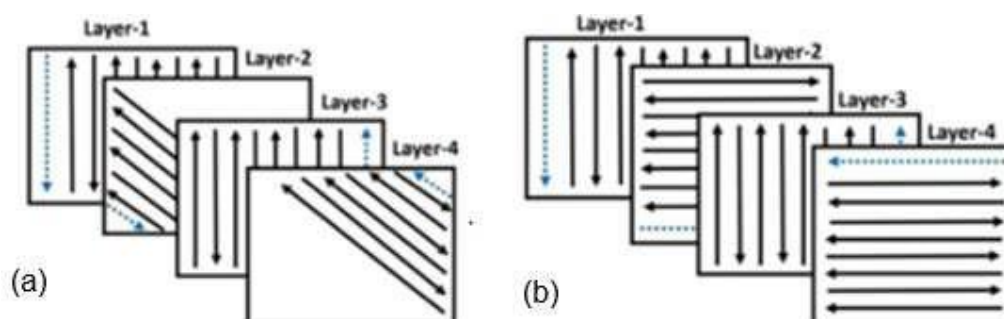


**Figure 2.14:** Alternating block patterns at rotation-angles of  $45^\circ$  (a), and  $90^\circ$  (b) (Ali, 2018).

## Chessboard/Island Scanning Strategy

The scan region is divided into small cells for this scanning approach. This shortens the scanning vector's length. Long scanning vectors produce an excessive accumulation of thermal stress, which degrades the quality of components. Therefore, the chessboard strategy shown in Figure 2.15 can be an alternative method to produce large-size parts with improved quality (Ali, 2018).

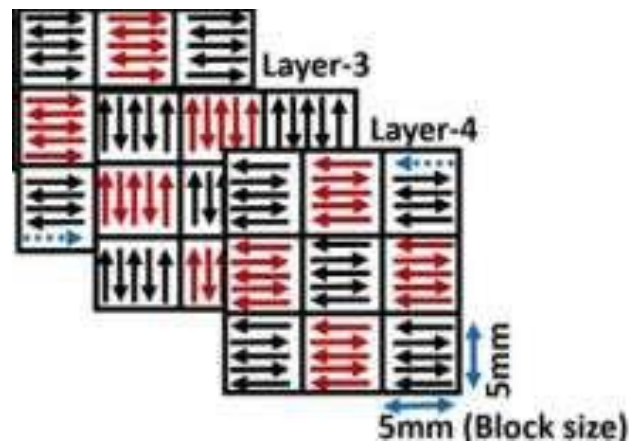


**Figure 2.15:** Diagram of chessboard scanning strategy (Ali, 2018)

In the current study, only single layers were built, therefore the back-and-forth formations of single tracks (bi-directional scans) were done to complete a layer.

### 2.5.2. Powder Mixing Technologies

Powder mixing is an important process in the blending of powders as it combines different powders into single products that must meet specifications and standards based on the homogeneity of mixes (Desai et al., 2018).

#### 2.5.2.1. Mechanisms and methods of mixing powder

Mixing of powders refers to the setting in motion of different particles inside a mixer. The external supply of energy needed is either provided by the motion of a vessel, a blade passing in between the particles, gravity, or a combination of some of these methods (Mayer et al., 2015; Mwanja et al., 2020). The mixing of powder proceeds by the three main processes of convective, diffusive and, shear mixing. Convective mixing means the collective transfer of groups of particles from one location to another within a mixture caused by the motion of a rotating blade (Paulsworth, 2017).

Convective mixing is usually carried out in large-scale mixing such as in continuous methods of mixing. In diffusive mixing, the individual particles of powder move randomly, typically rolling down when their container is rotated. Here, there is no forced pattern caused by the agitators in the mixer, but rather the particles move individually when the motor is switched on, causing the vessel to rotate. Shear mixing of powder is defined as the exchange of momentum of particles with different velocities between two clumps of particles of powder. In this mechanism, a shearing surface appears and leads to the reorganization of particles (Hogg et al., 2009; Mwanja et al., 2020). The inter-particle forces are broken between the two groups of particles thus causing dislocation of particles, which are then reorganized by both convection and diffusion mixing mechanisms. Shear mixing applies in both batch and continuous methods of mixing (Poux et al., 1991).

There are two broad categories of methods of mixing powder, which are referred to as continuous and batch methods.

#### **2.5.2.2. Continuous methods of mixing**

Continuous methods of mixing involve the mixing of different powders, which are fed continuously into a mixer and an equal amount of powder discharged continuously on the other side of the mixer, as mixing continues. The equipment used in this method includes ribbon blend machines, paddle blenders, and vertical screws (Oka et al., 2012).

The convective mixing mechanism is used in continuous methods of mixing as the impellers present move the groups of particles from one location to another. The advantages of continuous mixing of powder include reduction of segregation and product loss because the mixed products are discharged from a continuous mixer in an uninterrupted flow. Additionally, less power and manual labour are required in continuous mixing methods. Greater efficiency and consistency in mixing are achieved in continuous mixing because all mixing stages from loading to discharge take place simultaneously (Oka et al., 2012; Hogg et al., 2009).

Continuous mixing methods are suitable for automatic control and their operation can be monitored online. In addition, large quantities of powder can be mixed in short

periods. However, there are some drawbacks to this method of mixing, which include a reduction in flexibility, because continuous mixers are programmed for one formulation and their settings cannot be changed quickly (Yeow et al., 2011; Mwanja et al., 2020). Careful calibration and frequent checking of feeding devices are required for accuracy. Continuous methods are expensive due to higher overall maintenance costs since they depend on feeders. Moreover, a failure or malfunction of instrumentation and the online control system in one component leads to the stoppage of the whole machine. Continuous methods of mixing require sampling and testing to keep track of the quality of the mixture. Continuous mixers are not suited for critical applications where the formulation of products needs to be exact (Nienow et al., 1985). Figure 2.16 shows a schematic view of a continuous powder mixer.

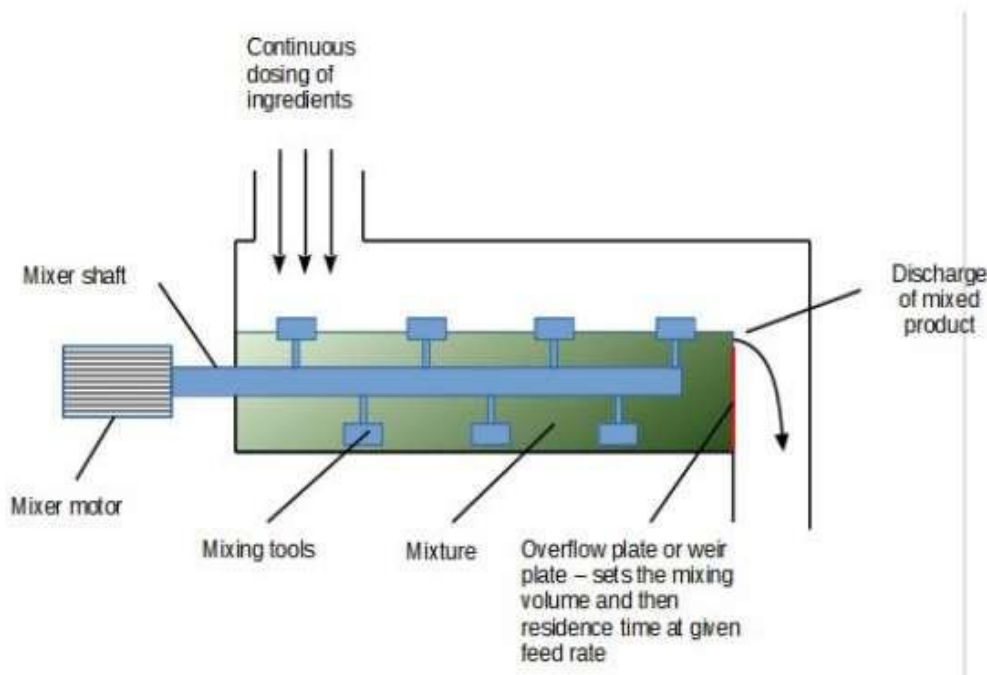


**Figure 2.16:** A schematic diagram of a continuous powder mixer (Yeow et al., 2011)

As illustrated in Figure 2.16, the constituent powders are continuously fed into the vessel while the motor rotates the mixer shaft that has mixing tools on it. The continuous rotation of the mixer shaft mixes the constituent powders, and the powder mixture is discharged continuously as the mixing proceeds.

### 2.5.2.3. Batch methods of mixing

Batch mixing is the preferred method used in this study for mixing SiC and Ti6Al4V (ELI) powders (Nienow et al., 1985). In batch methods of mixing, the constituent powders are loaded into a mixer, mixed until the powder is homogenous and then discharged as a single batch. The loading, mixing, and discharge processes are done consecutively, one after another. The diffusive mechanism is the main mixing mechanism prevalent in the batch method of mixing, as it encourages the individual movement of particles within the vessel and does not require impellers to move the particles. Examples of batch mixers are tumbling machines such as V-blenders and double-cone blenders (Mwania et al., 2020; Hogg, 2009). A schematic of a V-blender is shown in Figure 2.17.

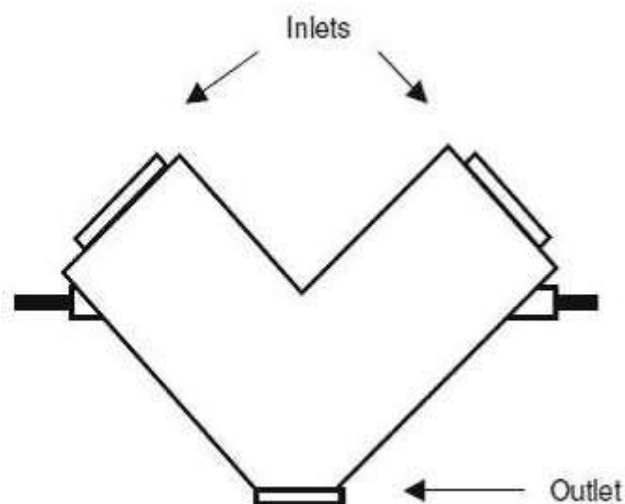


**Figure 2.17:** A schematic of a V-blender machine (Bauman et al., 2008)

The constituent powders are first fed into the inlets. The V-shaped vessel then rotates around a fixed shaft, thus mixing the powders. When the powders are thoroughly mixed, the machine is stopped, and the powders discharged at the outlet. The advantages of batch mixing include better control of the quality of the mixture and traceability of batches of powder (Hogg, 2009).

The disadvantages of batch mixing include more intensive labour, since this method involves several steps and change overs, thus making the powder mixing more

hands-on. Moreover, batch mixing is time-consuming because only one stage of production takes place while others await completion of the stage. In addition, batch mixing is not suitable for large-scale production, noting that scaling-up of production requires an increase in the size of equipment (Oka et al., 2012; Mwanja et al., 2020). Batch mixing is less expensive when compared to continuous mixing, because of lower operational and installation costs. Batch mixing allows pre-mixing of minor ingredients, flexibility of production, control of mixing time because the mixing stages run one after another, easy cleaning, and lower costs of cleaning when changes of products are required frequently (Nienow et al., 1985). The **afore mentioned advantages of batch mixing were the reason for its selection as the most appropriate method to be used in the present study.**

## **2.6. Conclusions**

The traditional materials used in aircraft structures were required to have a combination of good mechanical properties such as strength, stiffness and hardness and low physical property of density, as well as low thermo-physical properties such as CTE and thermal conductivity. However, these traditional materials do have some limitations. Steels have high strength and high stiffness but also high density, which reduce the efficiency of aircraft due to their weight. Aluminium is the lightest of the traditional materials used but has relatively low strength. The poor wear resistance of conventional aluminium alloys significantly limits their potential application in the aerospace and automotive fields for components such as pistons and cylinder heads, where wear resistance is critical. Ti6Al4V is a preferred alloy in aerospace applications for airframes and engine components, since it has an excellent strength-to-weight ratio (211 kNm/kg) compared to steel (54–139 kNm/Kg) and aluminium (18–24 kNm/Kg). The specific strength of Ti6Al4V (211 kNm/kg) is much higher than that of steel (54–139 kNm/kg) and aluminium (18–24 kNm/kg), which gives it an advantage over aluminium and steel in the manufacture of lightweight structures in the aircraft industry and it is considered the best material to use in the present study.

SiC particles were selected as the appropriate particles to reinforce Ti6Al4V(ELI) matrix than other discussed particles of silicon nitride, boron nitride, and tungsten carbide because of their outstanding mechanical and thermo-physical properties.

The specific stiffness of silicon carbide particles of 132 MNm/kg is the highest of all the particles in Table 2.2. Silicon carbide has a low density of  $3.1 \text{ g/cm}^3$  which is lower than that of Ti6Al4V ( $4.5 \text{ g/cm}^3$ ), tungsten carbide, and alumina but higher than those of boron nitride and silicon nitride. The lowest value in the range of specific strength of silicon carbide (75 kNm/kg) is higher than those of silicon nitride, boron nitride, and tungsten carbide and is the same as that of alumina, while its upper value (490 kNm/kg) is higher than that of Ti6Al4V (211 kNm/kg) (Krenkel, 2008). The limiting lower and higher values of strength and hardness of SiC particles given in Table 2.2, are expected to cause divergence of predicted curves of strength and hardness of SiC/Ti6Al4V(ELI) based on the elastic theories of composites.

The addition of SiC particles is expected to reduce the overall density and CTE of an SiC/Ti6Al4V(ELI) composite. When applied to the joints of aircraft structures, an SiC/Ti6Al4V(ELI) composite with a CTE closer to that of carbon fibre/epoxy resin composites would minimize thermal-related buckling or separation at the interfaces. Silicon carbide has a sublimation temperature of  $2730 \text{ }^\circ\text{C}$ , which is higher than the melting point of Ti6Al4V ( $1604\text{-}1660 \text{ }^\circ\text{C}$ ) (Rehman et al., 2022). The higher temperature for SiC ensures that its particles do not melt to form an alloy with the Ti6Al4V matrix during AM.

The batch mixing method is the most suitable approach to use in the study because of the previously mentioned benefits of batch mixing over continuous mixing, which include the ability to pre-mix minor ingredients, production flexibility, and control over mixing time because the mixing stages occur one after the other.

The four most critical process parameters are scanning speed, laser power, layer thickness, and hatch distance. Laser power determines the depth of penetration of the laser beam, while scanning speed is an important parameter that determines the width of the heat-affected zone (HAZ) and melt pool. It was discussed in this chapter that LED decreases with increasing scanning speed and vice versa. To ensure there is strong fusion between the layers of SiC/Ti6Al4V(ELI) to be built in the study, the LED must be enough to melt the current layer of powder and previously fused layers.

It has been studied that when the hatch spacing is reduced, the rate of overlapping increases, thus leading to the formation of pores between the adjacent overlapping tracks while the increase of hatch distance beyond the optimum value, the rate of

overlapping decreases, and in cases where no overlapping occurs, unmelted powder exists between neighbouring tracks. Therefore from the study in this chapter it is concluded that an ideal overlap rate of 50% and higher will be taken into account because it has been demonstrated in the literature that single tracks are adequately remelted. The optimum depth to width ratio to be considered is 0.5. It has been shown from the literature that the increase of depth to width ratio above 0.5 leads to keyholes while the decrease of the ratio to less than 0.5 leads to insufficient penetration.

## 2.7. REFERENCES

- [1]. **Aboulkhair, N.T., Maskery, I., Tuck, C., Ashcroft, I., and Everitt, N.M.**, 2016. On the formation of AlSi10Mg single tracks and layers in selective laser melting: Microstructure and nano-mechanical properties. *Journal of Materials Processing Technology*, 230, pp. 88-98.
- [2]. **Adams, J.M.**, 1993. Particle size and shape effects in materials science: examples from polymer and paper systems. *Clay Minerals*, 28(4), pp. 509-530.
- [3]. **Ahmed, S., and Jones, F.R.**, 1990. A review of particulate reinforcement theories for polymer composites. *Journal of Materials Science*, 25(12), pp. 4933-4942.
- [4]. **Akay, M.**, 2015. *An introduction to polymer matrix composites*. 1<sup>st</sup> Edition Ventus Publishing APs. [https://www.kompozit.org.tr/wp-content/uploads/2021/01/An\\_introduction\\_to\\_polymer\\_matrix\\_compos.pdf](https://www.kompozit.org.tr/wp-content/uploads/2021/01/An_introduction_to_polymer_matrix_compos.pdf)
- [5]. **Akhtar K., Khan S.A., Khan S.B., and Asiri A.M.**, 2018. *Scanning Electron Microscopy: Principle and Applications in Nanomaterials Characterization*. In: Sharma, S. (eds) *Handbook of Materials Characterization*. © 2018 Springer International Publishing, [https://doi.org/10.1007/978-3-319-92955-2\\_4](https://doi.org/10.1007/978-3-319-92955-2_4)
- [6]. **Ali, H., Ghadbeigi, H., and Mumtaz, K.**, 2018. Effect of scanning strategies on residual stress and mechanical properties of selective laser melted Ti6Al4V. *Materials Science and Engineering: A*, vol.712, pp. 175-187.
- [7]. **Anam, M.A., Dilip, J.J.S., Pal, D., and Stucker, B.**, 2014. Effect of scan pattern on the microstructural evolution of Inconel 625 during selective laser melting. In *Proceedings of 25th Annual International Solid Freeform Fabrication Symposium*. University of Texas at Austin. <http://dx.doi.org/10.26153/tsw/15692>
- [8]. **Arif, M.N., Bukhari, M.Z., Brabazon, D. and Hashmi, M.S.J.**, 2019, December. Coefficient of thermal expansion (CTE) study in metal matrix composite of CuSiC vs AlSiC. In *IOP Conference Series: Materials Science and Engineering* (Vol. 701, No. 1, p. 012057). IOP Publishing

- [9]. **Askeland, D.R., Phulé, P.P. and Wright, W.J.** *The science and engineering of materials*, 6<sup>th</sup> edition, © 2011, 2006, Cengage Learning, Stamford, USA, BN-13:978-0-495-29602-7, ISBN-10: 0-495-29602-3.
- [10]. **Azimpour-Shishevan, F., Akbulut, H. and Mohtadi-Bonab, M.A.**, 2019. The effect of thermal shock cycling on low velocity impact behavior of carbon fiber reinforced epoxy composites. *Journal of Dynamic Behavior of Materials*, 5, pp.161-169.
- [11]. **Bauman, I., Curic, D., and Boban, M.**, 2008. Mixing of solids in different mixing devices. *Sadhana*, India, vol.33, pp. 721.731.  
<https://link.springer.com/article/10.1007/s12046-008-0030-5>.
- [12]. **Binelli, A.R.R., Peres, A.P.G., Jardini, A.L., and Maciel Filho, R.**, 2011. Direct metal laser sintering (DMLS): Technology for design and construction of micro-reactors. 6<sup>th</sup> *Brazilian Conference on Manufacturing Engineering*, April 11<sup>th</sup> to 15<sup>th</sup>, Caxias do Sul, Brazil, Vol. 11.
- [13].
- [14]. **Callister, W.D. and Rethwisch, D.G.**, 1999. *Materials science and engineering: an introduction*, 9<sup>th</sup> Edition, © 2014, 2010, 2007, 2003, 2000 John Wiley & Sons, USA, pp. 123-133. ISBN: 978-1-118-32457-8.
- [15]. **Calvo-Jurado, C., and Parnell, W.J.**, 2015. Hashin–Shtrikman bounds on the effective thermal conductivity of a transversely isotropic two-phase composite material. *Journal of Mathematical Chemistry*, 53(3), pp. 828-843.
- [16]. **Campbell, F.C.**, 2010. *Structural composite materials*. © 2010 by ASM International, Materials Park, Ohio, ISBN-13: 978-1-61503-037-8, ISBN-10: 0-61503-037-9.
- [17]. **Ciurana, J., Hernandez, L., and Delgado, J.**, 2013. Energy density analysis on single tracks formed by selective laser melting with CoCrMo powder material. *The International Journal of Advanced Manufacturing Technology*, 68, pp. 1103-1110.

- [18]. Dejene, N.D., Tucho, W.M. and Lemu, H.G., 2025. Effects of Scanning Strategies, Part Orientation, and Hatching Distance on the Porosity and Hardness of AlSi10Mg Parts Produced by Laser Powder Bed Fusion. *Journal of Manufacturing and Materials Processing*, 9(3), p.78.
- [19]. Desai, K.E., 2019. Improving scale-up of powder mixing in the pharmaceutical industry. Doctoral dissertation, Monash University, Australia, <https://doi.org/10.26180/5db8e8a9d186b>
- [20]. Dong, P., Li, Z., Li, D., Yu, Y. and Zhang, W., 2024. Track trajectory, molten pool and defect characterization in NiTi single-track selective laser melting (SLM) experiments. *Journal of Materials Research and Technology*, 33, pp.5210-5222
- [21]. Dong, Z., Liu, Y., Wen, W., Ge, J., and Liang, J., 2019. Effect of hatch spacing on melt pool and as-built quality during selective laser melting of stainless steel: Modeling and experimental approaches. *Materials*, 12(1), p. 50.
- [22]. Dzogbewu, T.C., 2017. *Direct metal laser sintering of titanium alloys for biomedical applications*. Doctoral dissertation, Bloemfontein: Central University of Technology, Free State. P.p. 75-84, <http://hdl.handle.net/11462/1695>
- [23]. El Messiry, M., 2013. Theoretical analysis of natural fiber volume fraction of reinforced composites. *Alexandria Engineering Journal*, 52(3), pp. 301-306.
- [24]. Els, J., 2016. Optimal process parameters for Direct Metal Laser Sintering of Ti64 for medical implant production. Doctoral dissertation, Bloemfontein: Central University of Technology, Free State. <http://hdl.handle.net/11462/1306>
- [25]. Fan, Y., Tian, W., Guo, Y., Sun, Z., and Xu, J., 2016. Relationships among the microstructure, mechanical properties, and fatigue behavior in thin Ti6Al4V. *Advances in Materials Science and Engineering*. Vol. 2016, pp. 1-9, <https://doi.org/10.1155/2016/7278267>
- [26]. Findlay, S.J. and Harrison, N.D., 2002. Why aircraft fail. *Materials today*, 5(11), pp.18-25.
- [27]. Froes, F.S., 2018. Titanium for medical and dental applications - An introduction. In *Titanium in Medical and Dental Applications*, Woodhead Publishing. Duxford.

- [28]. **Fu, S.Y., Feng, X.Q., Lauke, B., and Mai, Y.W.**, 2008. Effects of particle size, particle/matrix interface adhesion and particle loading on mechanical properties of particulate - polymer composites. *Composites Part B: Engineering*, 39(6), pp. 933-961.
- [29]. **Gibbons, J.H.**, 1988. *Advanced materials by design*. Government Printing Office. Washington, United States:
- [30]. **Gibson, R.F.**, 2016. *Principles of composite material mechanics*, 4<sup>th</sup> ed. CRC Press. <https://doi.org/10.1201/b19626>.
- [31]. **Gospodinov, D., Ferdinandov, N., and Dimitrov, S.**, 2016. Classification, properties and application of titanium and its alloys. *Proceedings of University of Ruse*, 55(2), pp. 27-32.
- [32]. **Haolin, J., Sun, H., Wang, H., Wu, Y., and Wang, H.**, 2021. Scanning strategy in selective laser melting (SLM): a review. *The International Journal of Advanced Manufacturing Technology*, shanghai, China, pp. 1-23. <https://link.springer.com/article/10.1007/s00170-021-06810-3>
- [33]. **Hogg, R.**, 2009. Mixing and segregation in powders: evaluation, mechanisms and processes. *KONA Powder and Particle Journal*, 27, pp. 3-17. <http://alvarestech.com/temp/cobef2011/grima.ufsc.br/cobef2011/media/trabalhos/COF11-0502.pdf>.
- [34]. **Hu, N. (Ed.)**, 2012. *Composites and their properties*. Intechopen, Chongqing University, China, pp. 245, <http://dx.doi.org/10.5772/2816>.
- [35]. **Jaswin, M.A., Geetha, R., Saravanan, M. and Elvin, R.P.**, 2024. Direct Metal Laser Sintering to Develop Complex Contours of AlSi10Mg Aluminium Alloy—Build Parameters Optimization. *Surface Review and Letters*, 31(12), p.2450096.
- [36]. **Jhabvala, J., Boillat, E., Antignac, T., and Glardon, R.**, 2010. On the effect of scanning strategies in the selective laser melting process. *Virtual and Physical Prototyping*, 5(2), pp. 99-109.

- [37]. Jia, H., Sun, H., Wang, H., Wu, Y., and Wang, H., 2021. Scanning strategy in selective laser melting (SLM): a review. *The International Journal of Advanced Manufacturing Technology*, 113, pp. 2413-2435.
- [38]. Jiang, J., Xu X., and Stringer, J., 2018. Support structures for additive manufacturing: A review, *Journal of Manufacturing and Materials Processing*, Vol. 2(64), pp. 1-23.
- [39]. Jordan, J.L., Siviour, C.R., Richards, D.W., Rumchik, C.G., and Dick, R.D., 2005. Particle size effects on mechanical properties of particulate composites. In Society for Experimental Mechanics Conference. Portland. [https://www.researchgate.net/publication/266501750\\_Particle\\_Size\\_Effects\\_on](https://www.researchgate.net/publication/266501750_Particle_Size_Effects_on)
- [40]. Justin, J.F., and Jankowiak, A., 2011. Ultra-high temperature ceramics: Densification, properties and thermal stability. *Aerospace Lab*, (3), p.1.
- [41]. Kar, A., Sharma, A. and Kumar, S., 2024. A critical review on recent advancements in aluminium-based metal matrix composites. *Crystals*, 14(5), p.412.
- [42]. Karabulut, Y. and Ünal, R., 2022. Additive manufacturing of ceramic particle-reinforced aluminum-based metal matrix composites: a review. *Journal of Materials Science*, 57(41), pp.19212-19242.
- [43]. Kusuma, C., 2016. The effect of laser power and scan speed on melt pool characteristics of pure titanium and Ti-6Al-4V alloy for selective laser melting, master's thesis, Wright state University, pp 1-127.
- [44]. Kyada, T., Shant, J.R., Goyal, R.K., and Kathayat, T. S., 2014. Understanding the delamination and its effect on Charpy impact energy in thick wall line pipe steel. *Journal of Materials and Metallurgical Engineering*, 4(1), pp. 31-39.
- [45]. Li, J., Wei, L., Shen, J., Zhang, X., Li, S. and Wang, Z., 2024. Research progress of the metal powder reuse for powder bed fusion additive manufacturing technology. *Powder Technology*, p.119815.
- Sarmah, P. and Gupta, K., 2024. Recent advancements in fabrication of metal matrix composites: A systematic review. *Materials*, 17(18), p.4635.

- [46]. **Lisiecki, A., and Piwnik, J.**, 2016. Tribological characteristic of titanium alloy surface layers produced by diode laser gas nitriding. *Archives of Metallurgy and Materials*, 61(2A), pp. 543-552.
- [47]. **Low, I.M.** 2018. *Advances in ceramic matrix composites*, 2<sup>nd</sup> edition, Woodhead publishing, Cambridge, USA, ISBN: 9780081021668.
- [48]. **Luo, Z., Li, X., Shang, J., Zhu, H., and Fang, D.**, 2018. Modified rule of mixtures and Halpin–Tsai model for prediction of tensile strength of micron-sized reinforced composites and Young’s modulus of multiscale reinforced composites for direct extrusion fabrication. *Advances in Mechanical Engineering*, 10(7), <https://doi.org/10.1177/1687814018785286>
- [49]. **Lütjering, G.E.R.D.**, 1998. Influence of processing on microstructure and mechanical properties of ( $\alpha+\beta$ ) titanium alloys. *Materials Science and Engineering: A*, 243(1-2), pp. 32-45.
- [50]. **Macke, A., Schultz, B.F., and Rohatgi, P.**, 2012. Metal matrix composites. *Advanced Material Processes*, 170(3), pp.19-23.
- [51]. **Madhu, K.S., Sharath, B.N., Karthik, S., Pradeep, D.G., Puttegowda, M., TG, Y.G., Premkumar, B.G. and Rao, R.R.**, 2025. An introduction to metal matrix composites and their applications. In *Applications of Composite Materials in Engineering* (pp. 45-73). Elsevier Science Ltd.
- [52]. **Manfredi, D., Ambrosio, E.P., Calignano, F., Krishnan, M., Canali, R., Biamino, S., and Badini, C.**, 2013. Direct metal laser sintering: an additive manufacturing technology ready to produce lightweight structural parts for robotic applications. *La Metallurgia Italiana*.  
<https://www.fracturae.com/index.php/aim/article/view/1210/1163>.
- [53]. **Mani, M., Lyons, K.W., and Gupta, S.K.**, 2014. Sustainability characterization for additive manufacturing. *Journal of Research of the National Institute of Standards and Technology*, 119, p. 419.

- [54]. **Maringa, M.**, 2018. Improving the predictive capacity of Newtonian fluid theories on the elastic moduli ratio ( $\frac{E_c}{E_m}$ ) of particulate composites, *Eleventh South African Conference on Computational and Mechanics*, Vanderbijlpark.
- [55]. **Mayer, C., Gatume, C., and Berthiaux, H.**, 2015. Mixing dynamics for easy flowing powders in a lab scale Turbula mixer. *Chemical Engineering Research and Design*, 95, pp. 248-261.
- [56]. **Moss, D. R.**, 2004, *Pressure vessel design manual*. 3<sup>rd</sup> Edition. Gulf professional publishing, Burlington, USA. ISBN 0080524125, 9780080524122.
- [57]. **Mugwagwa, L., Dimitrov, D., Matope, S., and Yadroitsev, I.**, 2018. Influence of process parameters on residual stress related distortions in selective laser melting. *Procedia Manufacturing*, 21, pp. 92-99.
- [58]. **Mukerji, J.**, 1993. Ceramic matrix composites. *Defence Science Journal*, 43(4),
- [59]. **Mwania, F.M., Maringa, M., and van der Walt, K.**, 2020. A review of methods used to reduce the effects of high temperature associated with polyamide 12 and polypropylene laser sintering. *Advances in Polymer Technology*, 2020, pp.1-11.
- [60]. **Nagavally, R.R.**, 2017. Composite materials-history, types, fabrication techniques, advantages, and applications. *International Journal of Mechanical and Production Engineering*, 5(9), pp. 82-7.
- [61]. **Newby, E.B.**, 2018. Investigation of in-situ alloying grade 23 titanium with copper by selective laser melting process for biomedical applications, Master's Thesis, Central University of Technology, Free state, South Africa.
- [62]. **Nienow, A.W., Edwards, M.F., and Hamby, N.**, 1985, *Mixing in the process industries*, 2<sup>nd</sup> edition, Butterworth-Heinemann, 1997, London. ISBN0080536581, 9780080536583.
- [63]. **Oka, S., and Muzzio, F.**, 2012. Chapter 4 - Continuous powder mixing and lubrication, Pages 59-92, ISBN 9780128134795, <https://doi.org/10.1016/B978-0-12-813479-5.00013-6>.  
<https://doi.org/10.1016/B978-0-12-813479-5.00013-6>.

- [64]. Olmos, L.G., Lovo, J.F.P., De Camargo, I.L., Consoni, C.R., and Fortulan, C.A., 2017. 3D DLP additive manufacturing: printer and validation. In *24th ABCM International Congress of Mechanical Engineering*. Rio de Janeiro: ABCM. December 3-8, Curitiba, Brazil.  
<http://dx.doi.org/10.26678/ABCM.COBEM2017.COB17-2761>
- [65]. Osoka, E.C., and Onukwuli, O.D., 2018. A modified Halpin-Tsai model for estimating the modulus of natural fiber reinforced composites. *International Journal of Engineering and Science Invention*, 7(5), pp. 63-70.  
p. 385.
- [66]. Pang, J., Huang, L., Liu, H. and Yi, X., 2025. Melt pool dynamics and pore formation in selective laser melting: Mechanisms and microstructural insights. *Materials & Design*, p.114043.
- [67]. Paulsworth, C., 2017. Choosing a mixer for low shear batch mixing, CSC Publishing, United States. <https://www.hmicronpowder.com/wp-content/uploads/2020/10/Low-Shear-Batch-Mixing-11.pdf>
- [68]. Poux, M., Fayolle, P., Bertrand, J., Bridoux, D., and Bousquet, J., 1991. Powder mixing: some practical rules applied to agitated systems. *Powder Technology*, vol. 68, no.3, pp. 213-234.
- [69]. Qiu, C., Panwisawas, C., Ward, M., Basoalto, H.C., Brooks, J.W., and Attallah, M.M., 2015. On the role of melt flow into the surface structure and porosity development during selective laser melting. *Acta Materialia*, 96, pp. 72-79.
- [70]. Ramosena, L.A., Parker, B.S., Dzugbewu, T.C., du Preez, W.B., and Blaine, D.C., 2019. Optimum process parameters for DMLS in-situ alloying of a Ti-10 (60Al40V) powder blend. Proceedings of the 20th International Conference of the Rapid Product Development Association of South Africa, Bloemfontein, South Africa, 6-8 November, pp. 78-93.
- [71]. Rosso, M., 2006. Ceramic and metal matrix composites: Routes and properties. *Journal of Materials Processing Technology*, 175(1-3), pp. 364-375.

- [72]. **Saba, N., Jawaid, M., and Sultan, M.T.H.**, 2019. An overview of mechanical and physical testing of composite materials. Woodhead publishing, pp. 1-12. <http://dx.doi.org/10.1016/B978-0-08-102292-4.00001-1>
- [73]. **Schulz, K.J., DeYoung, J.H., Seal, R.R., and Bradley, D.C., (Eds.)**, 2018. Critical mineral resources of the United States: economic and environmental geology and prospects for future supply, U.S. Geological Survey Professional Paper 1802, p.797, <http://doi.org/10.3133/pp1802>.
- [74]. **Sefer, B., Roa, J.J., Mateo, A., Pederson, R., and Antti, M.L.**, 2016. Evaluation of the bulk and alpha-case layer properties in Ti-6Al-4V at micro-and nano-metric length scale. In Proceedings of the 13th World Conference on Titanium, NJ, USA, John Wiley & Sons, pp. 1619-162, <http://dx.doi.org/10.1002/9781119296126.ch271>
- [75]. **Serin, G., Kahya, M., Unver, H.O., Gulec, Y., Durlu, N. and Eroglu, O.**, 2016, July. A review of additive manufacturing technologies. In *17th International Conference on Machine Design and Production. 12-15 July, Bursa. Turkiye*
- [76]. **Shellabear, M., and Nyrhilä, O.**, 2004. DMLS-development history and state of the art. *Laser Assisted Netshape Engineering 4*. In *proceedings of the 4th LANE*, Erlangen, Germany, Sept. 21<sup>st</sup>-24<sup>th</sup>, pp. 21-24. <https://www.i3dmfg.com/wp-content/uploads/2015/07/History-of-DMLS.pdf>.
- [77]. **Shrestha, S., Starr, T., and Chou, K.**, 2019. A study of keyhole porosity in selective laser melting: single-track scanning with micro-CT analysis. *Journal of Manufacturing Science and Engineering*, 141(7), p.p. 071004.
- [78]. **Shrivastava, S., Rajak, D.K., Joshi, T., Singh, D.K. and Mondal, D.P.**, 2024. Ceramic matrix composites: classifications, manufacturing, properties, and applications. *Ceramics*, 7(2), pp.652-679.
- [79]. **Sieniawski, J., Ziaja, W., Kubiak, K., and Motyka, M.**, 2013. Microstructure and mechanical properties of high strength two-phase titanium alloys. Chapter 4, in *Titanium Alloys-Advances in Properties Control*, Poland, pp. 69-80. <http://dx.doi.org/10.5772/56197>.

- [80]. **Song, S., Zhang, J., Liu, M., Li, F. and Bai, S., 2023.** Effect of build orientation and layer thickness on manufacturing accuracy, printing time, and material consumption of 3D printed complete denture bases. *Journal of Dentistry*, 130, p.104435.
- [81]. **Sun, J., Ye, D., Zou, J., Chen, X., Wang, Y., Yuan, J., Liang, H., Qu, H., Binner, J. and Bai, J., 2023.** A review on additive manufacturing of ceramic matrix composites. *Journal of Materials Science & Technology*, 138, pp.1-16.
- [82]. **Tavares, S.M.O. and De Castro, P.M.S.T., 2017.** An overview of fatigue in aircraft structures. *Fatigue & Fracture of Engineering Materials & Structures*, 40(10), pp.1510-1529.
- [83]. **Thijs, L., Verhaeghe, F., Craeghs, T., Van Humbeeck, J., and Kruth, J.P., 2010.** A study of the microstructural evolution during selective laser melting of Ti-6Al-4V. *Acta Materialia*, 58(9), pp. 3303-3312.
- [84]. **Thori, P., Sharma, P., and Bhargava, M., 2013.** An approach of composite materials in industrial machinery: advantages, disadvantages and applications. *International Journal of Research in Engineering and Technology*, 2(12), pp. 350-355.
- [85]. **Vaidya, A., and Pathak, K., 2019.** Mechanical stability of dental materials. In *Applications of Nanocomposite Materials in Dentistry*, Uttar Pradesh University of Medical Sciences, Woodhead Publishing, Saifai, India, pp. 285-305, <https://doi.org/10.1016/B978-0-12-813742-0.00017-1>
- [86]. **Viteri, V.S., and Fuentes, E., 2013.** Titanium and titanium alloys as biomaterials. *Tribology-Fundamentals and Advancements*, Vol.1, (5), pp.155-181.
- [87]. **Wang, Y. and Monetta, T., 2023.** Systematic study of preparation technology, microstructure characteristics and mechanical behaviors for SiC particle-reinforced metal matrix composites. *Journal of Materials Research and Technology*, 25, pp.7470-7497.

- [88]. Wang, Z., Zhang, Y., Tan, S., Ding, L. and Bernard, A., 2021. Support point determination for support structure design in additive manufacturing. *Additive Manufacturing*, 47, p.102341.
- [89]. Yao, B., Peng, Y., Li, Z., Liu, M., Li, H. and Wang, C., 2024. Process parameter optimization for selective laser melting Ti-6Al-4V with high layer thickness. *Materials Today Communications*, 41, p.110781.
- [90]. Yeow, S.T., Shahar, A., Aziz, N.A., Anuar, M.S., Yusof, Y.A., and Taip, F.S., 2011. The influence of operational parameters and feed preparation in a convective batch ribbon powder mixer. *Drug Design, Development and Therapy*, vol.5, pp. 465-469. <https://doi.org/10.2147%2FDDDT.S25047>.
- [91]. Yu, N., 2005. Process parameter optimization for direct metal laser sintering (DMLS). Ph.D. Thesis, Scholarbank @ NUS Repository. <http://scholarbank.nus.edu.sg/handle/10635/14768>.
- [92]. Zang, J., Yang, Z., Song, P., Sun, M., Li, Z. and Li, C., 2023. Investigating the influence of SiC particle characteristics on the mechanical properties and damage behaviors of SiCp/A356 composites. *Applied Composite Materials*, 30(5), pp.1645-1665.
- [93]. Zheng, Z., Sun, B. and Mao, L., 2024. Effect of scanning strategy on the manufacturing quality and performance of printed 316L stainless steel using SLM process. *Materials*, 17(5), p.1189.

## CHAPTER 3: MATERIALS AND METHODS

This chapter contains details on the sieving and weighing of powders carried out at the Centre for Rapid Prototyping and Manufacturing (CRPM), the mixing of Ti6Al4V(ELI) and SiC powders, as well as the mixing equipment. The methodologies used to characterize individual and mixed powders, as well as a matrix for analyzing the effect of process parameters, are also provided in the chapter. Information on the preparation processes for specimens, equipment used to make single and multiple tracks, and methods applied to characterize single tracks and layers are also presented in this chapter. The research methodology of the present work is illustrated in the flow diagram in Figure 3.1.

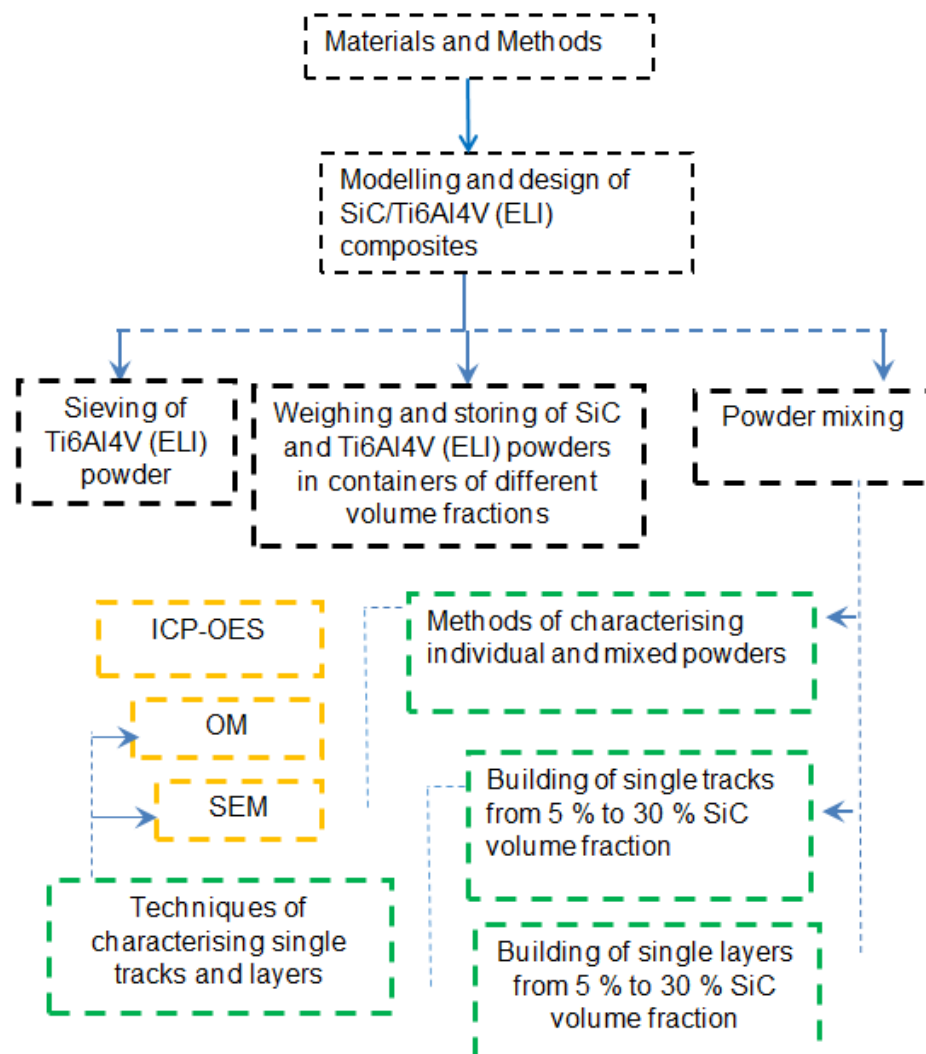


**Figure 3.1:** Research flow diagram

### 3.1. Modelling and design of SiC/Ti6Al4V(ELI) Composites

The elastic behaviour of composite materials was modelled in the present work using a variety of analytical models, such as the Hashin and Strickman bounds, Halpin-Tsai semi-empirical equations, the Rule of Mixtures (RoM) or upper bounds, and the Inverse Rule of Mixtures (IRoM) or lower bounds. The Hashin and Strickman equations are widely used to predict the properties of particulate composites and yield results that fall between the upper and lower bounds. The properties of SiC and Ti6Al4V given in Table 2.2 were used in Equations 2.1, 2.2, 2.4, 2.11 and 2.14 to predict the values of strength, stiffness and coefficient of thermal expansion of the SiC/Ti6Al4V(ELI) composite at different volume fractions of the reinforcing SiC particles.

### 3.2. Sieving of Ti6Al4V(ELI) Powders

The Ti6Al4V(ELI) powder was first sieved before use to remove any agglomerates and large particles to ensure even consistency of the powder. This was done using the 80  $\mu\text{m}$  manual sieve shown in Figure 3.2. The sieve had an area of 223 mm $\times$ 260 mm. During sieving, the recommended protective gear, including masks, gloves, laboratory coats, and antistatic shoes, were worn. A small amount of Ti6Al4V(ELI) powder was added gradually onto the sieve and the powder was moved back and forth using a spatula to encourage particles of the right size to drop through the sieve. It took 20 minutes to sieve all the powder and no agglomerates were found amongst the sieved powder at the end of this exercise.



**Figure 3.2:** Manual sieve used to sieve Ti6Al4V(ELI) powder at CRPM

### 3.3. Weighing of SiC and Ti6Al4V(ELI) Powders for Mixing

At the onset, it was determined to mix volume fractions of SiC powder in Ti6Al4V(ELI) powder with SiC percentages of 5 %, 10 %, 15 %, 20 %, 25 %, and 30 % for testing in the present work. The volume fractions to be used were calculated with reference to the total quantity of powder that will be required for printing tensile specimens to be built in the x- direction and Charpy Impact test specimens built in the y-direction. **Though the tensile and Charpy Impact specimens were eventually not built in this study because of limitations of time, it is expected that they will be built in future work for purposes of conducting mechanical testing.**

From this total quantity of powder, the quantities of SiC and Ti6Al4V powders to be utilized in building specimens for a given percentage of SiC powder were calculated as follows:

$$v_p = \frac{V_p}{V_p + V_m} \quad (3.1)$$

where the symbols  $v_p$ ,  $V_m$  and  $V_p$  represents the volume fraction of SiC particles, volume of matrix and volume of SiC particles. For a total volume of powder of 37 500 mm<sup>3</sup> required for building the tensile and Charpy Impact specimens, Equation 3.1 can be rewritten as:

$$v_p = \frac{V_p}{V_p + V_m} = \frac{V_p}{37,500} \quad (3.2)$$

For a 5% SiC volume fraction of powder, the volume of SiC powder was calculated from the foregoing equation as:

$$5 \% = \frac{V_p}{37,500} \quad (3.3)$$

$$V_p = \frac{5}{100} \times 37\,500 = 1\,875 \text{ mm}^3 \quad (3.4)$$

The remaining 95% of the powder was Ti6Al4V(ELI), whose volume was obtained as follows:

$$V_m = \frac{95}{100} \times 37\,500 = 35\,625 \text{ mm}^3 \quad (3.5)$$

The volumes of SiC and Ti6Al4V powders required for the other volume fractions from 10 to 30 % were calculated following a similar approach.

The values of mass ( $m$ ) of SiC and Ti6Al4V required were then calculated from the respective calculated values of volumes ( $V_p$  and  $V_m$ ) and their respective densities ( $\rho_p$  and  $\rho_m$ ) provided by their respective suppliers of  $0.0031\text{g/mm}^3$  and  $0.0045\text{g/mm}^3$  and from the known Equations 3.6 and 3.7 relating mass, volume and density.

$$M_p = \rho_p V_p \quad (3.6)$$

$$M_m = \rho_m V_m \quad (3.7)$$

The mass fractions of SiC and Ti6Al4V (ELI) were then obtained from these calculated values of mass substituted into Equation 3.8 and 3.9 as follows:

$$m_p = \frac{M_p}{M_p + M_m} \quad (3.8)$$

$$m_m = \frac{M_m}{M_m + M_p} \quad (3.9)$$

where the symbols  $m_p$ ,  $m_m$ ,  $M_p$ ,  $M_m$  represents the mass fraction of SiC particles, mass fraction of Ti6Al4V(ELI) particles, mass of SiC particles and mass of Ti6Al4V(ELI) particles, respectively. The required amounts of powder were measured in masses since it was easier to measure the mass of powders on a scale. However, because there is very little information in literature on composites in terms of mass fractions or percentages, the volume fractions of powders set at the beginning were used for analysis throughout this work.

The mass of a container ( $m_c$ ) was first measured and then the respective calculated mass fractions of a mixture of the two powders poured into the container whose total mass ( $m_T$ ) was then measured. The mass of each container was then subtracted from the total determined mass to obtain the mass of mixed powder ( $m_p + m_m$ ) in each container, as shown in Equation 3.10.

$$m_T - m_c = (m_p + m_m) \quad (3.10)$$

The weighed mixtures of powder for each volume fraction of SiC are tabulated in Table 3.1.

**Table 3.1: The total mass of SiC, Ti6Al4V(ELI) and mixed powders required for two types of test specimens for each volume fraction of SiC**

Percentage of SiC Powder (%)	Type of Powder	Tension Test Specimen (g)	+10% Contingency (g)	Charpy Impact Test Specimen (g)	+10% Contingency (g)
5	SiC	5.8	6.4	5.0	5.5
	Ti6Al4V	160.3	176.3	138.9	152.8
10	SiC	11.6	12.8	10.1	11.1
	Ti6Al4V	151.9	167.1	131.6	144.8
15	SiC	17.4	19.1	15.1	16.6
	Ti6Al4V	143.4	157.7	124.3	136.7
20	SiC	23.3	25.6	20.2	22.2
	Ti6Al4V	135.0	148.5	117.0	128.7
25	SiC	29.1	32	25.2	27.7
	Ti6Al4V	126.6	139.3	109.7	120.7
30	SiC	34.9	38.4	30.2	33.2
	Ti6Al4V	118.1	129.9	102.4	112.6

The mixed powders were placed in plastic containers each with a diameter of 42 mm and a length of 140 mm. Each of the containers weighed 16.3 g when empty. Figure 3.3 shows an image of the plastic containers used to store the mixed powders.



**Figure 3.3: Plastic containers used for storing mixed powder**

The length and diameter of the containers were chosen considering the dimensions of the tubes of the multi-batch mixer used in the laboratory of the Department of Geology at the University of the Free State (UFS). This required the plastic containers to have a length and diameter slightly lower than those of the mixer tubes to ensure they could fit well inside the tubes and allow some movement during mixing.

### 3.4. Mixing of Powder

Batch mixing of the SiC and Ti6Al4V(ELI) powders was carried out with a multi-tube rotary batch mixer. The multi-tube batch mixer, shown in Figure 3.4, had five tubes of diameter and a length of 45 mm and 160 mm, respectively, into each of which was inserted a sealed container with a mixture of SiC and Ti6Al4V(ELI) powders of selected mass fractions for mixing. Because there were six containers, each bearing a different volume fraction of the mixture, only four containers were used for mixing during the first round and the last two were used in the second round of mixing. The powders were mixed for 30 minutes and then analysed in a scanning electron microscope (SEM).



*Figure 3.4: An image of the multi-batch mixer used in this study*

### 3.5. Building of DMLS SiC/Ti6Al4V(ELI) Single Tracks

Firstly, Ti6Al4V substrate plates with dimensions of 50 mm×50 mm were obtained and machined to provide smooth and flat surfaces on which to build. The plates were

installed onto the build platform of the EOSINT M280 machine, which is shown in Figure 2.8 of Chapter 2. A coating of SiC/Ti6Al4V(ELI) powder with a thickness of 45–50  $\mu\text{m}$  was deposited onto the Ti6Al4V substrate plate and then levelled. A laser beam with an 80  $\mu\text{m}$  spot diameter and a maximum generated laser power of 400 W was focused on this base powder. The technical parameters of the EOSINT M280 machine used are listed in Table 2.7. To produce single tracks, the process parameters listed in Table 3.2 were employed. Three tracks were made for each scanning speed. A prior investigation using the same EOSINT M280 equipment determined the best process parameters of laser power and scanning speed for Ti6Al4V(ELI) as 200 W and 1.2 m/s (Ramosena et al., 2021). The laser power and scanning speeds were varied below and above these optimum values to generate the values shown in Table 3.2. Equation 2.15 was used to calculate the linear energy density for the seven scanning speeds employed for each value of laser power.

**Table 3.2: Process parameters used for building SiC/Ti6Al4V(ELI) single tracks**

<b>100 W</b>	Scanning speed (m/s)	0.3	0.4	0.5	0.6	0.7	0.8	0.9
	Linear energy density (J/m)	333	250	200	167	143	125	111
<b>150 W</b>	Scanning speed (m/s)	0.6	0.7	0.8	0.9	1	1.1	1.2
	Linear energy density (J/m)	250	214	188	167	150	136	125
<b>200 W</b>	Scanning speed (m/s)	0.8	0.9	1	1.2	1.4	1.5	1.6
	Linear energy density (J/m)	250	222	200	167	143	133	125
<b>250 W</b>	Scanning speed (m/s)	1.1	1.2	1.3	1.5	1.7	1.8	1.9
	Linear energy density (J/m)	227	208	192	167	147	139	132
<b>300 W</b>	Scanning speed (m/s)	1.2	1.4	1.6	1.8	2	2.2	2.4
	Linear energy density (J/m)	250	214	188	167	150	136	125
<b>350 W</b>	Scanning speed (m/s)	1.5	1.7	1.9	2.1	2.3	2.5	2.7

Linear energy density (J/m)	233	206	184	167	152	140	130
-----------------------------	-----	-----	-----	-----	-----	-----	-----

### 3.6. Building Single Layers at Different SiC Mass Fractions

Multiple tracks were built using different process parameters at each volume fraction. According to literature, the best hatch distance for Ti6Al4V is 80  $\mu\text{m}$ , with track widths ranging from 80  $\mu\text{m}$  to 160  $\mu\text{m}$  (Ramosena et al., 2021). To determine the best hatch distance for the different SiC/Ti6Al4V(ELI) composites, the hatch distance was adjusted with three values below and three values above this value of 80  $\mu\text{m}$ . Multiple tracks were built for each hatch distance to form single layers. At each volume fraction of SiC (5 %, 10 %, 15 %, 20 %, 25 %, and 30 %), the laser power and laser scanning speed parameter sets were kept constant at the best values determined in the testing and analysis of single tracks, for different values of hatch distance. Table 3.3 shows the process parameters used to build single layers at each volume fraction.

**Table 3.3: Process parameters used at each volume fraction to build single layers**

SiC Volume Fraction (%)	Laser Power (W)	Laser Scan Speed (m/s)	Hatch Distance ( $\mu\text{m}$ )	Layer Thickness ( $\mu\text{m}$ )	Volumetric Energy Density ( $\text{J}/\text{mm}^3$ )	Linear Energy Density (J/m)
<b>5</b>	200	1.2	50	45	74	167
	200	1.2	60	45	62	167
	200	1.2	70	45	53	167
	200	1.2	80	45	46	167
	200	1.2	90	45	41	167
	200	1.2	100	45	37	167
	200	1.2	110	45	34	167
<b>10</b>	200	1	50	45	89	200
	200	1	60	45	74	200
	200	1	70	45	63	200
	200	1	80	45	56	200
	200	1	90	45	49	200
	200	1	100	45	44	200
	200	1	110	45	41	200
<b>15</b>	150	0.8	50	45	83	188
	150	0.8	60	45	69	188
	150	0.8	70	45	60	188
	150	0.8	80	45	52	188
	150	0.8	90	45	46	188

	150	0.8	100	45	42	188
	150	0.8	110	45	38	188
						50
<b>20</b>	200	0.9	50	45	99	222
	200	0.9	60	45	83	222
	200	0.9	70	45	71	222
	200	0.9	80	45	62	222
	200	0.9	90	45	55	222
	200	0.9	100	45	49	222
	200	0.9	110	45	45	222
						60
<b>25</b>	200	1.2	50	45	74	167
	200	1.2	60	45	62	167
	200	1.2	70	45	53	167
	200	1.2	80	45	46	167
	200	1.2	90	45	41	167
	200	1.2	100	45	37	167
	200	1.2	110	45	34	167
<b>30</b>	350	1.7	50	45	92	206
	350	1.7	60	45	77	206
	350	1.7	70	45	65	206
	350	1.7	80	45	57	206
	350	1.7	90	45	51	206
	350	1.7	100	45	46	206
	350	1.7	110	45	42	206

A schematic top view of the single layers built for each SiC volume fraction at different hatch distances is shown in Figure 3.5. The dimensions in micrometres shown below each layer in this figure represent the hatch distance for each printed layer.

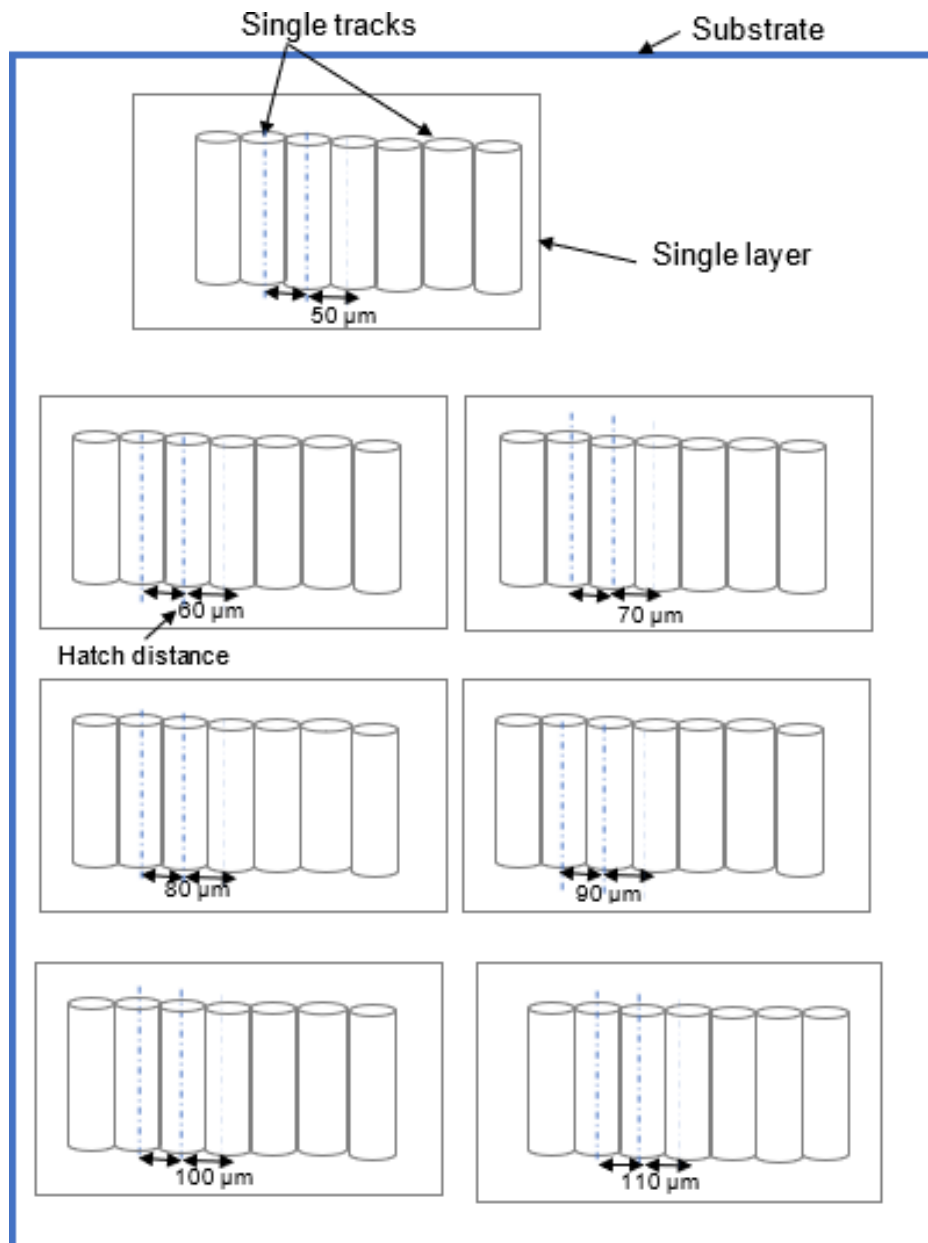


**Figure 3.5:** Schematic view of the layout on the substrate of the single layers built

### 3.7. Preparation of Specimens for Analyses using a SEM and an Optical Microscope

An electrical discharge machine (EDM) was used to cut cross-sections perpendicular to the length of the built tracks and layers for investigation of their features. The same procedure of mounting was performed for preparing the mixed powders, single tracks, and single layers for analysis. Small amounts of mixed powder and cut sections of

single tracks and layers were separately placed on a piston of the Struers Cito Press machine, which was lowered thereafter, to create space in the cylinder above the particles of powder or cut sections, so that the resin could spread all over to cover the particles or samples. An image of the Cito Press-1 machine is shown in Figure 3.6(a). Thereafter, the piston was lowered again and stopped automatically at the lower limit. The mounting of powder and samples each took 3.5 minutes and was done at a temperature and pressure of 180 °C and 250 bar, respectively. The samples were subsequently cooled with water for two minutes. Thereafter, the samples were ground and polished using the Struers Tegramin-25 polishing machine shown in Figure 3.6(b).

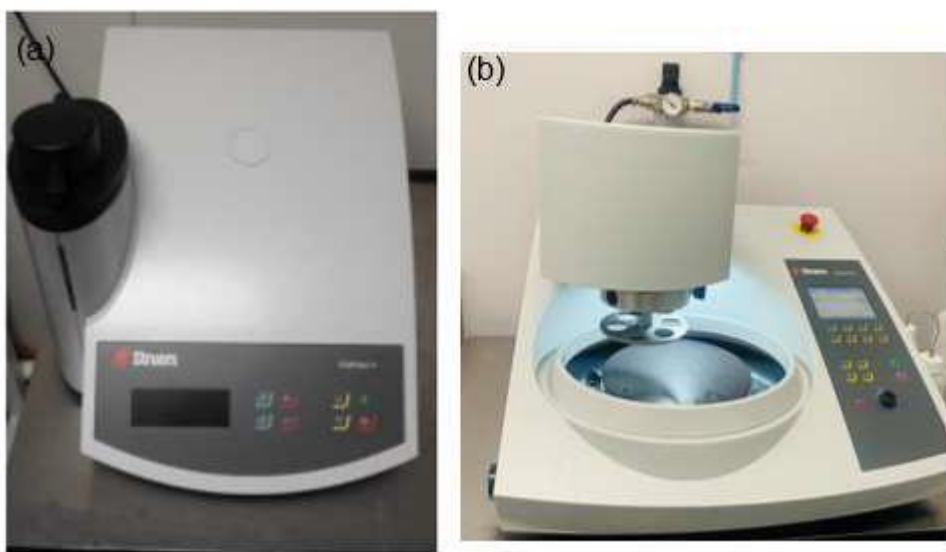


**Figure 3.6:** Images of (a) the Struers Cito Press-1 machine and (b) the Struers Tegramin-25 polishing machine

Grinding and polishing were carried out in accordance with the Struers technique for Ti-based alloys. Table 3.2 contains information on the grinding and polishing steps proposed by Struers. After polishing of the samples, they were etched with a Kroll's reagent in a ductless fume cabinet to reveal their surface structure.

**Table 3.4:** Details of the grinding and polishing steps recommended by Struers (Dzogbewu et al., 2017)

Process	Wheel	Lubricant	Force (N)	Speed (rpm)	Time (min)
Coarse grinding	320 SIC	water	25 N	300	1.5

Fine grinding	MD-Largo	Diapro All/Lar.9	30 N	150	5.0
First polishing	MD-Mol	Diapro Mol.3	25 N	150	2.2

### 3.8. Characterization of Powder and Specimens

The mixed powders and the specimens of single tracks and single layers were characterized using a JSM-6610 SEM and ZEISS Axio Scope.A1 OM.

#### 3.8.1. Scanning Electron Microscopy

A SEM is a type of electron microscope that produces images of a sample by scanning the surface with a focused beam of electrons (Ahktar et al., 2018). As the electrons hit the surface of the specimen, different signals from secondary electrons, characteristic X-rays, and backscattered electrons, are each detected by respective detectors to provide information about morphology, topography, composition, and crystallographic structure and the results displayed as digital images and X-ray spectra on a screen. The morphologies of the mixed and individual powders, as well as single tracks and layers, were determined using the JSM-6610 SEM of the UFS.

The Ti6Al4V(ELI), SiC and mixed powders, the latter with different SiC volume fractions, were sampled using a spatula and were mounted on double-sided carbon tapes where after they were placed on the platform inside the SEM. The shape, size, and surface topography of individual powders, as well as mixed powders, were studied. An energy-dispersive spectrum of the characteristic X-rays was used to provide information on the composition of SiC and Ti6Al4V(ELI) powder, defining the elements that the powders were composed of. Backscattered electrons were used to provide high contrast images dependent on the elemental composition of the specimens and were useful for identifying regions of different elemental composition on the single tracks and mixed powders. The samples of the top view of the single tracks and single layers as well as their cross-sections were also investigated. Secondary electrons were used on the single tracks and layer specimens to obtain images of the topography and morphology of the specimens, showing surface features of the specimens such as texture, smoothness, and roughness, continuity of tracks, spatter particles and discontinuity. An image of the JSM-6610 SEM used in this

study is shown in Figure 3.7.



**Figure 3.7:** An image of a JSM-6610 scanning microscope

### 3.8.2. Optical Microscopy

The ZEISS Axio Scope.A1 OM was used to examine the top view of the manufactured single tracks and layers. The widths of the tracks were measured and recorded at several points along the length of each individual track to determine the average track width. Surface features such as continuity and discontinuity of tracks, pre-balling, balling, spatter particles, and un-melted Ti6Al4V(ELI) powder were identified on each track and layer. Under an optical microscope, cut cross-sections of single tracks were examined for geometrical characteristics such as width, height above the substrate, and depth of penetration into the substrate, whereas cross-sections of layers were examined for overlapping between adjacent tracks, depth of penetration, evenness, and unevenness of the top surfaces of the layers. An image of the ZEISS Axio Scope.A1 OM is shown in Figure 3.8.



**Figure 3.8:** An image of the ZEISS Axio Scope.A1 Optical Microscope (OM)

### **3.8.3. Inductively Coupled Plasma-Optical Emission Spectrometry**

The chemical composition of the Ti6Al4V(ELI) powder was determined through Inductively Coupled Plasma-Optical Emission Spectrometry (ICP-OES). This technique uses argon plasma as the excitation source to determine how many trace elements are in a sample and atomic composition of a particular sample. The sample of powder was dissolved in an acid solution and fed into plasma that can operate at temperatures in the range 5727–9727 °C, which are high enough to break down the samples into atoms and provide energy for ionization and excitation. The energy provided by the argon plasma causes movement of electrons in atoms and ions from a ground state to an excited state. Return of the excited electrons to their respective ground states is accompanied by a release of light at wavelengths specific to the type of atom and energy levels between which the electrons move, thus providing an identity signature of the atom. The photon wavelengths produced this way are measured by an optical spectrometer. Identification of the elemental type depends on the position of the photon rays in the spectrometer and the concentration of each element is determined based on the intensity of the rays. This measurement of the intensity of the emission lines of the different elements produces quantitative elemental data on the types of atoms.

### 3.9. REFERENCES

- [1]. **Akhtar K., Khan S.A., Khan S.B., and Asiri A.M.,** 2018. *Scanning Electron Microscopy: Principle and Applications in Nanomaterials Characterization.*, In: Sharma, S. (eds) Handbook of Materials Characterization. © 2018 Springer International Publishing, [https://doi.org/10.1007/978-3-319-92955-2\\_4](https://doi.org/10.1007/978-3-319-92955-2_4)
- [2]. **Dzogbewu, T.C.,** 2017. *Direct metal laser sintering of titanium alloys for biomedical applications.* Doctoral dissertation, Bloemfontein: Central University of Technology, Free State. P.p. 75-84, <http://hdl.handle.net/11462/1695>
- [3]. **Ramosena, L., Dzogbewu, T., and du Preez, W.,** 2021, Direct metal laser sintering production of Ti6Al4V parts from a purely elemental powder blend. *RAPDASA-RobMech-PRASA Conference – 22<sup>nd</sup> Annual International RAPDASA Conference, International Conference Centre CSIR, Pretoria, Gauteng, 3<sup>rd</sup>–5<sup>th</sup> November 2021*, pp. 73-75. <https://site.rapdasa.org/past-proceedings-2021/>

## CHAPTER 4: ANALYTICAL MODELLING OF THE PROPERTIES OF SiC/Ti6Al4V(ELI) COMPOSITES

Some of the material presented in this chapter has been published in peer-reviewed media as detailed below:

1. Seleso, M., Maringa, M., and du Preez, W., 2020. "Designing a ceramic particulate composite to enhance selected mechanical properties of Ti6Al4V"., Rapid Product Development Association of South Africa (RAPDASA) 21st Annual International Conference, Japie van Lill Auditorium, Central University of Technology, Free State, 3rd November 2020, South Africa, pp. 41-55. <https://site.rapdasa.org/past-proceedings-2020/>.

### 4.0. Introduction

In this chapter the application of analytical models for predicting the elastic behaviour of composites, discussed in Chapter 2, and applied to model SiC/Ti6Al4V(ELI) composites, is presented.

### 4.1. Modelling the Properties of SiC/Ti6Al4V(ELI) Particulate Composites

To predict the specific mechanical properties of strength and stiffness of SiC/Ti6Al4V(ELI) composites at varying volume fractions of reinforcing SiC particles, the upper bound Voigt rule may be used. Figure 4.1 shows the strength of composites of SiC/Ti6Al4V(ELI) with varying volume fractions of SiC particles from zero to 100 vol %, based on the Voigt rule for both the high strength of SiC of 1625 MPa and the low strength of SiC of 240 MPa.

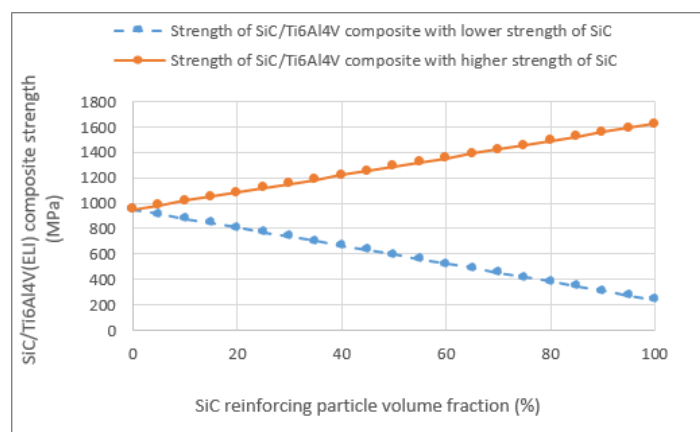


**Figure 4.1:** Curves of the strength of SiC/Ti6Al4V(ELI) composites versus volume fraction of SiC particles based on the Voigt rule for high and low specific strength of SiC particles

The low and high values of tensile strength of SiC particles given in Table 2.2 as 240-1625 MPa, were used to predict the values of strength of SiC/Ti6Al4V(ELI) composites plotted in Figure 4.1. For the higher value of strength of SiC that is higher than that of Ti6Al4V(ELI), the Voigt rule predicts increased values of strength of the resulting composites. Conversely, for the lower value of strength of SiC that is lower than that of Ti6Al4V(ELI), the Voigt rule predicts reduced values of strength of the resulting composites. These two trends led to the diverging predicted curves plotted in Figure 4.1 for the SiC/Ti6Al4V(ELI) composite, which emphasises the need to confirm the mechanical properties of SiC to be used. The predicted values plotted in this figure are indicative of the values expected from mechanical testing of built 3D specimens of the composite. However, building and testing of 3D specimens could not be carried out due to limitations of time and is expected to be done in the future.

The curve of the composite with SiC particles of higher strength (continuous orange curve) is seen in this figure to increase with increasing volume fraction of the particles, while that of the SiC particles with lower strength (hatched blue curve) is seen to decrease with increasing volume fraction of the particles. At 20 % volume fraction, the hatched curve shows a composite strength of 808 MPa, which is lower than that of Ti6Al4V(ELI) (950 MPa) and higher than that of the lower strength of SiC (240 MPa), resulting in a 15 % drop in the strength of Ti6Al4V(ELI). At the same volume fraction of high strength SiC filler, the continuous orange curve shows a composite strength of 1 085 MPa, which is higher than that of Ti6Al4V (ELI) and lower than that of the higher strength SiC value of 1 625 MPa, representing a 14 % enhancement of the strength of Ti6Al4V(ELI). The particulate filler volume fraction of 20 vol % is referred to here based on the work of Ramah et al. (2014), for SiC/Al composites, which showed that filler volume fractions above 20 % volume fraction in MMCs lead to an increase in the hardness of the particles, thus encouraging initiation of cracks at the interface and consequent failure of the composites.

Figure 4.2 shows the elastic modulus of SiC/Ti6Al4V (ELI) composites with varying volume fractions of SiC particles based on the Voigt and the lower bound Reuss rules.

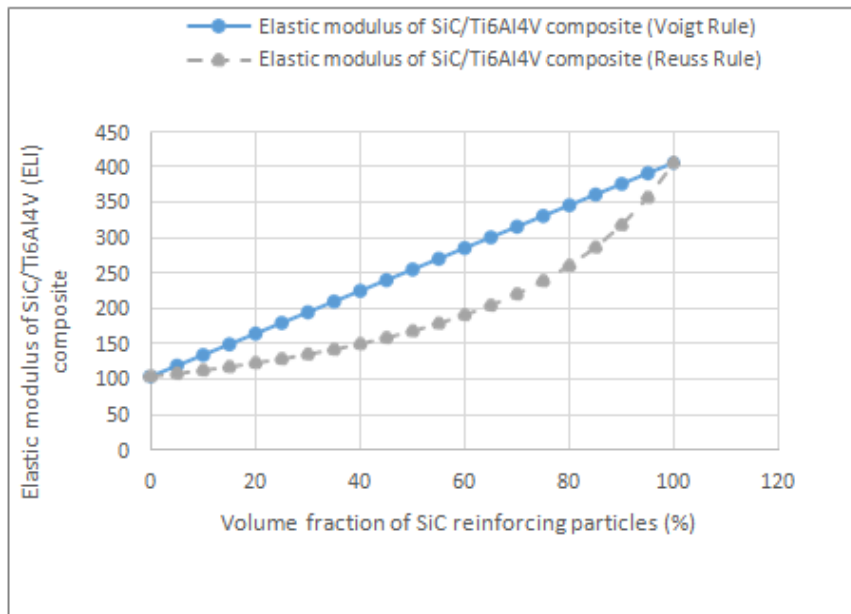


**Figure 4.2:** Variation of the elastic modulus of SiC/Ti6Al4V (ELI) composites with varying volume fractions of SiC particles

It is seen from the curve of the IROM in this figure that the rate of increase of stiffness of a composite increases with increasing mass fraction of the reinforcing particles. At a mass fraction of the reinforcing SiC particles of 20 %, the curve for the IROM gives a value of the elastic modulus of the SiC/Ti6Al4V(ELI) composite of 130 GPa, which is higher than that of Ti6Al4V (110 GPa) and lower than that of the SiC particles (410 GPa). This is an 18 % increase in modulus over that of Ti6Al4V. At the same volume fraction, the Voigt curve gives a value of 170 GPa, which is a 55% increase in modulus over that of Ti6Al4V. At a volume fraction of the reinforcing SiC particles of 40 %, the Reuss curve gives a value of 156 GPa while the Voigt rule gives a value of 230 GPa, which represent increases of 42 % and 109 % over that of Ti6Al4V(ELI), respectively. The higher and lower values predicted by the Voigt and Reuss rules, respectively, are not surprising as the first rule defines the upper bound while the Reuss rule defines the lower bound for composites. The reinforcing volume fractions of 20 % and 40 % are selected for use in analysis here based on the separate works of Ramah et al. (2014), and Yilmaz et al. (2017), which showed the former and the latter to be limiting volume fractions at which cracks at the interfaces were initiated and where maximum stiffness of particulate composites occurred, respectively.

The Voigt and Reuss rules, Equations 2.1 and 2.3, respectively, as well as the Halpin-

Tsai Equations 2.6 and 2.8 in Chapter 2, were used to plot values of the elastic modulus of SiC/Ti6Al4V composites for different SiC particle volume fractions, as shown in Figure 4.3. For idealised, spherical particles, a shape parameter ( $\xi=2$ ) was employed, and the ratio ( $l/d$ ) for the stress partitioning factor ( $\eta$ ) was set to unity as prescribed in the text by Harris et al. (1999). The Halpin Tsai Equations were used here as they model randomly oriented short fibres, which better approximates particulate fillers when their aspect ratio ( $l/d$ ) is set to unity (Ghafaar et al., 2006).

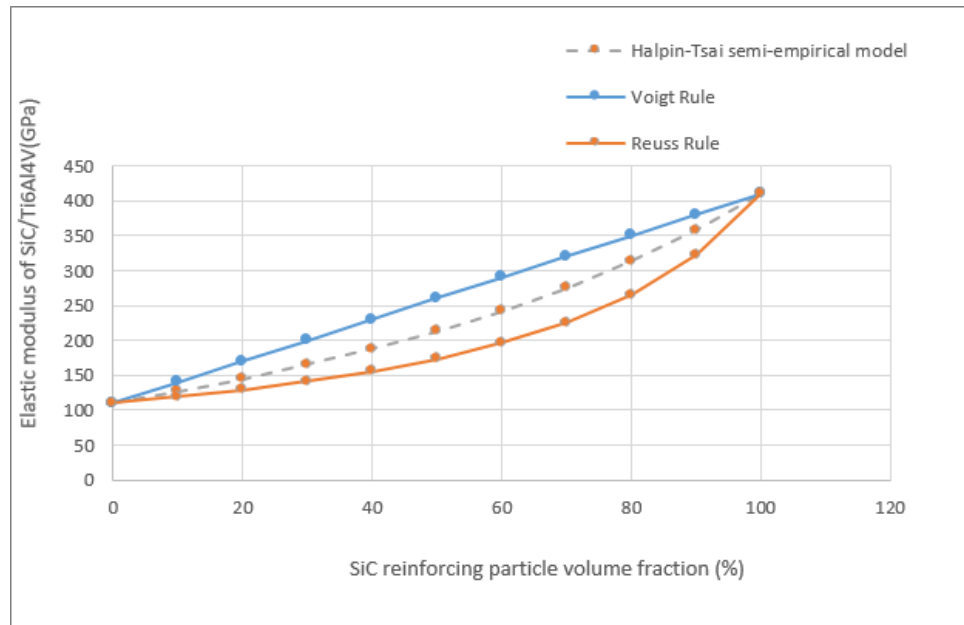


**Figure 4.3:** Curves of elastic modulus based on the Reuss and Voigt rules, as well as the Halpin-Tsai semi-empirical equations for different volume fractions of SiC

All three curves in Figure 4.3 show effective reinforcement at all volume fractions of the SiC reinforcing particles. At 20 % volume fraction, the curves based on the Voigt rule, Halpin-Tsai semi-empirical equations, and Reuss rule, show values of elastic modulus for SiC/Ti6Al4V(ELI) composites of 170 GPa, 145 GPa and 129 GPa, respectively. This translates to increases of stiffness of 55 %, 31 %, and 17 %, respectively. At a volume fraction of 40 %, the curves based on the Voigt rule, Halpin-Tsai semi-empirical equations and Reuss rule show values of elastic modulus for SiC/Ti6Al4V(ELI) composites of 230 GPa, 188 GPa and 155 GPa, respectively, which results in improvements of elastic modulus over that of Ti6Al4V of 110 %, 70 % and 41 %, respectively. **These predicted values of elastic modulus serve as a guide of the values expected upon conducting experimental testing on built 3D**

specimens, for the selected reinforcing volume fractions of SiC lying between 5 - 30%. The large increase in the values of stiffness shows significant positive reinforcement of Ti6Al4V(ELI) by SiC. However, there was not enough time to undertake printing of three dimensional specimens upon which such tests could be conducted and it is expected to get this done in future.

As noted in Chapter 2 of this document, the Halpin-Tsai semi-empirical equations can be used to produce lower or upper bound curves, depending on the magnitude of the shape parameter ( $\xi$ ). Thus, when the value of  $\xi$  becomes very small ( $\xi \rightarrow 0$ ), the Halpin-Tsai semi-empirical model tends to approach the IRoM or Reuss rule. For large values of ( $\xi \rightarrow \infty$ ), the Halpin-Tsai semi-empirical model tends to approach the RoM or Voigt rule. This is clearly illustrated in Figure 4.4, with curves of the Halpin-Tsai semi-empirical equation for randomly oriented short fibres, for which the shape parameter ( $\xi$ ) was set to 0.05, 0.5, 1, 2, 5, 10, and 5 000.

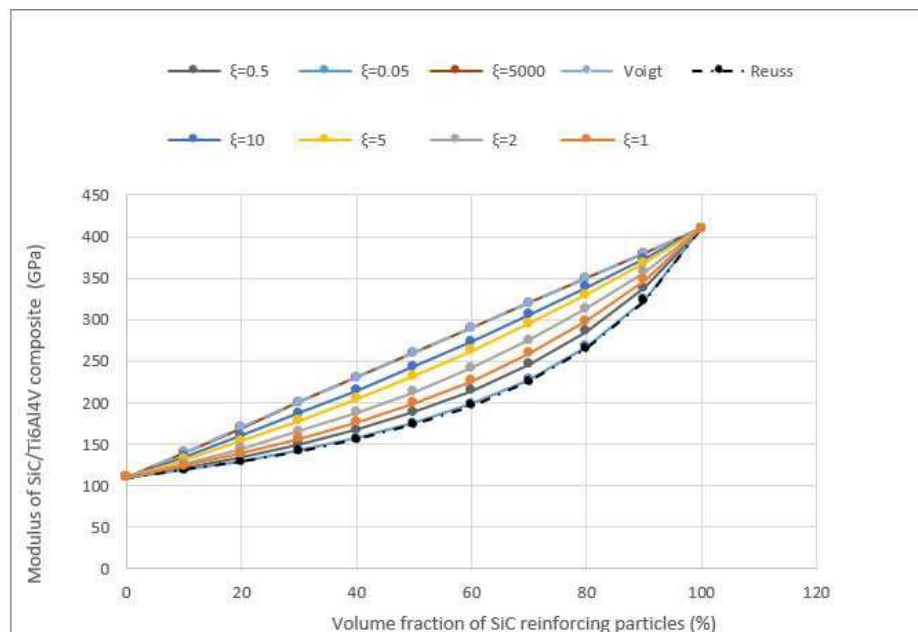


**Figure 4.4:** *Plots of Halpin-Tsai semi-empirical curves of elastic modulus versus SiC volume fraction with different magnitudes of the shape parameters*

It is observed from the curves in Figure 4.4 that as the value of the shape parameter increases, the curves of elastic modulus tend towards the Voigt curve. The curve with the largest value of shape parameter of 5 000 plotted in Figure 4.4 is seen to coincide with the Voigt curve. It is further clear from Figure 4.4 that as the value of the shape

parameter decreases toward zero, the curves approach the Reuss curve. Therefore, the curve with the smallest value of 0.05 almost coincides with the Reuss curve. The power of the Halpin-Tsai semi-empirical equations is seen in the variation of the curves with changing values of the shape factor, as this enables the curves to be fitted to composites with widely varying values of elastic modulus. As was noted for Figure 4.3, the significant increase in the values of stiffness in Figure 4.4 indicates significant positive reinforcement of Ti6Al4V (ELI) by SiC. These predicted values of elastic modulus serve as a guide of expected values upon conducting experimental testing on built 3D specimens, for the selected reinforcing volume fractions of SiC lying between 5-30%. Unfortunately, there was not enough time to print 3D specimens upon which such tests could be performed and this forms the subject of future work on this composite.

The values of the coefficient of thermal expansion (CTE) of SiC and Ti6Al4V in Table 2.2 were used together with Equations 2.4 (Reuss Rule), 2.5 (Voigt Rule), 2.11 and 2.13 (Hashin and Strickman (HS) upper and lower bounds, respectively) to plot curves of the variation of the CTE for SiC/Ti6Al4V (ELI) composites with volume fraction of SiC to give the curves shown in Figure 4.5.

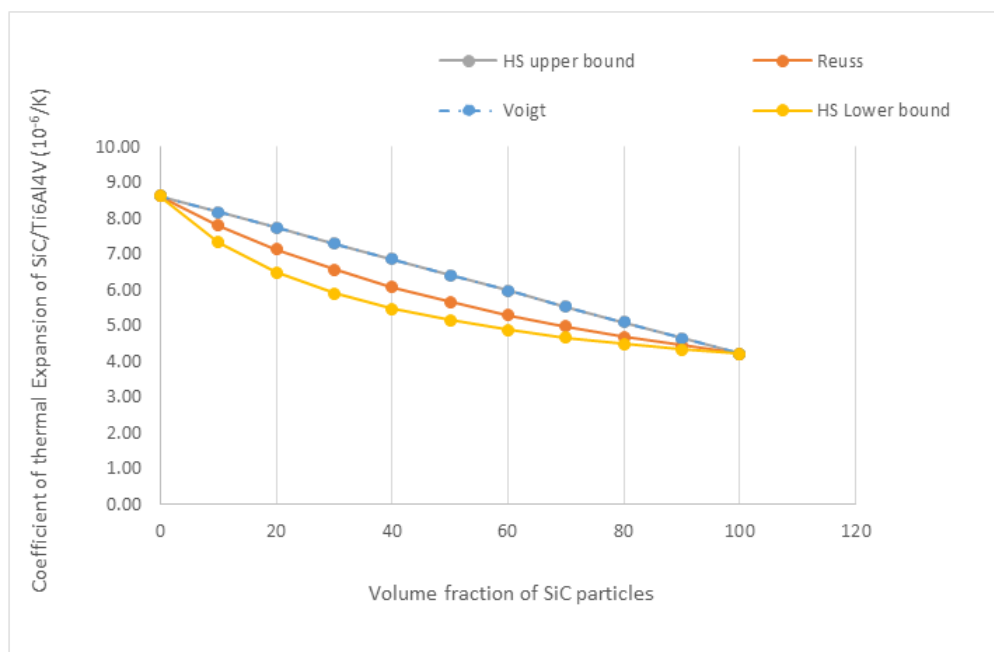


**Figure 4.5:** *Plots of the Voigt, Reuss, as well as Hashin and Strickman, models for predicting the CTEs of SiC/Ti6Al4V(ELI) composites for different volume fractions of SiC particles*

In Figure 4.5, the CTE is seen to decrease with increasing volume fraction of SiC particles. At a volume fraction of 20 %, the CTE predicted by the HS lower bound equations is  $6.5 \times 10^{-6}/K$ , the Reuss rule  $7.71 \times 10^{-6}/K$  and by the HS upper bound equations and Voigt rule the same value of  $7.72 \times 10^{-6}/K$ . The values of CTE predicted by these models are lower than that of Ti6Al4V ( $8.6 \times 10^{-6}/K$ ) and higher than that of carbon fibre/epoxy reinforced composite sheets of  $2.1 \times 10^{-6}/K$  and carbon fibre tubes of  $0.1 \times 10^{-6}/K$ . At a volume fraction of 40 %, the HS lower bound equation predicts a CTE of  $5.5 \times 10^{-6}/K$ , the Reuss rule  $6.06 \times 10^{-6}/K$  and the HS upper bound equation and Voigt rule  $6.8 \times 10^{-6}/K$ .

At 40 % volume fraction, the values of the CTE that are predicted by these three models are all lower than most of the values predicted at fraction of 20 %. Clearly, by closely matching the CTEs of SiC/Ti6Al4V(ELI) composites to those of carbon fibre epoxy resin composites, the effects of differential expansion and contraction at their joints during thermal cycling can be reduced.

The Reuss and Voigt models can also be used to explore the hardness ( $H$ ) of SiC/Ti6Al4V (ELI) through Equations 4.1 and 4.2.

$$H_c = H_m V_m + H_p V_p \quad (4.1)$$

$$H_c = \frac{H_m H_p}{H_m V_p + H_p V_m} \quad (4.2)$$

where  $H_c$  is the hardness of the composite,  $H_m$  is the hardness of the matrix and  $H_p$  represent the hardness of the particles, while  $V_m$  and  $V_p$  represents the volume fraction of the matrix and the volume fraction of the particles, respectively. Figure 4.6 represents the Knoop hardness of SiC/Ti6Al4V composite using Equations 4.1 and 4.2, respectively.

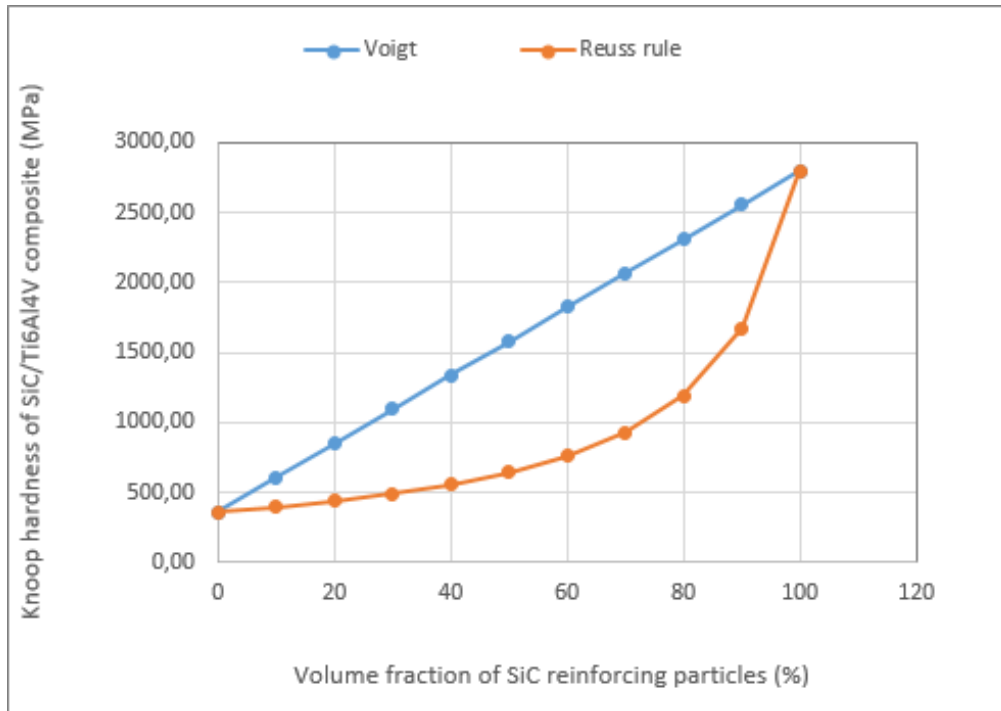


**Figure 4.6:** *Theoretical values of the hardness of the SiC/Ti6Al4V(ELI) composite for different SiC volume fractions, based on the Reuss and Voigt rules*

The Voigt and Reuss rules estimate hardness values of 850 MPa and 440 MPa for the SiC/Ti6Al4V(ELI) composite at a volume mass fraction of 20 % in Figure 4.6. The Voigt and Reuss models predict hardness values of 1 338 MPa and 557 MPa, respectively, at a mass volume fraction of 40 %. Both rules forecast a harder material than Ti6Al4V(ELI), which has a hardness of 363 MPa (Welsch et al., 1993). Both data demonstrate that the hardness of SiC/Ti6Al4V(ELI) increases with increasing SiC reinforcing particle mass volume fraction.

## 4.2. Conclusions

The following conclusions arose from the study and discussion of Figures 4.1 to 4.6 in this chapter.

- The low and high values of tensile strength of SiC particles led to divergence of the predicted curves. For the higher value of strength of SiC that is higher than that of Ti6Al4V(ELI), the Voigt rule predicted increased values of strength of the resulting composites with increasing SiC volume fraction. Conversely, for the lower value of strength of SiC that is lower than that of Ti6Al4V(ELI), the Voigt rule predicted reduced values of strength with increasing SiC volume fraction.

- The elastic modulus of SiC/Ti6Al4V(ELI) composites increased as indicated by the IRoM, Voigt and the Halpin-Tsai empirical equations. The elastic modulus of SiC/Ti6Al4V(ELI) was observed in the plotted curves to increase by 55%, 18%, and 31% for the three models, respectively, over that of Ti6Al4V at 20% SiC volume fraction, while an improvement of 109%, 42%, and 70% over that of Ti6Al4V (ELI) was predicted at 40% SiC volume fraction.
- The Voigt and Reuss models, as well as Hashin and Strickman bounds gave rise to predicted values of CTE of SiC/Ti6Al4V(ELI) composites with decreasing values for increasing SiC volume fraction. At 40 % volume fraction, the values of the CTE that were predicted by these three models were all lower than most of the values predicted at volume fraction of 20 %. Therefore, it is expected that the predicted values of the CTEs of SiC/Ti6Al4V (ELI) composites will much more closely match those of carbon fibre epoxy resin composites than the case for Ti6Al4V(ELI) alone, and thus reduce the effects of differential expansion and contraction at their joints during thermal cycling.
- The Voigt and Reuss models predicted increasing values of hardness of SiC/Ti6Al4V(ELI) composites.

### 4.3. REFERENCES

- [1]. **Affdl, J.H., and Kardos, J.L.**, 1976. The Halpin-Tsai equations: a review. *Polymer Engineering and Science*, 16(5), pp. 344-352.
- [2]. **Ghafaar, M.A., Mazen, A.A., and El-Mahallawy, N.A.**, 2006. Application of the rule of mixtures and Halpin-Tsai equations to woven fabric reinforced epoxy composites. *JES. Journal of Engineering Sciences*, 34(1), pp. 227-236.
- [3]. **Harris, B.**, 1999. Engineering composite materials, *The Institute of Metals*, London., [https://learn.skillman.eu/pluginfile.php/1902/mod\\_resource/content/0/Engineering%20Composites.pdf](https://learn.skillman.eu/pluginfile.php/1902/mod_resource/content/0/Engineering%20Composites.pdf).
- [4]. **Rahman, M.H., and Mamun, H.M.R.**, 2014. Characterization of silicon carbide reinforced aluminum composites, *Procedia Engineering*, 90, pp. 103-109.
- [5]. **Welsch, G., Boyer, R., and Collings, E.W., Eds.**, 1993. *Materials properties handbook: Titanium Alloys*. ASM International. ISBN: 978-0-87170-481-8.
- [6]. **Yilmaz, O., Turan, B.C., and Gurbuz, M.**, 2019. Production and characterisation of SiC reinforced aluminium alloy matrix composites from waste beverages cans, *Journal of Metals and Minerals*, 29(04), pp. 28-33.

## CHAPTER 5: CHARACTERIZATION OF SiC, Ti6Al4V(ELI) AND MIXED SiC AND Ti6Al4V(ELI) POWDERS

Some of the material presented in this chapter has been published in peer-reviewed media as detailed below:

1. Seleso, M., Maringa, M., and du Preez, W., 2021. Parameters affecting the mixing of powders and the results of mixing SiC and Ti6Al4V (ELI) powders. RAPDASA-RobMech-PRASA Conference – 22nd Annual International RAPDASA Conference, International Conference Centre CSIR, Pretoria, Gauteng, 3<sup>rd</sup>–5th November 2021, pp.73-75. <https://site.rapdasa.org/past-proceedings-2021/>

### 5.0. Introduction

In this chapter, SEM characterization of separate SiC and Ti6Al4V(ELI) powders before and after mixing, as well as their mixture is discussed. Analysis of the changes in agglomeration and segregation of mixed powders as the volume fraction SiC increases is also presented.

#### 5.1. Morphology of Ti6Al4V(ELI) Powder Before and After Mixing

The overall shape of Ti6Al4V(ELI) particles was confirmed to be spherical, as evident in the SEM secondary electron (SE) micrograph shown in Figure 5.1(a). Finer particles were observed on the surfaces of large Ti6Al4V(ELI) particles, as indicated by the blue arrows, while clustered particles of Ti6Al4V(ELI) occurred and are circled in red in Figure 5.1 (a). Microscopic inspection of the particles of silicon carbide showed them to be of irregular shapes, as shown in Figure 5.1 (b).

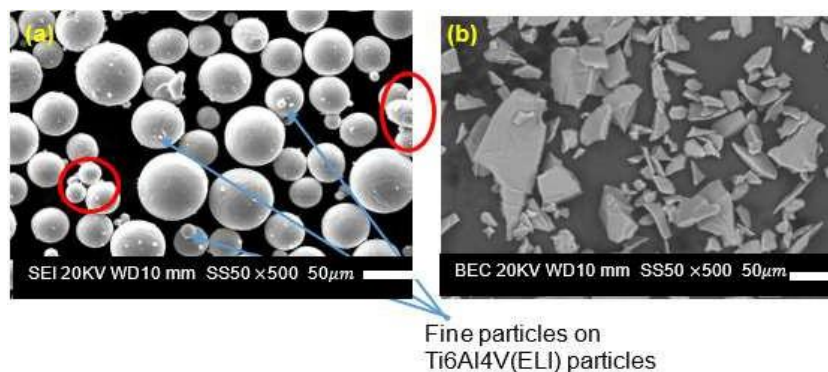


**Figure 5.1:** SEM (a) SE micrograph of Ti6Al4V(ELI) particles and, (b) BE images of SiC particles before mixing

Figure 5.2 (a) depicts Ti6Al4V(ELI) particles before mixing with small spherical particles adhering to the surfaces of the larger particles, whereas Figure 5.2 (b) depicts fine spherical particles and SiC particles adhering to large Ti6Al4V(ELI) particles after mixing.

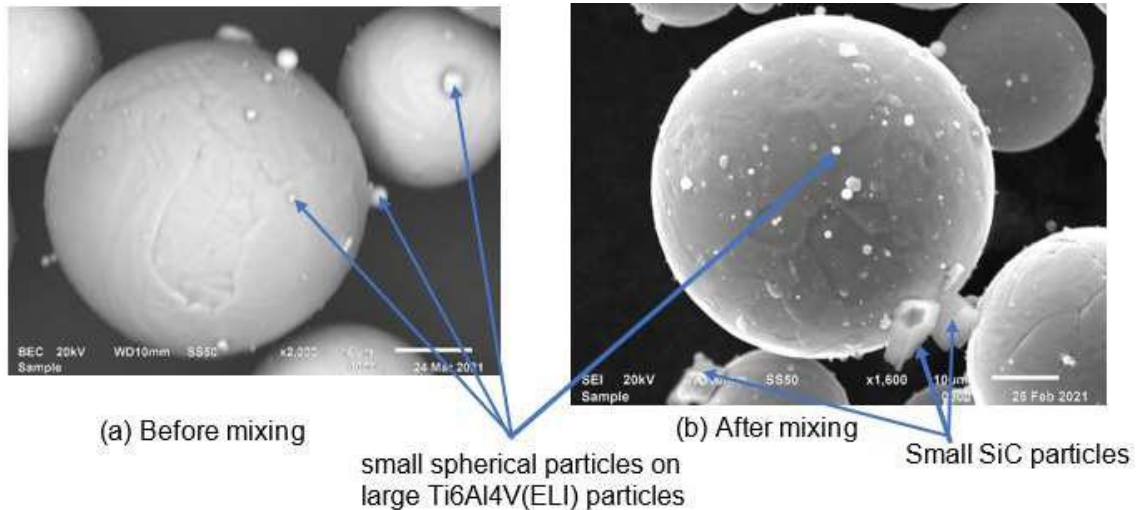


**Figure 5.2:** SEM SE micrographs of (a) Ti6Al4V(ELI) particles, (b) small SiC particles and satellites adhering to Ti6Al4V(ELI) particles after mixing.

Additively manufactured parts are affected by the segregation and agglomeration of powder during production. Powder segregation is defined as the separation of portions of particles caused by differences in their physical properties such as size, shape, and density (Mwania et al., 2020; Zhon et al., 2003; Deveswaran et al., 2008). Agglomeration on the other hand is defined as the sticking of individual particles to one another because of the existence of forces between them (Poux et al., 1991). Segregation and agglomeration have been observed to be major problems in the mixing of powders intended for use in AM and the prevention and limitation of these phenomena are very important in powder-mixing (Leitz et al., 2018; Mwania et al., 2020).

The segregation and agglomeration of SiC and Ti6Al4V(ELI) mixed powder were assessed from the SEM micrographs shown in Figure 5.3 (a–f) and Figure 5.4 (a–f).

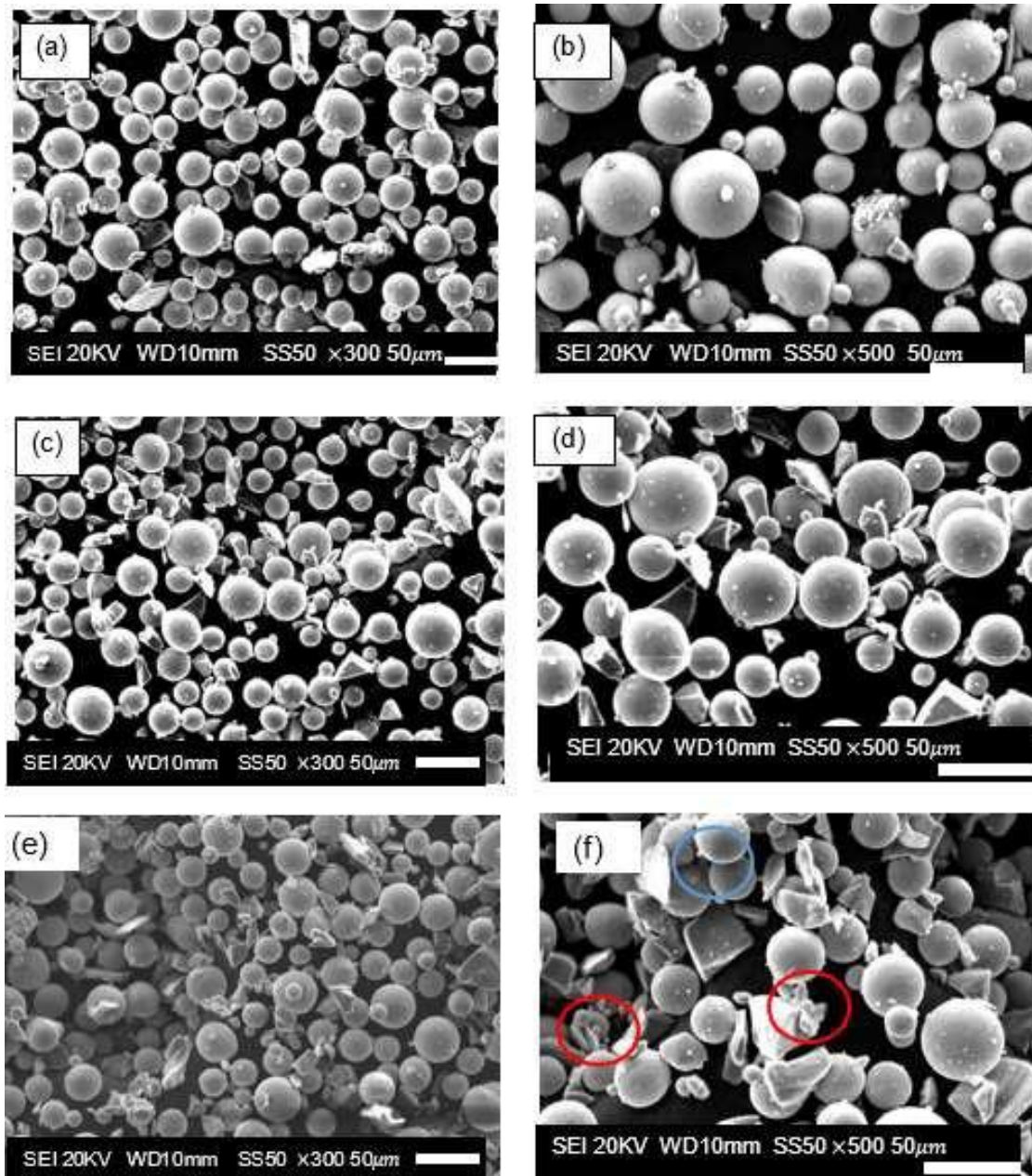


**Figure 5.3:** SEM SE micrographs of SiC/Ti6Al4V(ELI) mixtures at different SiC volume fractions, at magnifications of  $\times 300$  (images in the left column) and  $\times 500$  (images in the right column), (a) and (b) 5% SiC vol. fraction, (c) and (d) 10% SiC vol. fraction, (e) and (f) 15% SiC vol. fraction

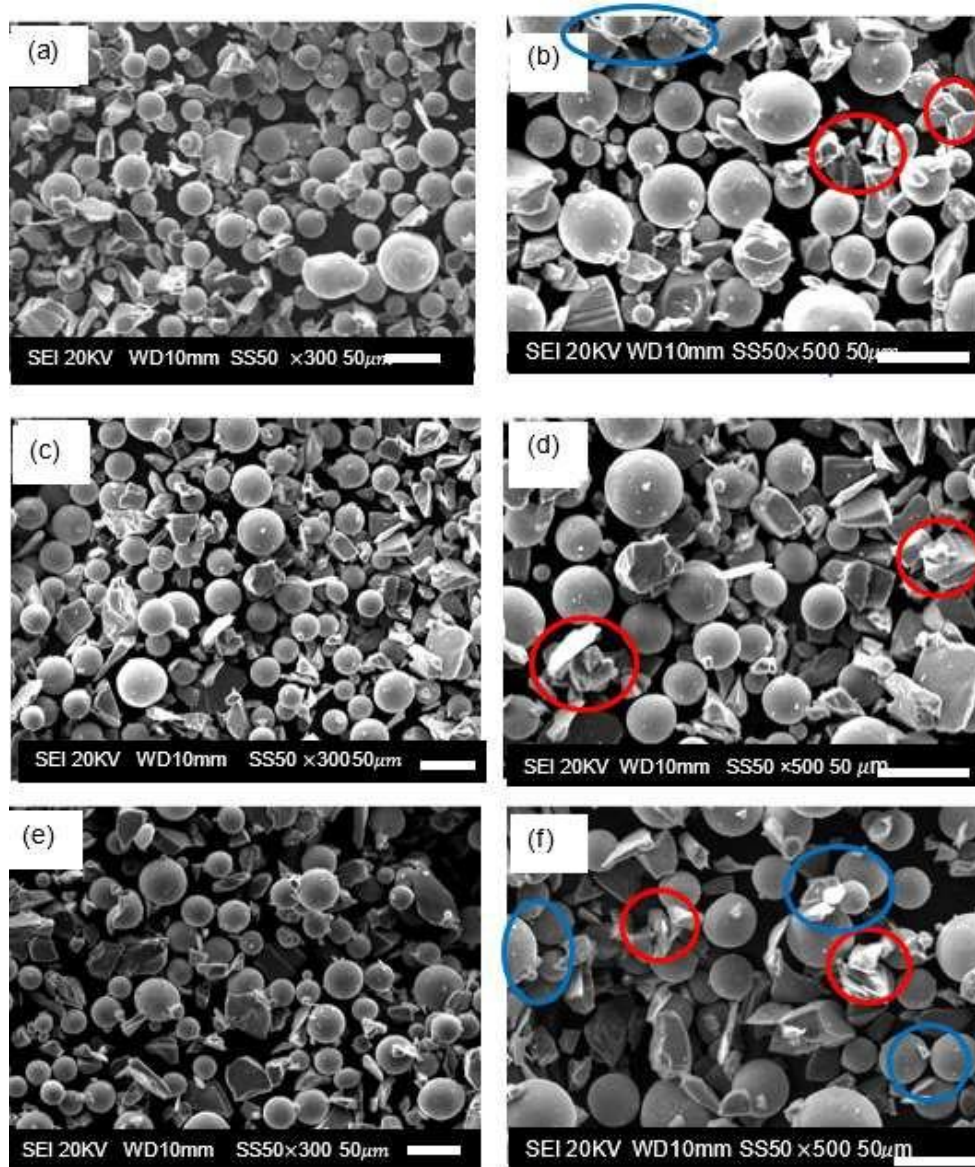


**Figure 5.4:** SEM SE micrographs of SiC/Ti6Al4V(ELI) mixtures at different SiC volume fractions, at magnifications of  $\times 300$  (images in the left column) and  $\times 500$  (images in the right column) (a) and (b) 20 % vol. fraction, (c) and (d) 25 % vol. fraction, (e), and (f) 30 % vol. fraction

Figure 5.3 shows that for 5 %–10 % volume fractions, the SiC particles were dispersed randomly among the Ti6Al4V(ELI) particles without clustering. Clustering of particles was seen to occur at a 15 % SiC volume fraction and higher. Clustering of SiC particles is indicated in the figures by red circles, while that of Ti6Al4V(ELI) particles is indicated by blue circles.

These observations indicate a cut-off below which no agglomeration of particles

occurs. Therefore, agglomeration of the constituent particles of the mixture can be said to be dependent on the increase in loading of SiC particles. Agglomeration of particles is caused by electrostatic and intermolecular forces (Zhon et al., 2003). Electrostatic attraction occurs when oppositely charged surfaces of particles are attracted to each other and is believed to have played a role here (Leitz et al., 2018). Intermolecular forces occur when molecules in one particle interact with molecules in another particle thus bonding them together. Intermolecular forces cannot be inferred in the present work as the scale of particles dealt with here is much higher.

## 5.2. Conclusions

In this study, it was concluded that the powders were thoroughly mixed at low SiC volume fractions up to 15 %. However, increasing the SiC volume fraction above 15 % resulted in increased agglomeration, which was undesirable, and was particularly high at the highest SiC volume fraction of 30 %. Because SiC particles have a lower density than that of Ti6Al4V(ELI), raising the volume percentage encouraged them to gather together. However, building specimens at volume fractions where agglomeration occurred was considered useful to study the significance of agglomeration on the best process parameters and eventually on the mechanical properties of the resulting composites. It was also expected that the effects of Marangoni flow during printing would further redistribute the reinforcing particles and possibly then minimise this agglomeration.

### 5.3. REFERENCES

- [1]. **Desai, A.T., Kumbar, G., Deokar, R.H., Mandare, A.M.,** 2018. Design and analysis of powder mixing ribbon blender. *IOSR Journal of Mechanical and Civil Engineering*, pp. 39-43. <https://www.iosrjournals.org/iosr-jmce/papers/NCRIME-2018/Volume-6/8.%2039-43.pdf>
- [2]. **Deveswaran, R., Bharath, S., Basavaraj, B.V., Abraham, S., Furtado, S., and Madhavan, V.,** 2009. Concepts and techniques of the pharmaceutical powder mixing process: A current update, *Research Journal of Pharmacy and Technology*, Vol. 2, No. 2, pp. 245-249.
- [3]. **Leitz, K.H., Grohs, C., Singer, P., Tabernig, B., Plankensteiner, A., Kestler, H., and Sigl, S.L.,** 2018. Fundamental analysis of the influence of powder characteristics in selective laser melting of molybdenum based on a multi-physical simulation model. *International Journal of Refractory Metals and Hard Materials*, 72. pp.1-8.
- [4]. **Mwania, F.M., Maringa, M., and van der Walt, J.G.,** 2020. A review of the techniques used to characterize laser sintering of polymeric powders for use and re-use in additive manufacturing. *Manufacturing Review*, 8, p.14.
- [5]. **Poux, M.P., Fayole, P., and Beertrand, J.,** 1991. Powder mixing, some practical rules applied to agitated systems. *Powder Technology*, 68, pp. 213-234.
- [6]. **Z h o n , Y.C., Bridgwater, J.,** 2003. Segregation of binary mixture of particles in a bladed mixer. *Journal of Chemical Technology and Biotechnology*, 78, pp. 1187-193.

## CHAPTER 6: ANALYSIS OF SiC/Ti6Al4V(ELI) SINGLE TRACKS

Some of the material presented in this chapter has been published in peer-reviewed media as detailed below:

1. **Seleso, M., Maringa, M., and du Preez, W.,** 2022. Influence of selective laser melting process parameters on the characteristics of SiC/Ti6Al4V (ELI) single tracks. RAPDASA-RobMech-PRASA-CoSAAMI Conference – Digital Technology in Product Development – 23<sup>rd</sup> Annual International RAPDASA Conference, Somerset West, South Africa, November 9–11, pp. 1-15. <https://doi.org/10.1051/mateconf/202237001003>
2. **Seleso, M., Maringa, M., and du Preez, W.** 2024. A comparative analysis of low and high SiC volume fraction additively manufactured SiC/Ti6Al4V (ELI) composites based on the best process parameters of laser power, scanning speed and hatch distance, *Materials Journal*, Vol.17, No,11.2606. <https://www.mdpi.com/1996-1944/17/11/2606>.

### 6.0. Introduction

The focus of this chapter is on the analysis of single tracks for each SiC volume fraction from 5 % to 30 %, based on SEM micrographs of their top views and cross-sections. To explore the effect of increasing laser scanning speed, SEM scans based on the value of laser power that produced the best single tracks for all or most values of laser scanning speed used at SiC volume fractions of 5 %–30 % are discussed here. Discussions of the SEM scans obtained from other values of laser power at these volume fractions of SiC are presented in appendices A to F. As described in Chapter 3, multiple combinations of laser power and scanning speed were used for building single tracks, while the diameter of the laser beam and thickness of the layer of powder were all kept constant. Discussions of the characteristics of pre-balling, balling, continuity of tracks, as well as width, depth of penetration and height of tracks, are presented in this chapter. The track with the best characteristics for each volume fraction was identified and its building process parameters used later in building of single layers.

#### 6.1. Analysis of Single Tracks at a 5 % SiC Volume Fraction in an SiC/Ti6Al4V(ELI) Composite

At a 5 % SiC volume fraction, various tracks were produced at values of laser power of 100 W, 150 W, 200 W, 250 W, 300 W, and 350 W, with laser scanning speeds ranging from 0.3 m/s to 2.7 m/s. The top surface characteristics of the built tracks of discontinuity, continuity, pre-balling, and balling are summarized in Table 6.1, to help

identify the best combinations of laser power and scanning speed for use in the building of single layers. The brown blocks in Table 6.1 indicate discontinuous single tracks that are thought to have arisen due to sublimation of SiC particles and evaporation of Ti6Al4V(ELI), while the red blocks indicate single tracks that are continuous. The yellow blocks indicate single tracks with pre-balling or necking, and finally, the balling phenomena are indicated by the green blocks. From the details in this table, it is clear that the continuous tracks (the best tracks) were built for all the scanning speeds used at a laser power of 200 W. The tracks built at this value of laser power were, therefore, selected for detailed analysis in this chapter. Detailed analysis of the tracks built at this volume fraction of SiC for the different values of laser power of 100 W, 150 W, 250 W, 300 W, and 350 W are presented in appendices A1, A2, A3, A4, and A5, respectively.

**Table 6.1: Categorisation of single tracks based on the continuity and discontinuity tracks, pre-balling/necking and balling**

Laser Power (W)								
100	Scanning speed (m/s)	0.3	0.4	0.5	0.6	0.7	0.8	0.9
	Linear energy density (J/m)	333	250	200	167	143	125	111
150	Scanning speed (m/s)	0.6	0.7	0.8	0.9	1	1.1	1.2
	Linear energy density (J/m)	250	214	188	167	150	136	125
200	Scanning speed (m/s)	0.8	0.9	1	1.2	1.4	1.5	1.6
	Linear energy density (J/m)	250	222	200	167	143	133	125
250	Scanning speed (m/s)	1.1	1.2	1.3	1.5	1.7	1.8	1.9
	Linear energy density (J/m)	227	208	192	167	147	139	132
300	Scanning speed (m/s)	1.2	1.4	1.6	1.8	2	2.2	2.4
	Linear energy density (J/m)	250	214	188	167	150	136	125
350	Scanning speed (m/s)	1.5	1.7	1.9	2.1	2.3	2.5	2.7
	Linear energy density (J/m)	233	206	184	167	152	140	130

From Table 6.1, it is clear that the low values of laser power of 100 W and 150 W, track discontinuities occurred at high LEDs ranging from 333 J/m to 200 J/m, with laser scanning speeds from 0.3 m/s to 0.5 m/s for the former value of laser power and LEDs from 250 J/m to 214 J/m, with scanning speeds from 0.6 m/s to 0.7 m/s for the latter. Pre-balling occurred at high laser scanning speeds and low LEDs for both values of low laser power (100 W and 150 W). Balling on the other hand occurred at the lowest values of LED for a laser power of 100 W, medium to low values of LED at a laser power of 250 W, the lowest value of LED at the highest laser scanning speed for a laser power of 300 W, and at all values of LED at all scanning speeds for a laser power

of 350 W. Continuous tracks were produced at a laser power of 100 W, scanning speed of 0.6 m/s, and LED of 167 J/m, while at 150 W continuous tracks were observed for LEDs of 188 J/m to 156 J/m and scanning speeds from 0.8 m/s to 1.1 m/s. At the increased laser power of 200 W, all tracks produced were continuous for all scanning speeds used (0.3 m/s–0.9 m/s). However, those produced at the higher value of laser power of 250 W showed discontinuity of tracks at the high LED of 227 J/m and a scanning speed of 1.1 m/s. A continuous track built at a laser power of 250 W was obtained at an LED and scanning speed of 208 J/m and 1.2 m/s, respectively. Increasing the scanning speed from 1.3 m/s to 1.9 m/s at this value of laser power, resulted in single tracks with discontinuities and balling. At a laser power of 300 W, the built single tracks were continuous, with LEDs and scanning speeds from 250 J/m to 136 J/m and 1.2 to 2.2 m/s, respectively, above which the balling phenomenon occurred. Figure 6.1 depicts optical micrographs of single tracks showing some features that were detected at different values of laser power and scanning speed shown in Table 6.1.

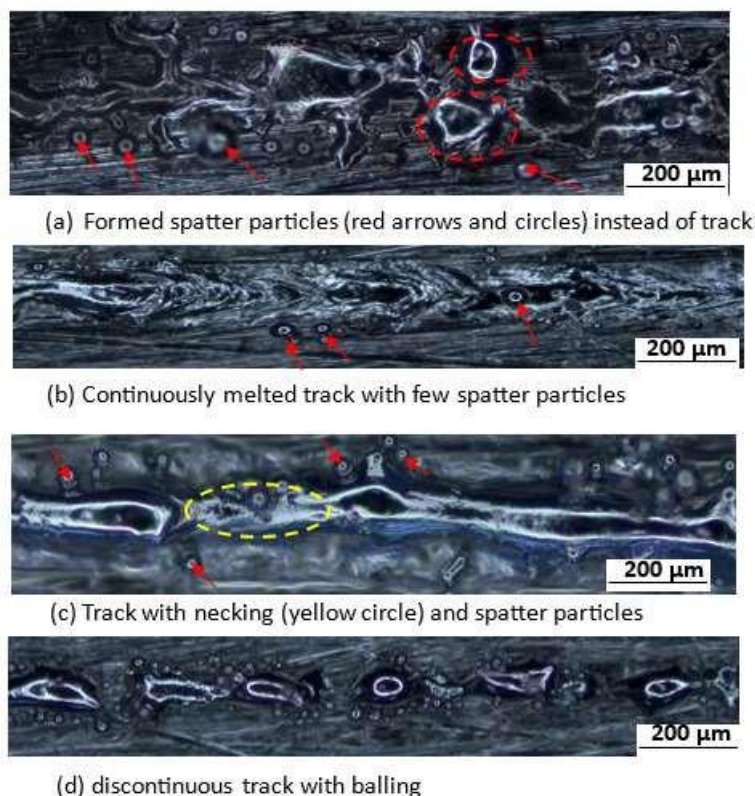


**Figure 6.1:** Top view of single tracks indicating the surface characteristics of track continuity, spatter particles, necking and balling for a 5 % SiC volume fraction of an SiC/Ti6Al4V(ELI) composite

Discontinuous tracks, such as the one shown in Figure 6.1 (a), occurred at high LEDs for power ratings of 100 W, 150 W, and 250 W, as is evident in Table 6.1. This was due to high values of LED that raised the temperatures of the melt pool to cause evaporation. The evaporation temperature of Ti6Al4V(ELI) of 2860 °C is higher than the sublimation temperature of SiC of 2700 °C, with Ti6Al4V having a melting temperature of 1667 °C (Zhang et al., 2020). Therefore, at these high values of LED, Ti6Al4V(ELI) particles will melt and evaporate, whilst SiC particles sublime, with the former resulting in the creation of Ti6Al4V(ELI) spatter particles rather than the formation of tracks.

The presence of necking and balling at high scanning speeds, seen in the yellow and green blocks towards the right in Table 6.1, shows that as the scanning speed increased at the same power in the present work, the melt pool temperature decreased. This is expected to have led to an increase of surface tension and melt pool viscosity, thus resulting in the formation of discontinuous tracks with uneven widths, as was observed in the separate works of Vilardeli et al. (2020) and Ramosena et al. (2022). Moreover, according to Equation 2.15, increased laser scanning speed at constant power leads to a reduction of LED, and, therefore, insufficient energy to yield good melt flow characterized due to low values of surface tension and viscosity thus resulting in the balling phenomenon.

The tracks in red blocks which are represented by the image in Figure 6.1 (b) exhibit continuity of tracks as a result of combinations of laser power and laser scanning speed with sufficient energy to melt the powder and generate a good melt flow. This observation is consistent with the work of Dzogbewu et al. (2023).

The cross-sections of the single tracks shown in Table 6.1 were examined and their dimensional characteristics used to categorise them, as shown in Table 6.2, to help in selecting the ideal process parameters at a 5 % SiC volume fraction of an SiC/Ti6Al4V(ELI) composite. The grey blocks in this table represent tracks with a depth-to-width ratio less than 0.5, indicating insufficient depth of penetration. The purple blocks represent the formation of a keyhole with a depth-to-width ratio larger than 0.5, whereas the blue blocks represent tracks with a ratio of 0.5, which denotes sufficient penetration.

**Table 6.2: Categorisation of the cross-sections of single tracks based on depth-to-width ratios**

Laser Power (W)								
100	Scanning speed (m/s)	0.3	0.4	0.5	0.6	0.7	0.8	0.9
	Linear energy density (J/m)	333	250	200	167	143	125	111
150	Scanning speed (m/s)	0.6	0.7	0.8	0.9	1	1.1	1.2
	Linear energy density (J/m)	250	214	188	167	150	136	125
200	Scanning speed (m/s)	0.8	0.9	1	1.2	1.4	1.5	1.6
	Linear energy density (J/m)	250	222	200	167	143	133	125
250	Scanning speed (m/s)	1.1	1.2	1.3	1.5	1.7	1.8	1.9
	Linear energy density (J/m)	227	208	192	167	147	139	132
300	Scanning speed (m/s)	1.2	1.4	1.6	1.8	2	2.2	2.4
	Linear energy density (J/m)	250	214	188	167	150	136	125
350	Scanning speed (m/s)	1.5	1.7	1.9	2.1	2.3	2.5	2.7
	Linear energy density (J/m)	233	206	184	167	152	140	130

From Table 6.2, it can be seen that a keyhole occurred at a laser power, scanning speed, and LED of 200 W, 1 m/s, and 200 J/m, respectively. At values of laser power of 200 W and 250 W, optimal cross-sections with depth-to-width ratios of 0.5 are attained, the former with laser scanning speeds of 1.2 m/s and 1.4 m/s and matching LEDs of 167 J/m and 143 J/m, and the latter with a laser scanning speed and LED of 1.2 m/s and 208 J/m, respectively. All other values of laser power highlighted with grey led to cross-sections with poor depths of penetration. These features and more of the cross-sections categorised in Table 6.2 are illustrated in the images shown in Figure 6.2.

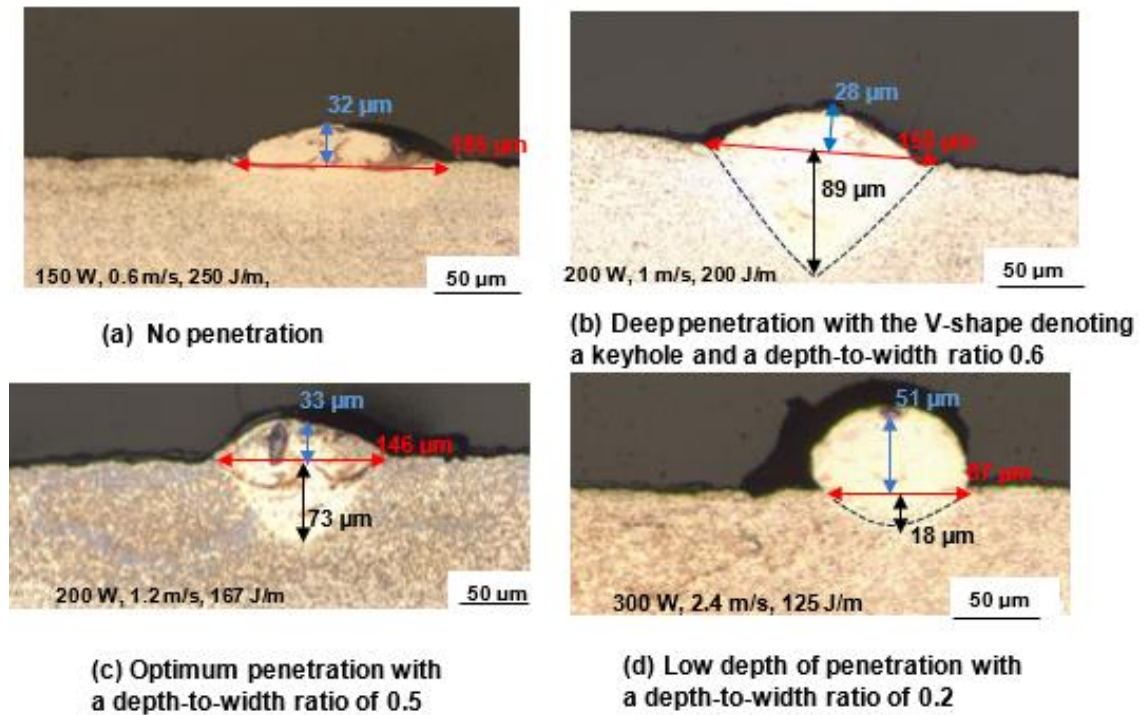


**Figure 6.2:** Cross-sections obtained at a 5 % SiC volume fraction of an SiC/Ti6Al4V(ELI) composite showing the dimensions of their critical geometrical features

The optimal cross-sections are generally semi-circular, with the melt pool depth roughly equal to its half-width (Ramosena et al., 2022). The dimensions shown in Figure 6.2 (c) that indicate a depth-to-width ratio of 0.5 are consistent with the model proposed by Eagar and Tsai (1983). The grey blocks in Table 6.2 depict no or low depth of penetration, as shown in Figure 6.2 (a), indicating that there was insufficient energy to melt and permeate through the substrate. However, shallow penetration does also occur at values of high LED and is explained by the extent of lateral flow of the melt. High LEDs cause the melt pool to heat up, thus lowering the surface tension and viscosity of the melt, which are temperature dependent (Ramosena et al., 2022; Ferro et al., 2020). This reduction of surface tension and viscosity with increasing temperature, in turn, leads to more extensive radial outward flow of the molten pool metal from the central regions to the outer regions and hence production of wider and shallower melt pools. This is consistent with the separate findings of Newby et al. (2018), Yadroitseva et al. (2015), and Chandrakanth et al. (2016), who reported that the direction of melt flow is determined by the Marangoni convection which is defined as the thermo-capillary flow of fluid from areas of low surface tension to areas of high surface tension.

### 6.1.1. Comparative analysis of the best single tracks at a 5% SiC volume fraction in an SiC/Ti6Al4V(ELI) composite

From a study of Table 6.1 and 6.2, the process parameters that led to building of continuous tracks with an optimum depth-to-width ratio, were obtained at laser powers, scanning speeds, and LEDs of 200 W, 1.2 m/s, and 167 J/m: 200 W, 1.4 m/s and 142 J/m, and 250 W, 1.2 m/s and 208 J/m. The top views and cross-sections of these tracks were examined and compared to help select one set of process parameters that would be used for further building of single layers and specimens. To this end, the top views, and cross-sections of the best single tracks at a 5 s% SiC volume fraction are illustrated in Figure 6.3.

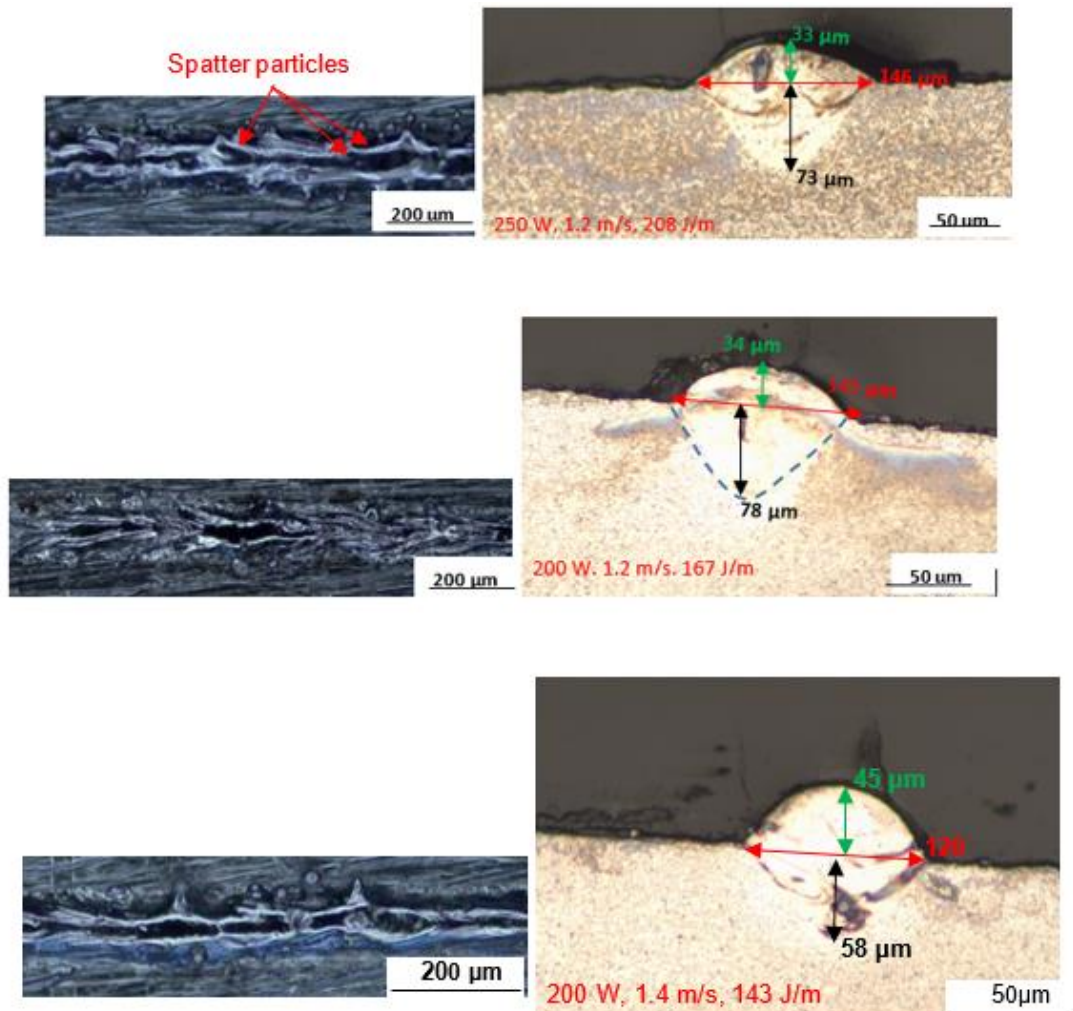


**Figure 6.3:** Top views and cross-sections of the best single tracks produced at a 5% SiC volume fraction in an SiC/Ti6Al4V(ELI) composite

The top views of the tracks in Figure 6.3 showed good continuity with almost constant track widths of average values of 146  $\mu\text{m}$ , 145  $\mu\text{m}$ , and 120  $\mu\text{m}$  from the top image to the bottom image. The cross-sections of the tracks showed good depths of penetration of 73  $\mu\text{m}$ , 78  $\mu\text{m}$ , and 58  $\mu\text{m}$  from the top cross-section to the bottom one, which all led to the optimum depth-to-width ratio of 0.5. Although the cross-sections of the tracks built at laser powers of 250 W and 200 W had identical measured values of width and height, as well as equal values of depth-to-width ratio, the top surface scan built at a laser power of 250 W showed a lot more spatter particles along the sides of the track than the track built at a laser power of 200 W. Spatter particles lead to the generation of porosity and uneven powder layers during part production. The cross-section of the track built at a laser power, scanning speed and LED of 200 W, 1.4 m/s, and 143 J/m, shows higher height (45  $\mu\text{m}$ ) above the substrate than the other cross-sections in Figure 6.3. The height of this track that is equal to or higher than the layer thickness of (45  $\mu\text{m}$ –50  $\mu\text{m}$ ) is expected to lead to unevenness of the next deposited layer, which will result in the formation of internal pores during the building of the 3D parts. From the foregoing analysis, it is concluded that the best set of process parameters at a 5 % SiC volume fraction in an SiC/Ti6Al4V(ELI) composite is obtained at a laser power, scanning speed, and LED of 200 W, 1.2 m/s, and 167 J/m.

### **6.1.2 Analysis of single tracks at different scanning speeds and constant laser power of 200 W**

The best value of laser power selected from section 6.1.1 is used now to study the effect of different scanning speeds on the quality of built tracks. Figure 6.4 depicts micrographs of single tracks produced with a constant laser power of 200 W and at different laser scanning speeds ranging from 0.8 m/s to 1.6 m/s, with corresponding LEDs from 250 J/m to 125 J/m.

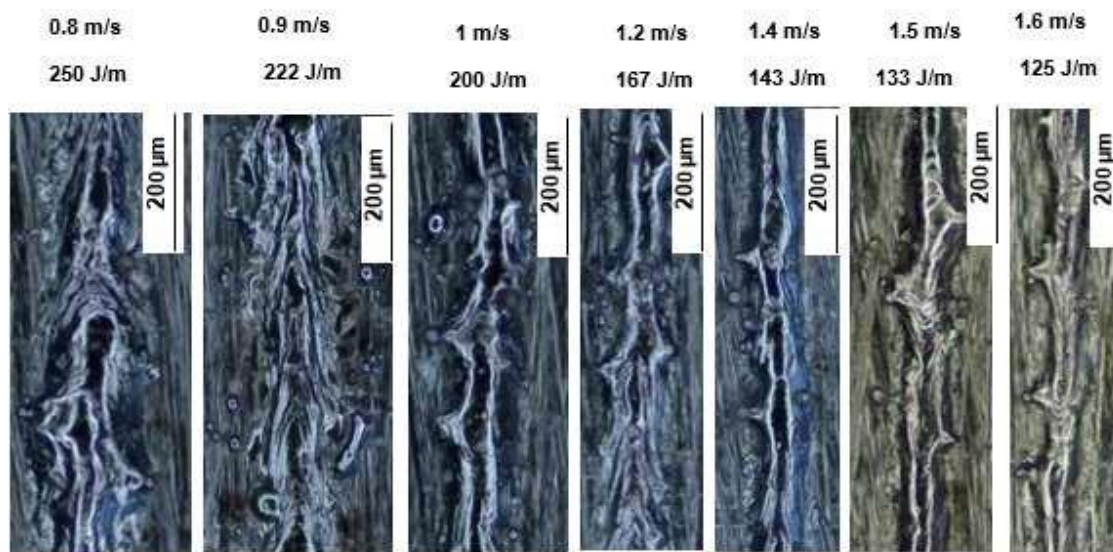


**Figure 6.4:** Micrographs of single tracks built at a laser power of 200 W and different laser scanning speeds from 0.8 m/s to 1.6 m/s

All the tracks in Figure 6.4 are continuous and narrow down as the laser scanning speed increases, with those that were built at the lower speeds of 1.2 m/s and 0.9 m/s being the widest. What appears to be spatter particles are detected at the lowest laser scanning speed of 0.8 m/s, which reduce in number as the laser scan speed increases. The presence of these particles may be because when the laser beam moves across the powder bed, it does not only melt the particles of powder beneath it, but also attempts to melt the particles at the edges of the tracks, as was noted by Darsun et al. (2020). As a result of the Gaussian distribution of energy in the beam, the energy density at the periphery of the track is insufficient to entirely melt the particles, thus resulting in partially melted particles near the edges of the solidified track, which thus appear as spatter particles, as was observed by Dzogbewu et al. (2022).

The high LEDs of 250 J/m and 222 J/m for the two leftmost tracks in this figure are expected to have reduced the surface tension and viscosity of the melt which resulted in radially outward flow of the molten pool metal from the central regions to the outer regions of the melt pool and hence production of wider melt pools. This is consistent with the separate findings of Ramosena et al. (2022), and Ferro et al. (2020). Narrowing of the widths of tracks with rising values of laser scanning speed, in this case, were thought to have been due to the decreased dwell time of the laser beam

on the powder bed, which led to reduced temperatures that caused higher values of surface tension and viscosity and, therefore, less radial or lateral flow of the melt, as was observed separately by Yadroitseva et al. (2015), and Chandrakanth et al. (2016).

Figure 6.5 depicts the cross-sections of single tracks produced at a laser power of 200 W and different laser scanning speeds, used to study the effects of laser scanning speed on the geometrical properties of width, height, and depth of penetration of the built tracks.

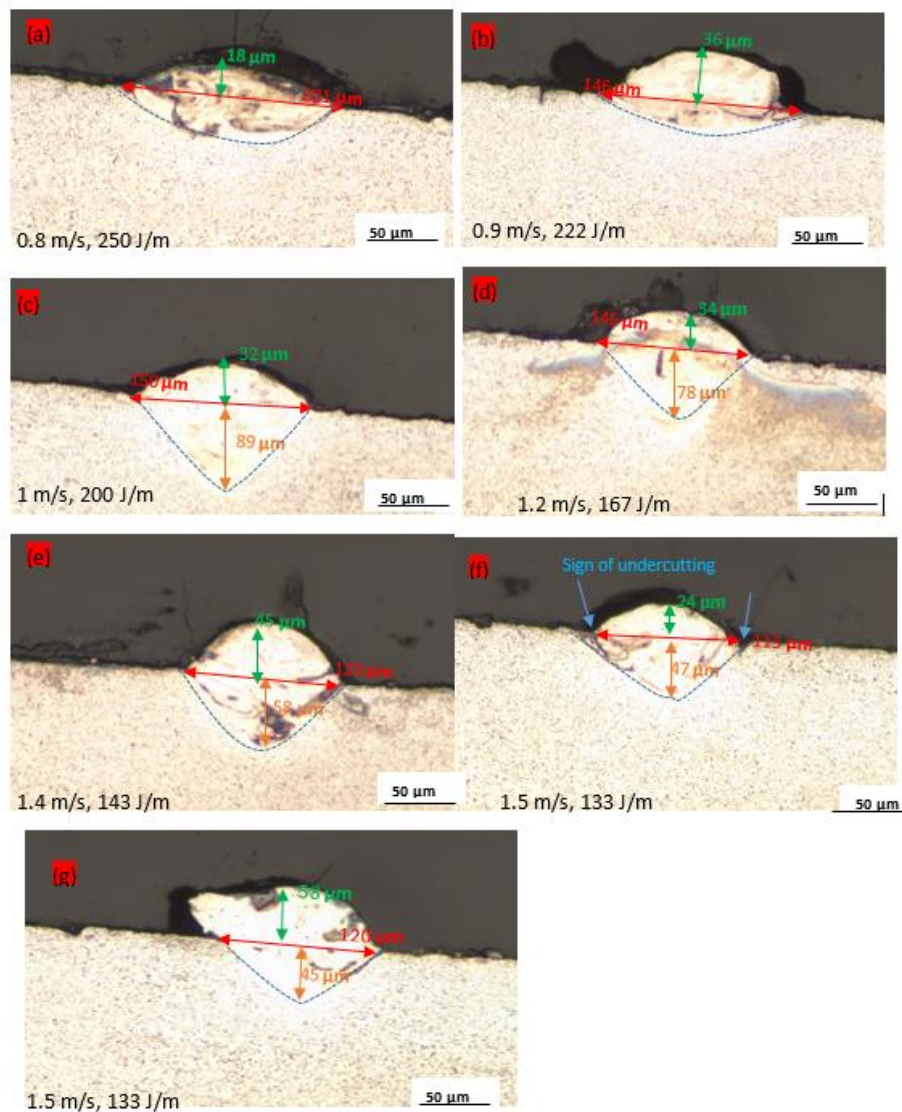


**Figure 6.5:** Cross-sectional images of single tracks produced at a laser power of 200 W at different scanning speeds from 0.8 m/s to 1.5 m/s

The cross-sections at the slowest scanning speeds of 0.8 m/s and 0.9 m/s exhibited

wide tracks with shallow penetration. From Figure 6.5 (c to g), there is a pattern of decreasing width and depth of penetration with increasing laser scanning speed. However, the measured values of width and depth of the cross-section in Figure 6.5 (c) led to a depth-to-width ratio of 0.6, whereas the cross-sections in Figures 6.2 (d and e) gave rise to a ratio of 0.5 and those in Figure 6.2 (f and g) a ratio of 0.4. The height of the tracks above the substrate varied non-linearly as the laser scanning speed increased or decreased. The low scanning speeds of 0.8 m/s and 0.9 m/s led to high values of LED that increased the energy input and temperature of the melt pool relative to the other tracks built at this power, with similar results on the width of the built tracks to the case reported by Yuang et al. (2020).

The high LEDs and temperatures at these two laser scanning speeds is thought to have led to good wettability of the melt on the surfaces of substrates and faster movement of the melt, resulting in wide tracks with shallow penetration as observed separately by Yadroitsev et al. (2007), Xia et al. (2017), and Dilip et al. (2017). Yuang et al. (2020) reported that at a high energy density, the accumulation of heat in the melt pool increased and the melt pool temperature reached the melting point, above which circulation of evaporated melt vapour occurred. At this point, vapour recoil pressure caused deep depressions into the substrate that led to the formation of keyholes. The effect of vapour recoil pressure is seen in Figure 6.5 (c). Undercutting is observed in Figure 6.5 (f), which signifies the formation of a hump similar to the reported case by Kaserer et al. (2020), to be a result of suppressed wetting on the sides of tracks at high scanning speeds. This is also consistent with the findings in the work of Dzogbewu et al. (2022).

Figure 6.6 (a) shows a top-view SEM image of a single track built at 200 W and 1 m/s, and Figure 6.6 (b), a higher magnification of Figure 6.6 (a). The two images showed the presence of SiC particles indicated by red arrows and spatter Ti6Al4V(ELI) particles pointed to with blue arrows on the top and along the side of the track. The presence of SiC particles was a good sign that the temperatures prevailing during scanning were not high enough to cause them to sublime. This was the preferred end target to ensure that a composite of the constituent components was formed.

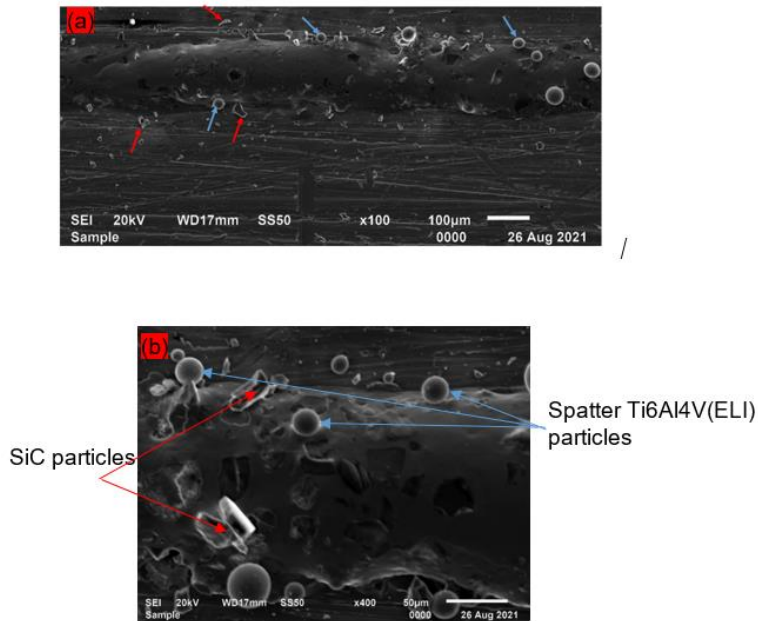


**Figure 6.6:** Top surface (a) SEM micrograph, (b) magnified SEM micrograph, both of single tracks built at 200 W, 1 m/s (200 J/m) showing particles of SiC and spatter Ti6Al4V(ELI)

### 6.1.3. Analysis of single tracks at constant scanning speeds with different values of laser power

Figure 6.6 shows single tracks built at a laser scanning speed of 0.8 m/s and different values of laser power varying from 100 W to 200 W.

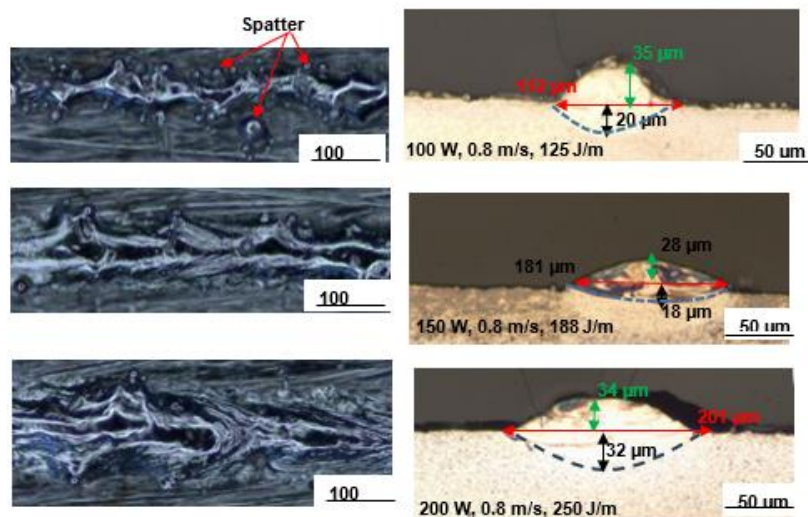


**Figure 6.7:** Top surface scans and cross-sections of single tracks built at a scanning speed of 0.8 m/s and different laser powers of 100 W, 150 W, and 200 W

Both the power and the scanning speed affect the degree of melting and depth of penetration of the laser beam. Power is the most significant process parameter determining the depth of penetration of the laser beam, while the scanning speed is a significant parameter in determining the width of the heat-affected zone (HAZ) and the size of the melt pool (Kruth et al., 2010). It was observed from Figure 6.7 that at the lowest power (100 W), the track was narrow with a lot of spatter particles along the sides of the track. The corresponding image of a cross-section of this track showed a depth of penetration of 20  $\mu\text{m}$  through the substrate and a width of 112  $\mu\text{m}$  and depth-to-width ratio of 0.2. The low depth of penetration of the track at this low energy density (125 J/m) was due to insufficient heat, which was only able to melt small amounts of the powder, thus resulting in the formation of an irregular track, in consistence with the work of Andani et al. (2018).

When the power was increased to 150 W, the track became more continuous and wider, with fewer spatter particles on the sides. However, the cross-section of the track showed a lesser depth of penetration of 18  $\mu\text{m}$  than at 100 W. The lower depth of penetration and greater width of 181  $\mu\text{m}$  result in a corresponding depth-to-width ratio of 0.1, indicating a shallow penetration that is insufficient to enable good bonding between previously melted layers. Increasing the power further to 200 W at the same speed was seen in the figure to lead to the formation of a continuous track and a decrease in the number of spatter particles. The cross-section of the track built at this value of laser power showed a depth of penetration through the substrate of 32  $\mu\text{m}$  and a track with a width of 201  $\mu\text{m}$ , giving rise to a depth-to-width ratio of 0.2. This implies that at this higher energy density, the penetration into the substrate is better than at the lower laser powers of 100 W and 150 W, with their lower LEDs, which is consistent with the work of Siao et al. (2021).

It can be concluded that increasing the laser power caused the width and depths of penetration of the tracks to increase continuously with rising laser power but an inconsistency in the change of the depth-to-width ratio. However, in all three cases in Figure 6.7, the depth-to-width ratios of all the tracks were all well below the optimum value of 0.5.

## 6.2. Analysis of Single Tracks of a 10 % SiC Volume Fraction in an SiC/Ti6Al4V(ELI) Composite

Top surface analysis of single tracks produced at different values of laser power from 100 W to 350 W and different laser scanning speeds ranging from 0.3 m/s to 2.7 m/s with their corresponding LEDs at a 10 % SiC volume fraction of an SiC/Ti6Al4V(ELI) composite led to the categorisation shown in Table 6.3.

**Table 6.3: Categorisation of single tracks based on continuity and discontinuity tracks, pre-balling/necking and balling**

Laser Power (W)								
100	Scanning speed (m/s)	0.3	0.4	0.5	0.6	0.7	0.8	0.9
	Linear energy density (J/m)	333	250	200	167	143	125	111
150	Scanning speed (m/s)	0.6	0.7	0.8	0.9	1	1.1	1.2
	Linear energy density (J/m)	250	214	188	167	150	136	125
200	Scanning speed (m/s)	0.8	0.9	1	1.2	1.4	1.5	1.6
	Linear energy density (J/m)	250	222	200	167	143	133	125
250	Scanning speed (m/s)	1.1	1.2	1.3	1.5	1.7	1.8	1.9
	Linear energy density (J/m)	227	208	192	167	147	139	132
300	Scanning speed (m/s)	1.2	1.4	1.6	1.8	2	2.2	2.4
	Linear energy density (J/m)	250	214	188	167	150	136	125
350	Scanning speed (m/s)	1.5	1.7	1.9	2.1	2.3	2.5	2.7
	Linear energy density (J/m)	233	206	184	167	152	140	130

Table 6.3 show that discontinuous tracks were built at 100 W for laser scanning speeds from 0.6 m/s to 0.9 m/s, below which the tracks were continuous. The table also shows the obvious decrease in LED with increasing laser scanning speed. The tracks created at 150 W and 200 W were continuous, except the one built at the highest laser scanning speed of 1.6 m/s at 200 W. The tracks built at 250 W all displayed discontinuity. When the laser power was increased to 300 W, the tracks built were continuous between laser scanning speeds of 1.2 m/s and 1.6 m/s, above which necking of the tracks was seen. All tracks built at the highest power of 350 W were unsatisfactory, with necking and discontinuities being observed in them.

As was noted by Siao et al. (2021), the scanning speeds between 0.6 m/s and 0.9 m/s at a laser power of 100 W in this case, limited the dwell time of the laser beam on the powder bed, thus preventing the laser beam from completely melting the powder particles at this low value of laser power, which resulted in the presence of discontinuities and necking of tracks. Shrestha et al. (2019) obtained similar results and stated that when the scanning speed increases and decreases at the same power, the amount of energy input per unit area reduces and vice versa, accompanied by a decrease and increase in the printed width of tracks, as shown in Appendix B1 to B3. Hu et al. (2019) and Dai et al. (2015) also highlighted the fact that discontinuities of tracks at high scanning speeds were caused by shorter melt pool lifetimes in addition to low melt fluid flow strengths, which resulted in ineffective spreading of the melt pool. Discontinuities of tracks at high scanning speeds for this volume fraction of SiC are shown in Appendix B, Figures B1, B5, and B7. Because of the instability and discontinuities of such tracks, the final produced parts will have a poor surface finish, as was noted by Dai et al. (2015). The tracks falling in the category of continuity in Table 6.3 indicate the use of sufficient energy to completely melt the particles of powder and cause good flow of the melt.

Categorisation of the cross-sections of these single tracks is presented in Table 6.4 and used to help identify an ideal set of process parameters.

**Table 6.4: Categorisation of the cross-sections of single tracks based on depth-to-width ratios**

Laser Power (W)								
100	Scanning speed (m/s)	0.3	0.4	0.5	0.6	0.7	0.8	0.9
	Linear energy density J/m	333	250	200	167	143	125	111
150	Scanning speed (m/s)	0.6	0.7	0.8	0.9	1	1.1	1.2
	Linear energy density (J/m)	250	214	188	167	150	136	125
200	Scanning speed (m/s)	0.8	0.9	1	1.2	1.4	1.5	1.6
	Linear energy density (J/m)	250	222	200	167	143	133	125
250	Scanning speed (m/s)	1.1	1.2	1.3	1.5	1.7	1.8	1.9
	Linear energy density (J/m)	227	208	192	167	147	139	132
300	Scanning speed (m/s)	1.2	1.4	1.6	1.8	2	2.2	2.4
	Linear energy density (J/m)	250	214	188	167	150	136	125
350	Scanning speed (m/s)	1.5	1.7	1.9	2.1	2.3	2.5	2.7
	Linear energy density (J/m)	233	206	184	167	152	140	130

Table 6.4 reveals that all the created tracks had poor penetration at values of laser power of 100 W, 250 W, and 350 W, while at 150 W, poor penetration occurred only at the highest LED of 250 J/m and lowest scanning speed of 0.6 m/s. When the scanning speed was increased to 0.7 m/s, a keyhole was produced; however, when the scanning speed was increased further to 0.8 m/s while maintaining the same power, an acceptable penetration resulted. From the scanning speed of 0.9 m/s to 1.1 m/s, irregular tracks were seen. An acceptable penetration was achieved by increasing the scanning speed further to 1.2 m/s. At a laser power of 200 W, all the tracks had ratios of depth-to-width less than 0.5, except the cross-section for the track printed at a speed of 1.4 m/s and an LED of 143 J/m that had an optimum depth-to-width ratio.

According to Fan et al. (2018), the observed poor penetration at high LED is explained by the fact that the higher melt temperature caused by the high LED decreases surface tension and viscosity, thereby improving wettability of the melt on the substrate. This typically happens when surface tension forces are stronger than recoil pressure forces, which limits the melt's ability for deep penetration (Caprio et al., 2020). Deeper penetration (formation of keyholes) is seen when the recoil pressure forces are greater than the surface tension forces, as is shown in Appendix B, Figures B4 and B9. Dzogbewu et al. (2022) reported that the LPBF melting process is non-linear with respect to the various controlling process parameters, and, therefore, ideal parameters can only be reached through extensive and careful evaluation and combination of them. This was proven by an unexpected result of acceptable penetration at the laser power of 150 W, the highest scanning speed of 1,2 m/s and LED of 122 J/m.

A comparative analysis of the single tracks for the three cross-sections marked in blue in Table 6.4 was next conducted, as detailed in the next section, to determine between them, the best set of process parameters to be used for creating single layers and 3D parts.

### **6.2.1. Comparative analysis of the best single tracks at a 10% SiC volume fraction of an SiC/Ti6Al4V(ELI) composite**

To obtain the best set of process parameters for use in producing parts at a 10 % SiC volume fraction, the best cross-sections and top surfaces obtained from the categories presented in Tables 6.3 and 6.4 were evaluated and compared based on

the images shown in Figure 6.8.

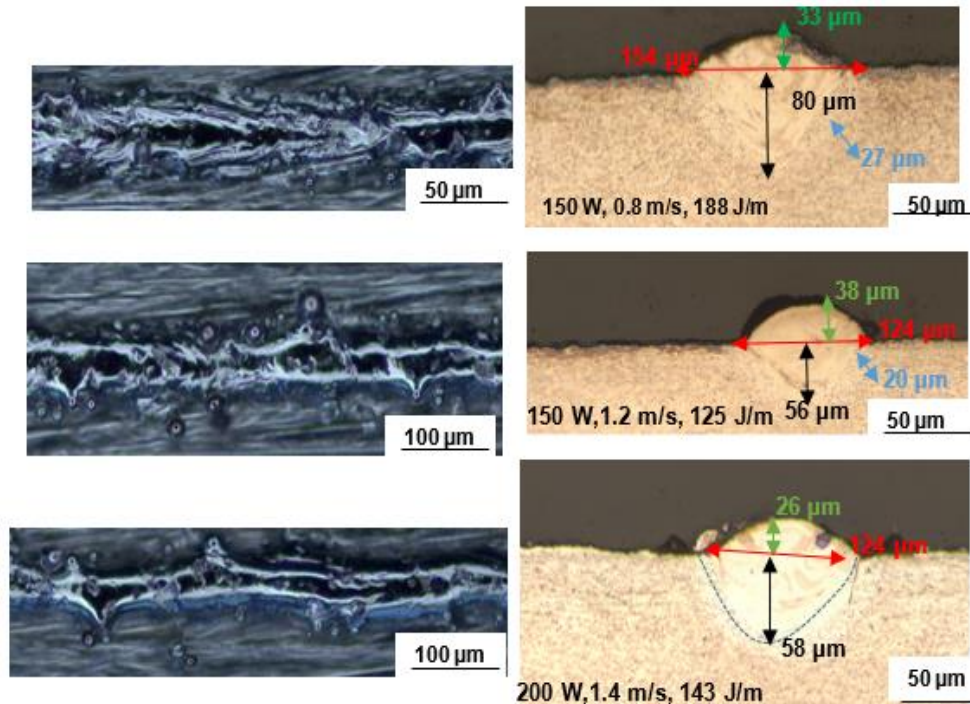


**Figure 6.8:** Top views and cross-sections of the best single tracks produced at a 10 % SiC volume fraction in an SiC/Ti6Al4V(ELI) composite

For the laser powers and scanning speeds of 150 W, 1.2 m/s, and 200 W, 1.4 m/s, the top views of the tracks show thin or narrow tracks with spatter particles at their sides. Narrow tracks increase the consumption of powder and manufacturing time while creating parts (Ramosena et al, 2022). It is noted from Figure 6.8 that spatter particles were greatest in number at the highest LED of 188 J/m of the set of three scans in this figure. As was reported separately by Dzogbewu et al. (2023) and Liu et al. (2015), it is thought here that increased LED raised the temperature of the melt pool, resulting in a stronger wave current within the melt due to the Marangoni effect. Because of the increased wave current, the molten pool is thought to have pinched off powder ahead of the laser spot, thus resulting in an increased number of spatter particles.

The cross- section at a laser power and scanning speed of 200 W and 1.4 m/s, respectively, showed a track with a height of 26  $\mu\text{m}$ , which is too low to be employed in the construction of parts because it will result in the necessity for numerous layers to complete a part. The cross-section at a laser power and scanning speed of 150 W and 1.2 m/s, respectively, revealed a depth of penetration of 56  $\mu\text{m}$ , which is just a little deeper than the layer thickness of (45  $\mu\text{m}$ –50  $\mu\text{m}$ ) and, therefore, will not sufficiently re-melt the prior layer. The single track produced at a laser power of 150

W, with a scanning speed of 0.8 m/s and LED of 188 J/m, is favoured over the other two in this figure, due to wider track seen from the top perspective and deeper depth of penetration that is higher than the layer thickness (45  $\mu\text{m}$ –50  $\mu\text{m}$ ). This higher depth of penetration indicates that a prior layer will be sufficiently re-melted to enable good fusion between it and the current one. Therefore, it is concluded from the foregoing discussion that the optimal single track at a 10% SiC volume fraction is obtained with the laser power, scanning speed and LED of 150 W, 0.8 m/s and 188 J/m.

### 6.3. Analysis of Single Tracks of a 15 % SiC Volume Fraction in an SiC/Ti6Al4V(ELI) composite

Top view analysis of single tracks at 15 % SiC volume fraction produced with values of laser power from 100 W to 350 W and scanning speeds from 0.3 m/s to 2.7 m/s are categorised, as shown in Table 6.5.

**Table 6.5: Categorisation of single tracks based on continuity and discontinuity tracks, pre-balling/necking and balling**

Laser Power (W)									
100	Scanning speed (m/s)	0.3	0.4	0.5	0.6	0.7	0.8	0.9	
	Linear energy density (J/m)	333	250	200	167	143	125	111	
150	Scanning speed (m/s)	0.6	0.7	0.8	0.9	1	1.1	1.2	
	Linear energy density (J/m)	250	214	188	167	150	136	125	
200	Scanning speed (m/s)	0.8	0.9	1	1.2	1.4	1.5	1.6	
	Linear energy density (J/m)	250	222	200	167	143	133	125	
250	Scanning speed (m/s)	1.1	1.2	1.3	1.5	1.7	1.8	1.9	
	Linear energy density (J/m)	227	208	192	167	147	139	132	
300	Scanning speed (m/s)	1.2	1.4	1.6	1.8	2	2.2	2.4	
	Linear energy density (J/m)	250	214	188	167	150	136	125	
350	Scanning speed (m/s)	1.5	1.7	1.9	2.1	2.3	2.5	2.7	
	Linear energy density (J/m)	233	206	184	167	152	140	130	

All tracks produced at 100 W and 150 W were continuous while tracks produced at 200 W exhibited necking and discontinuity at laser scanning speeds of 1.5 m/s and 1.6 m/s, with corresponding energy densities of 133 J/m and 125 J/m. At 250 W, continuous tracks were produced at scanning speeds ranging from 1.1 m/s to 1.7 m/s and energy densities from 227 J/m to 147 J/m. Upon increasing the laser power to 300 W, necking was observed at the last two highest scanning speeds of 2.2 m/s and 2.4 m/s with energy densities of 136 J/m and 125 J/m, below which all tracks were

continuous. Only the first three single tracks were continuous at the highest laser power of 350 W, while the rest showed necking and discontinuities. The data in Table 6.5 shows that as the scanning speed increased above the values used to produce continuous tracks, necking and discontinuous tracks occurred due to decreased LED that led to insufficient energy to fully melt and form continuous tracks. Investigations of the cross-sections of tracks built at values of laser power and scanning speeds that were identified from Table 6.5 as having led to the formation of continuous tracks were conducted with the resulting categorisation shown in Table 6.6.

**Table 6.6: Categorisation of the cross-sections of single tracks based on depth-to-width ratios**

Laser Power (W)								
100	Scanning speed (m/s)	0.3	0.4	0.5	0.6	0.7	0.8	0.9
	Linear energy density (J/m)	333	250	200	167	143	125	111
150	Scanning speed (m/s)	0.6	0.7	0.8	0.9	1	1.1	1.2
	Linear energy density (J/m)	250	214	188	167	150	136	125
200	Scanning speed (m/s)	0.8	0.9	1	1.2	1.4	1.5	1.6
	Linear energy density (J/m)	250	222	200	167	143	133	125
250	Scanning speed (m/s)	1.1	1.2	1.3	1.5	1.7	1.8	1.9
	Linear energy density (J/m)	227	208	192	167	147	139	132
300	Scanning speed (m/s)	1.2	1.4	1.6	1.8	2	2.2	2.4
	Linear energy density (J/m)	250	214	188	167	150	136	125
350	Scanning speed (m/s)	1.5	1.7	1.9	2.1	2.3	2.5	2.7
	Linear energy density (J/m)	233	206	184	167	152	140	130

Except for the two cross-sections at the power, scanning speed, and LED of 100 W, 0.4 m/s, and 250 J/m and 200 W, 0.9 m/s, and 222 J/m, all the other cross-sections indicate poor depths of penetration. It has previously been stated that cross-sections with depth-to-width ratios less than 0.5 are not suitable to produce specimen or 3D objects. Insufficient energy to melt the powder and permeate the substrate causes poor depth of penetration at higher laser scanning speeds and low LEDs, as observed by Dilip et al. (2017) and Yadroitsev et al. (2013). The cross-sections with poor depth of penetration at 100 W and 150 W are shown in Appendix C, Figures C1 and C2. However, inadequate depth of penetration was found at high LEDs due to large lateral

flow of the melt pool, arising from high-temperature-induced reduction of surface tension and viscosity. It was observed that the track-widths varied inconsistently with increasing laser scanning speed, while the track-heights increased consistently with rising laser scanning speed, as shown in Appendix C, Figure C2, which is consistent with the work of Shrestha et al. (2021). The two cross-sections with the appropriate depth of penetration were thereafter compared and analysed in the next section, to aid in the selection of a suitable process parameter set for the building of single layers.

### 6.3.1. Comparative analysis of the best single tracks at a 15% SiC volume fraction in an SiC/Ti6Al4V(ELI) composite

Top surface micrographs and cross-sections of the best single tracks from Tables 6.6 and 6.7 are shown in Figure 6.9 for use in determining the best set of process parameters to be employed at 15 % SiC volume fraction for building single layers and 3D specimens.

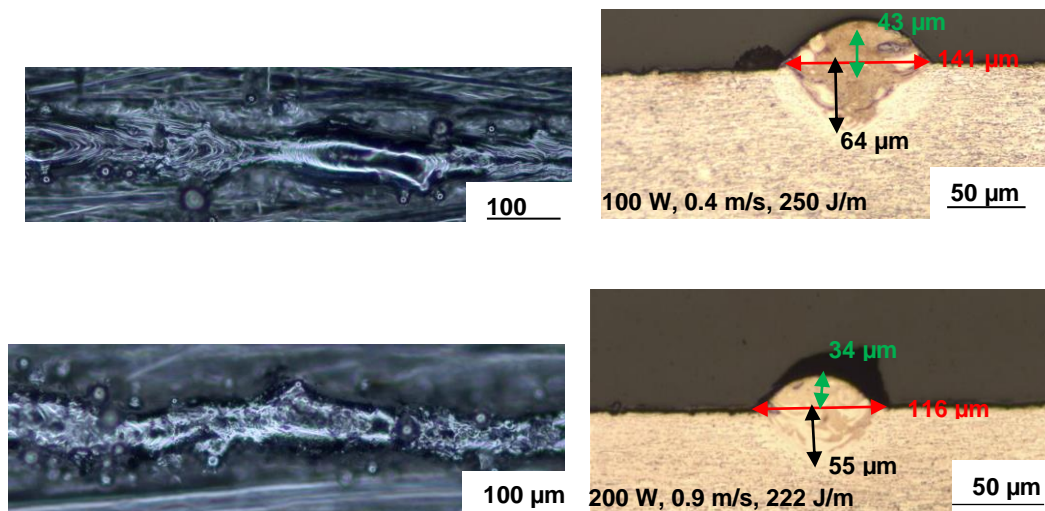


**Figure 6.9:** Top view images and cross-sections of the best single tracks produced at a 15% SiC volume fraction in an SiC/Ti6Al4V(ELI) composite

The top view of the track built at a laser power of 200 W and scanning speed of 0.9 m/s showed a higher number of spatter particles at the periphery than the track produced at a laser power and scanning speed of 100 W and 0.4 m/s, respectively. The formation of spatter particles for both single tracks in Figure 6.9 is thought to have occurred because of high energy densities. At high LEDs, the powder is melted and evaporated

leading to the creation of vapour recoil pressure that ejects part of the molten material out of the melt pool, which then solidifies quickly to form spherical particles (Andani et al., 2018, Liu et al., 2017, Dzogbewu et al., 2022). The two cross-sections in this figure show depths of penetration of 64  $\mu\text{m}$  and 55  $\mu\text{m}$ , for the top and bottom images, respectively, both of which are deeper than the layer thickness range of (45  $\mu\text{m}$ -50  $\mu\text{m}$ ). However, the higher depth of penetration of 64  $\mu\text{m}$  indicates that during printing of parts, not only will the layer of powder be melted but so will the previous layer be re-melted by 28 %, resulting in better bonding of the two layers than for the lower depth of penetration, with a re-melting of the lower layer by 10%. The low scanning speed of 0.4 m/s enhanced the LED, despite the low value of laser power of 100 W, thus resulting in greater energy input and, therefore, sufficient melting of powder and substrate to an increased depth of penetration when compared to the other case considered here. This is consistent with the observations of Karimi et al. (2019). According to Yadroitsev et al. (2013), re-melted depth is an important factor that influences the quality of the manufactured parts, as it supports better bonding of adjacent layers and a layer and the substrate. Lastly, the track heights of the two cross-sections are less than the layer thickness, which minimizes irregularity of the top surface of layers.

As a result of this discussion, it is concluded that the best set of process parameters to be used for building specimens at a 15 % SiC volume fraction are laser power, scanning speed, and LED of 100 W, 0.4 m/s, and 250 J/m, which produced a track with sufficient depth of penetration, an acceptable height above the substrate and formation of few spatter particles that can be removed by rescanning during the production of specimens.

#### **6.4. Analysis of Single Tracks at a 20 % SiC Volume Fraction in an SiC/Ti6Al4V(ELI) Composite**

At a 20 % SiC volume fraction, top view analysis of single tracks produced at different values of laser power from 100 W to 350 W, and different values of laser scanning speed from 0.3 m/s to 2.7 m/s, led to the categorisation shown in Table 6.7. The red blocks in Table 6.8 denote single tracks that are continuously melted, while the yellow blocks denote single tracks with pre-balling or necking, and green blocks represent balling.

**Table 6.7: Categorisation of single tracks based on track continuity, discontinuity, pre-balling/necking and balling**

Laser Power (W)								
100	Scanning speed (m/s)	0.3	0.4	0.5	0.6	0.7	0.8	0.9
	Linear energy density (J/m)	333	250	200	167	143	125	111
150	Scanning speed (m/s)	0.6	0.7	0.8	0.9	1	1.1	1.2
	Linear energy density (J/m)	250	214	188	167	150	136	125
200	Scanning speed (m/s)	0.8	0.9	1	1.2	1.4	1.5	1.6
	Linear energy density (J/m)	250	222	200	167	143	133	125
250	Scanning speed (m/s)	1.1	1.2	1.3	1.5	1.7	1.8	1.9
	Linear energy density (J/m)	227	208	192	167	147	139	132
300	Scanning speed (m/s)	1.2	1.4	1.6	1.8	2	2.2	2.4
	Linear energy density (J/m)	250	214	188	167	150	136	125
350	Scanning speed (m/s)	1.5	1.7	1.9	2.1	2.3	2.5	2.7
	Linear energy density (J/m)	233	206	184	167	152	140	130

It is clear from this table that continuous tracks were generated with a laser power of 100 W at laser scanning speeds and LEDs ranging from 0.3 m/s to 0.7 m/s and 333 J/m to 143 J/m, above which the necking phenomenon occurred. At a laser power of 150 W, necking only occurred at the highest scanning speed of 1.2 m/s and a LED of 125 J/m. Increasing of the value of laser power to 200 W and 250 W led to the formation of continuous tracks for laser scanning speeds from 0.8 m/s to 1.2 m/s with corresponding LEDs from 250 J/m to 167 J/m, and laser scanning speeds from 1.1 m/s to 1.5 m/s with LEDs from 227 J/m to 167 J/m, respectively. The tracks built with the lower value of laser power exhibited necking from laser scanning speeds of 1.4 m/s to 1.6 m/s, while those built at the higher value of laser power showed balling from the scanning speeds of 1.7 m/s to 1.9 m/s. Except for the one track built at the highest laser scanning speed of 2.4 m/s and a LED of 125 J/m, increasing the laser power to 300 W resulted in the formation of continuous tracks for all other laser scanning speeds used. Continuous tracks were also obtained at the highest value of laser power in the set of powers shown in this table, at the low laser scanning speeds of 1.5 m/s and 1.7 m/s with corresponding LEDs of 233 J/m and 206 J/m. The built tracks showed necking as the scanning speed increased to 1.9 m/s and up to 2.3 m/s, while discontinuities were seen at the maximum scanning speeds of 2.5 m/s and 2.7 m/s at the same value of laser power of 350 W.

Further investigation to assist in identifying the best set of process parameters for

manufacturing single layers and 3D specimens, based on the single tracks built at this volume fraction of SiC and the range of process parameters shown in Table 6.7, was carried out from a study of their cross-sections, and led to the categorisation presented in Table 6.7.

**Table 6.8: Categorisation of the cross-sections of single tracks based on depth-to-width ratios**

Laser Power (W)									
100	Scanning speed (m/s)	0.3	0.4	0.5	0.6	0.7	0.8	0.9	
	Linear energy density (J/m)	333	250	200	167	143	125	111	
150	Scanning speed (m/s)	0.6	0.7	0.8	0.9	1	1.1	1.2	
	Linear energy density (J/m)	250	214	188	167	150	136	125	
200	Scanning speed (m/s)	0.8	0.9	1	1.2	1.4	1.5	1.6	
	Linear energy density (J/m)	250	222	200	167	143	133	125	
250	Scanning speed (m/s)	1.1	1.2	1.3	1.5	1.7	1.8	1.9	
	Linear energy density (J/m)	227	208	192	167	147	139	132	
300	Scanning speed (m/s)	1.2	1.4	1.6	1.8	2	2.2	2.4	
	Linear energy density (J/m)	250	214	188	167	150	136	125	
350	Scanning speed (m/s)	1.5	1.7	1.9	2.1	2.3	2.5	2.7	
	Linear energy density (J/m)	233	206	184	167	152	140	130	

The data in Table 6.8 showed that cross-sections with the optimum depth-to-width ratio of 0.5 occurred at a laser power of 200 W, laser scanning speed of 0.9 m/s, 1.5 m/s and 1.6 m/s, and related LEDs of 222 J/m, 133 J/m, and 125 J/m, respectively. The formation of keyholes was observed at laser scanning speeds of 0.8 m/s and 1 m/s, with related LEDs of 250 J/m and 200 J/m, respectively. Keyholes were also formed at a laser power of 350 W, with scanning speeds of 1.5 m/s and 1.7 m/s and corresponding LEDs of 206 J/m and 233 J/m, respectively. All the other cross-sections of single tracks built at different laser powers of 100 W, 150 W, 250 W, and 300 W, at different scanning speeds in this instance, had insufficient depth of penetration.

#### 6.4.1. Comparative analysis of the best single tracks at a 20% SiC volume fraction in an SiC/Ti6Al4V(ELI) composite

According to Tables 6.7 and 6.8, single tracks with sufficient depth of penetration and continuity at a 20% SiC volume percent were produced at laser powers, scanning speeds, and LEDs of 200 W, 0.9 m/s and 222 J/m; 200 W, 1.5 m/s, and 133 J/m; and

200 W, 1.6 m/s, and 125 J/m, respectively. Figure 6.10 depicts top views and cross-sections of these single tracks that were studied to help choose the best one for use in the building of single layers.

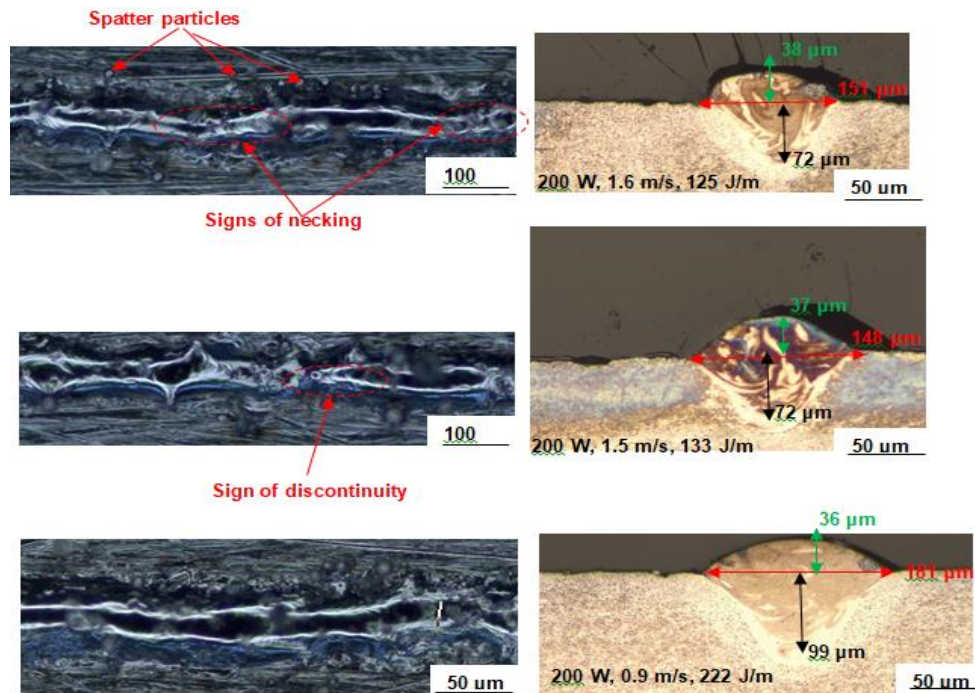


**Figure 6.10:** Top view and cross-sections of the best single tracks produced at 20% SiC volume fraction in an SiC/Ti6Al4V(ELI) composite

It is noted that the best tracks obtained at this value of SiC volume fraction shown in Figure 6.10 were obtained using the same value of laser power of 200 W but at different laser scanning speeds. At the fastest scanning speed of 1.6 m/s, the top surface scan in the figure showed numerous spatter particles at the margins of the track, which are not apparent at the two lower scanning speeds. According to Equation 2.17, raising the laser scanning speed decreases the LED, as was observed separately by Shi et al. (2017) and Stasic et al. (2016), which in this case appears to have led to the reduction of spatter particles.

The top surfaces of the tracks built at laser scanning speeds of 1.6 m/s and 1.5 m/s showed signs of necking and discontinuity, respectively. Their cross-sections, on the other hand, showed depths of penetration that were greater than the layer thickness and heights above the substrate that were lower than the layer thickness, both which are positive traits. Despite this, the necking and discontinuity observed in the tracks make their related process parameter sets unsuitable for use in building single layers

or 3D specimens, due to costs and integrity of the built parts.

From the preceding discussion, it is concluded that the process parameter set of a scanning speed of 0.9 m/s, laser power of 200 W and LED of 222 J/m, is the best one at a 20 % SiC volume fraction. The cross-section of the track built with these process parameters had a depth of penetration (99  $\mu\text{m}$ ), twice the thickness of the layer of powder, indicating that the previous layers would have re-melted fully. It had a larger width (181  $\mu\text{m}$ ) than in the other two cases thus signifying a shorter building process, and a height (36  $\mu\text{m}$ ) that was very similar to the heights of the other two tracks considered here. Furthermore, its top-view perspective, showing a continuous track with no visible spatter particles and more even width than in the other two cases, is expected to ensure better alignment of adjacent tracks during multi-track printing, as was observed by Shi et al. (2017).

### 6.5. Analysis of Single Tracks at a 25 % SiC Volume Fraction in an SiC/Ti6Al4V(ELI) Composite

The top view analysis of single tracks at a 25 % SiC volume fraction in an SiC/Ti6Al4V(ELI) composite led to the categorisation presented in Table 6.9.

**Table 6.9: Categorisation of single tracks based on continuity and discontinuity tracks, pre-balling/necking and balling**

Laser Power (W)								
100	Scanning speed (m/s)	0.3	0.4	0.5	0.6	0.7	0.8	0.9
	Linear energy density (J/m)	333	250	200	167	143	125	111
150	Scanning speed (m/s)	0.6	0.7	0.8	0.9	1	1.1	1.2
	Linear energy density (J/m)	250	214	188	167	150	136	125
200	Scanning speed (m/s)	0.8	0.9	1	1.2	1.4	1.5	1.6
	Linear energy density (J/m)	250	222	200	167	143	133	125
250	Scanning speed (m/s)	1.1	1.2	1.3	1.5	1.7	1.8	1.9
	Linear energy density (J/m)	227	208	192	167	147	139	132
300	Scanning speed (m/s)	1.2	1.4	1.6	1.8	2	2.2	2.4
	Linear energy density (J/m)	250	214	188	167	150	136	125
350	Scanning speed (m/s)	1.5	1.7	1.9	2.1	2.3	2.5	2.7

Linear energy density (J/m)	233	206	184	167	152	140	130
-----------------------------	-----	-----	-----	-----	-----	-----	-----

As shown in Table 6.9, the production of continuous tracks was observed at all scanning speeds used for laser power levels of 100 W, 150 W, and 200 W, except for the track built at the highest scanning speed of 1.6 m/s and LED of 125 J/m at 200 W. The increase in power to 250 W caused necking at scanning speeds of 1.8 m/s and 1.9 m/s and corresponding LEDs of 139 J/m and 132 J/m, respectively. At a laser power of 300 W, necking and balling occurred at scanning speeds of 1.8 m/s and 2 m/s, with corresponding LEDs of 167 J/m and 150 J/m, while discontinuity at the same power of 300 W occurred at laser scanning speeds of 2.2 m/s and 2.4 m/s with corresponding LEDs of 136 J/m and 125 J/m respectively. Continuous tracks were achieved at 350 W only at the low scanning speeds of 1.5 m/s and 1.7 m/s.

Although the tracks produced at the values of laser power of 100 W and 150 W were continuous, their widths decreased with increasing laser scanning speed, as shown in Appendix E, Figures E1 to E5. The tracks that were built at the lower scanning speeds were noticeably wider than those at the higher speeds. The necking and balling observed at high laser scanning speeds, as has been mentioned previously in this chapter, are thought to have occurred due to the known fact that an increase in laser scanning speed at the same power leads to a reduction of energy density and, therefore, reduction in temperature of the melt pool (Ramosena et al., 2022; Shi et al., 2017). Because surface tension and viscosity are known to be temperature dependent, as previously indicated in this work, surface tension and viscosity are expected to be greatest at the highest laser scanning speed, where the LED and temperature are the lowest (Yadroitsev et al., 2010). High surface tension and viscosity reduce the spreading ability of melt and adhesion onto the substrate thus causing narrowing down of tracks and creating discontinuities (Dzogbewu et al., 2023).

Further investigation of these tracks was carried out based on their cross-sections with the resulting categorisation presented in Table 6.10 to assist in identifying the best set of process parameters for manufacturing single layers. The purple blocks in the table indicate depth-to-width ratios of the cross-sections that are greater than 0.5 point to the formation of keyholes, blue blocks, optimum penetration with a depth-to-width ratio of 0.5, and dark grey blocks, poor penetration with a depth-to-width ratio less than 0.5.

**Table 6.10: Categorisation of the cross-sections of single tracks based on depth-to-width ratios**

Laser Power (W)								
100	Scanning speed (m/s)	0.3	0.4	0.5	0.6	0.7	0.8	0.9
	Linear energy density (J/m)	333	250	200	167	143	125	111
150	Scanning speed (m/s)	0.6	0.7	0.8	0.9	1	1.1	1.2
	Linear energy density (J/m)	250	214	188	167	150	136	125
200	Scanning speed (m/s)	0.8	0.9	1	1.2	1.4	1.5	1.6
	Linear energy density (J/m)	250	222	200	167	143	133	125
250	Scanning speed (m/s)	1.1	1.2	1.3	1.5	1.7	1.8	1.9
	Linear energy density (J/m)	227	208	192	167	147	139	132
300	Scanning speed (m/s)	1.2	1.4	1.6	1.8	2	2.2	2.4
	Linear energy density (J/m)	250	214	188	167	150	136	125
350	Scanning speed (m/s)	1.5	1.7	1.9	2.1	2.3	2.5	2.7
	Linear energy density (J/m)	233	206	184	167	152	140	130

The data in Table 6.10 shows the occurrence of keyholes at a value of laser power of 100 W with scanning speeds of 0.3 m/s and 0.4 m/s and corresponding LEDs of 333 J/m and 250 J/m, respectively. The occurrence of keyholes was also noted at a laser power of 300 W, and laser scanning speeds and LEDs of 2.2 m/s, 2.4 m/s, and 136 J/m, and 125 J/m, respectively. The optimum depth-to-width ratio of 0.5 was identified at a laser power, scanning speed and related LED of 100 W, 0.5 m/s, and 200 J/m, respectively, and at a laser power value of 200 W, scanning speeds from 0.9 m/s to 1.4 m/s and related LEDs from 222 J/m to 143 J/m. Undercutting, which signals the advent of balling, was observed at scanning speeds of 1.5 m/s and 1.6 m/s, at a laser power of 200 W as shown in Appendix E, Figure E6. The remaining tracks built at laser powers of 150 W, 250, and 350 W led to cross-sections with poor depth-to-width ratios, as shown in Appendix E, Figures E2, E4 and E6. It has been discussed in literature that poor penetration will lead to delamination of layers during the production of 3D parts (Yadroitsev et al., 2013). Chernyshikhin et al. (2021) reported that tracks with poor penetration could be displaced by the recoater blade during the levelling of the next layer of powder, leading to disruption of the process.

The keyhole effect at 100 W occurred at the low prevailing laser scanning speeds of 0.3 m/s and 0.4 m/s, which provided the laser beam enough time to penetrate through

the powder to the substrate (Guo et al., 2019 and Yu et al., 2016). The keyhole effect is highly undesirable as it will lead to formation of pores during the multilayer process (Chernyshikhin et al., 2021).

The results obtained at these two scanning speeds are similar to those reported separately by Antony et al. (2015), and Andani et al. (2018), who observed that slow scanning speeds coupled with high energy densities caused the evolution of high temperatures that led to evaporation of molten pools and the formation of strong recoil pressure. They further mentioned that when the recoil pressure exceeds the surface tension forces, it causes the formation of depressions into the substrate, thus forming keyholes. It is clear from Table 6.10 that increasing the laser scanning speed from these two levels to a value of 0.5 m/s at 100 W led to a decrease in the depth of penetration to one with an optimum depth-to-width ratio and, thus, a change from keyhole melting to conduction melting, which is consistent with the work of Chernyshikhin et al. (2021).

#### **6.5.1. Comparative analysis of the best single tracks at a 25% SiC volume fraction in an SiC/Ti6Al4V(ELI) composite**

A study of Tables 6.9 and 6.10 revealed that the values of laser power of 100 W and 200 W led to production of tracks with the best depth-to-width ratios and continuity. To determine the best parameter set for building single layers, the top views of the best tracks produced at laser powers of 100 W and 200 W and their respective scanning speeds, as well as their cross-sections, were then compared and discussed based on the images shown in Figure 6.11.

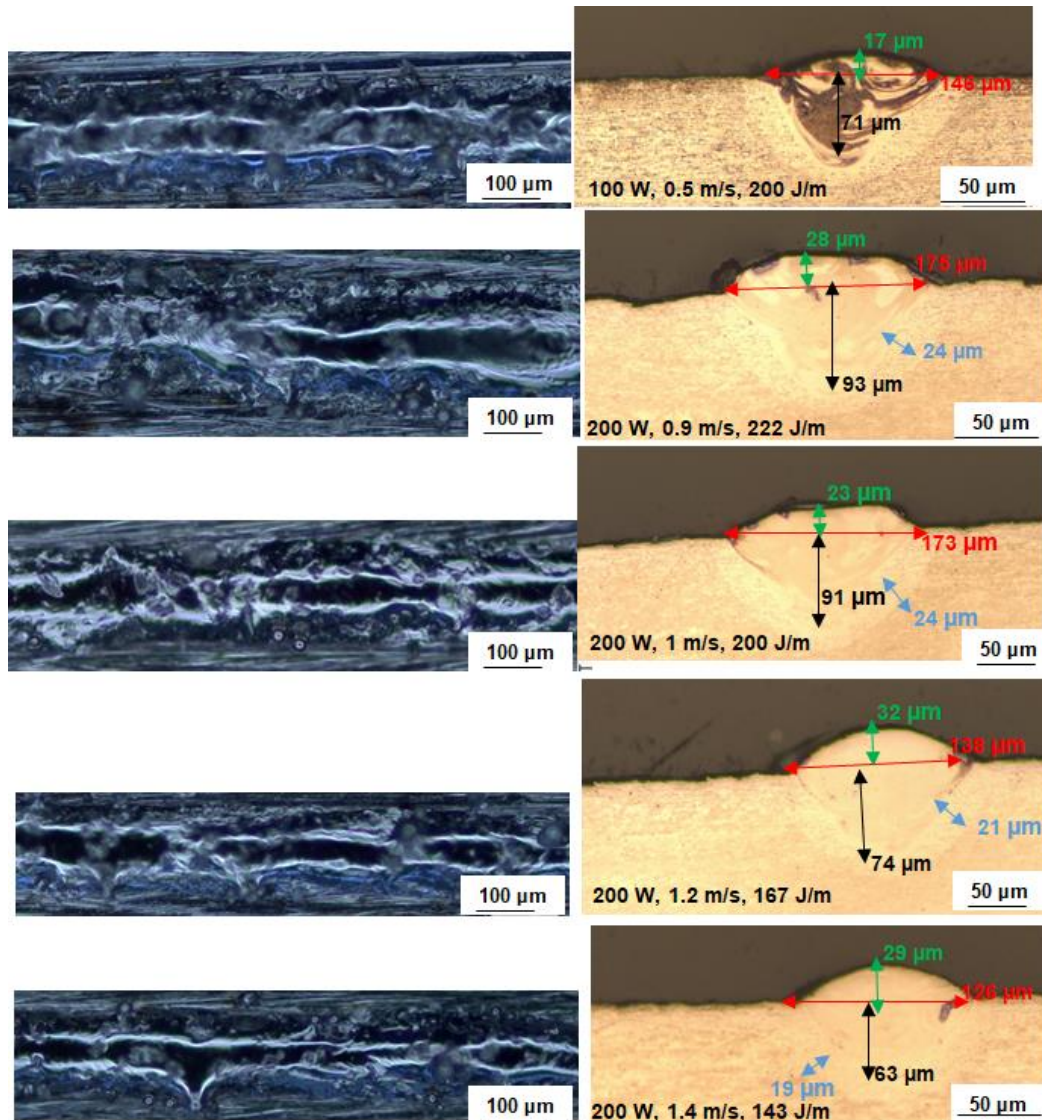


**Figure 6.11: Top views and cross-sections of the best single tracks at laser powers of 100 W and 200 W produced at a 25% SiC volume fraction in an SiC/Ti6Al4V (ELI) composite**

Figure 6.11 shows that the cross-section of the track printed at a laser power of 100 W and a scanning speed of 1 m/s had a low height above the substrate, which would increase production time and consumption of powder, as noted by Ramosena et al. (2023). As a result, even though the track was continuous, its process parameters were not considered for use in building single layers. The cross-sections in this figure that were built at scanning speeds of 0.9 m/s and 1 m/s showed a V-shaped profile with a depth of penetration larger than half the track width, thus indicating the presence of keyholes. Furthermore, both the cross-sections had heights above the substrate that were significantly lower than the layer thickness, thus demanding additional layers to

complete a 3D part. Therefore, the process parameters used to build these two cross-sections were not considered ideal to produce single layers.

The cross-section built at a scanning speed of 1.4 m/s, showed a depth of penetration that was exactly half the width of the track, indicating a U-shape profile. However, its top view showed a narrow track with necking and the presence of partially melted particles at the edges. The low LED for this build is thought to have caused necking and partially melted particles because it was inadequate to totally melt the particles on the track and its sides. Partially melted particles cause uneven layering during subsequent deposition of powder, while narrow tracks increase production time during the fabrication of parts, as was noted by Stasic et al. (2016). Therefore, the process parameters used to build this track were considered not ideal for building single layers.

The cross-section built with process parameters of 200 W, 1.2 m/s, and 167 J/m gave rise to a top view showing a fairly continuous track with few spatter particles, while its cross-section showed an optimum depth-to-width ratio of 0.5 with a depth of 74  $\mu\text{m}$  that was significantly greater than the layer thickness of 45  $\mu\text{m}$ –50  $\mu\text{m}$  and an acceptable height of 32  $\mu\text{m}$  above the substrate. A depth of penetration greater than the layer thickness ensures that the previous layer is suitably re-melted, resulting in a strong link between the layers. A track with a height above the substrate that is both sufficient and smaller than the layer thickness will lower the number of layers required to finish 3D parts, thus saving the consumption of powder. It is concluded that at a 25% SiC volume fraction, the best set of process parameters of laser power, scanning speed and LED of are 200 W, 1.2 m/s, and 167 J/m.

#### **6.6. Analysis of Single Tracks at a 30 % SiC Volume Fraction in an SiC/Ti6Al4V (ELI) Composite**

A study similar to the foregoing ones was done at a 30 % SiC volume fraction and the tracks built for all process parameter sets used in this case categorised as indicated in Table 6.11.

**Table 6.11: Categorisation of single tracks based on continuity and discontinuity tracks, pre-balling/necking and balling**

Laser Power (W)								
100	Scanning speed (m/s)	0.3	0.4	0.5	0.6	0.7	0.8	0.9
	Linear energy density (J/m)	333	250	200	167	143	125	111
150	Scanning speed (m/s)	0.6	0.7	0.8	0.9	1	1.1	1.2
	Linear energy density (J/m)	250	214	188	167	150	136	125
200	Scanning speed (m/s)	0.8	0.9	1	1.2	1.4	1.5	1.6
	Linear energy density (J/m)	250	222	200	167	143	133	125
250	Scanning speed (m/s)	1.1	1.2	1.3	1.5	1.7	1.8	1.9
	Linear energy density (J/m)	227	208	192	167	147	139	132
300	Scanning speed (m/s)	1.2	1.4	1.6	1.8	2	2.2	2.4
	Linear energy density (J/m)	250	214	188	167	150	136	125
350	Scanning speed (m/s)	1.5	1.7	1.9	2.1	2.3	2.5	2.7
	Linear energy density (J/m)	233	206	184	167	152	140	130

The findings in Table 6.11 reveal that at a laser power of 100 W, all the tracks were continuous except for the tracks built at the lowest and highest laser scanning speeds and corresponding LEDs of 0.3 m/s and 333 J/m, and 0.9 m/s and 111 J/m, respectively, which exhibited discontinuities. Increasing the laser power to 150 W resulted in the formation of continuous tracks at scanning speeds ranging from 0.6 m/s to 1.1 m/s, and corresponding LEDs ranging from 250 J/m to 136 J/m. The exception was the track built at the highest laser scanning speed of 1.2 m/s and LED of 125 J/m which exhibited necking and balling. Further increase of laser power to 200 W and 250 W led to the formation of continuous tracks at all scanning speeds used. Continuous tracks built at 300 W were obtained only at the two lowest laser scanning speeds of 1.2 m/s and 1.4 m/s with corresponding LEDs of 250 J/m and 214 J/m, above which necking and balling was observed. At a laser power of 350 W, continuous tracks were achieved at the two lowest laser scanning speeds of 1.5 m/s and 1.7 m/s with corresponding LEDs of 233 J/m and 206 J/m; while necking and balling was detected at laser scanning speeds ranging from 1.9 m/s to 2.5 m/s with corresponding LEDs ranging from 184 J/m to 140 J/m. The highest scanning speed and corresponding LED of 2.7 m/s and 333 J/m, respectively, led to the formation discontinuous tracks.

Further investigation of the cross-section was done leading to the categories shown in Table 6.12 that were used to determine the best process parameters at 30% SiC volume fraction in an SiC/Ti6Al4V(ELI) composite.

**Table 6.12: Categorisation of the cross-sections of single tracks based on depth-to-width ratios**

Laser Power (W)									
100	Scanning speed (m/s)	0.3	0.4	0.5	0.6	0.7	0.8	0.9	
	Linear energy density (J/m)	333	250	200	167	143	125	111	
150	Scanning speed (m/s)	0.6	0.7	0.8	0.9	1	1.1	1.2	
	Linear energy density (J/m)	250	214	188	167	150	136	125	
200	Scanning speed (m/s)	0.8	0.9	1	1.2	1.4	1.5	1.6	
	Linear energy density (J/m)	250	222	200	167	143	133	125	
250	Scanning speed (m/s)	1.1	1.2	1.3	1.5	1.7	1.8	1.9	
	Linear energy density (J/m)	227	208	192	167	147	139	132	
300	Scanning speed (m/s)	1.2	1.4	1.6	1.8	2	2.2	2.4	
	Linear energy density (J/m)	250	214	188	167	150	136	125	
350	Scanning speed (m/s)	1.5	1.7	1.9	2.1	2.3	2.5	2.7	
	Linear energy density (J/m)	233	206	184	167	152	140	130	

The data in Table 6.12 only shows the presence of grey blocks, indicating that all the cross-sections at a 30% SiC volume fraction exhibited low depths of penetration, with depth-to-width ratios much less than 0.5 for the entire range of laser power used here from 100 W to 350 W. The effects of the thermal properties of SiC particles, such as their high heat capacity, high conductivity, and poor reflectivity, as well as low density in comparison to those of Ti6Al4V (ELI), on the laser melting process of SiC/Ti6Al4V (ELI) composites are now considered. Due to the differing densities of the two powders, SiC particles with lower densities were expected to and did float on top of the melt pool and absorbed substantial amounts of energy without fully transferring it to the Ti6Al4V particles. As a result, the Ti6Al4V (ELI) received less energy to completely melt and transferred less energy to the substrate than would have been received in the absence of SiC particles. This resulted in the formation of tracks with cross-sections that had poor depths of penetration, as shown in Table 6.12 and in Appendices F1 to F4.

It was expected that as the volume fraction of SiC particles increased, more laser energy would be required to melt the powder, raise the temperature of the melt and penetrate the substrate. The results obtained at 30% SiC volume fraction at the higher values of laser power of 300 W and 350 W, as shown in Appendix F5 and F6, revealed that the laser beam did not penetrate the substrate adequately, resulting in tracks with lower widths and higher heights, both signs of insufficient heat even at these two high values of laser power. As a result, while some of the top surface scans of the tracks in Table 6.11 exhibited some continuity, they all had low depths of penetration, leading to the conclusion that there were no optimal process parameters for a 30% SiC volume fraction of the SiC/Ti6Al4V (ELI) composite amongst those used.

## 6.7. Discussions and summary

A summary of all the best process parameters obtained at SiC volume fractions from 5 % to 30 % are shown in Table 6.11.

**Table 6.13: Summary of the best process parameters from 5 % to 30 % SiC volume fractions of SiC in SiC/Ti6Al4V (ELI) composites determined in this chapter**

SiC Volume Fraction (%)	Laser Power (W)	Laser Scanning Speed (m/s)	Linear Energy Density (J/m)
5	200	1.2	167
10	150	0.8	188
15	100	0.4	250
20	200	0.9	222
25	200	1.2	167
30	none	none	none

The data in Table 6.13 was used to plot the graphs shown in Figure 6.12 to help study the trends of laser power, scanning speed and LED with increasing SiC volume fraction.

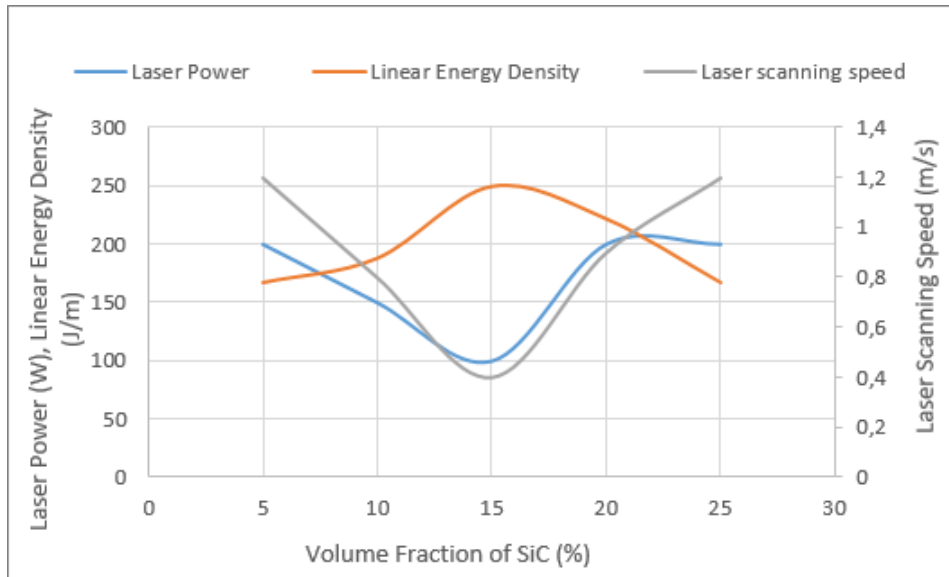


**Figure 6.12: Graphs of the variation of best process parameter set values of laser power, linear energy density and laser scanning speed with SiC volume fraction**

The graphs in this figure demonstrate a consistent drop in the best process parameter set values of laser power and scanning speed, while the LED increases as the SiC volume fraction increased from 5 % to 15 %. The best process parameter set values of laser power and scanning speed are seen in this figure to be a minimum at an SiC volume fraction of 15 %, while the LED is at its maximum value. This denotes a faster rate of decrease of the best process parameter set values of scanning speed than laser power and, therefore, a consistent increase in the ratio of the best process parameters set values of laser power to scanning speed in this range of SiC volume fraction. As the volume fraction of SiC increased from 15 % to 25 %, the LED decreased, while laser power and scanning speed increased, the latter at a higher rate. It is concluded that the amount of heat needed to create the best SiC/Ti6Al4V(ELI) composites continually increased from 5 % to 15% at low volume fractions of SiC, and subsequently decreased from 15 % to 30 % at larger volume fractions of SiC. This trend is likely to be a result of predominant heat shielding of the particles of Ti6Al4V (ELI) by the lighter particles of SiC, that increases up to an SiC volume fraction of 15 %, followed at higher volume fractions of SiC by a predominance of the transfer of heat from the particles of SiC with their higher heat conductivity and, therefore faster equilibration of temperature, to the proximal particles of Ti6Al4V (ELI) as a result of the higher content of the former.

High SiC volume fractions from 20 % to 30 % led to an increase of the width of tracks and HAZ, and a small reduction of the depth of penetration, compared to the case for lower volume fractions. The first two phenomena are likely to have arisen due to the high heat conductivity and low reflectance of SiC particles resulted in faster increase and equilibration of temperature in them and, therefore, that of the adjacent particles of Ti6Al4V (ELI). The second trend is likely to have arisen from the lower density of SiC particles that makes them act as heat shields that limit the transfer of heat to Ti6Al4V (ELI) powder and thus cause insufficient penetration into the substrate.

Following the determination of the best process parameters for each volume fraction, the average track widths of the best tracks for each volume fraction were calculated for use in determining the overlap rates to be used in building of single layers, with the results shown in Tables 7.1 to 7.6 of Chapter 7. Ten measurements of the width of tracks were obtained at different locations along the length of each best single track and the values of mean and standard deviations as well as variance of deviation calculated, as shown in these tables.

From the analysis of the cross-sections in this chapter, a summary of the geometrical characteristics of width of tracks, depths, and heights of tracks above the substrate of the best selected single tracks produced from SiC volume fraction of 5 % to 30 % are represented in Table 6.14.

**Table 6.14: Summary of the geometrical characteristics of width, depth and height of tracks printed with the best process parameters for 5% to 30% SiC volume fractions of SiC in SiC/Ti6Al4V (ELI) composites**

SiC Volume Fraction (%)	Width (µm)	Depth (µm )	Height (µm)
5	145	78	34
10	124	56	38
15	141	64	43
20	181	99	36
25	138	63	29
30	119	49	41

It was evident from a quick perusal of the data in Table 6.14 that these geometrical characteristics differed for different SiC volume fractions. Therefore, the data in the table was used to plot the graphs shown in Figure 6.13 to study the trends for each factor with the increase of SiC volume fraction.

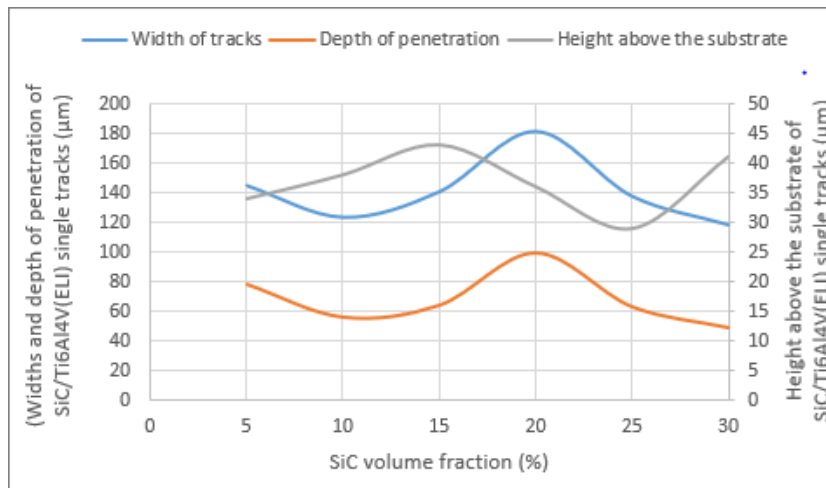


**Figure 6.13:** Graphs of width and height above the substrate and depth of penetration of SiC/Ti6Al4V (ELI) single tracks built at different volume fractions of SiC

As seen in Figure 6.13, the width of built tracks and their depths of penetration of SiC/Ti6Al4V(ELI) single tracks displayed a similar pattern. The highest points from both graphs were reached at 20 % SiC volume fraction. A decreasing trend of both widths of built tracks and their depths of penetration was observed from a 5 % SiC volume fraction to 10 % SiC volume fraction, while a continuous increase was noted between 10 % and 20 % SiC volume fractions. A decrease in the widths of built tracks and their depths of penetration was seen upon further increase of the SiC volume fraction from 20 % to 30 %. Nevertheless, the height of the tracks did not show the same behaviour. There was an increase from 5 % to 15 % and a maximum height at 15 % SiC volume fraction, while a decreasing trend was observed between 15 % and 25 % SiC volume fraction. Further increase of SiC volume from 25 % to 30 % SiC volume fraction led to a linear increase in the height of tracks.

The curve profiles in this figure reflect the competing effects of heat shielding of Ti6Al4V(ELI) by SiC particles at low volume fractions of SiC and more transfer of heat from the SiC to the Ti6Al4V(ELI) particles as a result of the high thermal conductivity of the former and, therefore, faster equilibration of temperature together with their

higher incidence amongst Ti6Al4V(ELI) particles at higher volume fractions of SiC particles.

It was observed previously in this chapter, section 6.4, that the low density, low reflectance, high heat capacity and high conductivity of SiC negatively affected the depth of penetration and widths of tracks at high SiC volume fraction between 25 % and 30 % SiC, where a declining trend of these two factors was observed. From work done on mixing of powders in Chapter 4 showed that agglomeration of SiC particles was more prevalent at higher SiC volume fractions. Because of the low density of SiC particles, it is thought that the agglomerated SiC particles floated on top of the Ti6Al4V(ELI) melt at high volume fractions and acted as heat shields, limiting the transfer of laser power to fully melt Ti6Al4V(ELI) particles and penetrate the substrate, thus leading to formation of narrower tracks, with smaller depths of penetration. Moreover, it was evident in Figure 6.13 that the LED decreased from a 15 % SiC volume fraction, implying that the melt's viscosity and surface tension, which are temperature dependent, also increased with the attendant lower temperatures, thus limiting the melt's wettability and resulting in the formation of narrower tracks. The increase in the height of built tracks with increasing volume fraction of SiC at high volume fractions is also a consequence of the foregoing observations.

## 6.8. Conclusion

1. From the study of the single tracks done in this chapter, the following conclusions arose;

- ✚ Excessive LED due to high power and low scanning speeds led to the formation of discontinuous tracks with no penetration and the occurrence of spatter particles, while low LED as a result of low power and high scanning speeds led to balling and discontinuities of tracks.
- ✚ The best single tracks were obtained at 5 % to 25 % SiC volume fractions. The best widths of tracks for SiC/Ti6Al4V(ELI) composites ranged from 146  $\mu\text{m}$  and 184  $\mu\text{m}$  and led to a non-linear trend of track-widths with their depths of penetration. The suitable heights of the built tracks lying between 30  $\mu\text{m}$  and 40  $\mu\text{m}$  were below the layer thickness of 45  $\mu\text{m}$  to 50  $\mu\text{m}$ . As a result, these best single tracks are expected to

lead to good quality single layers and 3D build parts.

- ✦ High SiC volume fractions, from 20 % to 30 %, led to increased widths of tracks and HAZ, possibly due to the high heat conductivity and low reflectance of SiC particles resulting into faster increase and equilibration of temperature in them and, therefore, that of the adjacent particles of Ti6Al4V(ELI).
- ✦ The thermo-physical properties of low density, high heat capacity for SiC particles led to undesirable geometrical and surface properties of poor depth of penetration and high surface roughness of single tracks, respectively, which effects increased with increasing volume fraction of SiC. In contrast, at lower volume fractions of SiC, the depths of penetration were higher, possibly as a result of the lower density of SiC particles, which acted as heat shields, thus limiting the reduction of the transfer of heat to Ti6Al4V(ELI) powder and, therefore, causing sufficient penetration into the layer of powder.

## 6.9. REFERENCES

- [1]. **Andani, M.T., Dehghani, R., Karamooz-Ravari, M.R., Mirzaeifar, R., and Ni, J.**, 2018. A study on the effect of energy input on spatter particle creation during selective laser melting process, *Additive Manufacturing*, 20, pp. 33-43.
- [2]. **Caprio, L., Demir, A.G., and Previtali, B.**, 2020. Observing molten pool surface oscillations during keyhole processing in laser powder bed fusion as a novel method to estimate the penetration depth. *Additive Manufacturing*, 36, p.101470.
- [3]. **Chernyshikhin, S.V., Firsov, D.G., and Shishkovsky, I.V.**, 2021. Selective laser melting of pre-alloyed NiTi powder: single-track study and FE modelling with heat source calibration. *Materials*, 14(23), p. 7486.
- [4]. **Dai, D., and Gu, D.**, 2015. Tailoring surface quality through mass and momentum transfer modelling using a volume of fluid method in selective laser melting of TiC/AlSi10Mg powder. *International Journal of Machine Tools and Manufacture*, 88, pp. 95-107.
- [5]. **Dilip, J.J.S., Zhang, S., Teng, C., Zeng, K., Robinson, C., Pal, D., and Stucker, B.**, 2017. Influence of processing parameters on the evolution of melt pool, porosity, and microstructures in Ti-6Al-4V alloy parts fabricated by selective laser melting. *Progress in Additive Manufacturing*, 2, pp. 157-167.
- [6]. **Dursun, G., Ibekwe, S., Li, G., Mensah, P., Joshi, G., and Jerro, D.**, 2020. Influence of laser processing parameters on the surface characteristics of 316L stainless steel manufactured by selective laser melting. *Materials Today: Proceedings*, 26, pp. 387-393.
- [7]. **Dzogbewu, T.C., and du Preez, W.B.**, 2022. In situ alloying of Ti10Mo fused tracks and layers via laser powder bed fusion. *Manufacturing Review*, vol.9, p. 23.
- [8]. **Dzogbewu, T.C., and du Preez, W.B.**, 2022. Producing Ti5Mo-fused tracks and layers via laser powder bed fusion, *Metals*, 12(6), p. 950.
- [9]. **Dzogbewu, T.C., de Beer, D.J., and du Preez, W.B.**, 2023. Laser powder bed fusion of Ti15Mo fused tracks and layers. *JOM*, pp.1-14.

- [10]. **Eagar, T.W., and Tsai, N.S.**, 1983. Temperature fields are produced by traveling distributed heat sources. *Welding Journal*, 62(12), pp. 346-355.
- [11]. **Eagar, T.W., and Tsai, N.S.**, 1983. Temperature fields produced by traveling distributed heat sources. *Weld. J*, 62(12), pp. 346-355.
- [12]. **Fan, Z., Lu, M., and Huang, H.**, 2018. Selective laser melting of alumina: A single track study. *Ceramics International*, 44(8), pp. 9484-9493.
- [13]. **Hu, Z., Nagarajan, B., Song, X., Huang, R., Zhai, W., and Wei, J.**, 2019. Formation of SS316L single tracks in micro selective laser melting: surface, geometry, and defects. *Advances in Materials Science and Engineering*, 2019.
- [14]. **Kaserer, L., Bergmueller, S., Braun, J., and Leichtfried, G.**, 2020. Vacuum laser powder bed fusion—track consolidation, powder denudation, and future potential. *The International Journal of Advanced Manufacturing Technology*, 110, pp. 3339-3346.
- [15]. **King, W.E., Barth, H.D., Castillo, V.M., Gallegos, G.F., Gibbs, J.W., Hahn, D.E., Kamath, C., and Rubenchik, A.M.**, 2014. Observation of keyhole-mode laser melting in laser powder-bed fusion additive manufacturing. *Journal of Materials Processing Technology*, 214(12), pp. 2915-2925.
- [16]. **Kruth, J., Thijs L., Verrhaeghe F., Craeghs JT., Van Humbeeck, J.**, 2010. A study of the microstructural evolution during selective laser melting of Ti6Al4V, *Acta Meaterialia*, vol. 58, no. 9, pp. 3303-3312.
- [17]. **Liu, Y., Yang, Y., Mai, S., Wang, D., and Song, C.**, 2015. Investigation into spatter behaviour during selective laser melting of AISI 316L stainless steel powder. *Materials & Design*, 87, pp. 797-806.
- [18]. **Ramosena, L.A., Parker, B.S., Dzogbewu, T.C., du Preez, W.B., Blaine, D.C.**, 2019. Optimum process parameters for DMLS in-situ alloying of a Ti10(60Al40V) powder blend, Proceedings of the 20th International Conference of the Rapid Product Development Association of South Africa, Bloemfontein.
- [19]. **Shi, X., Ma, S., Liu, C., and Wu, Q.**, 2017. Parameter optimization for Ti-47Al-2Cr-2Nb in selective laser melting based on geometric characteristics of single scan tracks. *Optics & Laser Technology*, 90, pp. 71-79.

- [20]. **Shrestha, S., Starr, T., and Chou, K.**, 2019. A study of keyhole porosity in selective laser melting: single-track scanning with micro-CT analysis. *Journal of Manufacturing Science and Engineering*, 141(7).
- [21]. **Siao, Y.H., and Wen, C.D.**, 2021. Examination of molten pool with Marangoni flow and evaporation effect by simulation and experiment in selective laser melting. *International Communications in Heat and Mass Transfer*, 125, p.105325.
- [22]. **Stasic, J., and Bozic, D.**, 2016. The effect of NiB additive on surface morphology and microstructure of 316L stainless steel single tracks and layers obtained by SLM. *Surface and Coatings Technology*, 307, pp. 407-417.
- [23]. **Vilardell, A.M., Takezawa, A., du Plessis, A., Takata, N., Krakhmalev, P., Kobashi, M., Albu, M., Kothleitner, G., Yadroitsava, I., and Yadroitsev, I.**, 2021. Mechanical behaviour of in-situ alloyed Ti6Al4V (ELI)-3 at. % Cu lattice structures manufactured by laser powder bed fusion and designed for implant applications. *Journal of the Mechanical Behaviour of Biomedical Materials*, 113, p.104130.
- [24]. **Xia, M., Gu, D., Yu, G., Dai, D., Chen, H., and Shi, Q.**, 2017. Porosity evolution and its thermodynamic mechanism of randomly packed powder-bed during selective laser melting of Inconel 718 alloy. *International Journal of Machine Tools and Manufacture*, 116, pp. 96-106.
- [25]. **Yadroitsava, I., Els, J., Booyesen, G., and Yadroitsev, I.**, 2015. Peculiarities of single-track formation from Ti6AL4V alloy at different laser power densities by selective laser melting. *South African Journal of Industrial Engineering*, 26(3), pp. 86-95.
- [26]. **Yadroitsev, I., Bertrand, P., and Smurov, I.**, 2007. Parametric analysis of the selective laser melting process. *Applied Surface Science*, 253(19), pp. 8064-8069.
- [27]. **Yu, G., Gu, D., Dai, D., Xia, M., Ma, C., and Chang, K.**, 2016. Influence of processing parameters on laser penetration depth and melting/re-melting densification during selective laser melting of aluminum alloy. *Applied Physics*

A, 122, pp. 1-12.

- [28]. Yuan, W., Chen, H., Cheng, T., and Wei, Q., 2020. Effects of laser scanning speeds on different states of the molten pool during selective laser melting: Simulation and experiment. *Materials & Design*, 189, p. 108542.

## CHAPTER 7: TOP SURFACE AND CROSS-SECTIONAL ANALYSIS OF SINGLE LAYERS OF SiC/Ti6Al4V(ELI) COMPOSITES

Some of the material presented in this chapter has been published in peer-reviewed media, as detailed below:

1. **Thamae, M., Maringa, M., and du Preez, W.**, Determining the best hatch distances for selective laser melted SiC/Ti6Al4V (ELI) composites of different volume fractions of SiC. paper submitted for publication in *Results in Materials Journal* on 26<sup>th</sup> of May 2024. <https://www.sciencedirect.com/journal/results-in-materials>

### 7.0. Introduction

This chapter contains details on the analysis of single layers, which was done by investigating the top and cross-sectional views of the layers at each SiC volume fraction from 5 % to 30 %. The characteristics of the top and cross-sectional views of the single layers were studied and discussed to identify the best hatch distances that could be used for printing 3D parts.

#### 7.1. Cross-section and Top Surface Analysis of Single Layers built with a 5% SiC Volume Fraction of an SiC/Ti6Al4V(ELI) Composite

The best single tracks produced with a 5 % SiC volume fraction of SiC/Ti6Al4V(ELI) composites from previous work on single tracks by the authors Thamae et al. (2022) were obtained at values of laser power, laser scanning speed and linear energy density of 200 W, 1.2 m/s, and 167 J/m, respectively, and were used to build the SiC/Ti6Al4V(ELI) single layers reported on here. The line-by-line arrangement of single tracks leads to the formation of complete layers; therefore, there is a need to determine an appropriate hatch distance between the tracks to provide sufficient re-melting and metallurgical bonding of adjacent tracks that would give rise to good mechanical properties (Dzogbewu et al., 2023). The degree of overlap of tracks is evaluated by their overlap rate, which plays a key role in determining the mechanical properties of built parts and is calculated using Equation 1 (Tian et al., 2017). The overlap rate is presented as a percentage and indicates the area where repeated melting by the laser beam occurs and is related to the prevailing hatch distance (Ren et al., 2021; Tian et al., 2017), thus

$$\varphi = 1 - \frac{h}{W} \quad (7.1)$$

where the variables  $\varphi$ ,  $h$ , and  $W$  represent the overlap rate, hatch distance, and average track width, respectively. To study the effect of different overlap rates, an average track width of 184  $\mu\text{m}$ , determined from the best single track produced at 5% SiC volume fraction (Thamae et al., 2022), was used to calculate theoretical overlap rates of layers for different values of hatch distance between 50  $\mu\text{m}$  and 110  $\mu\text{m}$ , that are shown in Table 7.1.

**Table 7.1: Theoretical, calculated overlap rates at different hatch distances from 50  $\mu\text{m}$  to 110  $\mu\text{m}$ , for a 5% SiC volume fraction of an SiC/Ti6Al4V(ELI) composite, built at a laser power and scanning speed of 200 W and 1.2 m/s, respectively**

Hatch Distance ( $\mu\text{m}$ )	Spot Size ( $\mu\text{m}$ )	Average Track Width ( $\mu\text{m}$ )	Standard Deviation	Overlap Rate (%)
50	80	184	7.2	73
60	80	184	7.2	67
70	80	184	7.2	62
80	80	184	7.2	57
90	80	184	7.2	51
100	80	184	7.2	46
110	80	184	7.2	40

The data in Table 7.1, showed sufficient overlap rates of 50% and higher at hatch distances ranging from 50  $\mu\text{m}$  to 90  $\mu\text{m}$ , while those with overlap rates less than 50% were obtained at hatch distances of 100  $\mu\text{m}$  and 110  $\mu\text{m}$ . Plotting the data of overlap rate against hatch distance in this table gave rise to the linear curve shown in Figure 7.1 that was consistent with the form of Equation 7.1.

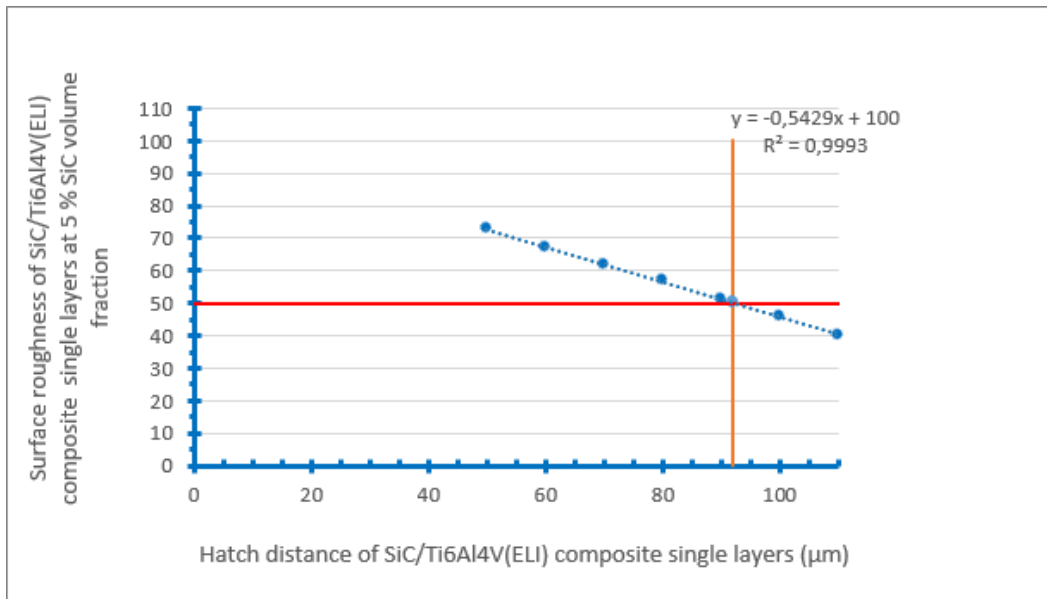


**Figure 7.1:** Graph of theoretical overlap rates versus hatch distances of an SiC/Ti6Al4V(ELI) composite at 5% SiC volume fraction at different hatch distances from 50 µm to 110 µm

The curve in Figure 7.1 demonstrated a linear decreasing trend of overlap rate with increasing hatch distance. The ideal overlap rate of 50% hatch distance that occurred at a hatch distance of 92 µm, as calculated with Equation 1, was represented by a solid horizontal red line in the figure. The points below the solid red line representing hatch distances with overlap rates less than 50% occurred at hatch distances of 100 µm and 110 µm. Those points occurring above the solid red line in the figure represented overlap rates of 50% or higher and occurred at hatch distances of 90 µm to 50 µm. As a result of the foregoing observations, layers built at hatch distances of 100 µm and 110 µm were considered unsuitable for use in the building of 3D parts. Cross-sections of the single layers built with all the values of hatch distance shown in Table 7.1 were cut out and prepared for inspection, with the resulting SEM SE micrographs displayed in Figure 7.2. These images were then utilized to assess the overlap of tracks, evenness of the top surfaces of the built layers, and depths of penetration of the tracks in each layer.

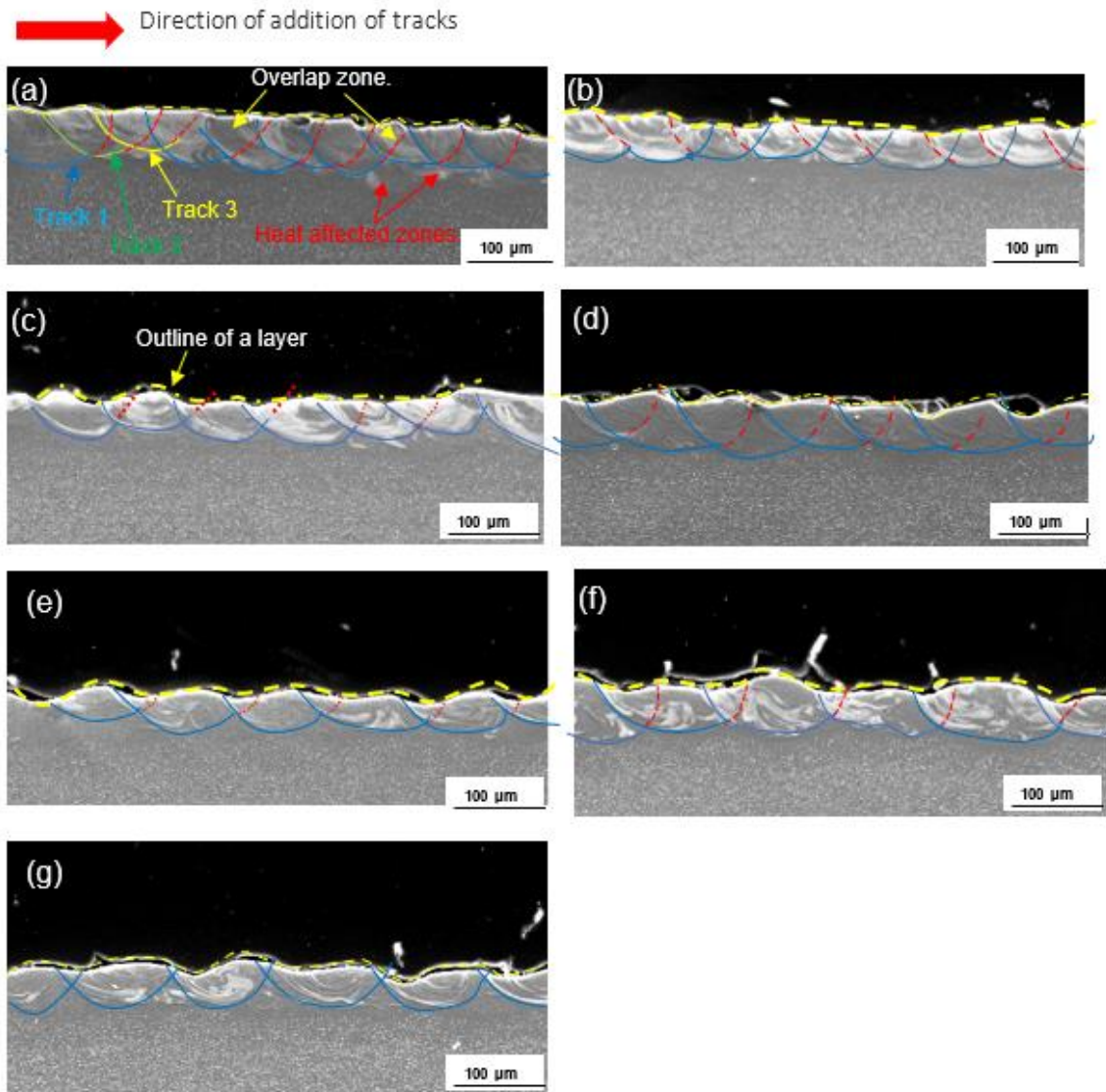


**Figure 7.2:** SEM SE images of the cross-sections of single layers at different hatch distances of (a) 50  $\mu\text{m}$ , (b) 60  $\mu\text{m}$ , (c) 70  $\mu\text{m}$ , (d) 80  $\mu\text{m}$ , (e) 90  $\mu\text{m}$ , (f) 100  $\mu\text{m}$ , and (g) 110  $\mu\text{m}$

Figure 7.2 (a) demonstrates that track 1 is re-melted by track 2 and subsequently re-melted by track 3 near its periphery due to substantial overlap, and the same is true for the following tracks. With increasing hatch distance, the thought of double re-melting is shown to decrease. This concept of single and double track re-melts based on the relationship between hatch distances and track widths is further shown by the schematics presented in Figures 7.3 and 7.4.

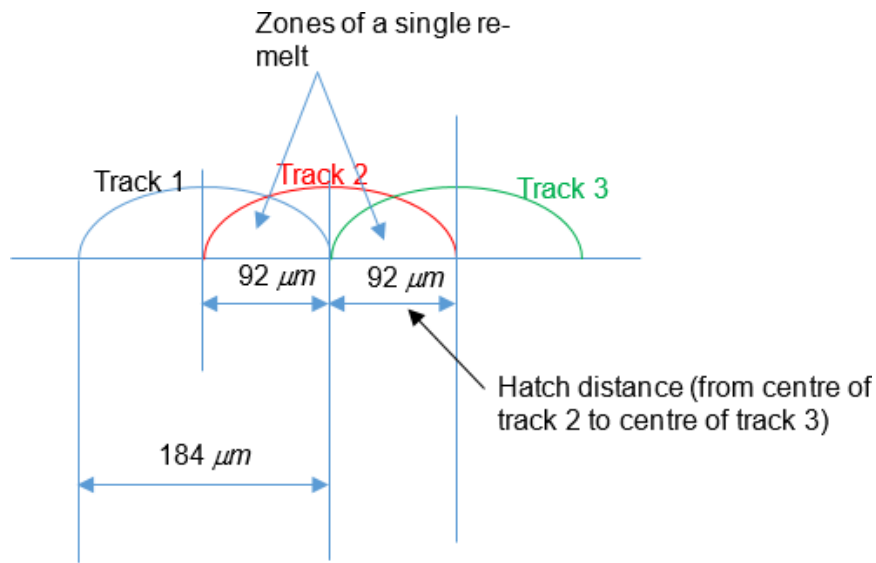


**Figure 7.3:** A schematic view of single re-melting of the tracks in a layer based on the relationship between hatch distances and the widths of track

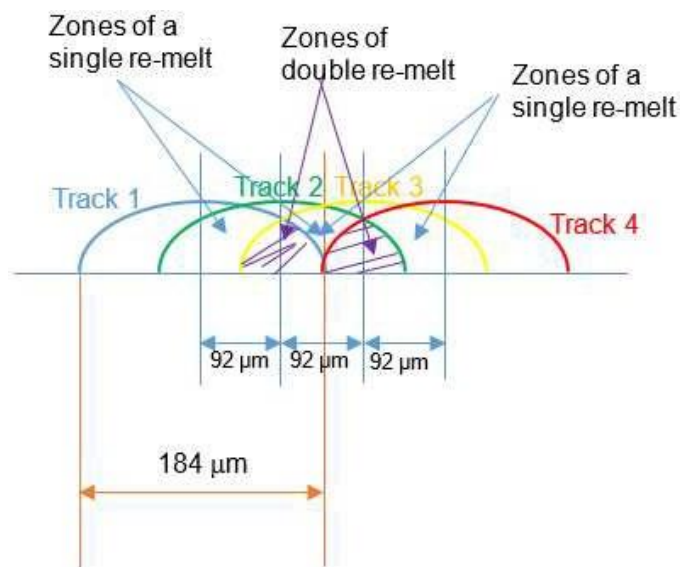


**Figure 7.4:** A schematic view of double re-melting of the tracks in a layer based on the relationship between hatch distances and the widths of track

It is worth noting that the layer built at a hatch distance of 50  $\mu\text{m}$  was more even than the others, with fewer humps or differences in the heights of tracks in it. These findings were consistent with those of AIMangour et al. (2017), who discovered that double re-melting of tracks resulted in more uniform and smooth layers. Vaithilingam et al. (2016) also observed a reduction of surface roughness from 3.4  $\mu\text{m}$  to 2.2  $\mu\text{m}$  after re-melting,

thus indicating that surface re-melting is effective for improving surface quality. The foregoing must be qualified by the observations of Chen et al. (2023), who used numerical simulation to investigate the track-by-track re-melting process and reported that when the number of re-melts was large, over-melting occurred, which is harmful to the surface quality of re-melted surfaces. The key distinction here is the reference to a high number of re-melts in the latter work.

At the hatch distance of 50  $\mu\text{m}$ , thicker HAZ was observed under the overlap zones, which were thought to have been caused by the accumulation of heat at the overlapped regions due to re-melting of neighbouring tracks. It was noticed that as the hatch distances increased, the upper surfaces of the layers became more uneven, and the depths of penetration decreased. An uneven layer is undesirable as it leads to non-uniformity of the next layer to be deposited and thus results in the formation of pores in 3D-built parts (Dzogbewu et al., 2023; Aboulkhair et al., 2016).

It was noted in this figure that an increase of hatch distance from 70  $\mu\text{m}$  to 110  $\mu\text{m}$  led to an increase of unevenness of the top surfaces of the single layers, which increased the surface roughness. However, a satisfactory overlap rate of 50% and above, as calculated in Table 7.1, was only observed at the hatch distances from 50  $\mu\text{m}$  to 90  $\mu\text{m}$ . An overlap rate of 50% has been shown in literature to be sufficient to ensure good bonding between tracks (Yadroitsev et al., 2007; Ramosena et al., 2022). To select the best of these hatch distances, an investigation of the top views of their related single layers was performed. In Figure 7.5 are SEM SE images of the single layers printed at the hatch distances shown in Table 7.1, which were examined to determine their quality concerning continuity and discontinuity of tracks, lack of fusion and finally, surface roughness.

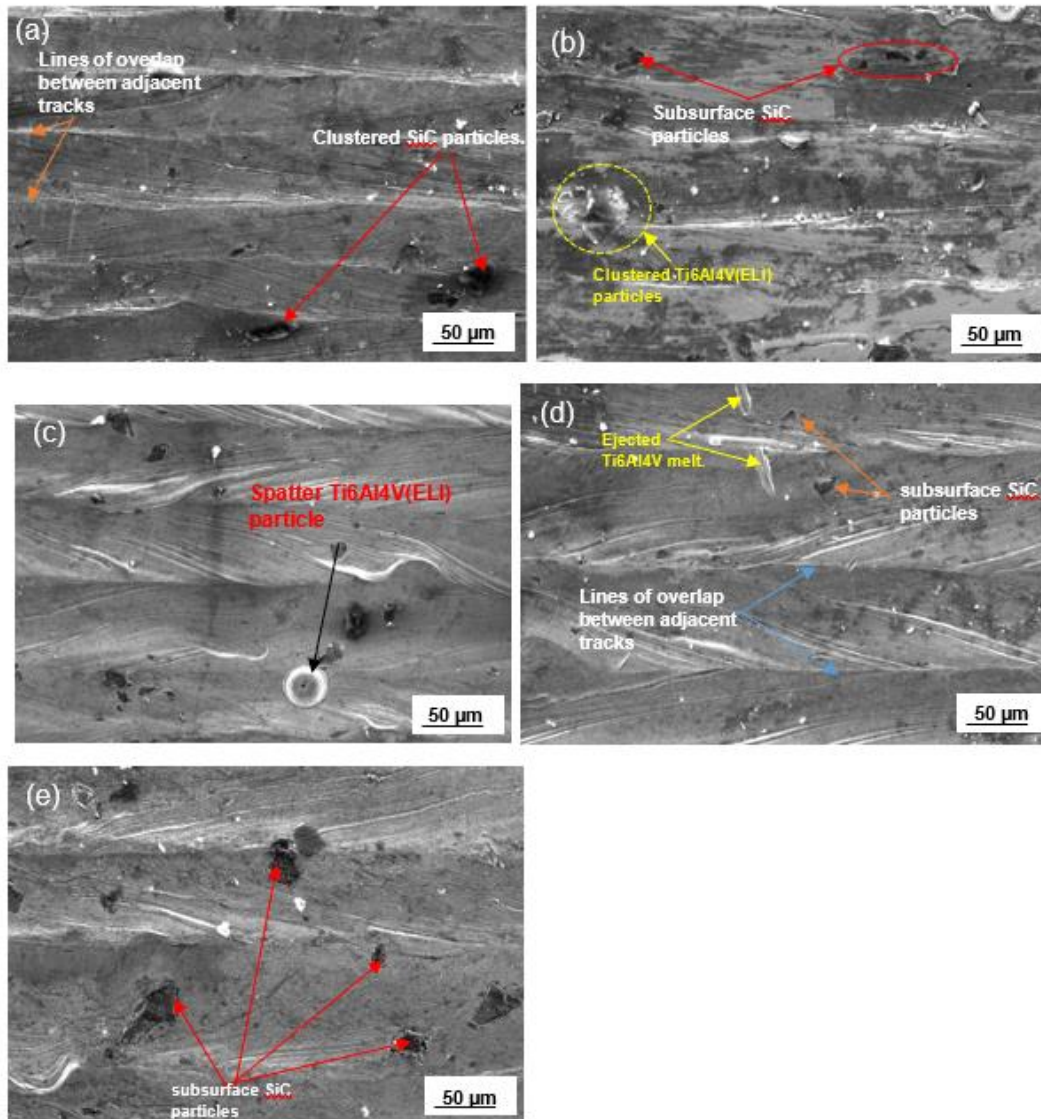


**Figure 7.5:** The SEM SE images of single layers at hatch distances of 50 μm, (b) 60 μm, (c) 70 μm, (d) 80 μm, and (e) 90 μm

The top surfaces of the single layers in Figure 7.5 showed continuous melted tracks that were fused to one another. Also shown in the Figure are surface and subsurface clusters of SiC particles, some of which were pointed out in Figure 7.5 (a and b). The clusters of SiC particles were seen to predominate near the lines of overlap of the tracks, which was attributed to the low density of the SiC particles leading to them being pushed by the Marangoni convective forces to the edges of the melt (Dzogbewu et al., 2021; Spierings et al., 2017). Similar results were reported by Dzogbewu et al. [25] where they mentioned that molybdenum and Ti6Al4V had different thermo-physical properties and molybdenum, which had higher density, was then pulled

towards the peripheries of the tracks due to the higher surface tension of the melt at the periphery and pushed to the edges of the tracks by the Marangoni effect. The presence of clusters of SiC particles would lead to unevenness of the next deposited layer, which is undesirable. The cross-sections from distances of 70  $\mu\text{m}$  to 90  $\mu\text{m}$  showed them to be uneven, which made them unsuitable for building the 3D specimens. However, a 50 % offset rescanning strategy, whereby a laser moves 50 % of the hatch distance before rescanning, has been reported in literature to eliminate the clusters of particles and improve the surface roughness (Dzogbewu et al., 2022).

In summary, the images in Figure 7.5 showed nearly even top surfaces of the single layers built at hatch distances of 50  $\mu\text{m}$  and 60  $\mu\text{m}$  and track overlap rates of 73 % and 67 %, respectively. Although their top views revealed the undesirable presence of clusters of SiC particles at their surfaces, these can be decreased or eliminated by employing a 50 % offset scanning strategy while building multiple layers. Additionally, the higher overlap rates for lower hatch distance, shown in Table 7.1, were expected to lead to a higher consumption of powder than for higher hatch distances with their lower overlap rates, and the possibility of excess fusion of layers and formation of keyholes in overlapped regions. This made building of layers at a hatch distance of 50  $\mu\text{m}$  less attractive than at 60  $\mu\text{m}$ . It was concluded that the best layer at a 5 % SiC volume fraction in an SiC/Ti6Al4V(ELI) composite was the one built with a hatch distance of 60  $\mu\text{m}$ . This layer had an even top surface that would lead to densification of parts and had an overlap rate of 67 % that would provide sufficient bonding of adjacent tracks.

## **7.2. Cross-section and Top Surface Analysis of Single Layers built with a 10 % SiC Volume Fraction of an SiC/Ti6Al4V(ELI) Composite**

Theoretical values of overlap rate for layers built for a 10 % SiC volume fraction of an SiC/Ti6Al4V(ELI) composite, were calculated using Equation 1, with the results presented in Table 7.2.

**Table 7.2:** Theoretical, calculated values of overlap rates at different hatch distances from 50  $\mu\text{m}$  to 110  $\mu\text{m}$  for a 10 % SiC volume fraction of an SiC/Ti6Al4V(ELI) composite built at a laser power and scanning speed of 150 W, 0.8 m/s, respectively

Hatch Distance ( $\mu\text{m}$ )	Spot Size ( $\mu\text{m}$ )	Average Track Width ( $\mu\text{m}$ )	Standard Deviation	Overlap Rate (%)
50	80	170	20	71
60	80	170	20	65
70	80	170	20	59
80	80	170	20	53
90	80	170	20	47
100	80	170	20	41
110	80	170	20	35

The data in Table 7.2 demonstrated that as the hatch distance increased, the overlap rate decreased for the same average width of tracks. Overlap rates less than 50 % at hatch distances of 90  $\mu\text{m}$  to 110  $\mu\text{m}$  are considered undesirable, and those that are greater than 50 % overlap rate at hatch distances of 50  $\mu\text{m}$  to 80  $\mu\text{m}$ , are assumed to allow adequate re-melting. The calculated overlap rates from Table 7.2 were plotted on the graph shown in Figure 7.5 to study the trends of overlap ratio with increasing hatch distance.

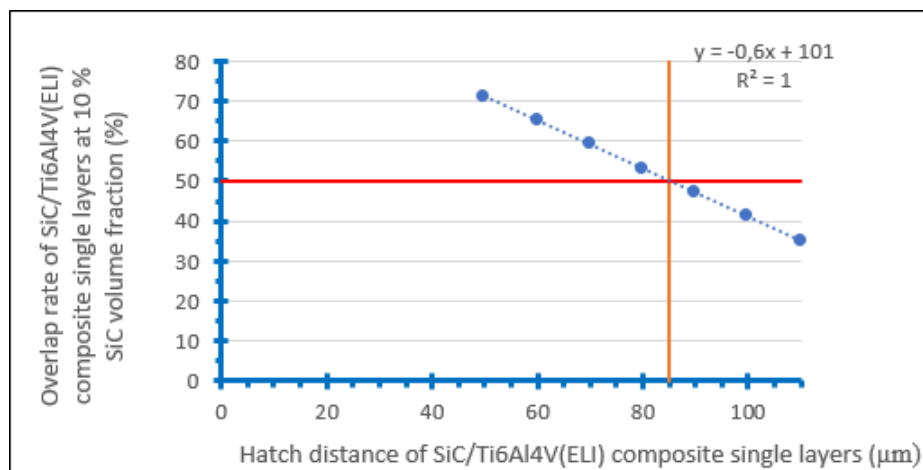


**Figure 7.6:** Graph of theoretical overlap rate versus hatch distance, at 10% SiC volume fraction in an SiC/Ti6Al4V(ELI) composite at different hatch distances from 50  $\mu\text{m}$  to 110  $\mu\text{m}$

The graph in Figure 7.6 showed a linear decrease in overlap rate with increasing hatch distance. The points below the horizontal red line of 50 % ideal overlap rate in Figure 7.6, for hatch distances from 90  $\mu\text{m}$  to 110  $\mu\text{m}$  were considered undesirable due to

their low overlap rates below 50 %. Lo et al. (2019) reported that small overlap rates lead to non-melted areas between tracks which lowers the density and yield stress of the final built parts. The overlap rates above the red line occurred in layers built at the hatch distances from 80  $\mu\text{m}$  to 50  $\mu\text{m}$ . The SEM SE images of the cross-sections of multiple tracks of a 10 % SiC volume fraction of an SiC/Ti6Al4V(ELI) composite built at a constant laser power, scanning speed, and LED of 150 W, 0.9 m/s, and 188 J/m, respectively, were shown in Figure 7.7.

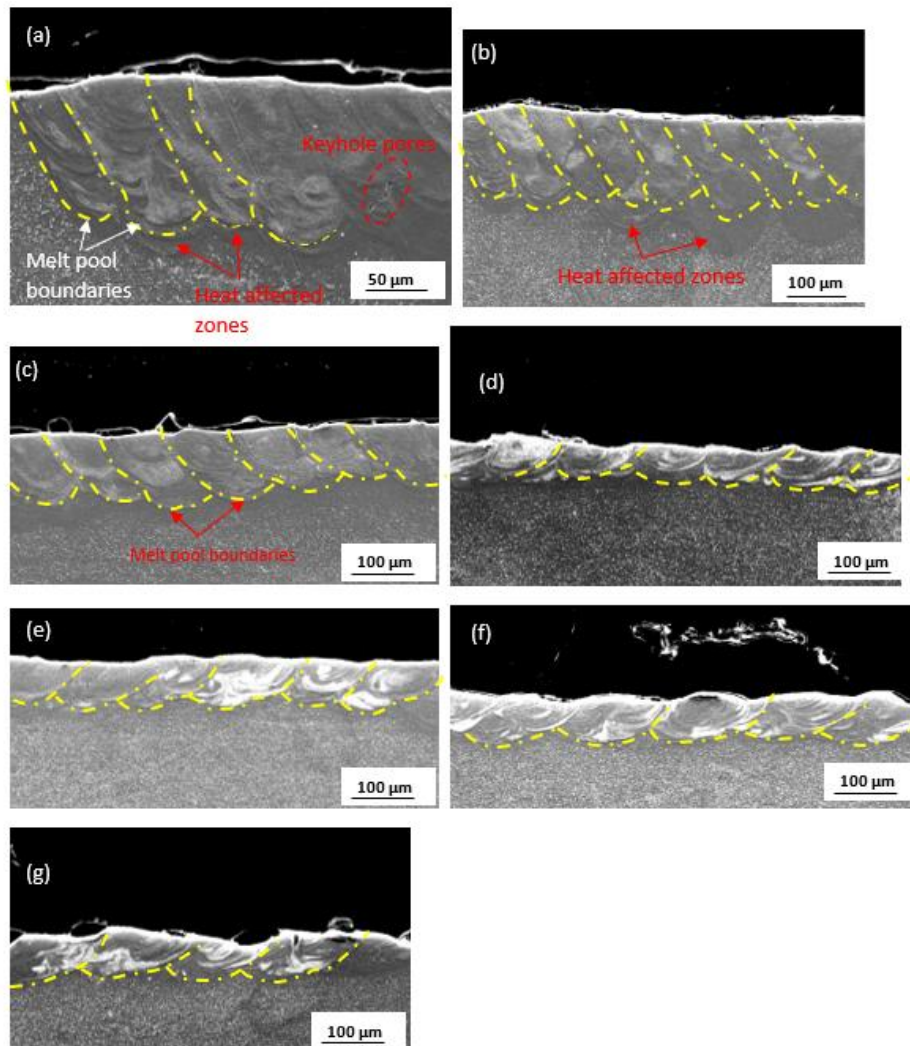


**Figure 7.7:** SEM SE images of cross-sections of single layers at different hatch distances of (a) 50  $\mu\text{m}$ , (b) 60  $\mu\text{m}$ , (c) 70  $\mu\text{m}$ , (d) 80  $\mu\text{m}$ , (e) 90  $\mu\text{m}$ , (f) 100  $\mu\text{m}$ , and (g) 110  $\mu\text{m}$

Keyhole pores were visible in Figure 7.7 (a) for the track built at the hatch distance of 50  $\mu\text{m}$ , due to the significant energy input caused by repeated re-melting because of

multiple overlaps arising from the small hatch distances. Similar results were reported by Su et al. (2012) that too small hatch distances imply too much energy input which may cause a deterioration of the surface quality of layers and lead to a decrease in the relative density of parts. Keyhole pore formation during the SLM process was affected by the volumetric energy density input and the keyhole pores present within the SLM parts would degrade the part performance (Lo et al., 2019). Volumetric energy density (VED), which is a measure of the quantity of energy delivered per unit volume of powder deposited in the powder bed (Ciurana et al., 2013), is defined as the ratio of power over the product of laser scanning speed, hatch distance, and layer thickness, as shown in Equation 7.2.

$$VED = \frac{P}{Vht} \quad (7.2)$$

where the symbols  $h$  and  $t$  represent the hatch distance and layer thickness respectively. It was noted in Figure 7.7 (a and b) that the melt pool boundaries were closer to each other at the smaller hatch distances of 50  $\mu\text{m}$  and 60  $\mu\text{m}$ . This was expected to lead to a higher consumption of powder during the building of the 3D parts and an increase in manufacturing time, which is undesirable as it increases the costs of parts (Su et al., 2012; Yadroitsev et al., 2007). This finding was similar to the one reported by Buhairi et al. (2023) that small hatch distances lead to increased fabrication time during manufacturing of parts. Lo et al. (2019) reported that excessive overlap rate increases local energy input into the powder bed and may prompt evaporation of the molten metal, resulting in the formation of pores within the melt pool. The SEM SEI images shown in Figure 7.7 (a and b) that were built at hatch distances of 50  $\mu\text{m}$  and 60  $\mu\text{m}$ , depicted HAZ, which was thought to have arisen due to increased VED in the overlapped regions. The depth of penetration was seen in Figure 7.7 (a to c) to decrease with increasing hatch distance. This finding was consistent with that of Dong et al. (2018), who observed that small overlap rates led to shallow depths of penetration, which reduced with increasing hatch distances. They further noted that a shallow depth of penetration caused poor metallurgical bonding between subsequent layers, resulting in delamination. The unevenness of the top surface of the layers increased with rising hatch distance in Figure 7.7 (d to g). It is known that uneven thickness of layers leads to unstable melting and is linked to the creation of defects such as interlayer porosity in the layer-building process, which affects the mechanical

qualities of built 3D parts (Zhao et al., 2022; Shi et al., 2016). Consequently, the layers formed with hatch distances between 90  $\mu\text{m}$  and 110  $\mu\text{m}$  were not expected to provide sufficient bonding between them and could contain interlayer pores. These two values of hatch distance were thus not recommended for building 3D parts and were not considered for further investigation of the top surfaces of layers.

However, the layers built at hatch distances of 50  $\mu\text{m}$ , 60  $\mu\text{m}$ , 70  $\mu\text{m}$ , and 80  $\mu\text{m}$  all had overlap rates above 50 %, as shown in Table 7.2. But taking into consideration the high consumption of powder at high overlap rates and formation of the keyhole pores in zones of high overlap, the layers formed at hatch distances of 50  $\mu\text{m}$  and 60  $\mu\text{m}$  in Table 7.2, which have overlap values of 71 % and 65 %, were not the best amongst the lot for building the 3D parts. Therefore, further investigation of the top surface of the built layers was carried out only for hatch distances of 70  $\mu\text{m}$  and 80  $\mu\text{m}$ , based on studies of the SEM SE images shown in Figure 7.7.

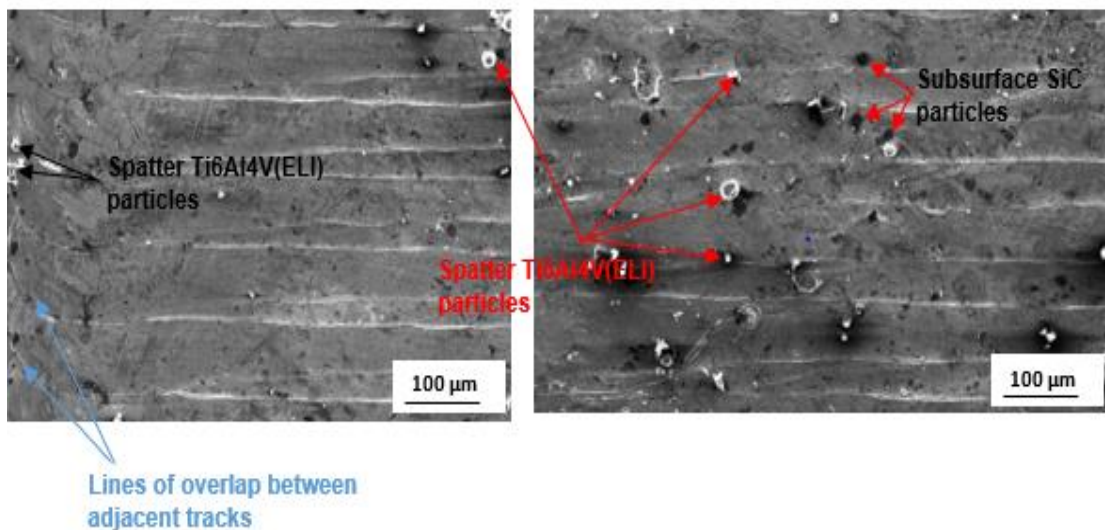


**Figure 7.8:** SEM SE images of the top surfaces of single layers built at hatch distances of 70  $\mu\text{m}$  (left), and 80  $\mu\text{m}$  (right)

The layer built at a hatch distance of 70  $\mu\text{m}$  illustrated continuous tracks of solidified melt with a smooth top surface and little spatter of Ti6Al4V(ELI) particles. Such a relatively smooth layer is desirable and is expected to lead to a fairly uniform deposition of the next layer of powder during building of 3D parts, which minimizes porosity (Shi et al., 2016). Continuous tracks were desirable in line with the observation by Yueling

et al. (2018) that obtaining continuous single tracks that are well bonded to the tracks in previous layers is a requirement to produce parts with high densities. As the hatch distance was increased to 80  $\mu\text{m}$ , the number of spatter particles increased, as well as the cluster of Ti6Al4V(ELI) particles. These clusters and spatter particles contribute to increased surface roughness of the layers (Shi et al., 2016). Therefore, of the two hatch distances, the best layer at 10 % SiC volume fraction was achieved at a hatch distance of 70  $\mu\text{m}$ , with a smooth surface and overlap rate of 59 %.

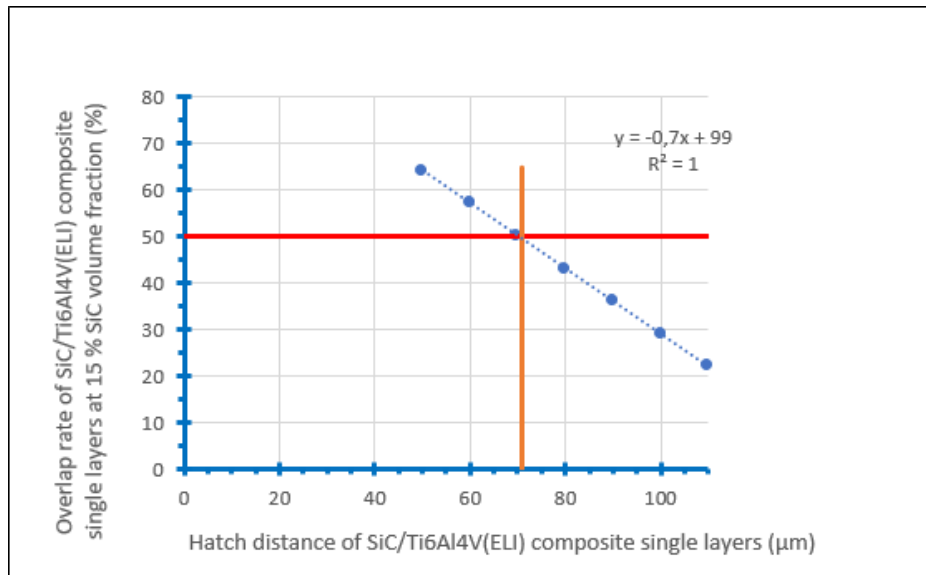
### 7.3. Cross-section and Top Surface Analysis of Single Layers built with a 15 % SiC Volume Fraction of an SiC/Ti6Al4V(ELI) Composite

Table 7.3 shows theoretical values of the overlap rate calculated with the average track width of 141  $\mu\text{m}$ , obtained from previous work by the authors Thamae et al. (2022) on single tracks with the best process parameters at 15 % SiC volume fraction.

**Table 7.3: Theoretical, calculated values of overlap rates at different hatch distances from 50  $\mu\text{m}$  to 110  $\mu\text{m}$  for a 15 % SiC volume fraction of an SiC/Ti6Al4V(ELI) composite built at a laser power and scanning speed of 100 W, 0.4 m/s, respectively**

Hatch Distance ( $\mu\text{m}$ )	Spot Size ( $\mu\text{m}$ )	Average Width ( $\mu\text{m}$ )	Track	Standard Deviation	Overlap Rate (%)
50	80	141		14	64
60	80	141		14	57
70	80	141		14	50
80	80	141		14	43
90	80	141		14	36
100	80	141		14	29
110	80	141		14	22

The data shown in Table 7.3 was used to plot a graph to study any existing trends of overlap rate with increasing hatch distance, with the results shown in Figure 7.8.



**Figure 7.9:** *Graph of theoretical overlap rates versus hatch distances of an SiC/Ti6Al4V(ELI) composite at 15% SiC volume fraction at different hatch distances from 50 µm to 110 µm*

As is evident in Figure 7.9, the 50 % overlap rate represented by a red solid horizontal line was observed at a hatch distance of 71 µm. The overlap rates that were below the solid horizontal red line occurred at hatch distances of 80 µm, 90 µm, 100 µm, and 110 µm. These overlap rates were all below the 50 % ideal overlap rate and were shown on Table 3 to all fall in the range 43 % to 22 %. These low overlap rates were insufficient for appropriate re-melting and bonding of tracks. Above this solid horizontal red line of 50 %, overlap rates for hatch distances of 70 µm to 50 µm resulted in overlap rates between 50 % to 64 %, in this order. Cross-sectional analyses of single layers built with 15 % SiC volume fraction of an SiC/Ti6Al4V(ELI) composite at a respective constant laser power, scanning speed, and linear energy density of 100 W, 0.4 m/s, and 250 J/m, were presented in Figure 7.9.

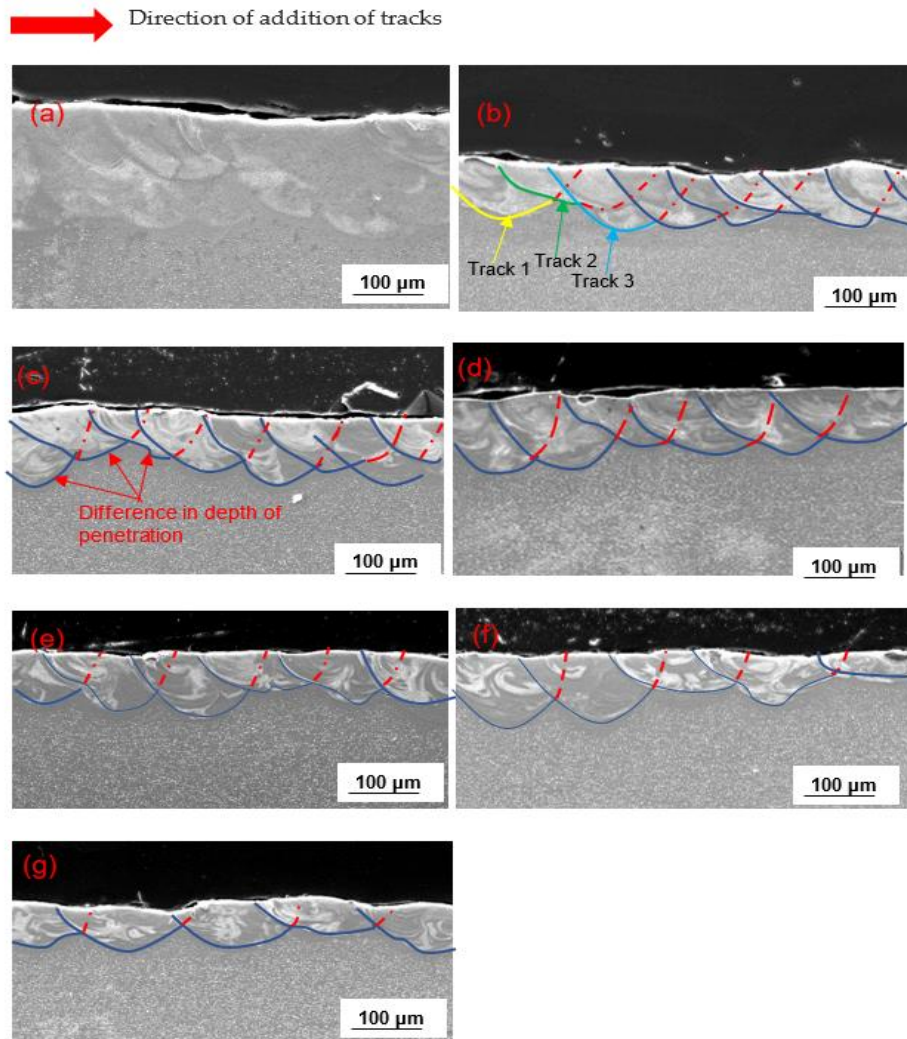


**Figure 7.10: SEM SE images of cross-sections of single layers built at different hatch distances of (a) 50  $\mu\text{m}$ , (b) 60  $\mu\text{m}$ , (c) 70  $\mu\text{m}$ , (d) 80  $\mu\text{m}$ , (e) 90  $\mu\text{m}$ , (f) 100  $\mu\text{m}$ , and (g) 110  $\mu\text{m}$**

Figure 7.10 (a) showed unclear track boundaries because of prevailing large, overlapped regions that led to tracks being very close to each other. Large overlaps lead to higher consumption of powder and longer production times during manufacturing of multiple layers. At the hatch distance of 60  $\mu\text{m}$ , the first built track (track 1) was observed to be re-melted twice by track 2 and track 3 due to this high degree of overlapping. This trend of several re-melting of the tracks decreased with rising hatch distances, as demonstrated in the schematic shown in Figure 7.3. Zhao et al. (2022) reported that multiple melting of the tracks leads to a stronger effect of the accumulation of heat at the overlapped regions, that causes the formation of keyhole

pores. As a result of the foregoing observations, the layers in Figure 7.10 (a and b) that were built at hatch distances of 50  $\mu\text{m}$ , and 60  $\mu\text{m}$ , were expected to lead to poor mechanical properties of built parts.

Furthermore, the first three tracks depicted in Figure 7.10 (b and c) demonstrated a difference in depth of penetration, which could be a result of powder and substrate denudation. Powder denudation is caused by the vaporization of powder where the laser beam is directed, as well as the entrainment of powder particles at the edges of tracks by shear flow of gas from the edges to the centre of the tracks (Liu et al., 2015). The entrainment of powder at the edges of track leaves the substrate with no or a small quantity of powder particles where the tracks to follow are to be created (Liu et al., 2015). As a result of shifting the laser beam by a small hatch distance, it runs over a substrate with no or less powder than the previously melted track resulting in a low depth of penetration of the subsequent track as well as height of subsequent tracks (Vilardell et al., 2021; Pupo et al., 2013, and Aboulkhair et al., 2016). As was observed by Vilardelli et al. (2021), this was a result of the solidified track and substrate having lower laser absorptivity than loose powder. Hence, substrate denudation influences the height, width, and depth of penetration of the next created track in this scenario. Denudation was noted in literature to have a negative effect on the quality of the surfaces of layers due to its effect on their heights (Yadroitsev et al., 2007). However, it was observed in the reference that this could be minimized by employing an appropriate rescanning method while constructing 3D parts.

The layers built at the larger hatch distances of 80  $\mu\text{m}$  to 110  $\mu\text{m}$  that had overlapping rates less than 50 %, as is evident in Table 7.3, were not considered suitable for building layers, as they were expected to lead to insufficient bonding of the layers (Yadroitsev et al., 2013). The layer shown in Figure 7.10 (c) depicted the lowest variation in the height of tracks amongst the images shown in Figure 7.9, and was, therefore, best for building another layer on top of it.

To reach a conclusion on the best layer in this series, an investigation of the top surfaces of SEM SE images was then undertaken to help identify the best hatch distance from values in the range 50  $\mu\text{m}$  to 70  $\mu\text{m}$ , that produced overlap rates of 50 % and above. The top views of the cross-sections discussed in Figure 7.10 are presented in Figure 7.11.

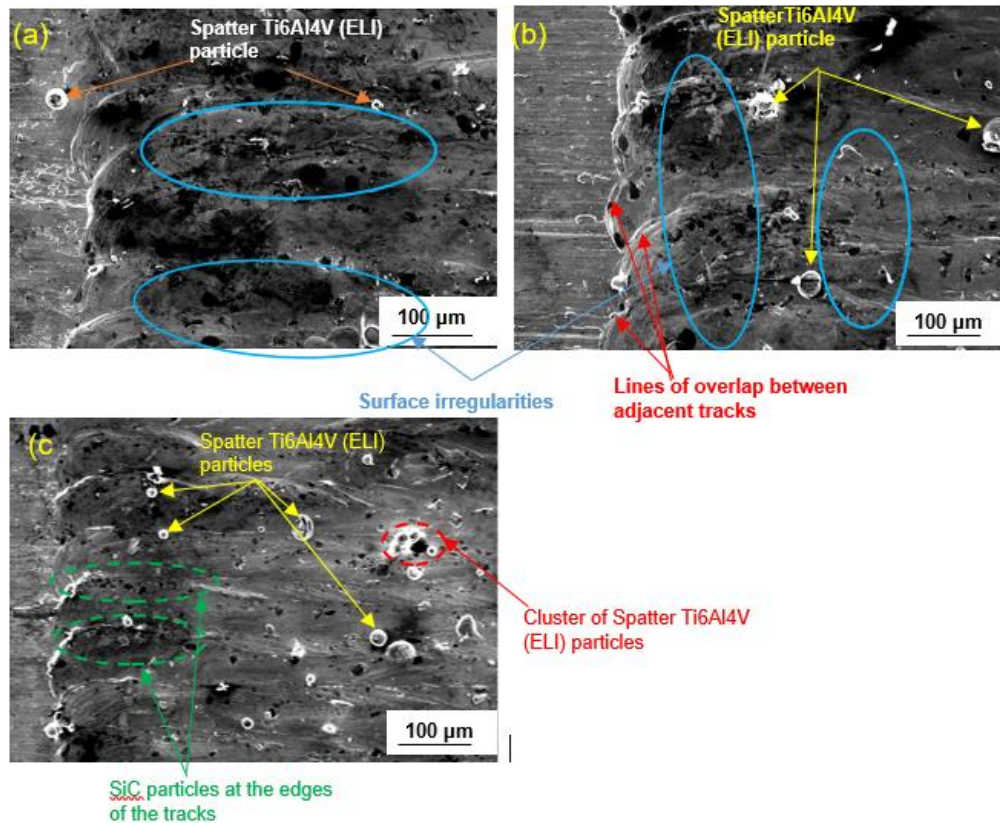


**Figure 7.11: SEM SE images of the top view of single layers built at hatch distances of (a) 50 μm, (b) 60 μm, and (c) 70 μm**

Figure 7.11(a) depicts few spatter Ti6Al4V(ELI) particles that increased progressively in number, as the hatch distance was increased to 70 μm. It was proposed that the high overlap rates induced by small hatch distance here allowed the previously built tracks to receive more energy, hence increasing the temperature in the overlap area and thus re-melting the spatter particles previously existing at the edges of the previously built tracks (Dzogbewu et al., 2021; Lo et al., 2019; Shi et al., 2016). Spatter particles have been observed to have a deleterious impact on the surface quality of produced parts and are, therefore, undesirable (Dzogbewu et al., 2021; Yadroitsev et al., 2016). However, they can be minimized by employing rescanning when producing 3D specimens, which improves the surface roughness of the built parts (Zhao et al., 2022; Yadroitsev et al., 2016).

Figure 7.11 (a and b) were visually seen to contain more uneven surfaces and unmelted SiC particles (circled in blue) than Figure 7.11 (c), which was not altogether surprising given their lower overlap rates. The layer shown in Figure 7.11(c) was,

therefore, the best of the three. This, in addition to the observation made earlier with reference to the SEM SE images shown in Figure 7.11, that the variation in track height was least for the layer built at this same hatch distance (70  $\mu\text{m}$ ), identified it as the best hatch distance amongst the lot, that would provide the most efficient metallurgical bonding between layers and thus increase the relative density of 3D built parts.

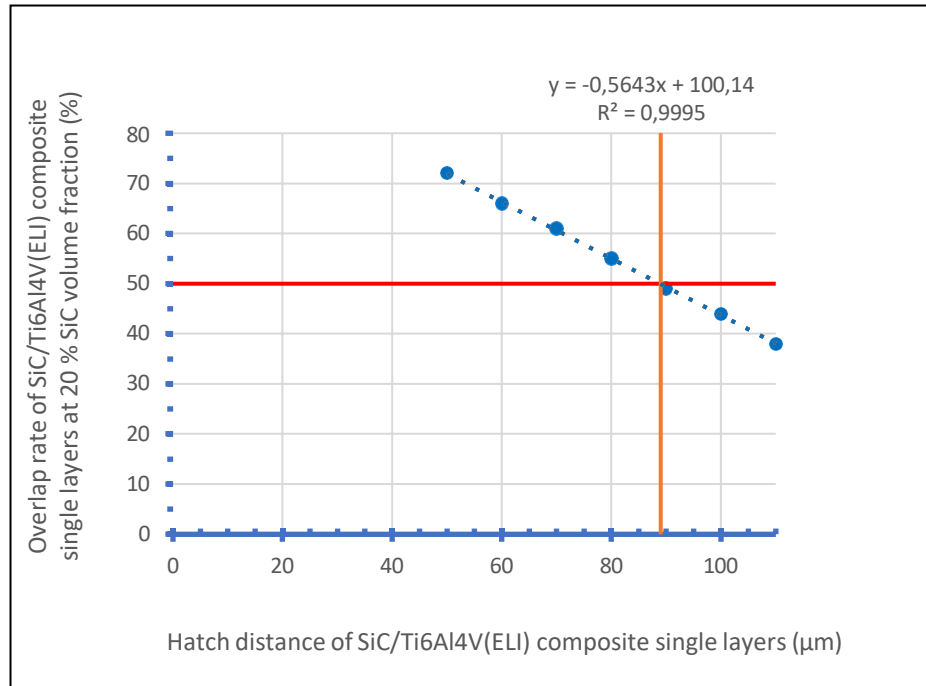
#### 7.4. Cross-section and Top Surface Analysis of Single Layers built with a 20 % SiC Volume Fraction of an SiC/Ti6Al4V(ELI) Composite

Table 7.4 shows theoretical values of overlap calculated with an average width of the track of 178  $\mu\text{m}$ , produced with the best process parameters of 200 W, 0.9 m/s, and 222 J/m, determined in previous work with different hatch distances from 50  $\mu\text{m}$  to 110  $\mu\text{m}$  (Thamae et al., 2022).

**Table 7.4: Theoretical, calculated values of overlap rates at different hatch distances from 50  $\mu\text{m}$  to 110  $\mu\text{m}$  for a 20% SiC volume fraction of an SiC/Ti6Al4V(ELI) composite built at a laser power and scanning speed of 200 W, 0.9 m/s, respectively**

Hatch Distance ( $\mu\text{m}$ )	Spot Size ( $\mu\text{m}$ )	Average Track Width ( $\mu\text{m}$ )	Standard Deviation	Overlap Rate (%)
50	80	178	11	72
60	80	178	11	66
70	80	178	11	61
80	80	178	11	55
90	80	178	11	49
100	80	178	11	44
110	80	178	11	38

The data shown in Table 7.4 was used to plot a graph of overlap rate against hatch distance to investigate the presence of any trends, with the results shown in Figure 7.12.



**Figure 7.12:** Graph of theoretical overlap rates versus hatch distances at 20% SiC volume fraction in an SiC/Ti6Al4V(ELI) composite at different hatch distances from 50 μm to 110 μm

Lo et al. (2019) investigated the effect of hatch distance on the defect mechanism of selective laser melted layers and reported that a 50 % overlap rate, led to an adequate re-melting of adjacent tracks. Above the solid horizontal red line in Figure 7.12, were the points of overlap rate that were higher than 50 %. The graph shows that when the hatch distance dropped from 80 μm to 50 μm, the overlap rates, which were all above the solid horizontal red line, rose linearly from 55 % to 72 %. The overlaps obtained at hatch distances of 90 μm, 100 μm, and 110 μm were below the optimal overlap rate and decreased linearly from 49 % to 38 %. Clearly, as was demonstrated in the preceding sections, the degree of overlap depended on the hatch distance; so, when building parts, the hatch distance would have to be selected appropriately. To help choose the optimum layer in this series of layers, the surface quality of the layers was further examined making use of SEM SE images of their top surfaces and cross-sections.

Figure 7.13 depicts cross-sections of single layers built at different hatch distances and with constant parameter settings of laser power, laser scanning speed, and energy density of 200 W, 0.9 m/s, and 222 J/m, respectively.

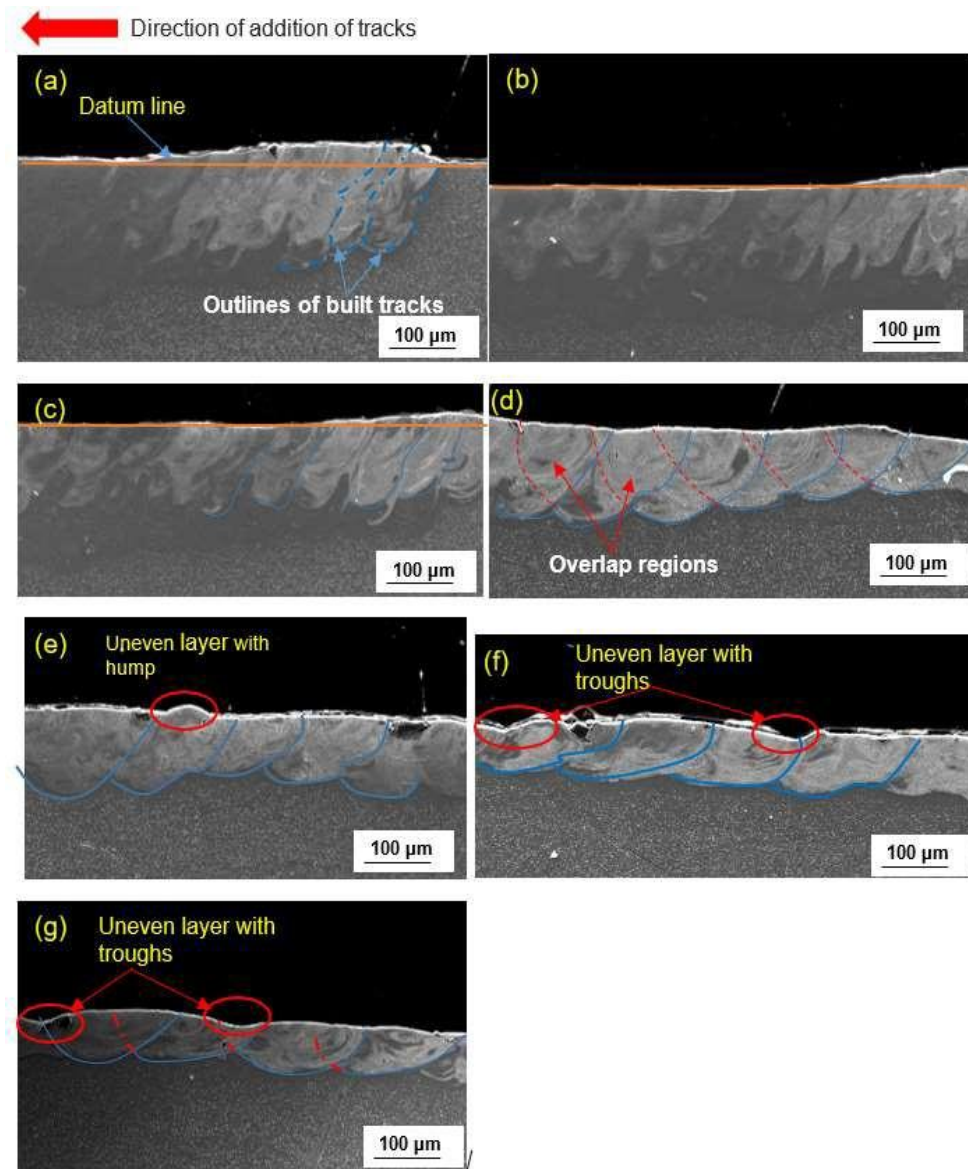


**Figure 7.13:** SEM SE images of cross-sections of single layers produced at constant laser power, scanning speed, and energy density of 200 W, 0.9 m/s, and 222 J/m, respectively, with different hatch distances of (a) 50 μm, (b) 60 μm, (c) 70 μm, (d) 80 μm, (e) 90 μm, (f) 100 μm, and (g) 110 μm

The orange line in Figure 7.13 (a) showed that when the substrate was utilized as a datum line, the layer thickness or height of tracks decreased from right to left. The first few tracks were higher above the substrate than the remaining tracks because of the denudation effect. Similar findings of the denudation effect during the building of single layers were reported by Pupo et al. (2013) and Aboulkhair et al. (2016). They found that substrate denudation made the initial track higher than the second track and so on and lessened the consolidation of powder.

Vilardelli et al. (2021) also showed that the solidified track and substrate had lower laser absorptivity than loose powder, therefore, powder and substrate denudation influenced the width of the next built track and depth of penetration in this instance. This meant that the first laser scan melted more material than subsequent scans (Yuan et al., 2020). The effect of denudation could result in internal porous structures and affect the mechanical properties of the built specimens (Yadroitsev et al., 2013). The layers in Figure 7.13 (b to g) did not display the top surface of the substrate, making it impossible to draw a datum line from the top surface of the substrate, as was done in Figure 7.13 (a), which made measuring the depth of penetration of the layers problematic. Therefore, the orange line in Figure 7.13 (b and c) was only used to highlight the difference in the heights of tracks. While Figure 7.13 (b to d) showed sections of the upper surface of the built layers that were relatively even, Figure 7.13 (e to g) showed uneven layers with humps and troughs that are circled in red. This denotes increasing surface roughness of the layers with increasing hatch distance, as shown in Figure 7.12, which has been noted previously in this paper as undesirable.

In this figure, the depth of penetration was observed visually to decrease with increasing hatch distance. This could be explained by Equation 7.2, from which it was surmised that when the laser power, scanning speed, and layer thickness were kept constant, the absorbed energy per unit volume increased as the hatch distance decreased (Pal et al., 2018). As a result, a smaller hatch distance implied a higher input of laser energy per unit area, which resulted in a larger depth of penetration. A shallow depth of penetration resulted in insufficient bonding between layers, which caused delamination of layers during building of 3D specimens (Aboulkhair et al., 2016 and Singla et al., 2009). The two outcomes discussed here, of lower surface roughness and greater depth of tracks for lower hatch distances, made them preferable to higher hatch distances.

An assessment of the top surface of single tracks built with hatch distances ranging from 50  $\mu\text{m}$  to 80  $\mu\text{m}$ , all with overlap rates of 50 % or greater, was next carried out to assist in determining the best hatch distance to be used for the building of parts at this volume fraction of SiC. Figure 7.14 shows SEM SE images of single layers built at hatch distances from 50  $\mu\text{m}$  to 80  $\mu\text{m}$ .

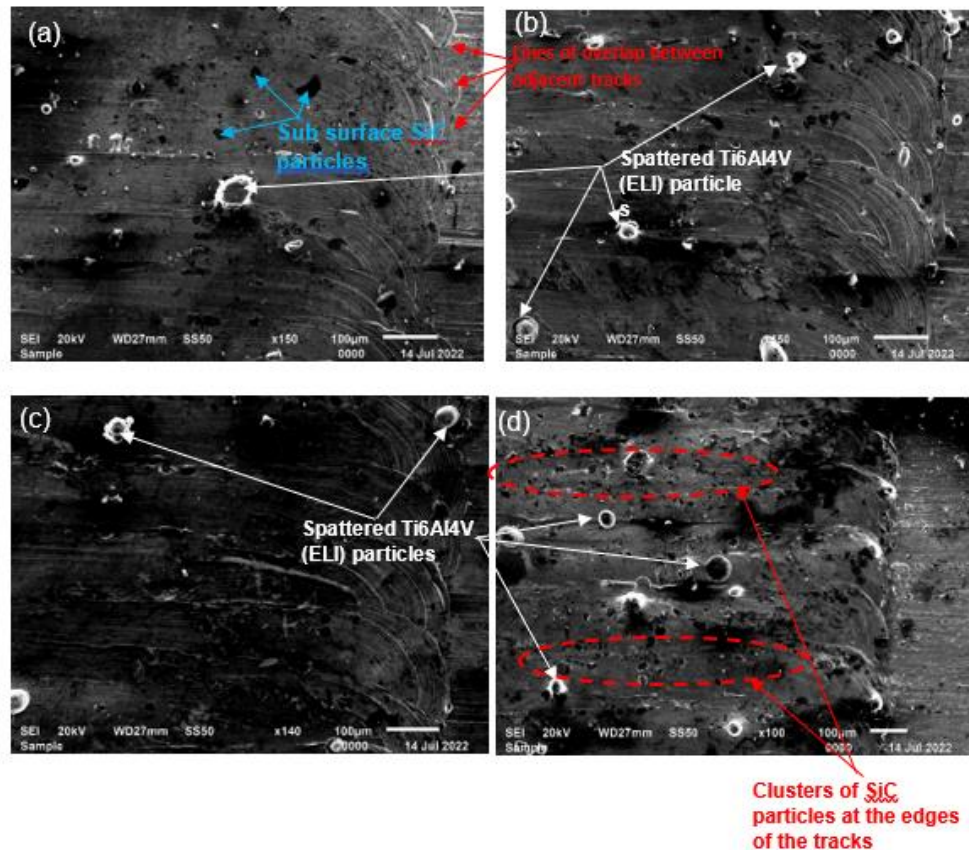


**Figure 7.14:** SEM SE micrographs of the top surfaces of single layers built at hatch distances of (a) 50  $\mu\text{m}$ , (b) 60  $\mu\text{m}$ , (c) 70  $\mu\text{m}$ , and (d) 80  $\mu\text{m}$

It was noted that at the lowest hatch distance of 50  $\mu\text{m}$ , the surface of the built layer was very fine with few spatter Ti6Al4V(ELI) particles. This was thought to have been due to a higher degree of overlapping that increased the possibility of re-melting the partially melted particles on the peripheries of previous tracks and spatter Ti6Al4V(ELI) particles on the surfaces of the built tracks, as was observed in references (Dzogbewu et al., 2021 and Vaithilingam et al., 2016). Dzogbewu et al. (2021), in the study of the in-situ alloyed Ti6Al4V fused layers, reported similar results that a higher degree of overlapping reduced the presence of spatter particles at low hatch distance of 80  $\mu\text{m}$  than at 90  $\mu\text{m}$  and 100  $\mu\text{m}$  that were used for the study. At a hatch distance of 70  $\mu\text{m}$ , there were a few spatter particles on the surface of the layer and less than number of spatter particles evident on the layer built at a hatch distance of 80  $\mu\text{m}$ . The layer built at a hatch distance of 80  $\mu\text{m}$  had a rough surface with clusters of SiC particles evident at the peripheries of the tracks. This presence of SiC particles on the edges of built tracks was because of their density (3.2  $\text{g}/\text{cm}^3$ ) that was lower than that of Ti6Al4V

(ELI) melt ( $4.5 \text{ g/cm}^3$ ). This caused them to float on top of the Ti6Al4V (ELI) melt and were then carried towards the edges of the built tracks by the convective flow of the melt, which prevails in SLM. (Dzogbewu et al., 2021).

As explained in previous sections, the close distances of track boundaries due to substantial overlapping of the layers built at hatch distances of  $50 \mu\text{m}$  and  $60 \mu\text{m}$  were expected to lead to an increase in manufacturing time and consumption of powder and mitigated against using low hatch distances. The layer built at a hatch distance of  $80 \mu\text{m}$  was characterised by a higher number of spatter particles and SiC clusters at the peripheries of the tracks, both which were expected to degrade the mechanical properties of built parts due to increased surface roughness. These observations together with the ones made from a study of the images in Figure 7.13 of higher heights, lower surface roughness and greater depth of tracks for lower hatch distances, led to the selection of the hatch distance of  $70 \mu\text{m}$ , with few spatter particles and a cross-section with no humps or troughs, as the best one to use in building of specimens at 20 % SiC volume fraction.

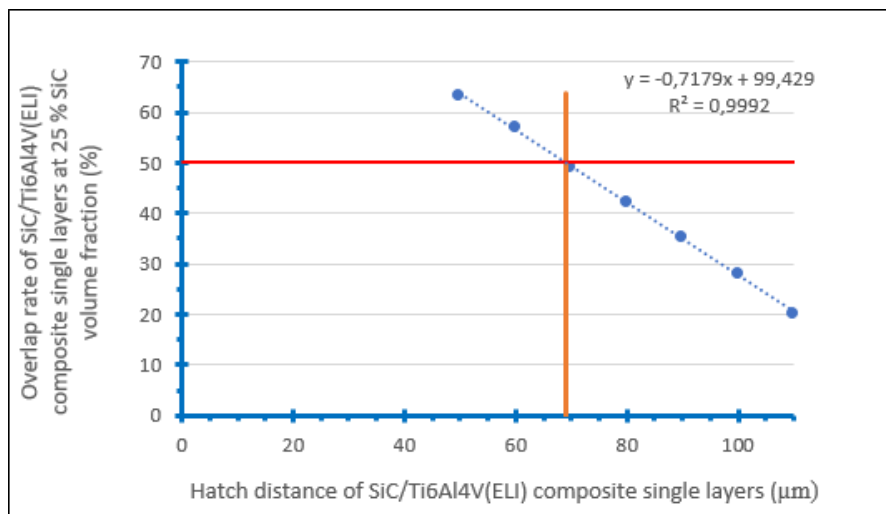
### 7.5. Cross-section and Top Surface Analysis Of Single Layers built with a 25% SiC volume fraction in an SiC/Ti6Al4V(ELI) Composite

Table 7.5 shows theoretical values of overlap calculated with an average width of the track of  $138 \mu\text{m}$  produced with the best process parameters of 200 W, 1.2 m/s, 167 J/m, determined in previous work by the authors Thamae et al. (2022), and with different hatch distances from  $50 \mu\text{m}$  to  $110 \mu\text{m}$ .

**Table 7.5: Theoretical, calculated values of overlap rates at different hatch distances from  $50 \mu\text{m}$  to  $110 \mu\text{m}$  for a 25% SiC volume fraction of an SiC/Ti6Al4V(ELI) composite built at a respective laser power and scanning speed of 200 W, 1.2 m/s**

Hatch Distance ( $\mu\text{m}$ )	Spot Size ( $\mu\text{m}$ )	Average Track Width ( $\mu\text{m}$ )	Standard Deviation	Overlap Rate (%)
50	80	146	9.4	66
60	80	146	9.4	59
70	80	146	9.4	52
80	80	146	9.4	45
90	80	146	9.4	38
100	80	146	9.4	32
110	80	146	9.4	25

It was clear from Table 7.5 that hatch distance between 80  $\mu\text{m}$  to 110  $\mu\text{m}$ , resulted in values of overlap that were less than the ideal overlap value of 50 %. It has previously been observed in this paper that overlap rates below the optimum value of 50% result in insufficient bonding of neighbouring tracks and the formation of porous structures (Ren et al., 2021; Dzogbewu et al., 2021; Yadroitsev et al., 2013). The data in Table 7.5 on hatch distances and overlap rates were plotted in Figure 7.15 to help identify any prevailing trends.



**Figure 7.15:** Graph of theoretical overlap rates versus hatch distances at 25 % SiC volume fraction in an SiC/Ti6Al4V(ELI) composite at different hatch distances from 50  $\mu\text{m}$  to 110  $\mu\text{m}$

The overlap rate in Figure 7.15 demonstrated an inverse linear relationship with hatch distance. The optimum overlap rate of 50 %, represented by the red solid horizontal line, was obtained at a hatch distance of 69  $\mu\text{m}$  shown with an orange solid vertical line in the figure. The points at hatch distances between 70  $\mu\text{m}$  and 110  $\mu\text{m}$  that were below the solid horizontal red line had overlap rates less than the ideal value of 50 %. Because overlap rates below the ideal value were predicted to result in insufficient re-melting of tracks, which in turn would negatively affect the mechanical properties of the manufactured parts, they were not acceptable for use in the building of 3D components (Lu et al., 2019). Consequently, the hatch distances of 50  $\mu\text{m}$ , 60  $\mu\text{m}$ , and 70  $\mu\text{m}$ , all above the solid horizontal red line, with overlap rates from 52 %, 59 % to 66 %, respectively, were preferable. Further examination of the cross-sections and top

surfaces of the built layers was performed to determine the best hatch distance, from amongst these three, for use in building 3D parts.

The cross-sectional view of layers of a 25 % SiC volume fraction of SiC/Ti6Al4V(ELI) composite produced at a constant laser power, speed, and linear energy density of 200 W, 1.2 m/s, 167 J/m, respectively, with different hatch distances from 50  $\mu\text{m}$  to 110  $\mu\text{m}$ , are presented in Figure 7.16 for use in studying the layers.

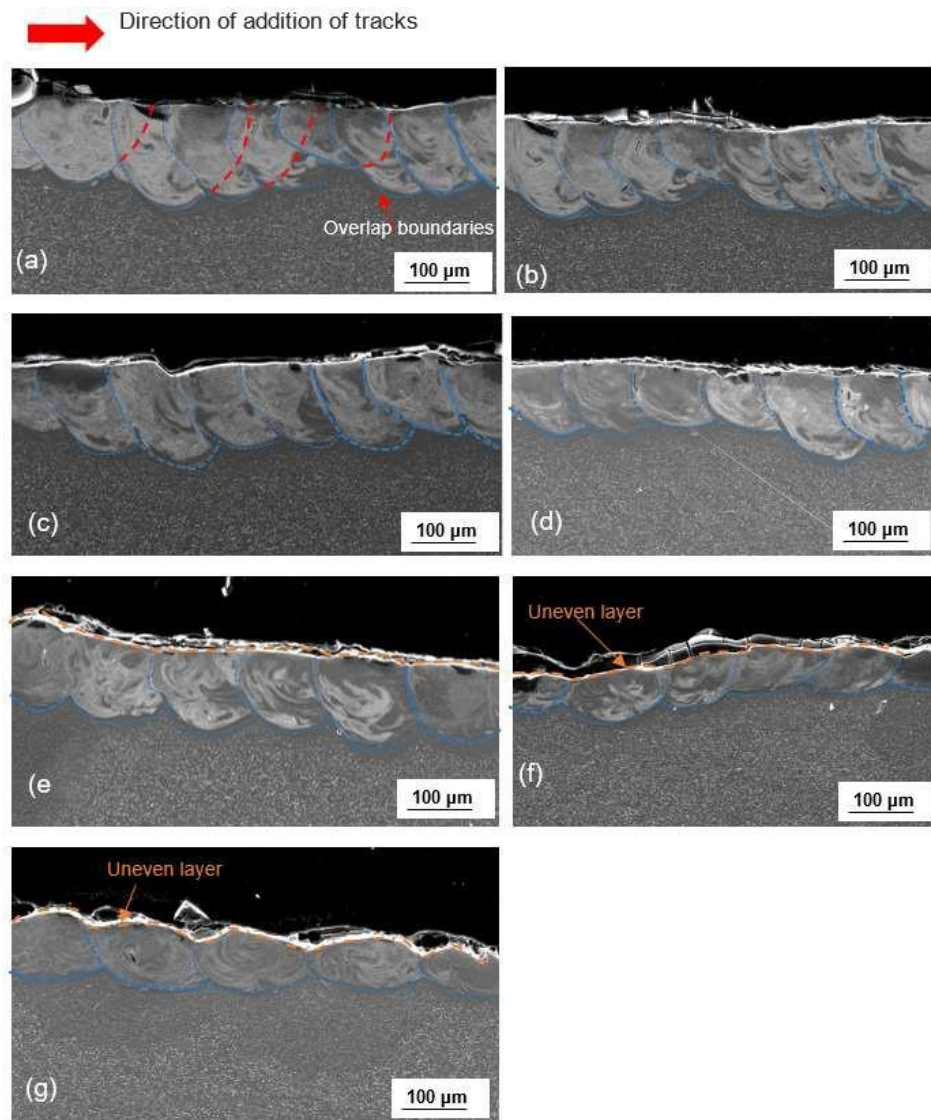


**Figure 7.16:** SEM SE images of cross-sections of single layers produced at a constant laser power, scanning speed, and energy density of 200 W, 1.2 m/s, and 167 J/m, respectively, with different hatch distances (a) 50  $\mu\text{m}$ , (b) 60  $\mu\text{m}$ , (c) 70  $\mu\text{m}$ , (d) 80  $\mu\text{m}$ , (e) 90  $\mu\text{m}$ , (f) 100  $\mu\text{m}$ , and (g) 110  $\mu\text{m}$

It was evident from Figure 7.15 (f and g) that uneven layers were formed at the highest hatch distances of 100  $\mu\text{m}$  and 110  $\mu\text{m}$ . As a result, and from the observation about overlap rates that were less than 50 % made below Table 5 and Figure 7.1, the layers at hatch distances ranging from 80  $\mu\text{m}$  to 110  $\mu\text{m}$  were deemed unsuitable for building of layers and were thus not investigated further. This further investigation was carried out based on the SEM SE images presented in Figure 7.17, for the purpose of identifying the best hatch distance, amongst the three in the figure, to use at this volume fraction of SiC for building 3D parts.

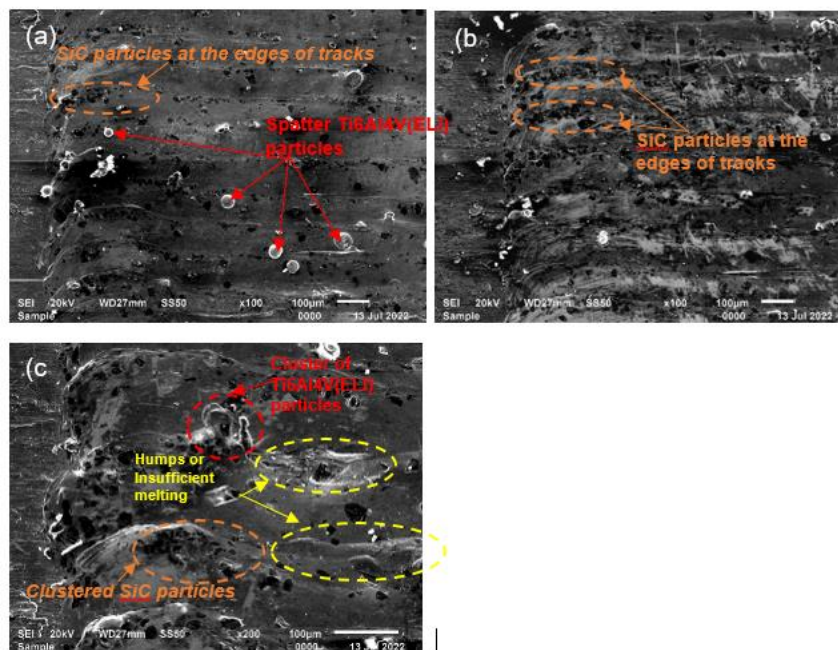


**Figure 7.16: SEM SE micrographs of top surface of single layers produced at hatch distances of (a) 50  $\mu\text{m}$  (b) 60  $\mu\text{m}$ , and (c) 70  $\mu\text{m}$**

It was observed from Figure 7.16 (a) that at hatch distance of 50  $\mu\text{m}$ , the formed layer was smooth with tracks that were closer to each other due to the large overlapping rate indicated in Table 7.5. Thin tracks that were closer to each other because of small hatch distance have been reported to increase the production time and smoother layer surfaces (Vaithilingam et al., 2016). The smooth surfaces of layers resulted in layers of the next deposition of powder with even top surfaces. Spatter Ti6Al4V(ELI) particles were observed in the image of the layer built at a hatch distance of 50  $\mu\text{m}$ , which can

be explained by the fact that decreasing hatch distance leads to increasing temperature of the overlapped regions due to increased VED, as was observed in reference (Lo et al., 2019). Clusters of Ti6Al4V(ELI) particles were observed at a hatch distance of 70  $\mu\text{m}$  because of inadequate energy to re-melt the partially melted particles at the periphery of tracks. Furthermore, clusters of SiC particles were visible along the margins of the tracks. These partially melted particles of Ti6Al4V(ELI) and clusters of SiC particles, shown in Figure 7.16 (c), indicated by yellow and brown dotted circles, respectively, were expected to cause surface imperfections. Therefore, this hatch distance was not good for printing layers at this volume fraction of SiC.

As a result, only the two layers at hatch distances of 50  $\mu\text{m}$  and 60  $\mu\text{m}$  were left for consideration. Given the fact that their cross-sections were nearly identical and from their overlapping rates of 66 % and 59 %, respectively, the former was expected to use more powder and consume more production time. The higher incidence of spatter particles on its surface was a further disincentive for its use. Therefore, the preferred hatch distance was 60  $\mu\text{m}$ , which was expected to provide good bonding between adjacent tracks and sufficient penetration. The smooth top surface of the layer built at a hatch distance of 60  $\mu\text{m}$  was expected to allow the deposition of an even or level layer of powder on it for the next build (Dzogbewu et al., 2021).

## 7.6. Cross-section and Top Surface Analysis of Single Layers built with 30% SiC Volume Fraction in an SiC/Ti6Al4V(ELI) Composite

Table 6 shows theoretical values of overlap calculated with an average width of the track of 114  $\mu\text{m}$  produced with the process parameters of 350 W, 1.7 m/s, and 206 J/m, determined in previous work by the authors (Thamae et al., 2022).

**Table 7.6: Theoretical, calculated values of overlap rates at different hatch distances from 50  $\mu\text{m}$  to 110  $\mu\text{m}$  for a 30 % SiC volume fraction of an SiC/Ti6Al4V(ELI) composite built at a laser power and scanning speed of 350 W, 1.7 m/s, respectively**

Hatch Distance ( $\mu\text{m}$ )	Spot Size ( $\mu\text{m}$ )	Average Track Width ( $\mu\text{m}$ )	Standard Deviation	Overlap Rate (%)
50	80	114	6	56
60	80	114	6	47
70	80	114	6	39
80	80	114	6	29

90	80	114	6	21
	80	114	6	12
	80	114	6	4

It was clear from Table 7.6 that at the lowest hatch distances of 50  $\mu\text{m}$ , adequate overlap rate of 56 % was achieved. Hatch distances of 60  $\mu\text{m}$  to 110  $\mu\text{m}$ , on the other hand, yielded overlap rates that were below 50 %, which were thought to be insufficient for the re-melting of neighbouring tracks. To investigate the trends that existed between overlap rates and hatch distances, a graph of overlap rate was plotted using the data in Table 7.6, with the results shown in Figure 7.17.

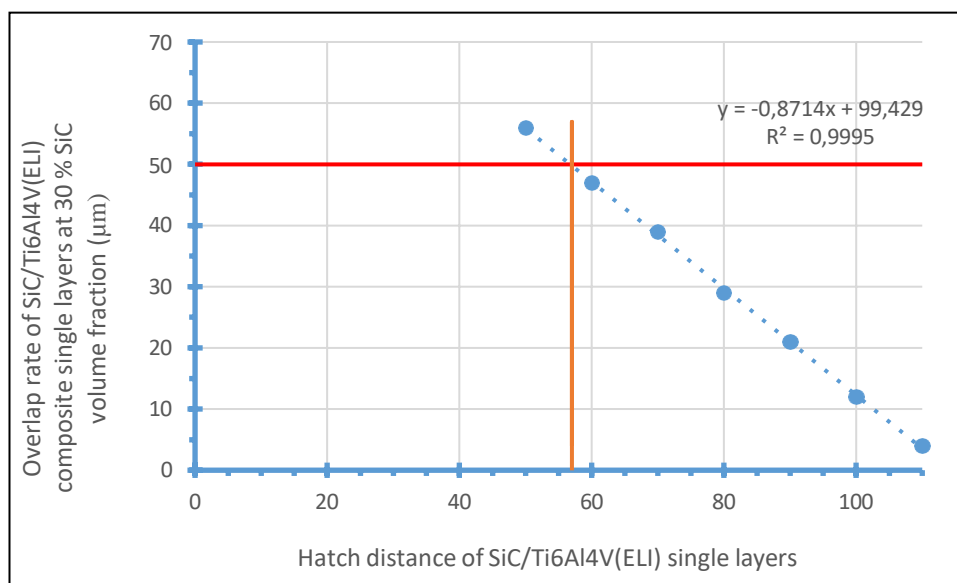


**Figure 7.17:** *Graph of theoretical overlap rate versus hatch distance of SiC/Ti6Al4V(ELI) at 30 % volume fraction of SiC in SiC/Ti6Al4V(ELI) composite at different hatch distances from 50  $\mu\text{m}$  to 110  $\mu\text{m}$*

Below the solid horizontal red line in Figure 7.17, were hatch distances ranging from 60  $\mu\text{m}$  to 110  $\mu\text{m}$ , with corresponding overlap rates ranging from 47 % to 4 %, respectively. Conversely, the hatch distances of 50  $\mu\text{m}$  that showed above this horizontal line represents overlap percentage of 56 %, respectively. Based on last observation and the previously stated fact that overlap rates below the ideal value of 50% indicate insufficient track re-melting, these hatch distances below the red solid horizontal line were deemed unsuitable to produce 3D build parts. To determine an appropriate hatch distance for use in the manufacture of parts at a 30 % SiC volume fraction, more investigation was conducted on the cross-sections and top surfaces of the built layers.

Figure 7.18 illustrates cross-sectional SEM SE micrographs of multiple tracks built at a 30 % SiC volume fraction.

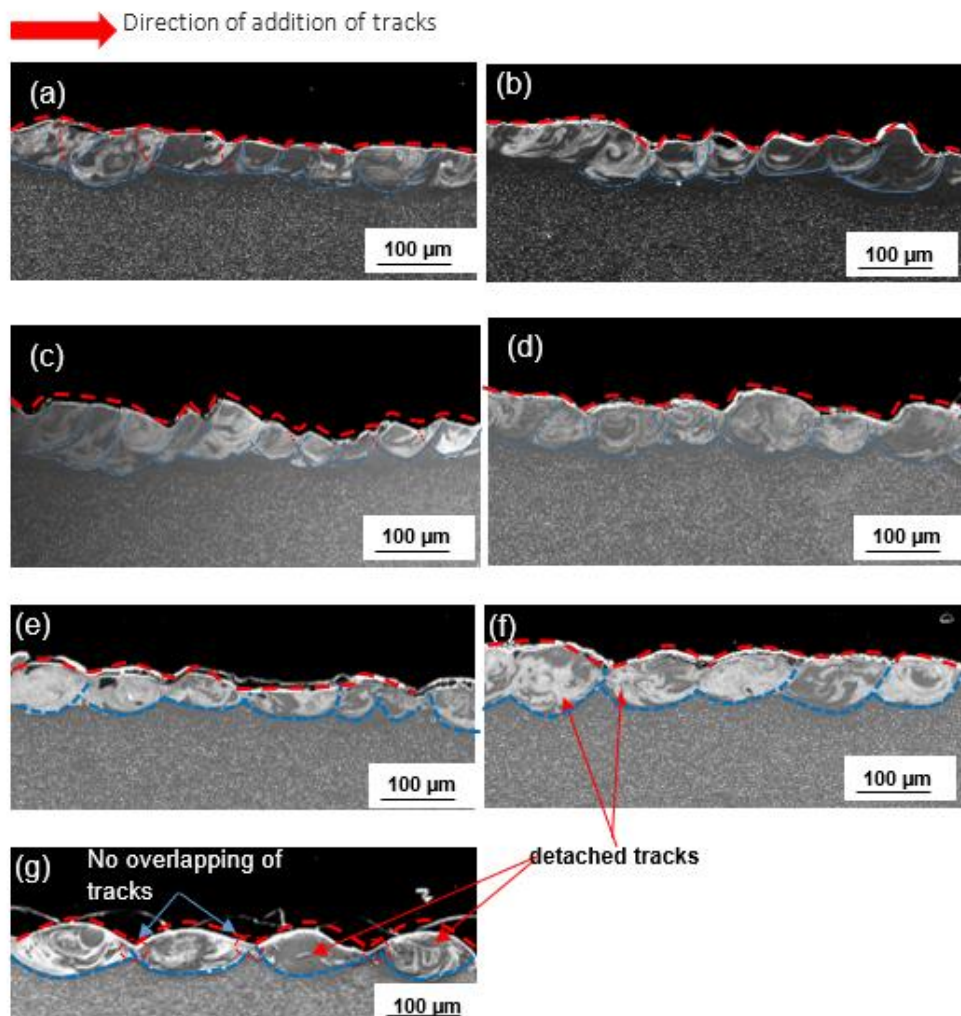


**Figure 7.18:** SEM SE images of cross-sections of single layers produced at a constant laser power, speed, and energy density of 350 W, 1.7 m/s, and 206 J/m, respectively, with different hatch distances (a) 50  $\mu\text{m}$ , (b) 60  $\mu\text{m}$ , (c) 70  $\mu\text{m}$ , (d) 80  $\mu\text{m}$ , (e) 90  $\mu\text{m}$ , (f) 100  $\mu\text{m}$ , and (g) 110  $\mu\text{m}$

All the cross-sections in Figure 7.18 show layers with uneven top surfaces that are traced with red dotted lines. The severity of unevenness was seen visually to increase with increasing hatch distance. It has been noted previously in this chapter that uneven layers are undesirable because they lead to the formation of pores in between them and eventual delamination of layers. The findings of increased surface roughness as a result of non-overlapped single tracks at hatch distances of 100  $\mu\text{m}$  and 110  $\mu\text{m}$  in this figure were consistent with findings published by Leary et al. (2017). In their work,

the authors stated that high values of hatch distance should be avoided because separate tracks in a layer resulted in a very rough surface considering that the material in-between the tracks was not completely re-melted. As noted below Table 7.6, all tracks apart from that built with hatch distance of 50  $\mu\text{m}$  had undesirable overlap rates below 50 %. Further analysis of the built layers at this volume fraction of SiC was thus only carried out for the lowest hatch distance of 50  $\mu\text{m}$  based on the SEM SE micrographs shown in Figure 7.19.

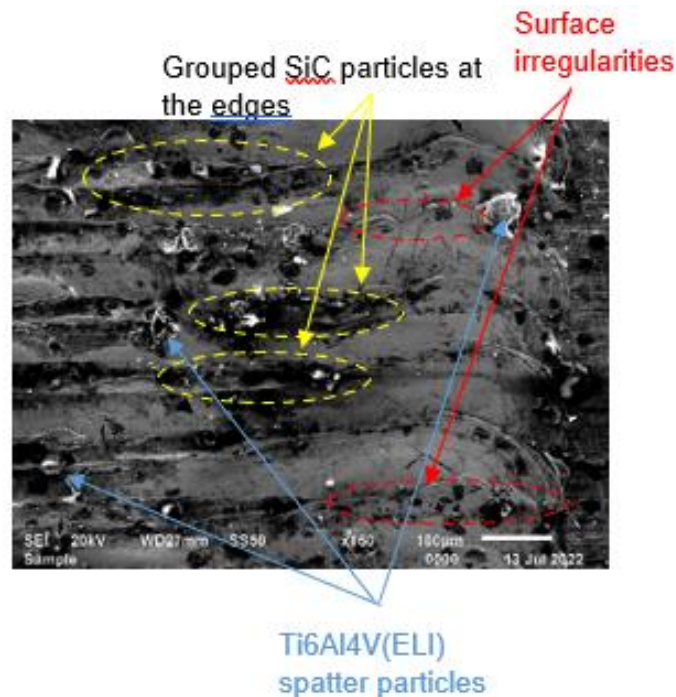


**Figure 7.19:** SEM SE micrographs of top surfaces of single layers produced at different hatch distances of 50  $\mu\text{m}$

The image in Figure 7.19 depicts a layer with SiC particles at the edges of tracks, as well as visible spatter particles and surface imperfections. As has been noted previously in this chapter, these surface characteristics caused increased surface roughness of built components and the presence of interior pores, both of which were expected to reduce the mechanical properties of the final built parts, as was also noted in references (Ventola et al., 2014; Tian et al., 2017; Leary et al., 2017). Though the overlap rate of the layer built with this hatch distance was above 50 %, the aforementioned two factors limited their utility in building good layers of 3D components. Therefore, there was no good hatch distance amongst those used at this volume fraction of SiC.

## 7.7. Conclusions

A summary of all the best process parameters obtained at SiC volume fractions from 5 % to 30 % are shown in Table 7.7.

**Table 7.7: Summary of the best process parameters from 5 % to 30 % SiC volume fractions of SiC in SiC/Ti6Al4V(ELI) composites determined in this chapter**

SiC volume fraction	Hatch distance	Overlap rate	Average width
5%	60	67	184
10%	70	59	170
15%	70	50	141
20%	70	61	178
25%	60	59	146
30%	-	-	-

The summarised data in Table 7.7 shows that there was no consistency in the hatch distance and overlap rate with increasing SiC volume fraction. The volume fraction of SiC was seen to have little impact on the best values of hatch distance determined in this work, with little significant variation of the values (either 60  $\mu\text{m}$  and 70  $\mu\text{m}$ ), for volume fractions of SiC of 5 %–25 %. The surface roughness of single layers of SiC/Ti6Al4V(ELI) composites was higher at high volume fractions of SiC due to increased clustering of SiC particles at the edges of built tracks.

In seeking for the best hatch distance at any volume fraction of SiC, a balance needs to be sought between several factors. These include the attendant risk of increased number of spatter particles and formation of keyholes due to multiple reheats, and low hatch distances that come with high overlap rates, increased surface roughness and low depths of penetration.

Based on the best process parameter sets for the SiC/Ti6Al4V(ELI) composites

studied here, it was concluded that overlap rates between 52 % and 67 % would result in the building of good layers for 5 %–25 % SiC volume fractions. Overlap rates of more than 67 % and less than 50 % were regarded as undesirable for reasons detailed in this chapter. It was concluded that 3D parts with good mechanical and physical properties could be built based on the best hatch distances found for single layers, for volume fractions of SiC 5 %–25 %. For a 30 % SiC volume fraction of an SiC/Ti6Al4V(ELI) composite, no ideal hatch distance was found, as the overlap rates of tracks were either too low or acceptable but produced tracks with spatter particles and very irregular top surfaces.

## 7.8. REFERENCES

- [1]. **Aboulkhair, N.T., Maskery, I., Tuck, C., Ashcroft, I., and Everitt, N.M.,** 2016. On the formation of AlSi10Mg single tracks and layers in selective laser melting: Microstructure and nano-mechanical properties. *Journal of Materials Processing Technology*, 230, pp. 88-98.
- [2]. **Aboulkhair, N.T., Everitt, N.M., Ashcroft, I., Tuck, C.,** 2014. Reducing porosity in AlSi10Mg parts processed by selective laser melting. *Addit. Manuf.* 1-4, pp. 77-86.
- [3]. **Bai, Y., Zhao, C., Wang, D., and Wang, H.,** 2022. Evolution mechanism of surface morphology and internal hole defect of 18Ni300 maraging steel fabricated by selective laser melting. *Journal of Materials Processing Technology*, 299, p. 117328.
- [4]. **Dong, Z., Liu, Y., Wen, W., Ge, J., and Liang, J.,** 2018. Effect of hatch spacing on melt pool and as-built quality during selective laser melting of stainless steel: Modelling and experimental approaches. *Materials*, 12(1), pp. 50.
- [5]. **Guo, Q., Zhao, C., Qu, M., Xiong, L., Escano, L.I., Hojjatzadeh, S.M.H., Parab, N.D., Fezzaa, K., Everhart, W., Sun, T., and Chen, L.,** 2018. In-situ characterization and quantification of melt pool variation under constant input energy density in laser powder bed fusion additive manufacturing process. *Additive Manufacturing*, 28, pp. 600-609.
- [6]. **Huang, J., Li, M., Wang, J., Pei, Z., McIntyre, P., and Ma, C.,** 2021. Selective laser melting of tungsten: Effects of hatch distance and point distance on pore formation. *Journal of Manufacturing Processes*, 61, pp. 296-302.
- [7]. **Karimi, J., Suryanarayana, C., Okulov, I. and Prashanth, K.G.,** 2021. Selective laser melting of Ti6Al4V: Effect of laser re-melting. *Materials Science and Engineering: A*, 805, p.140558.
- [8]. **Liu, B., Li, B.Q. and Li, Z.,** 2019. Selective laser remelting of an additive layer manufacturing process on AlSi10Mg. *Results in Physics*, 12, pp.982-988.
- [9]. **Liu, K., Gu, D., Guo, M., and Sun, J.,** 2022. Effects of processing parameters on densification behavior, microstructure evolution, and mechanical properties of W-Ti alloy fabricated by laser powder bed fusion. *Materials Science and*

*Engineering: A*, 829, p. 142177.

- [10]. **Lo, Y.L., Liu, B.Y., and Tran, H.C.**, 2019. Optimized hatch space selection in double-scanning track selective laser melting process. *The International Journal of Advanced Manufacturing Technology*, 105(7), pp. 2989-3006.
- [11]. **Morgan, R.H., Papworth, A.J., Sutcliffe, C., Fox, P., and O'Neill, W.**, 2002. High density net shape components by direct laser re-melting of single-phase powders. *Journal of Materials Science*, 37, pp. 3093-3100.
- [12]. **Mutua, J., Nakata, S., Onda, T., and Chen, Z.C.**, 2018. Optimization of selective laser melting parameters and influence of post-heat treatment on microstructure and mechanical properties of maraging steel. *Materials and Design*, 139, pp. 486-497.
- [13]. **Pal, S., Drstvensek, I., and Brajljh, T.**, 2018. Physical behaviors of materials in selective laser melting process. *DAAAM International Scientific Book, 2018*, pp. 239-256.
- [14]. **Pupo, Y., Delgado, J., Serenó, L., and Ciurana, J.**, 2013. Scanning space analysis in selective laser melting for CoCrMo powder. *Procedia Engineering*, 63, pp. 370-378.
- [15]. **Ramosena, L.A., Parker, B. S., Dzogbewu, T. C., du Preez, W. B., and Blaine, D.C.**, 2019. Optimum process parameters for DMLS in-situ alloying of a Ti-10 (60Al40V) powder blend. *20<sup>th</sup> Annual Internal RAPDASA Conference*, 5<sup>th</sup> November, Japie Van Lill Auditorium, Central University of Technology, Bloemfontein, South Africa., pp. 78-93.
- [16]. **Ramosena, L.A., Dzogbewu, T.C., and du Preez, W.B.**, 2021. Direct metal laser sintering production of Ti6Al4V parts from a purely elemental powder blend. *Rapid Product Development Association of South Africa (RAPDASA)*, pp. 78-93.
- [17]. **Thijs, L., Verhaeghe, F., Craeghs, T., Van Humbeeck, J., and Kruth, J.P.**, 2010. A study of the microstructural evolution during selective laser melting of Ti-6Al-4V. *Acta Materialia*, 58(9), pp. 3303-3312.
- [18]. **Vilardell, A.M., Takezawa, A., du Plessis, A., Takata, N., Krakhmalev, P.**,

- Kobashi, M., Albu, M., Kothleitner, G., Yadroitsava, I., and Yadroitsev, I.,** 2021. Mechanical behaviour of in-situ alloyed Ti6Al4V (ELI)-3 at. % Cu lattice structures manufactured by laser powder bed fusion and designed for implant applications. *Journal of the Mechanical Behaviour of Biomedical Materials*, 113, p. 104130.
- [19]. **Xia, M., Gu, D., Yu, G., Dai, D., Chen, H., and Shi, Q.,** 2016. Influence of hatch spacing on heat and mass transfer, thermodynamics, and laser process ability during additive manufacturing of Inconel 718 alloy. *International Journal of Machine Tools and Manufacture*, 109, pp. 147-157.
- [20]. **Yadroitsev, I., Bertrand, P., and Smurov, I.,** 2007. Parametric analysis of the selective laser melting process. *Applied Surface Science*, 253(19), pp. 8064-8069.
- [21]. **Yadroitsev, I., Bertrand, P., Antonenkova, G., Grigoriev, S., and Smurov, I.,** 2013. Use of track/layer morphology to develop functional parts by selective laser melting. *Journal of Laser Applications*, 25(5), p. 052003.
- [22]. **Yadroitsev, I., and Smurov, I.,** 2011. Surface morphology in selective laser melting of metal powders. *Physics Procedia*, 12, p. 264–270.

## CHAPTER 8: CONCLUSIONS AND RECOMMENDATIONS

### 8.0 Introduction

This chapter contains the conclusions drawn from the work presented in Chapters 4 to 7. The chapter is divided into two sections, namely conclusions and recommendations.

### 8.1. Conclusions

Experiments performed in this study confirmed that it was possible to additively manufacture good single tracks and layers for different volume fractions of SiC in SiC/Ti6Al4V(ELI) composites ranging from 5 % to 25 %. The following specific conclusions arose from this study:

1. From the prediction of the elastic behaviour of various compositions of the SiC/Ti6Al4V(ELI) composite, it was concluded that;
  - ✚ The low and high values of tensile strength of SiC particles led to divergence of the predicted curves of strength versus volume fraction of SiC particles. For the higher value of strength of SiC that was higher than that of Ti6Al4V(ELI), the Voigt rule predicted increased values of strength of the resulting composites with increasing SiC volume fraction. Conversely, for the lower value of strength of SiC that was lower than that of Ti6Al4V(ELI), the Voigt rule predicted reduced values of strength with increasing SiC volume fraction.
  - ✚ The curves of elastic modulus versus volume fraction of reinforcing SiC filler based on the IRoM, Voight, and Halpin-Tsai empirical equations, all showed an increase in the elastic modulus of SiC/Ti6Al4V(ELI) composites. At 20% SiC volume fraction, the predicted SiC/Ti6Al4V(ELI) elastic modulus was 55%, 18%, and 31% higher than that of Ti6Al4V for the three models, respectively, but at 40% SiC volume fraction, respective improvements of 109%, 42%, and 70% over that of Ti6Al4V(ELI) were predicted. These increases in the values of stiffness denote significant positive reinforcement of Ti6Al4V(ELI) by SiC fillers and serve as a guide of the values expected from experimental testing on built 3D specimens.
  - ✚ The CTEs of the SiC/Ti6Al4V(ELI) composite predicted using the Voigt, Reuss, Hashin and Strickman upper and lower bound equations, all demonstrated

decreasing values as the SiC volume fraction increased. At 40 % volume fraction, the values of the CTE that were predicted by these three models were all lower than most of the values predicted at volume fraction of 20 %. Therefore, it is expected that the predicted values of the CTEs of SiC/Ti6Al4V(ELI) composites will much more closely match those of carbon fibre epoxy resin composites compared to the case of Ti6Al4V(ELI) alone, and this way reduce the effects of differential expansion and contraction at their joints during thermal cycling.

- ✚ The Voigt and Reuss models predicted increasing values of hardness of SiC/Ti6Al4V(ELI) composites with increasing SiC volume fraction.

2. The batch mixing method was chosen as the best to mix SiC and Ti6Al4V(ELI) powders because of the ability to pre-mix minor ingredients, production flexibility, and control over mixing time.

3. Homogenous mixtures of SiC and Ti6Al4V(ELI) powders were obtained at low SiC volume fractions up to 15 % while agglomeration occurred above this percentage, possibly due to the lower density of SiC particles than that of Ti6Al4V(ELI) that encouraged the former to gather together more as the volume fraction of SiC was increased.

4. The following conclusion arose from a study of single tracks that were built for 5%-30% SiC volume fractions:

- ✚ The LPBF process of SiC/Ti6Al4V(ELI) composites is non-linear with respect to the relationship between the two critical process parameters of laser power and scanning speed, and the volume fraction of SiC

- ✚ Excessive LED due to high power and low scanning speeds led to the formation of discontinuous tracks with no penetration and the occurrence of spatter particles, while low LED as a result of low power and high scanning speeds led to balling and discontinuities of track

- ✚ For the best single tracks obtained at 5% to 25% SiC volume fractions and the attendance best widths of tracks ranging from 146  $\mu\text{m}$  and 184  $\mu\text{m}$  that depicted non-linear trend of widths with their depths of

penetration, the track-heights between 30  $\mu\text{m}$  and 40  $\mu\text{m}$  that were below the layer thickness of 45  $\mu\text{m}$  to 50  $\mu\text{m}$  indicated that good quality single layers and 3D build parts could be built.

- ✚ High SiC volume fractions, from 20 % to 30 %, led to increased widths of tracks and HAZ, possibly due to the high heat conductivity and low reflectance of SiC particles resulting into faster increase and equilibration of temperature in them and, therefore, that of the adjacent particle of Ti6Al4V(ELI).
  - ✚ The thermo-physical properties of SiC particles led to undesirable geometrical and surface properties of poor depth of penetration and high surface roughness of single tracks, respectively, which effects increased with increasing volume fraction of SiC. In contrast, at highervolume fractions of SiC, the depths of penetration are lower, possibly as a result of the lower density of SiC particles, which acted as heat shields, that limited the transfer of heat to Ti6Al4V(ELI) powder and, therefore, insufficient penetration into the substrate.
5. The investigation of the top surface morphology of single layers and cross-sections of different overlapping tracks from 5 %-30 % SiC volume fraction led to the following conclusions:
- ✚ The surface roughness of single layers of SiC/Ti6Al4V(ELI) composites was higher at high volume fractions of SiC due to increased clustering SiC particles at the edges of built tracks.
  - ✚ The surface roughness and presence of spatter particles was dependent on the increase and decrease of the hatch distance.High hatch distances led to insufficient melting of power and bonding of the neighbouring tracks which resulted to high roughness layers.
  - ✚ Based on the identified best process parameters set here, it was concluded from the study that overlap rates between 52 % and 67 % with hatch distances of 60  $\mu\text{m}$  or 70  $\mu\text{m}$  resulted in the building of good layers for 5 % to 25 % SiC volume fractions. Therefore, 3D parts with good mechanical and physical properties could be built with SiC volume fractions of 5 % to 25 %.
  - ✚ For a 30 % SiC volume fraction of an SiC/Ti6Al4V(ELI) composite, no

ideal hatch distance was found, as the overlap rates of tracks were either too low or acceptable with spatter particles and very irregular surfaces. it was concluded from the study that the building of parts at 30 % SiC volume fraction would reduce the mechanical properties of the SiC/Ti6Al4V(ELI) composite.

## 8.2. Recommendations

- Building of 3D specimens with the selected best process parameters for different volume fractions of SiC should be done to study the effect of SiC volume fraction on the mechanical properties and failure characteristics of SiC/Ti6Al4V(ELI) composites.
- Studies to determine the effect of different heat-treatment processes on the microstructure and, therefore mechanical properties of SiC/Ti6Al4V(ELI) composites are recommended.
- Further study is required to determine the interfacial bond strength and integrity of different SiC volume fractions of SiC/Ti6Al4V(ELI) composites and its effect on the mechanical properties and failure characteristics of the composites.
- Studies should be conducted to quantify the effect of volume fraction of SiC on the surface roughness and geometric accuracy of built samples of SiC/Ti6Al4V (ELI) composites.
- The best mechanical properties of SiC/Ti6Al4V(ELI) composites should be used to determine the optimal SiC volume fraction.

## APPENDIX A: ANALYSIS OF SINGLE TRACKS BUILT WITH A 5% VOLUME FRACTION OF SIC IN AN SiC/Ti6Al4V(ELI) COMPOSITE

### A1. The Effects of Scanning Speed at a Constant Laser Power of 100 W

Figure A1 depicts micrographs of single tracks produced with a constant laser power of 100 W and differing laser scanning speeds, ranging from 0.3 m/s to 0.9 m/s, to study their surface morphologies.

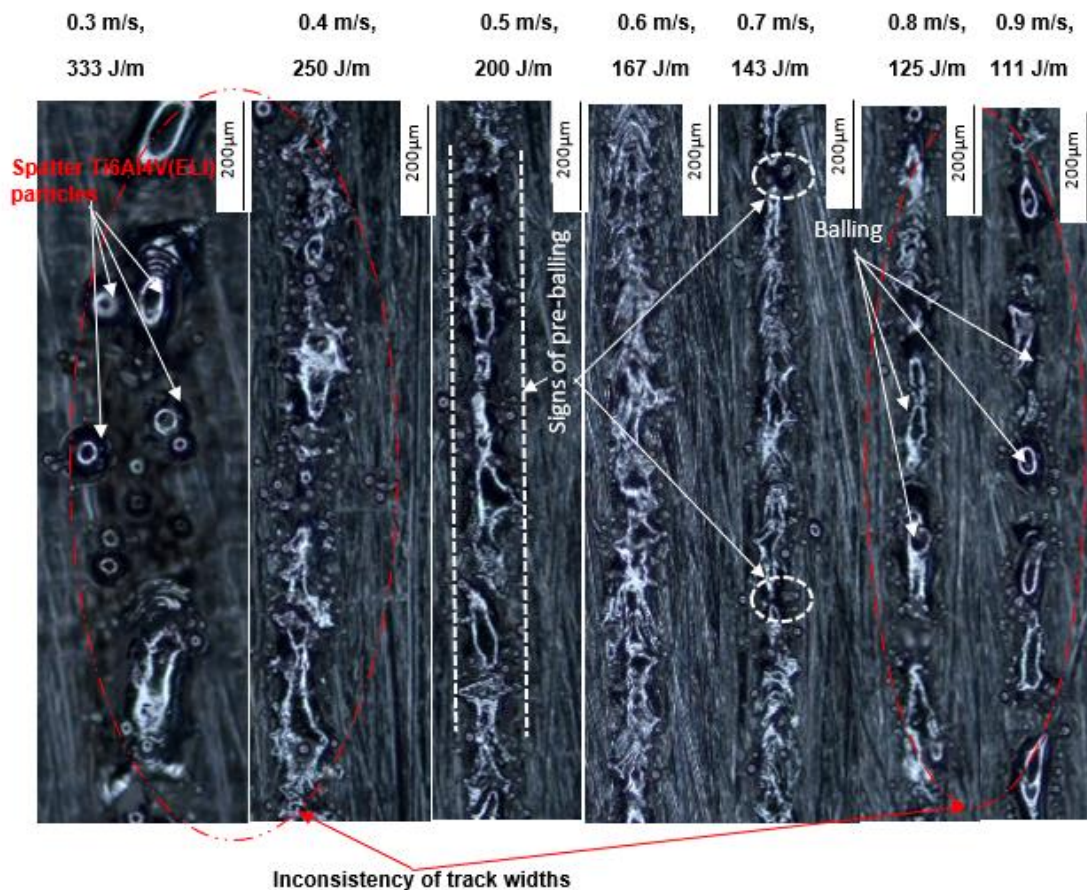


**Figure A1:** Single tracks built at a power of 100 W and different laser scanning speeds from 0.3 m/s to 0.9 m/s

The characteristics of the single tracks are seen to have been affected by the amount of energy input and interaction time of the powder and laser beam, which is consistent with the work of Vilardeli et al. (2020). The single tracks built at a linear energy density of 167 J/m were continuous, as is evident in Figure A1. However, as the scanning speed was increased to 0.7 m/s and the laser linear energy density dropped to 143 J/m, signs of pre-balling and discontinuity of the tracks occurred. Further increase of

the scanning speed and the accompanying decrease of laser linear energy density to 0.8 m/s and 125 J/m, and 0.9 m/s and 111 J/m, respectively, led to the formation of balls. Figure A1 illustrates the balling effect within the red hatched ellipses and the pre-balling within the white hatched circles. Higher scanning speed at constant power decreased the LED, which in turn lowered the melt pool's temperature. Surface tension and melt pool viscosity both increased with the reduced melt pool temperature, leading to the formation of discontinuous tracks with uneven widths, and the presence of pre-balling and balling, which is consistent with the work of Vilardeli et al. (2020). The occurrence of the balling phenomena at higher scanning speeds is known to reduce the energy conducted to the substrate, leading to a reduction of the depth of penetration (Hu et al., 2017). Reduced depth of penetration is known to cause poor bonding between the track and the substrate, as will be seen on the cross-sections to be presented in Figure A2, and is undesirable (Shrestha et al., 2019).

As the speed was decreased to 0.5 m/s and linear energy density increased to 200 J/m, from a speed of 0.6 m/s and a linear energy density 167 J/m, the track showed some signs of discontinuity. Decreasing the speed further to 0.4 m/s with an attendant increase in the linear energy density led to increased formation of spatter particles along the sides of the track. This was due to excessively high energy density which increased the temperature of the melt pool, causing the evaporation of Ti6Al4V(ELI) powder. The foregoing ties in with the work of Shrestha et. al. (2019), who concluded that metal vapour recoil pressure caused by rapid evaporation occurs on the surface of the melt pool resulting in a downward depression of the melt where the laser is directed. Therefore, melt droplets are pushed out to the edges of the melt pool and solidified later as spatter particles.

The leftmost image with the lowest speed of 0.3 m/s and the highest LED of 333 J/m, shows a discontinuous track with spattering. This high LED increased the temperature of the melt pool which caused evaporation of the melt and induced a strong recoil effect on the melt pool that blew the melt away, resulting in a lack of formation of a continuous track but rather droplets that solidified to what is commonly referred to as spatter particles. This is consistent with the work of Shrestha et al. (2019) and is identified in the leftmost micrograph in Figure A1.

Based on the examination of the surface scans of the tracks illustrated in Figure A1, the best track was achieved at a scanning speed of 0.6 m/s and a linear energy density of 167 J/m. However, further study on the cross-sections was needed to help decide on the most appropriate track, details of which are now presented. Figure A2 depicts cross-sectional views of the tracks at a laser power of 100 W with laser scan speeds ranging from 0.3 m/s to 0.9 m/s and LEDs ranging from 333 J/m to 111 J/m.

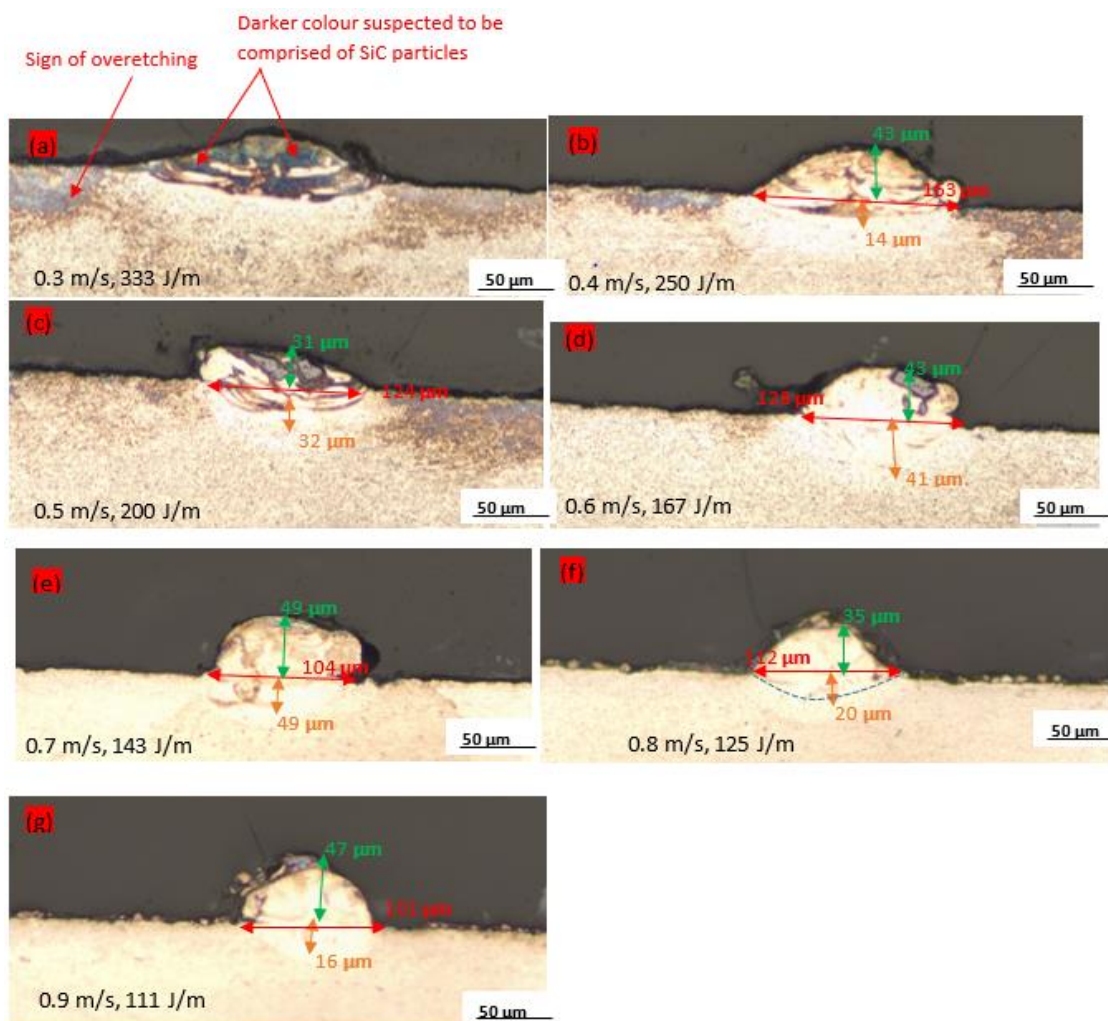


**Figure A2:** Cross-sectional images of single tracks produced at a laser power of 100 W, with laser scanning speeds from 0.3 m/s to 0.9 m/s

It was confirmed by SEM/EDS analysis that the darker colour on the cross-sections represents SiC particles. According to the model of Eagar and Tsai (1983), the cross-section of the melt pool formed in conduction mode is approximately semi-circular. Thus, the melt pool depth is about equal to its half-width. Therefore, the keyhole effect occurs when the depth of the melt pool is greater than a half-width, with a depth-to-

width ratio greater than 0.5. A ratio of 0.5 shows good penetration into the substrate, while a ratio less than 0.5 indicates poor penetration. All the tracks in Figure A2 showed low penetration into the substrate and were a sign of poor conduction melting. Poor conduction melting occurs when the power is too low to provide a good depth of penetration and is undesirable as it leads to poor interlayer bonding (Shrestha et al., 2019).

Although Figure A1 showed that the best track was obtained at a scanning speed of 0.6 m/s and a linear energy density of 167 J/m, its cross-section shown in Figure 6.2 reveals a depth-to-width ratio of 0.3. A depth-to-width ratio less than 0.5 has been noted in the preceding paragraph as indicating insufficient depth of penetration. As a result, the conclusion was that with a power of 100 W, none of the laser scanning speeds used produced tracks with desirable geometrical characteristics.

## A2. The Effects of Scanning Speeds at a Laser Power of 150 W

The single tracks produced at a constant laser power of 150 W with different laser scanning speeds from 0.6 m/s to 1.2 m/s are shown in Figure A3, for use to study their top surface characteristics.

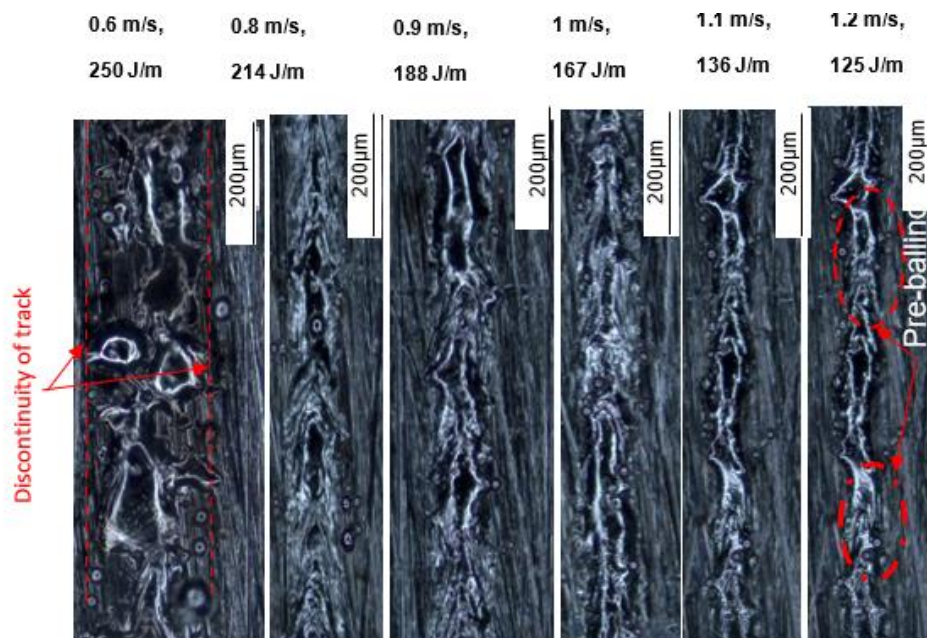


**Figure A3:** Single tracks built at a laser power of 150 W and different scanning speeds from 0.6 m/s to 1.2 m/s

Continuous tracks were noticeable at laser scanning speeds of 0.8 m/s to 1.0 m/s. Reductions in the widths of tracks were also observed as the laser scanning speed increased from 1.0 m/s to 1.1 m/s. Further increase of the laser scanning speed to the highest value of 1.2 m/s led to necking and discontinuity of the track. Necking and narrowing of the widths of tracks, in this case, were thought to have been due to the decreased dwell time of the laser beam on the powder bed, which provided insufficient time to fully melt the powder, as observed by Yadroitseva et al. (2015). The shorter dwell time also implied less time for the melt to diffuse sideways, causing a narrowing of the melt region and HAZ, as was noted by (Chandranth et al., 2016).

The leftmost image in Figure A3 shows a broken-up track at a high linear energy density of 250 J/m and a low speed of 0.6 m/s. A high LED increases the temperature of the melt pool, which causes evaporation of the melt. The boiling and melting temperatures of Ti6Al4V are 2 860 °C and 1 667 °C, respectively, while SiC does not melt but rather sublimates above 2 700 °C (Zhang et al., 2020; Wang et al., 2021; Semmelroth et al., 2004). Thus, the evaporation temperature of Ti6Al4V (ELI) is marginally higher than the sublimation temperature of SiC, while its melting temperature is significantly lower, ensuring that at the melting point of Ti6Al4V(ELI), SiC remains solid to form a composite. Therefore, the Ti6Al4V(ELI) particles are expected to melt and evaporate at this high energy input, while the SiC particles sublime, leading to a lack of formation of tracks but rather droplets of the re-solidified Ti6Al4V(ELI), referred to as spatter particles, as seen in the leftmost image in Figure A3. Pre-balling occurred at the highest laser scanning speed of 1.2 m/s, as seen in the rightmost image in Figure A.3.

The foregoing discussion clearly shows that the best tracks were obtained at laser scanning speeds of 0.8 m/s, 0.9 m/s, and 1 m/s, with linear energy densities of 214 J/m, 188 J/m, and 167 J/m, respectively, based on track continuity and stability of track width. However, further examination of the cross-sections is required before reaching a final determination on the best track, details of which are now presented.

Figure A4 shows cross-sectional views of the tracks built at a laser power of 150 W and scanning speeds ranging from 0.6 m/s to 1.2 m/s, for use to analyse their geometrical characteristics.

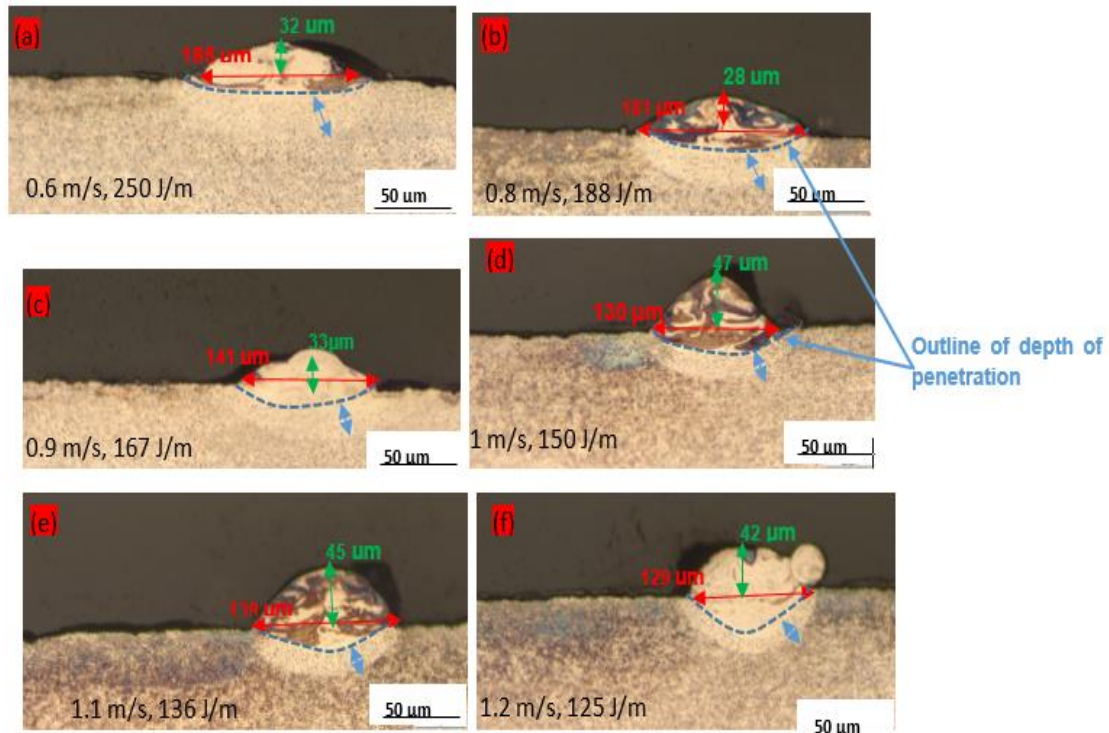


**Figure A4:** Cross-sectional images of single tracks built at scanning speeds from 0.6 m/s to 1.2 m/s at a laser power of 150 W

All the tracks shown in Figure A4 indicated poor penetration with depths-to-width ratios less than 0.5, which cannot provide strong bonds between them and the substrate and between layers as well. Wide and shallow tracks were observed at laser scanning speeds ranging from 0.6 m/s to 0.9 m/s because of the moderate laser power and high dwell times of the laser beam that created large reductions of surface tension and viscosity, which in turn allowed the melt to flow radially outwards. The height of tracks above the substrate increased as the scanning speed was increased from 0.6 m/s to 1 m/s and later decreased as the speed was raised further to 1.1 m/s and 1.2 m/s, as shown in Figure A4. The increasing height of tracks above the substrate and reduction in their widths, with increasing laser scanning speeds between 0.9 m/s and 1 m/s, is thought to have been a result of the lower dwell time of the laser beam that did not allow adequate reduction of surface tension and viscosity of the melt and led to less radial outward flow of the melt. This is consistent with the assertions made by Ganeriwala et al. (2015).

The consecutive reduction of height beyond a scanning speed of 1.0 m/s is likely to have arisen due to the consecutive reduction in the amount of melted powder as a result of the higher speeds and attendant lower dwell times and LED. The increased

presence of necking and pre-balling in the last two cross-sections in Figure A4 supports this assertion. It is clear from the previous discussion in this paragraph that the effect of an increase in temperature on the Ti6Al4V(ELI) melt is a reduction of surface tension and viscosity. Although the top surface scans produced the best tracks at laser scanning speeds ranging from 0.8 m/s to 1 m/s, as shown by the cross-sections in Figure A4, they had poor depths of penetration. As a result, it was decided that none of the process parameters used to print tracks at this value of laser power of 150 W were appropriate since they produce single tracks with poor penetration and continuity, which is likely to have a negative impact on 3D-built objects.

### A3. The Effects of Scanning Speed at a Laser Power of 250 W

The images of single tracks built at a constant laser power of 250 W and different scanning speeds are shown in Figure A5.

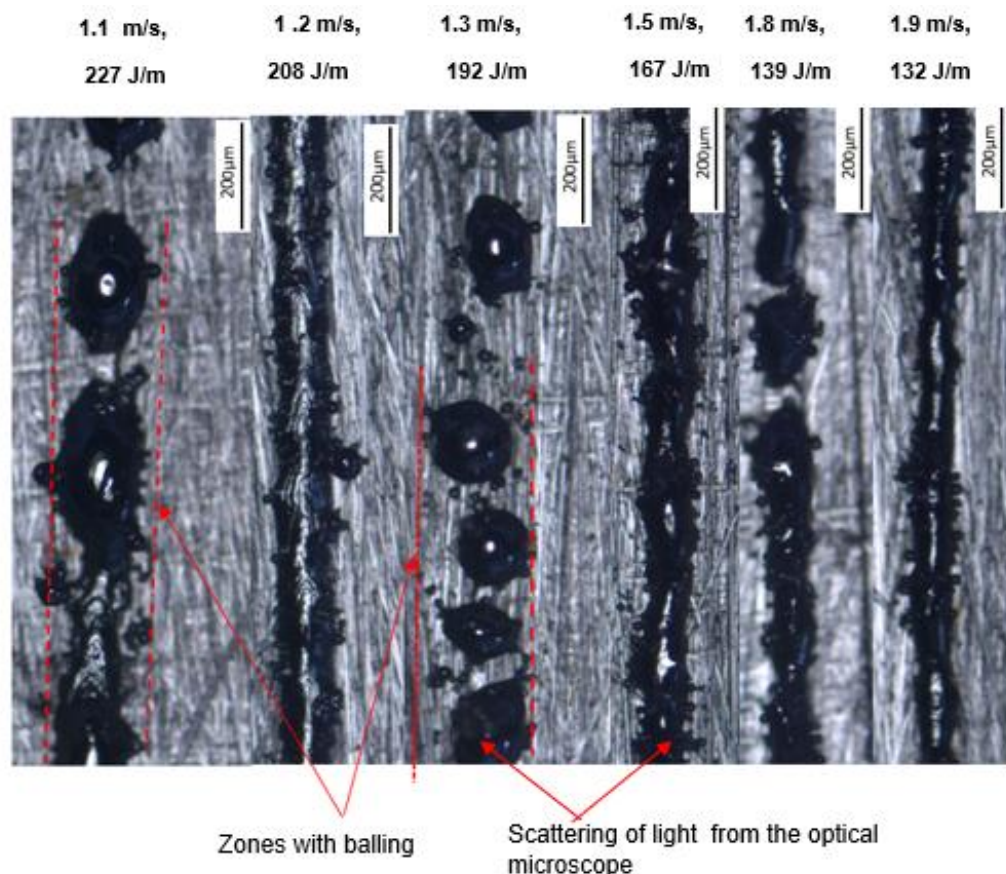


**Figure A5:** *Single tracks built at laser scanning speeds from 1.1 m/s to 1.9 m/s at a constant power of 250 W*

In Figure A5, only the track built at a scanning speed of 1.2 m/s were continuous, with a stable track width, while those built at scanning speeds of 1.1 m/s and 1.3 m/s exhibited balling shown by the red arrows. Mumtaz et al. (2010) reported that balling increases the surface roughness of the 3D parts and decreases their density. Moreover, they reported that balling occurs at high energy density and low laser scan speed. The increased LED leads to higher temperatures and a higher degree of melting of the powder, with the consequent formation of larger amounts of liquid melt (Dilip et al., 2017). The increased temperature lowers the melt viscosity and surface tension thereby leading to a break-up of the melt and a resulting formation of a large number of individual small balls with lower surface energy (Yuan et al., 2020). This is likely to be the situation leading to the track observed in Figure A5 at the lower laser scanning speed of 1.1 m/s.

Balling at the higher scanning speed of 1.3 m/s was likely to be a result of increased scanning speed that caused a drop in temperature with the attendant increase of surface tension and viscosity of the melt. On the other hand, the result of decreased melt pool temperature, as well as increased surface tension and melt pool viscosity at higher laser scanning speeds, from 1.5 m/s to 1.9 m/s, resulted in the formation of thin and irregular single tracks that were broken into different sections, as was also reported by Ramosena et al. (2019). The single track, built at a scanning speed and energy density of 1.2 m/s and 208 J/m, showed the best characteristics among these sets of tracks. Figure A6 depicts cross-sections of the tracks shown in Figure A5, for use in determining the depths of penetration, widths, and heights of the tracks.

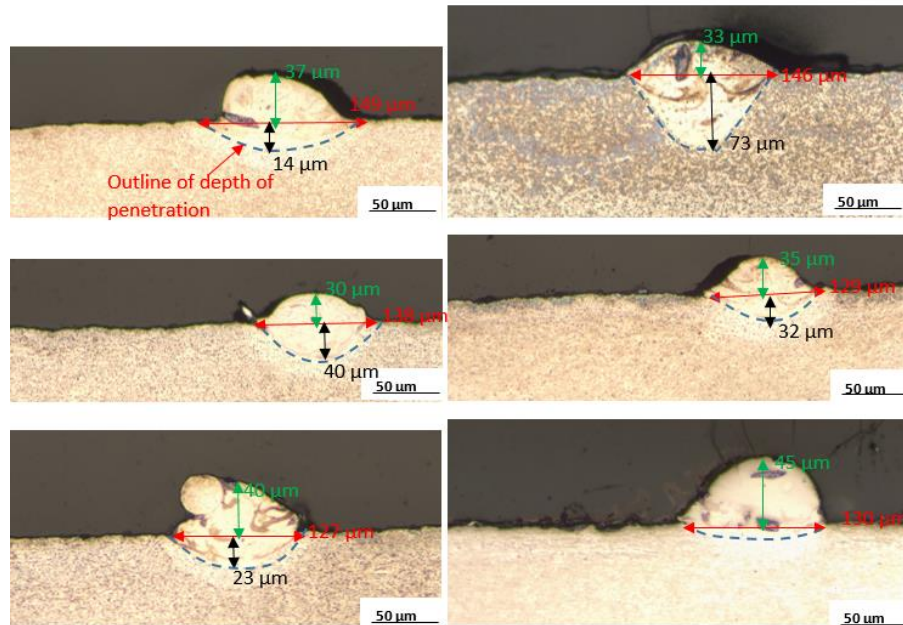


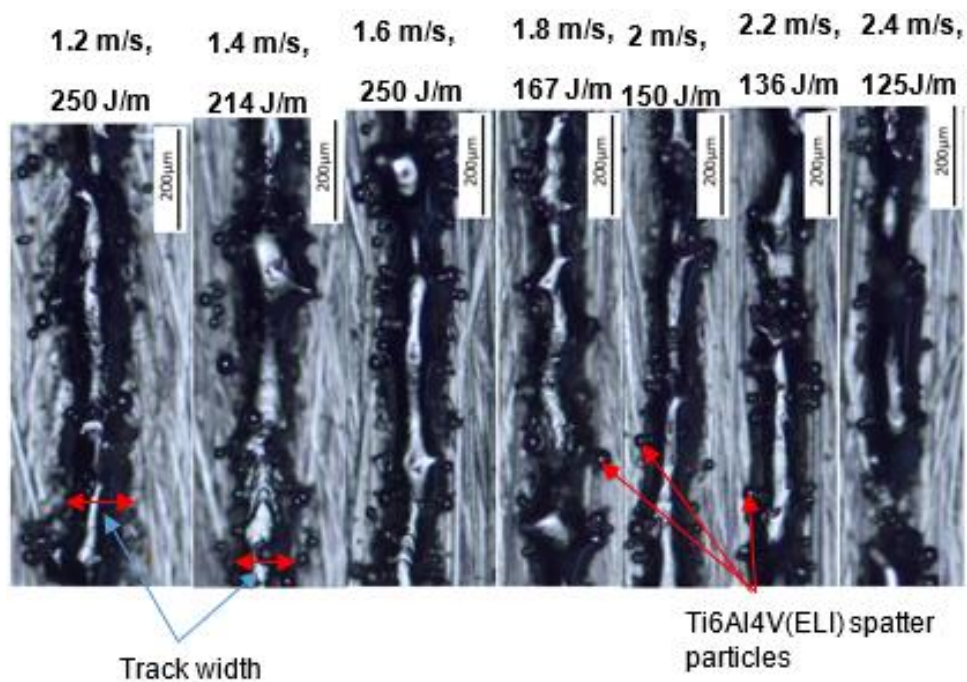
**Figure A6:** Cross-sections of tracks built at a laser power of 250 W with different scanning speeds from 1.1 m/s to 1.9 m/s

In this figure, the depth of penetration was seen to be highest at laser scanning speed of 1.2 m/s and diminished when the scanning speed was increased further. Furthermore, from the cross-sections, it was observed that the widths of the tracks decreased constantly as the scanning speed increased, a trend that was accompanied by increased heights of the tracks from a scanning speed of 1.3 m/s to 1.9 m/s. Except for the track built at the laser scanning speed of 1.2 m/s, all the cross-sections had depth-to-width ratios smaller than 0.5. The depth of penetration of this track was 73 µm with a width of 146 µm, which corresponded to a depth-to-width ratio of 0.5 and was indicative of good bonding with other layers or the substrate. The height of the track above the substrate was considered acceptable, at a value of 33 µm, given the observation in Chapter 6 that too low a layer thickness increases the building-time and vice-versa, for 3D specimens, while very high layer thicknesses lead to rough surfaces and poor interlayer bonding. Ramosena et al. (2019), in their research showed that the semi-circular depth of penetration was desirable in the DMLS process for defect-free components with good interlayer bonding, and bonding to the substrate.

Therefore, the preferred optimum process parameter set in this case were at a laser power of 250 W and scanning speed of 1.2 m/s and a linear power density of 208 J/m. It was noted from the top views of tracks in Figure A5 that the track built with these parameters was continuous with a stable track width.

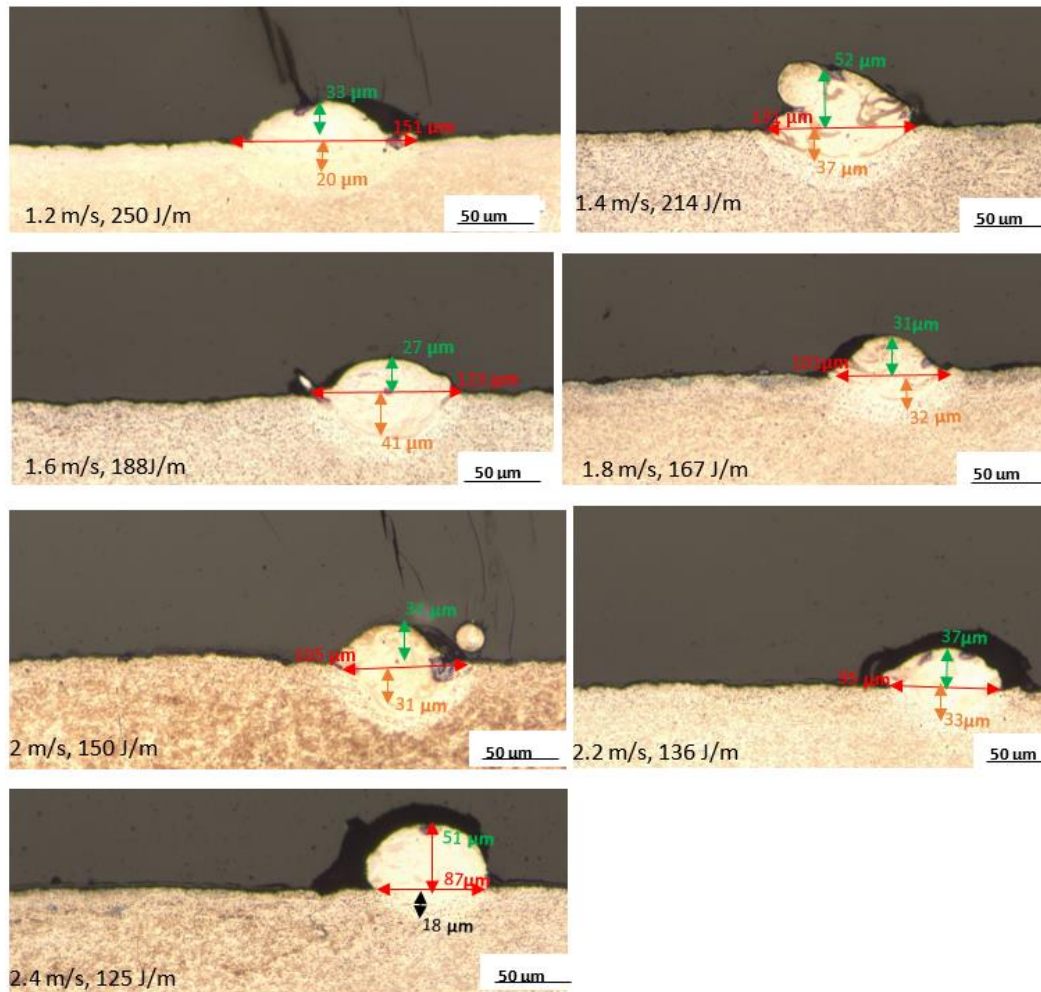
#### A4. The Effects of Scanning Speed at a Laser Power of 300 W

Figure A7 shows the micrographs of single tracks built at a laser power of 300 W and different scanning speeds from 1.2 m/s to 2.4 m/s to study their surface morphologies.



**Figure A7:** Single tracks built at a constant power of 300 W with scanning speeds from 1.2 m/s to 2.4 m/s

From the micrographs in Figure A7, all the tracks built at a laser power of 300 W are seen to be discontinuous with narrow and uneven widths, and with a lot of spatter particles occurring on their sides. Therefore, this magnitude of laser power and the corresponding speeds would not form any good set of process parameters, as they all led to undesirable tracks that would negatively affect any built 3D parts. The cross-sections of these tracks are shown in Figure A8.



**Figure A8:** Cross-sectional images of the tracks built at a laser power of 300 W with different laser scanning speeds from 1.2 m/s to 2.4 m/s

The cross-sections in Figure A8 confirmed that all the tracks had poor penetration into the substrate, with the measured values of width and depth of penetration of the tracks corresponding to depth-to-width ratios less than the optimum value of 0.5. Low penetration of the tracks into a substrate is known to be undesirable as it leads to delamination between the layers when printing the specimens (Shi et al., 2017; Dzogbewu et al., 2022). The widths of the tracks decreased continuously with increasing laser scanning speed, while their heights and depths of penetration did not show any consistent trend. The track built at the highest laser scanning speed of 2.4 m/s, showed the presence of a hump with clear signs of undercutting, which signals the advent of balling. It was concluded that at this value of laser power, no best

scanning speed amongst those used could lead to the production of tracks with good geometrical characteristic features, for building 3D parts with good properties.

#### A5. The Effects of Scanning Speed at the Highest Laser Power of 350 W

Figure A9 shows the micrographs of single tracks built at a laser power of 350 W and different scanning speeds from 1.5 m/s to 2.7 m/s.

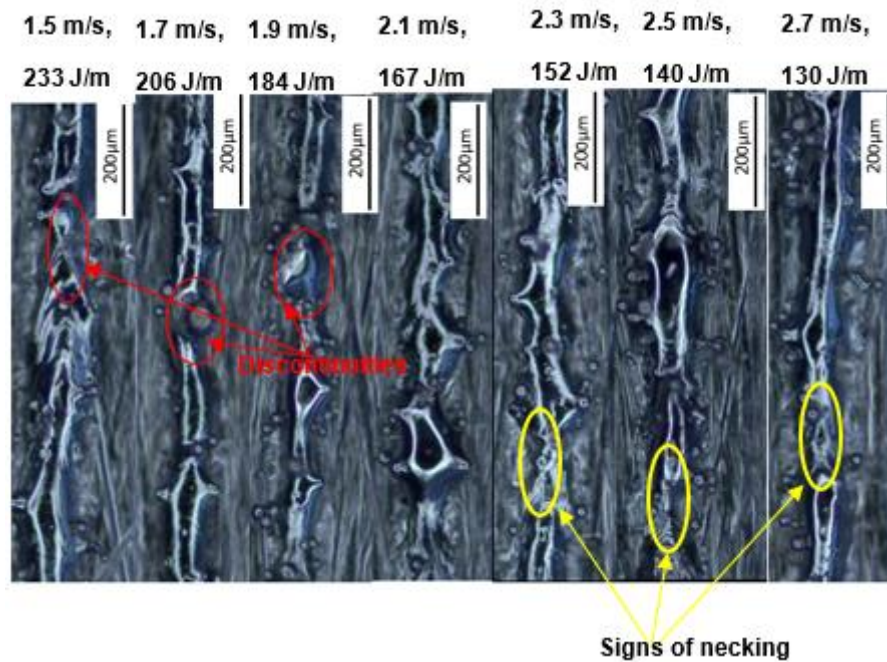


**Figure A9:** Single tracks built at a laser power of 350 W and different scanning speeds from 1.5 m/s to 2.7 m/s

The tracks in Figure A9 built with laser scanning speeds of 1.5 m/s to 2.1 m/s were discontinuous with unstable track widths, while necking was observed with further increase of scanning speeds from 2.3 m/s to 2.7 m/s. Therefore, all the sets of process parameters used to build the tracks shown in Figure A9 were considered unsuitable for printing 3D parts of good quality. The highest LED was lower at this highest power of 350 W than at low values of 100 W and 150 W because of the high laser scanning speeds used at 350 W, that were higher than those used at the lower values of power. Therefore, it was not expected that any SiC particles would sublime at this level of laser power with high scanning speeds. Instead, sublimation of SiC was found to occur at the maximum LED of 333 J/m (100 W and 0.3 m/s) and 250 J/m (150 W and 0.6 m/s). The high LEDs increased the energy input, causing the SiC particles to

sublimate and the Ti6Al4V(ELI) particles to evaporate. As a result, no track was produced; instead, the droplets of Ti6Al4V(ELI) solidified as spatter particles.

### A6. Analysis of Single Tracks at Constant Scanning Speed with Different Values of Laser Power

Figure A10 shows single tracks built at a laser scanning speed of 0.8 m/s and different values of laser power varying from 100 W to 200 W.

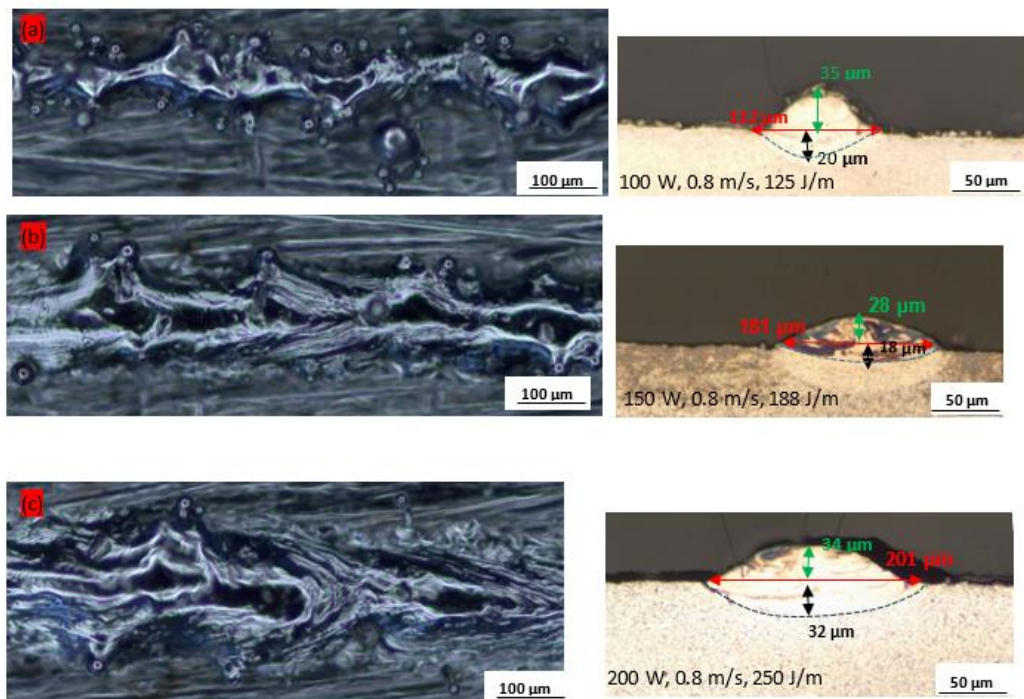


**Figure A10:** Top surface scans and cross-sections of single tracks built at a scanning speed of 0.8 m/s and different laser powers of 100 W, 150 W, and 200 W

Both the power and the scanning speed affect the degree of melting and depth of penetration of the laser beam. Power is the most significant process parameter determining the depth of penetration of the laser beam, while the scanning speed is a significant parameter in determining the width of the heat-affected zone (HAZ) and the size of the melt pool (Kruth et al., 2010). It was observed from Figure A10 that at the lowest power (100 W), the track was narrow with a lot of spatter particles along the sides of the track. The corresponding image of a cross-section of this track showed a depth of penetration of 20 μm through the substrate and a width of 112 μm and depth-to-width ratio of 0.2. The low depth of penetration of the track at this low energy density

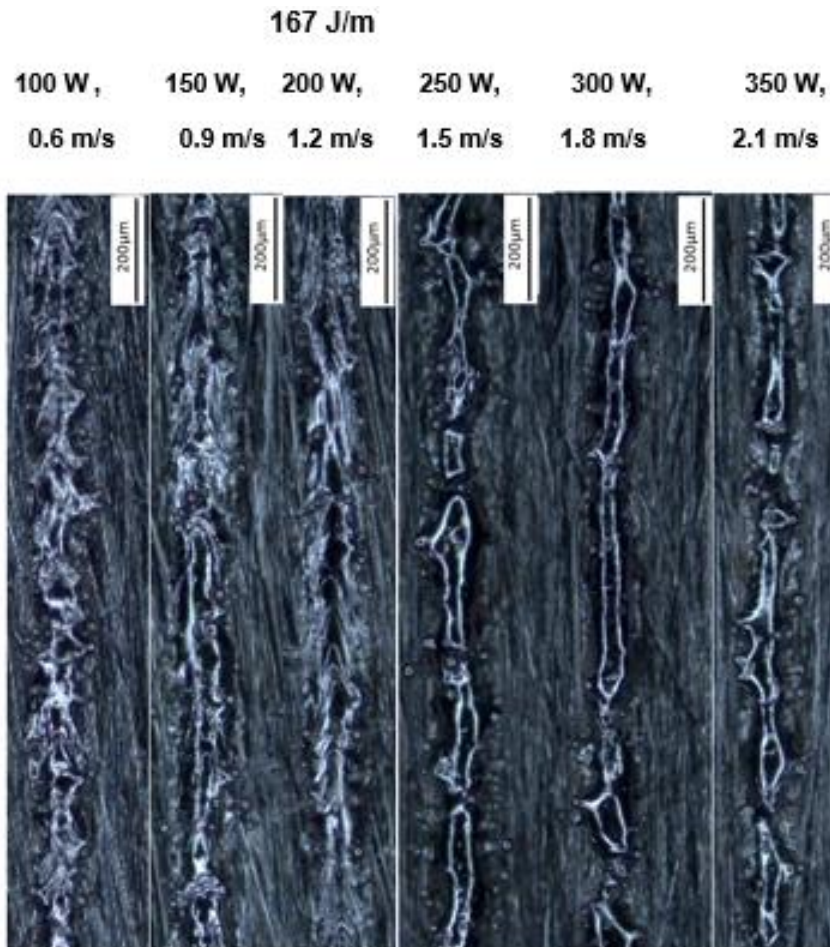
(125 J/m) was due to insufficient heat, which was only able to melt small amounts of the powder, resulting in the formation of an irregular track, which is consistent with the work of Andani et al. (2018).

When the power was increased to 150 W, the track built was continuous and wider, with fewer spatter particles on the sides. The cross-section of the track showed a lesser depth of penetration of 18  $\mu\text{m}$  than at 100 W. The lower depth of penetration and greater width of 181  $\mu\text{m}$  resulted in a corresponding depth-to-width ratio of 0.1, indicating a shallow penetration that is insufficient to enable good bonding between previously melted layers. Increasing the power further to 200 W at the same speed was seen to lead to the formation of a continuous track and a decrease in the number of spatter particles. The cross-section of the track built at this value of laser power showed a depth of penetration through the substrate of 32  $\mu\text{m}$  and a track with a width of 201  $\mu\text{m}$ , giving rise to a depth-to-width ratio of 0.2. This implies that at this higher energy density, the penetration into the substrate is better than at the lower laser powers of 100 W and 150 W, with their lower LEDs, which is consistent with the work of Siao et al. (2021).

It can be concluded that increasing the laser power caused the width and depths of penetration of the tracks to increase continuously with rising laser power but an inconsistency in the change of the depth-to-width ratio. However, in all three cases in Figure A10, the depth-to-width ratios of all the tracks were below the optimum value of 0.5.

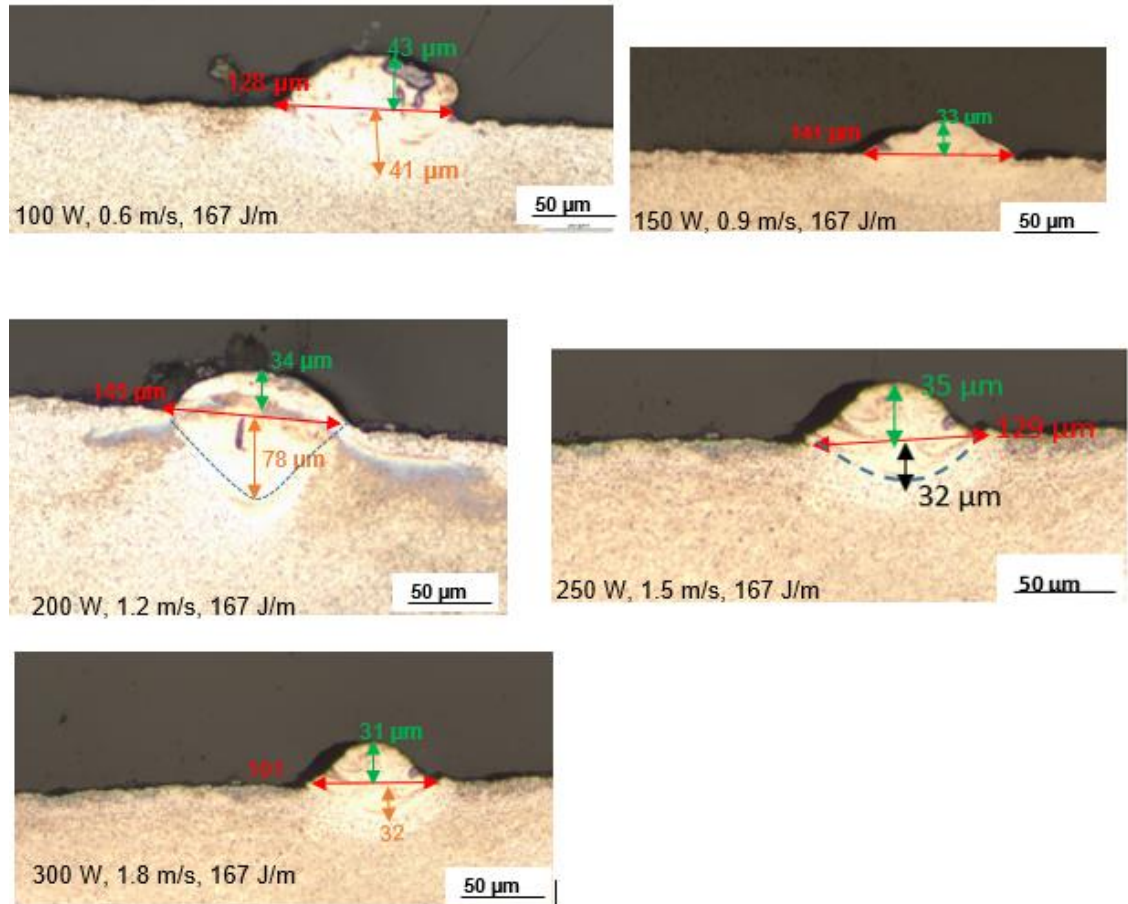
#### **A7. The Effects of Different Laser Scanning Speeds and Power at a Constant Linear Energy Density**

Figure A11 shows single tracks printed at a linear energy density of 167 J/m and different speeds from 0.6 m/s to 2.1 m/s and laser power ranging from 100 W to 350 W.



**Figure A11: Single tracks printed at a linear energy density of 167 J/m and different laser scanning speeds and power**

The single tracks in Figure A11 show that at the same linear energy density, the width of the single tracks reduced as the scanning speed and laser power increased. At low scanning speeds and power (0.6 m/s to 1.2 m/s and 100 W to 200 W), the tracks are almost continuous with constant widths. As the speed and power were increased to 250 W and 1.5 m/s and further to 350 W and 2.1 m/s, respectively, the widths of track became narrower and discontinuous and exhibited the pre-balling effect.



**Figure A12: Cross-sections of single tracks printed at a linear energy density of 167 J/m and different laser scanning speeds and power**

The figure shows that when the laser power increases, the widths of the tracks drop continuously while maintaining a constant linear energy density. However, the height of the tracks and depth of penetration did not follow a consistent trend as laser power increased. The micrographs in this figure show that at a laser power of 100 W and 200 W, the depths of penetration were higher than the other cross-sections in the figure. Figure A10 shows continuous tracks at 100 and 200 W, which confirms this.

## APPENDIX B. ANALYSIS OF SINGLE TRACKS BUILT AT A VOLUME FRACTION OF 10 % SiC IN AN SiC/Ti6Al4V(ELI) COMPOSITE

### B1. The Effects of Different Laser Scanning Speeds at a Laser Power of 100 W

The tracks built at the constant laser power of 100 W and different laser scan speeds from 0.3 m/s to 0.7 m/s are shown in Figure B1.

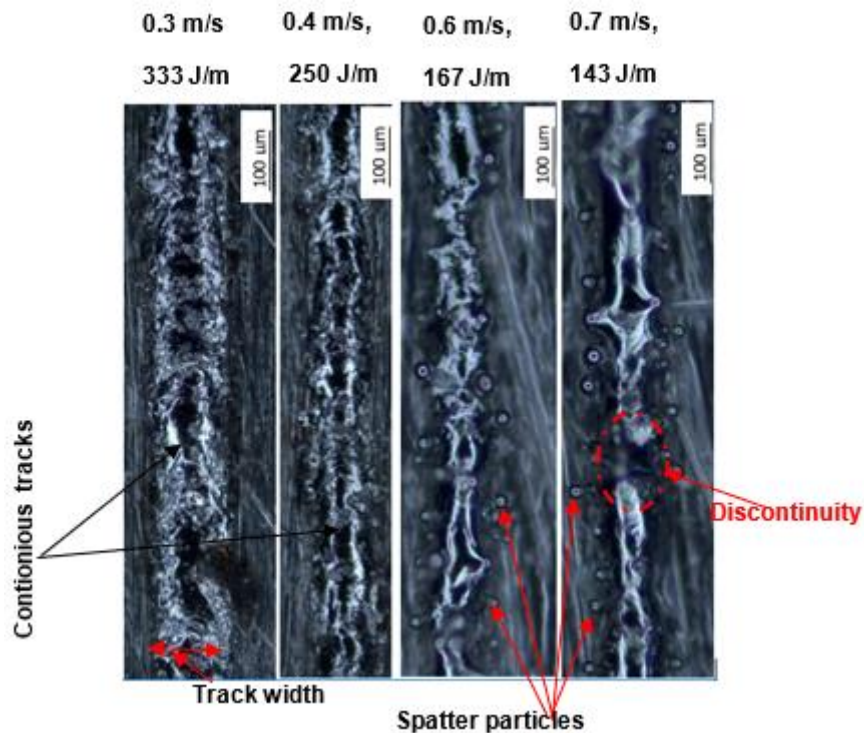


**Figure B1:** Single track images at a constant power of 100 W and different laser scanning speeds from 0.3 m/s to 0.7 m/s

The single track on the extreme left of this figure, which was built at the low laser scanning speed and high LED of 0.3 m/s and 333 J/m, respectively, was seen to be continuous with a constant track width. At the higher laser scanning speed of 0.4 m/s and LED of 250 J/m, the width of the track was also continuous and reasonably constant but with a smaller width than in the previous case. When the scanning speed was increased to 0.6 m/s, the width of the track decreased, and some discontinuities appeared. Spatter particles were also created along the edges of the tracks. Increasing the scanning speed to the maximum value of 0.7 m/s resulted in the formation of a thin and discontinuous track with more spatter particles.

At high laser scanning speeds, powder particles are ejected in front of the laser beam which is known as cold ejection thus forming spatter particles (Ullah et al., 2022). Spattering is one of the undesirable phenomena that will influence the quality of printed layers, surface morphology, overall density, and mechanical properties of the final parts (Ullah et al., 2022). The discontinuity of the track in this instance, built at scanning speed of 0.7 m/s, was thought to have been due to inadequate energy to fully melt the powder, which limited the dwell time of the laser beam on the powder bed and not allowing the laser beam sufficient time to entirely melt the particles of powder. Shrestha et al. (2019) discovered the same result of decreased track width when the laser scanning speed increased. They indicated that the width of the track is related to the LED. As a result, when the scanning speed increases and decreases at the same power, the quantity of energy input per unit area decreases and vice versa, accompanied by a decrease and increase in the width of tracks.

According to the preceding discussion, the best tracks were observed at laser scanning speeds of 0.3 m/s and 0.4 m/s, with no spatter particles and very consistent widths. However, in addition to the top surface analysis carried out in the preceding paragraph, the examination of the cross-sections of single tracks from Figure B1, as shown in Figure B2, was required to finally determine the best process parameters at this value of power.

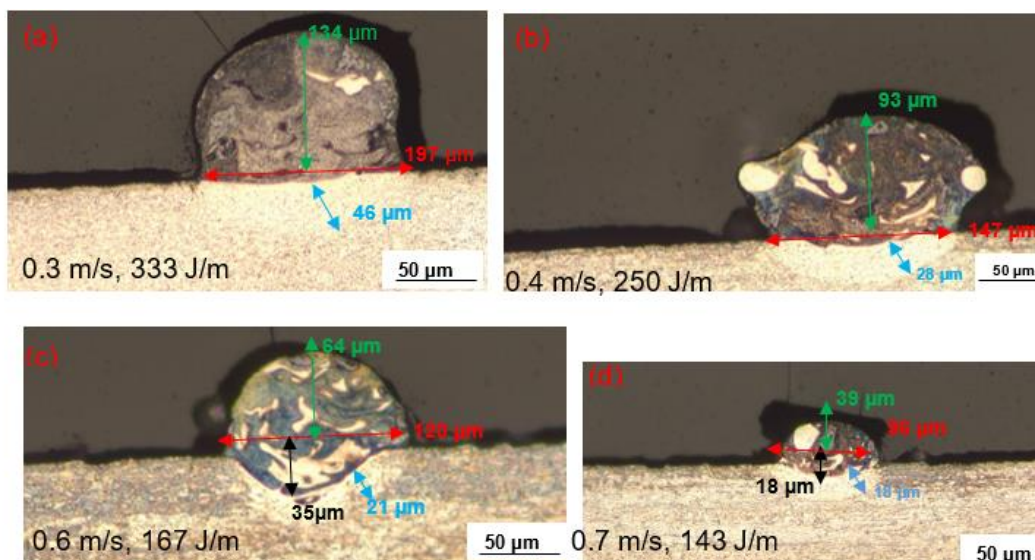


**Figure B2:** Cross-sectional views of tracks built at laser scanning speeds from 0.3 m/s to 0.7 m/s with a constant power of 100 W

Though it was concluded from the images in Figure B1 that the two leftmost tracks were the best choices, the cross-sections shown in Figure B2 indicate poor penetration into the substrate for both. Therefore, their corresponding parameters were considered unsuitable for the building of layers and 3D parts as they will cause delamination of the layers. The HAZ decreased with increasing laser scanning speed in Figure B2. All the tracks in Figure B2 showed a trend of decreasing height above the substrate and decreasing width with increasing laser scanning speed. The decreasing trend of width of tracks and HAZ showed that the increase in the laser scanning speeds reduces the dwell time of the laser on the powder bed, leading to insufficient melting of the powder and penetration through the substrate. Additionally, the humps or higher heights of the tracks were thought to be due to increased surface tension and viscosity. Li et al. (2017), Kornea et al. (2011), and Dzogbewu et al. (2022) reported separately that the formation of irregular track heights above the substrate was due to the complex behaviour of the melt pool that was governed by absorption of the energy in the laser beam, surface tension, viscosity, gravity, and capillary effects.

Moreover, the widths and heights of the tracks both decreased with increasing laser scanning speed, while the depth of penetration increased to a perceptible value at the laser scanning speed of 0.6 m/s, seen in in Figure B2 (c), and then decreased at the highest laser scanning speed of 0.7 m/s in Figure B2 (d). The increase and decrease in depth of penetration at the second highest and highest scanning speeds, respectively, is an abnormal behaviour that highlights an inconsistency in the variation of the depth of penetration at this value of laser power (100 W). This anomalous behaviour was also reported by Dzogbewu et al. (2022) in their work. The imperceptibly shallow depths of penetration at the two lowest scanning speeds were observed in Chapter 6 to be a result of very high LED that led to very wide and shallow tracks, as a result of induced very low surface tension and viscosity.

In conclusion, no best process parameter set was found, from amongst those used in this work for a laser power of 100 W and an SiC volume fraction of 10%, that could be used to print tracks with good characteristics.

## B2. The Effects of Different Laser Scanning Speeds at a Laser Power of 150 W

To study the effect of laser scanning speed on the characteristics of single tracks built at different laser scanning speeds and constant power, the tracks displayed in Figure B3 were used.

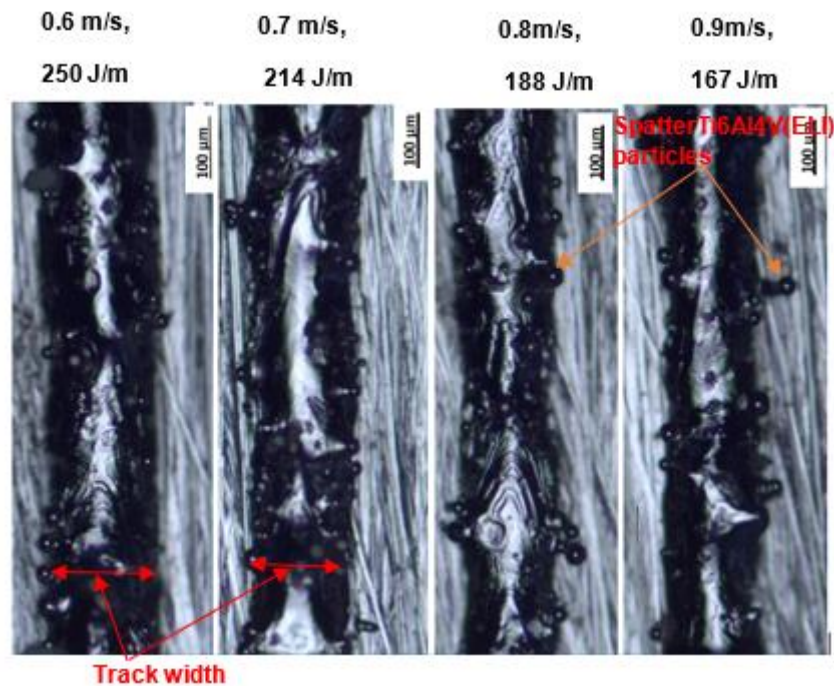


**Figure B3:** Single-track SEM images at a laser power of 150 W and different scanning speeds from 0.6 m/s to 0.9 m/s

All the tracks shown in Figure B3 indicated almost constant widths with a lot of spatter particles and partially melted particles at the sides of the tracks. Both tracks built with the lowest two scanning speeds exhibited some discontinuities. The widths of the tracks were observed to decrease with increasing laser scanning speed. However, the tracks at scanning speeds of 0.8 m/s and 0.9 m/s seemed to have better characteristics as it was noted that generally, their widths were wider than those of the other two scanning speeds. Wider track widths were obtained at low scanning speeds, which provided enough dwell time for the laser beam on the powder bed, thus allowing more time for the fusion of particles of powder, as was reported by Ullah et al. (2022).

It is known from literature that temperatures are high at the spot where the laser beam is directed and, therefore, the temperature of the melt pool is higher at the centre than at the periphery of a track (Yadroitsev et al., 2013). This means that the particles of

powder at the periphery of a track are not fully melted due to insufficient energy density and the accompanying decrease of temperature, leading to partially melted particles at the edges of the track, as was reported by (Dzogbewu et al., 2020), which in Figure B3 occurred at the higher laser scanning speeds. These partially melted particles are undesirable as they lead to poor quality of the surface of build parts.

Moreover, it has been reported that the spatter particles occur due to the ejection of the particles from the melt pool during the evaporation of the melt (Guo et al., 2021). This ejaculation of powder particles is caused by the low viscosity of the melt at high temperatures (Yadroitsev et al., 2013). Further investigation of the tracks built at a laser power of 150 W, whose top surface scans are shown in Figure B3, was done by studying their cross-sections in Figure B4, to verify their cross-sectional dimensions such as the depth of penetration into the substrate.

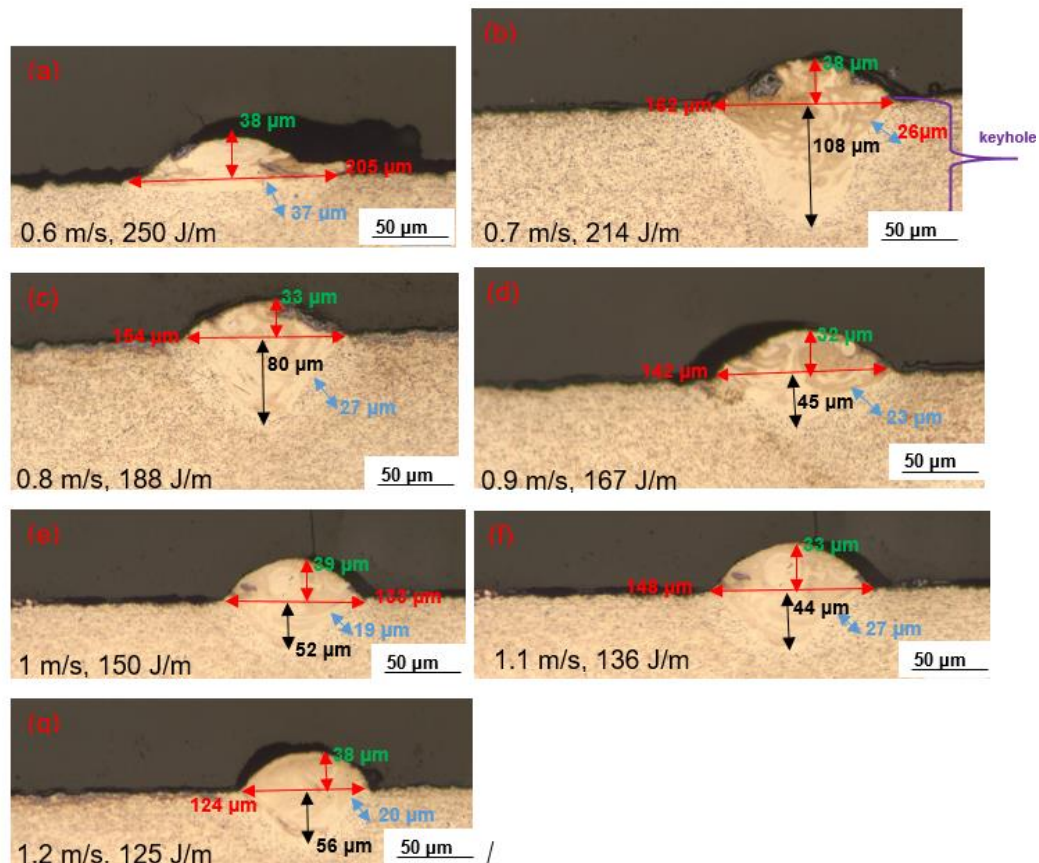


**Figure B4:** Cross-sections of tracks built at different laser scanning speeds from 0.6 m/s to 1.2 m/s at a constant laser power of 150 W

At the low scanning speed of 0.6 m/s, the cross-section was observed to have very little penetration into the substrate. This was thought to have been a result of the

Page | 220

outward flow of the melt pool at the high prevailing LED, that caused the formation of a shallow and wide track. This behaviour is consistent with the work of Antony et al. (2015). Shreshta et al. (2022) also observed unusual formation of discontinuous tracks at high energy density. They reported that at low values of laser power, discontinuous tracks were formed at low scanning speeds despite the prevailing high LED.

Dzogbewu et al. (2022) also obtained similar results where the powder was fully melted but with little penetration despite the energy density being high. An increase in the scanning speed to 0.7 m/s, led to the formation of a keyhole. This was a sign of the predominance of the keyhole mode mechanism of melting, whereby recoil pressure arising from evaporation of the melt pushed the melt downward and outward from the centre of the track to its edges, causing the formation of a deep depression into the substrate that is referred to as a keyhole, as was reported by Dzogbewu et al. (2022), Khairallah et al. (2015), and Xiao et al. (2021).

The depth of penetration and width of the tracks decreased with rising laser scanning speed from 0.7 m/s to 1.2 m/s because as the speed increased, LED decreased due to less dwell time of the laser beam that limited its time to penetrate through the substrate (Li et al., 2017). A change from the keyhole melting to conduction melting modes was seen to occur between the scanning speeds of the cross-sections shown in Figure B4 (c) and (d). The depth-to-width ratio of the cross-section of the track shown in Figure B4 (c) was 0.5 and nearly of a semi-circular shape. The former is known to be a sign of good penetration into the substrate or previous layer, while the latter provides a large surface area onto which a subsequent layer can bond and are both desirable traits. The track, at a scanning speed of 0.9 m/s, gives a depth-to-width ratio of the track a ratio of 0.3, which is less than the limiting value of 0.5 and denotes poor penetration. Therefore, it was concluded that the best scanning speed at a laser power of 150 W was 0.8 m/s, which worked out to an LED of 188 J/m.

### **B3. The Effects of Different Laser Scanning Speeds at a Laser Power of 200 W**

The micrographs of single tracks built at a constant laser power of 200 W and different laser scanning speeds from 0.8 m/s to 1.6 m/s are shown in Figure B5.

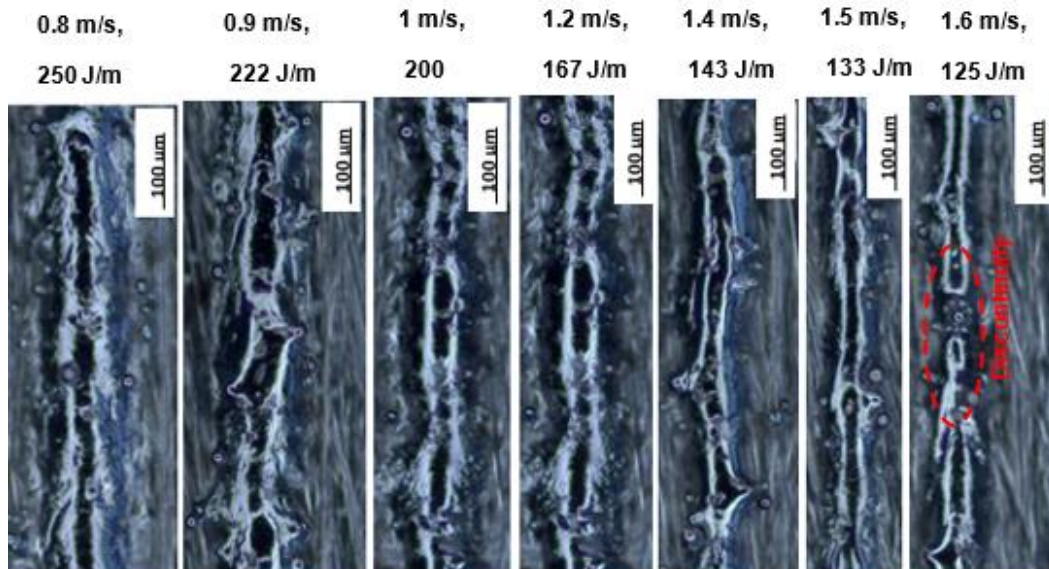


**Figure B5:** *Micrographs of single tracks built at a constant laser power of 200 W and different laser scanning speeds from 0.8 m/s to 1.6 m/s*

The images in Figure B5 showed tracks with widths that reduced with increasing scanning speed. The tracks built with laser scanning speeds from 0.8 m/s to 1.5 m/s were continuous with small variations of widths, while the track built at a laser scanning speed of 1.6 m/s exhibited discontinuities. The results indicated sufficient energy density to melt the powder except for the track at the high laser scanning speed of 1.6 m/s. Ullah et al. (2022) observed that the laser energy input per unit area reduces as the scanning speed increases, thus leading to insufficient melting of the powder. This agrees with the results in Figure B5 at the highest laser scanning speed of 1.6 m/s, where discontinuities of the printed track were seen to occur. It was noted that the variation of the widths of tracks was smallest for scanning speeds lying between 0.8 m/s. to 1.2 m/s.

At this stage, it was difficult to identify the best single tracks because all, but one track, indicated good continuity. Therefore, all their cross-sections shown in Figure B6 were studied to investigate their geometrical characteristics for purposes of determining the best parameters at this magnitude of laser power.

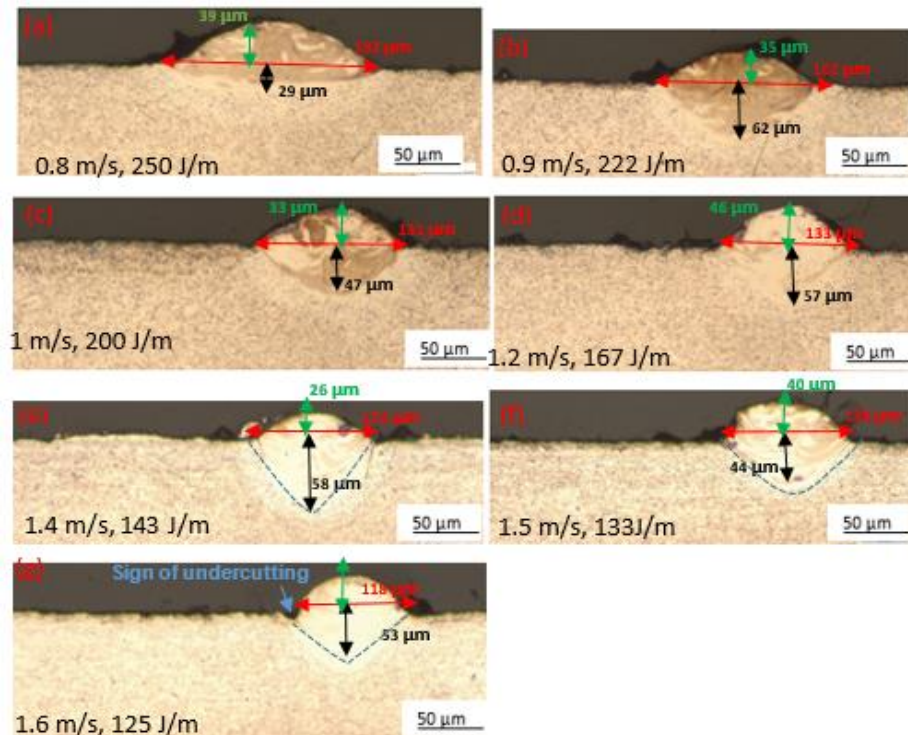


**Figure B6:** Cross-sectional images of tracks built at laser scanning speeds from 0.8 m/s to 1.6 m/s

At the lowest scanning speed of 0.8 m/s and highest LED of 250 J/m, it was clear from Figure B6 that penetration into the substrate was very poor. This was thought to be due to the prevailing high LED due to low scanning speed, which gave rise to the high temperatures of the melt pool. High temperatures in the melt pool cause a decrease in the viscosity and surface tension of the molten metal, thus improving its wetting ability, leading to wider melt pools that are shallow (show poor penetration) (Antony et al., 2017).

As the scanning speed was increased from 0.9 m/s to 1.6 m/s, there was no continuous decreasing trend in width and depth of penetration, or height of the tracks, which were rather seen to vary inconsistently with rising laser scanning speed. The tracks at scanning speeds of 0.9 m/s, and 1 m/s had a similar depth-to-width ratio of 0.4, which is below the optimum value of 0.5 and was an indication of poor penetration. The track built at a laser scanning speed of 1.4 m/s, and an LED of 143 J/m had a depth-to-width ratio of 0.5, which indicated good penetration. The top surface view of the track built at a laser scanning speed of 1.4 m/s showed its width to be narrower than those built at lower scanning speeds. This was considered to be disadvantageous for building

layers because it required more multiple tracks to complete a layer and increasing the production time for 3D printing of parts. However, considering both the top surface view and the cross-section with a satisfying depth-to-width ratio of 0.5, the set of process parameters used to build the track with the cross-section shown in Figure B6 (d), with a laser power of 200 W and laser scanning speed of 1.4 m/s, was deemed the best at this value of laser power.

#### **B4. The Effects of Different Laser Scanning Speeds at a Laser Power of 250 W**

The single tracks built at a constant laser power of 250 W, with different laser scanning speeds shown in Figure B7 were used to study and discuss the morphology of their top surfaces.

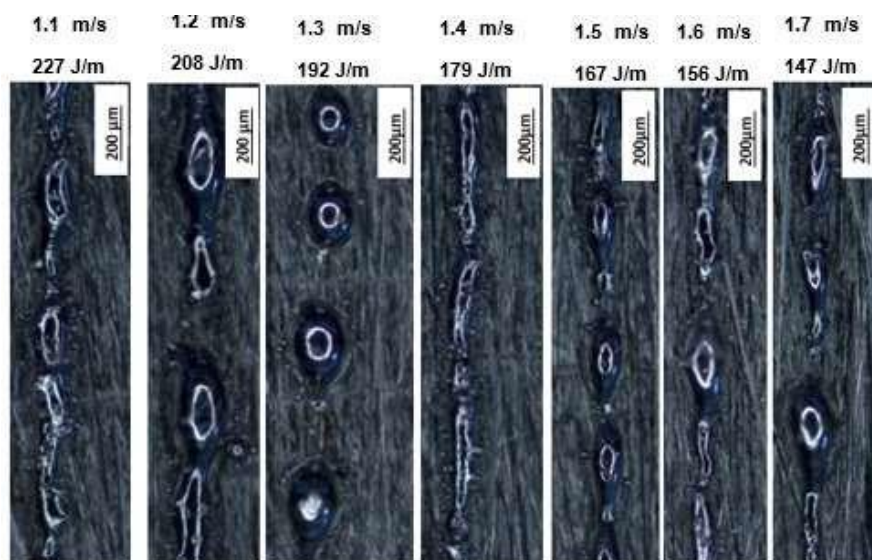


**Figure B7:** *Single tracks built at a constant laser power of 250 W and different laser scanning speeds from 1.1 m/s to 1.7 m/s*

All the tracks shown in Figure B7 depicted poor surface characteristics. From the lowest scanning speed of 1.1 m/s to the highest scanning speed of 1.7 m/s, they all showed the balling effect and discontinuities to different extents. Balling occurs when molten material does not wet well to the underlying substrate due to high surface tension and viscosity, normally as a result of low dwell times of the laser beam on the powder bed (Mumtaz et al., 2010). The micrographs in this figure showed that none of the combinations of process parameters used in this case were good. Therefore, none of them were considered best for printing the layers and 3D parts, and no further

analysis of the tracks was carried out.

### B5. The Effects of Different Laser Scanning Speeds at a Laser Power of 300 W

The single tracks produced at a constant laser power of 300 W, with different laser scanning speeds shown in Figure B8 were used to study and discuss the morphology of their top surfaces.

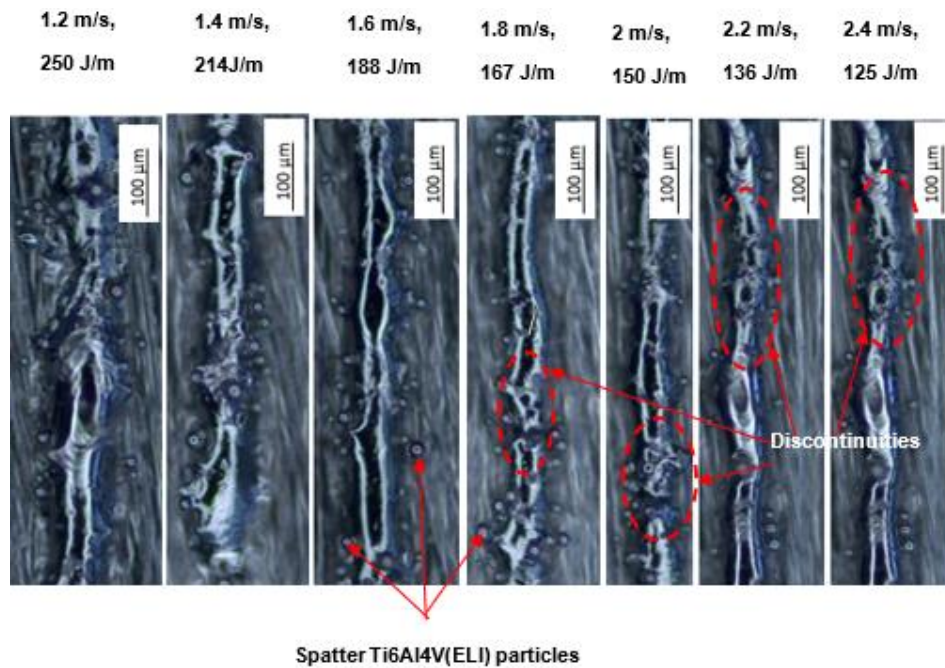


**Figure B8:** Single tracks built at a constant power of 300 W with different laser scanning speeds from 1.2 m/s to 2.4 m/s

All the tracks in Figure B8 exhibited the common trait of narrowing down with increasing laser scanning speed. The tracks built at laser scanning speeds of 1.8 m/s to 2.4 m/s showed discontinuities unlike those built at lower laser scanning speeds of 1.2 m/s, 1.4 m/s, and 1.6 m/s. This ties in with the separate observations of Shrestha et al. (2019) and Ullah et al. (2022). The track built at a scanning speed of 1.6 m/s had a fairly uniform width, with signs of necking, as indicated by the yellow dotted circle superimposed on it. It was observed that incidences of spatter particles decreased with increasing laser scanning speed. This was because of decreasing energy input per unit area with increasing laser scanning speed. Andani et al. (2018) noted that at high LED and low laser scanning speeds, the powder melts and evaporates. Consequently, a high vapour pressure, known as recoil pressure, is created that ejects Ti6Al4V(ELI)

powder particles away from the melt causing their occurrence as spatter particles (Andani et al., 2018). Cross-sections of the tracks in Figure B8 are presented in Figure B9 for use in studying their depths of penetration and widths.

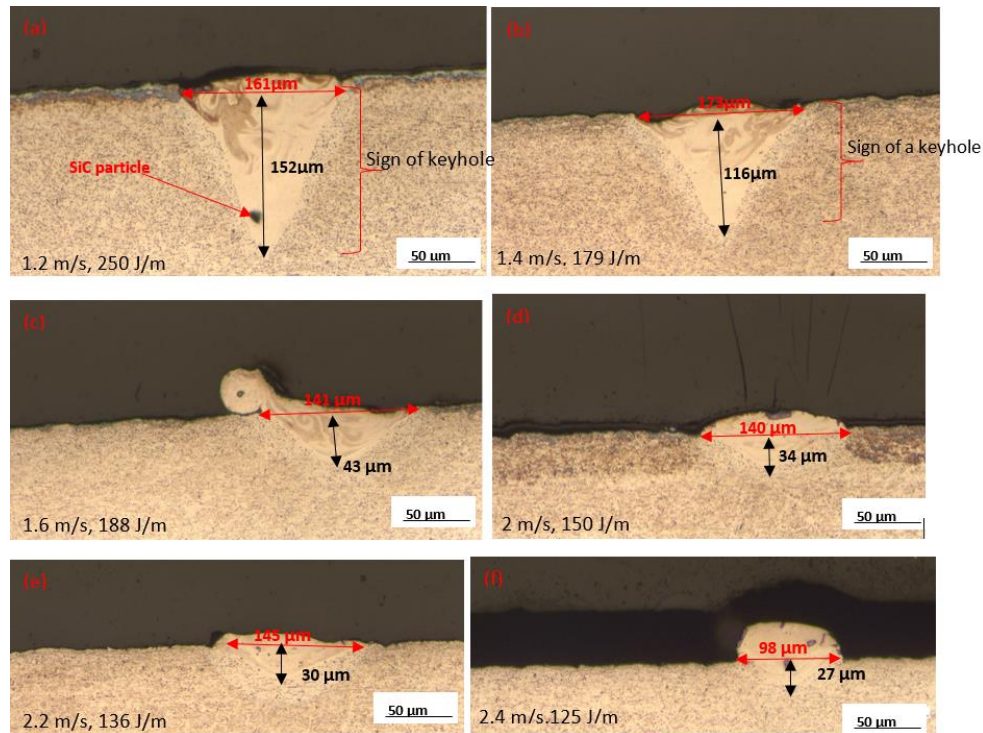


**Figure B9:** Cross-sections of the single tracks printed at the laser power of 300 W with different laser scanning speeds from 1.2 m/s to 2.4 m/s

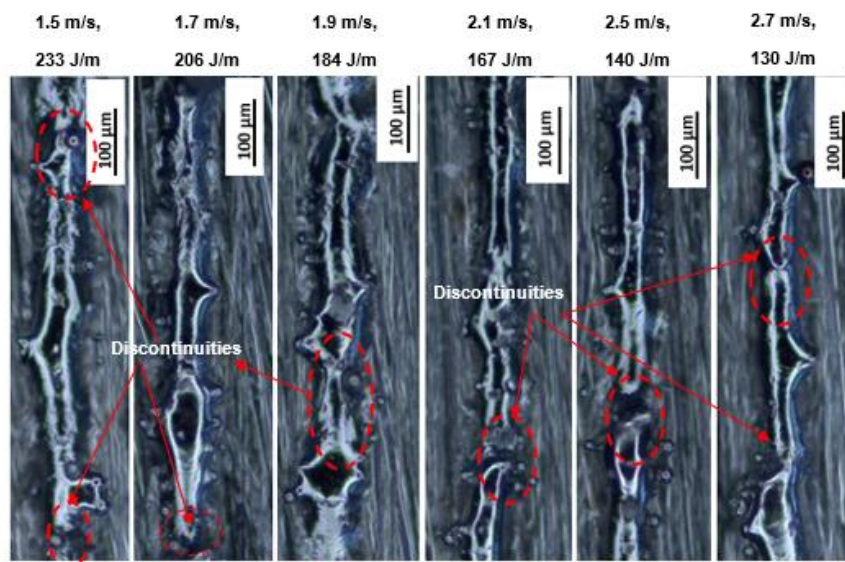
The cross-sections in Figure B9 (a and b) showed the keyhole effect with depth-to-width ratios of 0.9 and 0.7, respectively. It is known from literature that depth-to-width ratios above the optimum ratio of 0.5 denote the keyhole effect. The keyhole effect occurred at the low laser scanning speeds of 1.2 m/s and 1.4 m/s with correspondingly high energy densities of 250 J/m and 214 J/m. It is known that at high energy inputs, the laser beam melts and vaporizes powder to generate vapour recoil pressure that pushes the melt pool downward and sideways, thus facilitating deep penetration of the laser beam into the substrate (Dzogbewu et al., 2017, Kusuma et al., 2016, and Fotovvati et al., 2018). Both the width of the track and depth of penetration decreased with the increasing laser scanning speed.

Moreover, as has previously been discussed in this chapter, as the laser scanning speed increases, the laser beam runs faster over the powder and does not get enough time to melt powder or penetrate through to the substrate. The gradually decreasing

volume of melt with increasing laser scanning speed, represented by the progressively lower values of width and depth of the built tracks, were observed in Figure B9. These results tied in with the findings of (Jeon et al., 2022), who reported that the width, depth, and height of the melt pool decreased with increasing scanning speed, indicating that the increase in the scanning speed had an effect similar to a decrease in laser power. This was so in the present work, with the exception that there was no continuous decrease of the heights and widths of the printed tracks with increasing laser scanning speed. The same applied to the width of tracks apart from the second last width in Figure B9. Though the top view of the track built at a laser scanning speed of 1.6 m/s showed to be a good track with a fairly constant width and no discontinuities, its value of depth-to-width ratio of 0.2 was not optimal. The depth-to-width ratios of the other cross-sections in Figure B9, apart from the two mentioned had values of 0.9 and 0.7, which were all below 0.32. Therefore, there were no best process parameter sets in this case that could lead to creation of tracks with acceptable geometrical characteristics, at this value of power.

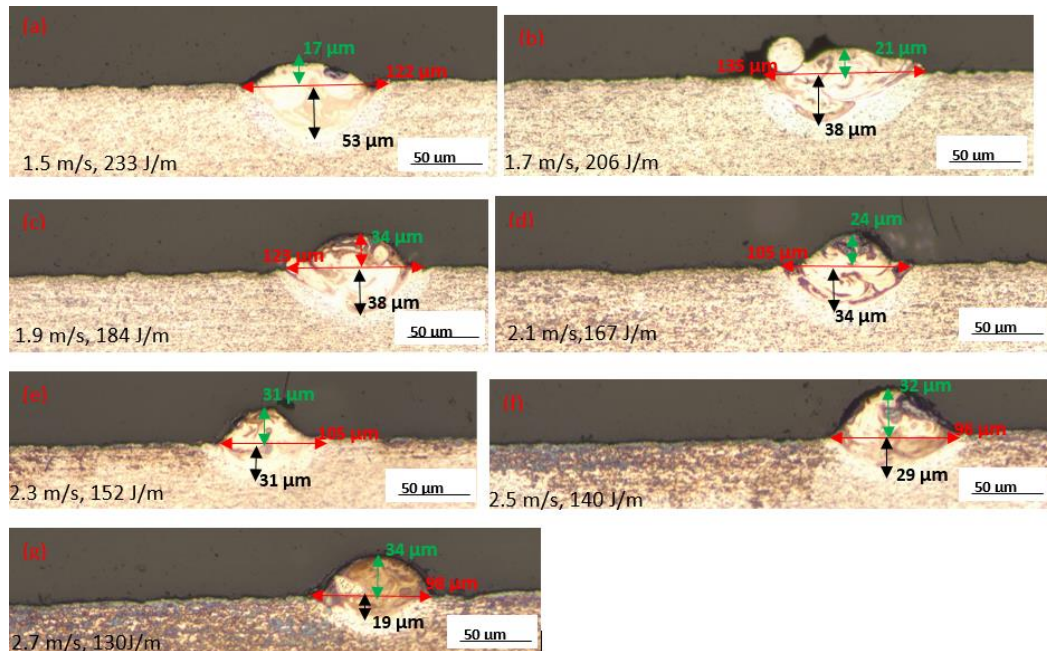
### **B6. The Effects of Different Laser Scanning Speeds at a Laser Power of 350 W**

The images of single tracks produced at a constant laser power of 350 W, with different laser scanning speeds from 1.5 m/s to 2.7 m/s, shown in Figure B10, are now used to study and discuss the morphology of their top surfaces.



**Figure B10: Single tracks built at the highest laser power of 350 W and different scanning speeds**

All the tracks shown in Figure B10 had signs of discontinuity within the highlighted hatched red ellipses, thus making their process parameters all unsuitable for building of multiple tracks and layers. Nevertheless, their cross-sections shown in Figure B10 were studied and discussed.



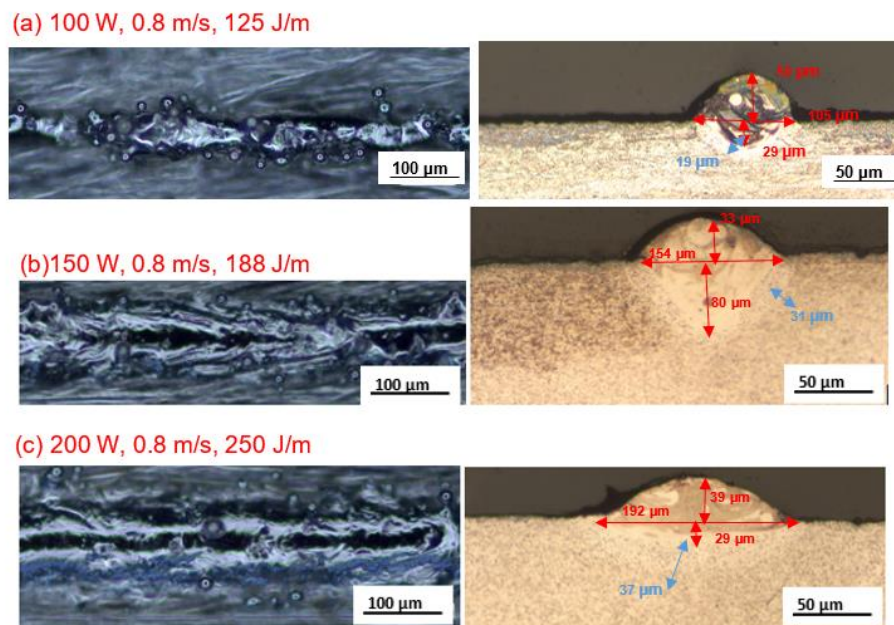
**Figure B11:** Cross-sections of single tracks printed at a laser power of 350 W with different laser scanning speeds from 1.5 m/s to 2.7 m/s

Figure B11 shows that the track-heights above the substrate generally increased with increasing laser scanning speed. The ratios of depth-to-width were also to decrease from just over 0.4, down to just above 0.3. As was noted earlier in this chapter, increased laser scanning speed comes with reduced dwell time of the laser beam and an attendant reduction of the LED. This led to reduced depths of penetration and increased viscosity that resulted in increased heights. The low depth-to-width ratios and the presence of discontinuities in all the tracks in this figure implied that there was no process parameter set suitable to build 3D specimens.

## **B7. The Effects of Constant Scanning Speed at Different Values of Laser Power**

To study the effect of laser power on the geometrical characteristics of the tracks, the top and cross-sectional views of the single tracks built at a constant laser scanning

speed of 0.8 m/s at different laser powers from 150 W to 200 W, shown in Figure B12, were used.



**Figure B12:** *Single tracks built at a constant scanning speed of 0.8 m/s with different powers of 150 W and 200W*

In the laser melting process, power is the most significant parameter in determining the depth of penetration, while laser scanning speed is a significant factor in determining the width of the HAZ (Shrestha et al., 2019). The cross-sections in Figure B12 and the top surface views showed that the magnitude of laser power affected the width of tracks. The top surface of the built tracks showed increasing track-widths with increasing laser power from 100 W to 200 W. The same trend was observed in the related cross-sections.

The depth of penetration increased from a value of power of 100 W to 150 W and then decreased as the power was raised to 200 W. In the first case, the ratio of depth-to-width of the track was 0.5, while for the second case it was a low value of 0.2. The reduction in the depth of penetration and attendant increase in the width of the built track with increasing power above 150 W was thought to have been caused by high temperatures created in the melt pool by the higher power, thus causing a decrease in the viscosity and surface tension of the molten metal. This in turn is thought to have led to improved wetting ability of the melt and, therefore, the formation of wider and shallower melt pool accompanied by poor penetration, which was consistent with the

work of Antony et al. (2017). Like the widths of the built tracks, the width of the HAZ in the cross-sections, shown in Figure 6.28, increased with increasing power.

## APPENDIX C. ANALYSIS OF SINGLE TRACKS BUILT AT A VOLUME FRACTION OF SIC OF 15 % IN AN SIC/TI6AL4V(ELI) COMPOSITE

### C1. The Effects of Different Laser Scanning Speeds at a Laser Power of 100 W

The morphological characteristics of the images of single tracks built at a laser power of 100 W and laser scanning speeds varying from 0.4 m/s to 0.9 m/s, shown in Figure C1, are now discussed.

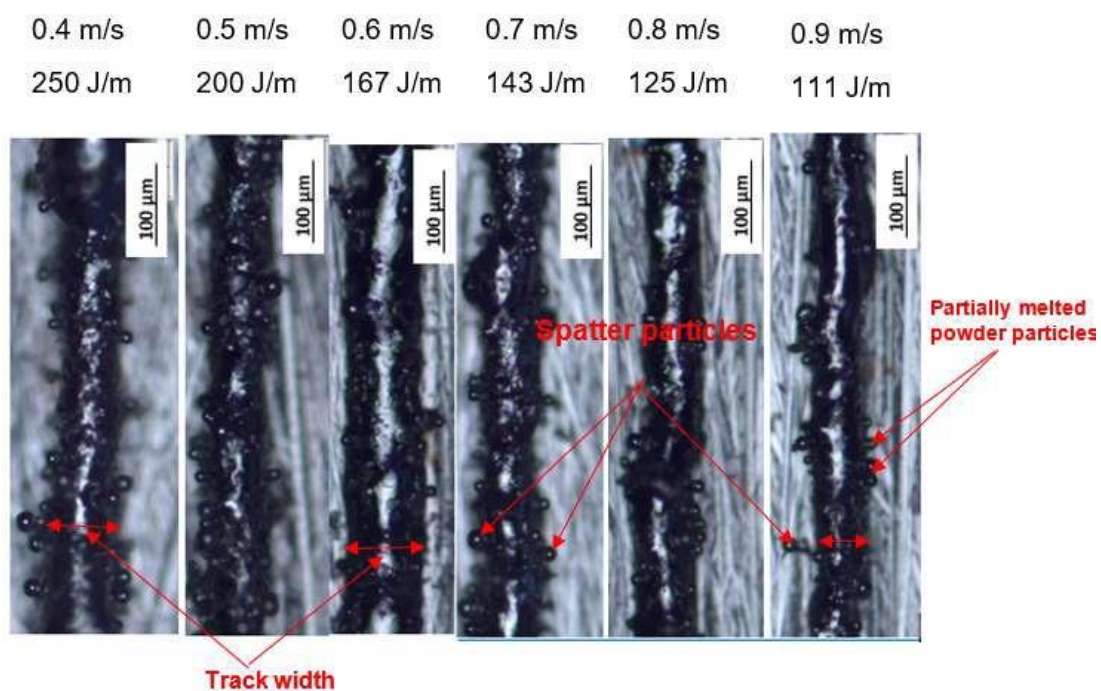


**Figure C1:** Single tracks at a constant laser power of 100 W with different laser scanning speeds from 0.4 m/s to 0.9 m/s

As previously discussed in this chapter, an increase in laser scanning speed at a constant laser power leads to a reduction in the width of tracks. This same phenomenon was noticeable in Figure C1. At the low power of 100 W, the top view of the track showed a lot of spatter particles at its sides. The spatter particles decreased in number as the scanning speed increased. Increasing the laser scanning speed leads to a decrease in width of the track and spatter particles (Lei et al., 2019). Andani et al. (2018) studied the effect of energy input on the formation of spatter particles and reported that at high energy densities, the powder is melted and evaporated leading

to the creation of vapour recoil pressure that ejects part of the molten material out of

the melt pool, which then solidifies quickly to form spherical particles known as spatter particles.

It was challenging to select the best track at this stage as they all had identical features. As a result, the influence of scanning speed on the single tracks displayed in Figure C1 was studied further by analysing their cross-sections presented in Figure C2 to help find the ideal process parameters.

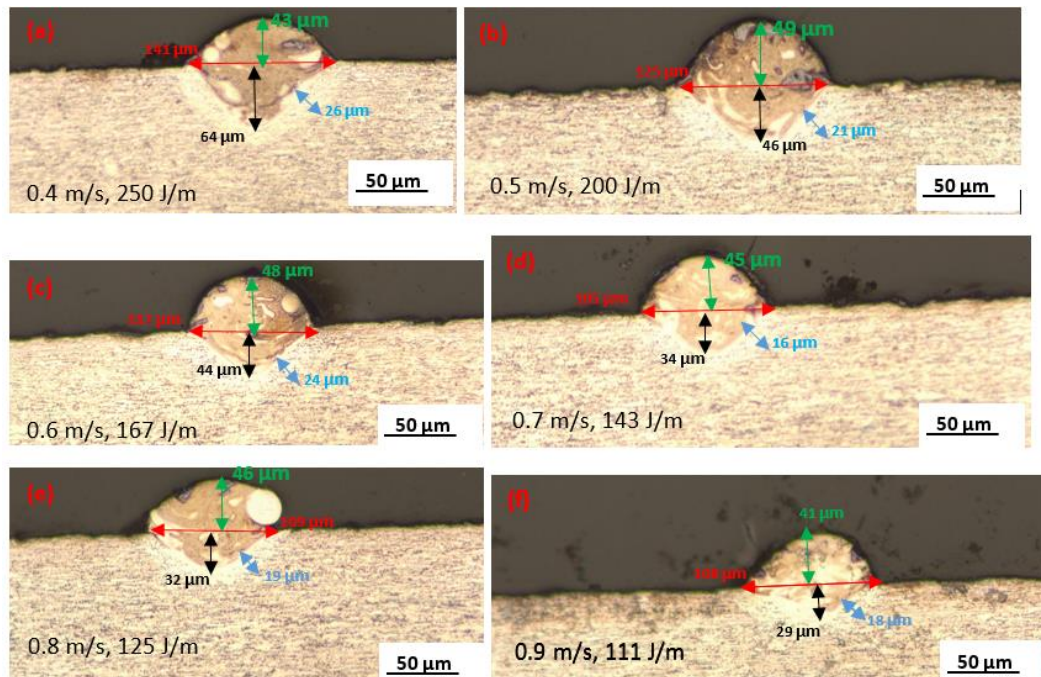


**Figure C2:** Cross-sectional views of single tracks produced at a constant laser power of 100 W with different scanning speeds from 0.4 m/s to 0.9 m/s

The cross-sections in Figure C2 showed that the depth of penetration into the substrate decreased continuously as the scanning speed increased. At a low scanning speed of 0.4 m/s and high LED of 250 J/m, a nearly semi-circular depth of penetration was observed, with a depth-to-width ratio of 0.5. A depth-to-width ratio of 0.5 is reported as the optimum ratio, leading to a good depth of penetration that is enough to sufficiently bond layers during the printing of parts and prevent delamination (Gao et al., 2019). Low laser scanning speeds at a constant power give rise to higher values of linear energy density, and there is enough time for the laser beam to melt the powder and penetrate the substrate, as was the case in Figure C2 (a). Lei et al. (2019) reported that at low laser scanning speeds, the spreadability and wettability of the melt are adequate. These findings tie in with the results presented in Figure C2 (a to d) that

showed reducing widths of tracks with increasing laser scanning speed, above which the track widths showed an inconsistent trend. This latter abnormality of trend was also reported separately by Dzogbewu et al. (2022) and Kusuma et al. (2016).

High scanning speeds are thought to have reduced the linear energy density, which led to reduced energy input in a given period and, therefore, insufficient melting of powder, giving rise to the decreased depth of penetration in Figure C2 (b to f), as was also noted by Karimi et al. (2019). There was no concurrent increase in the heights of the tracks with increasing laser scanning speeds that is expected of reducing wettability and spreadability. This is inconsistent with the observations by Koupryanoff et al. (2021) that insufficient energy density together with the related high melt viscosity and high surface tension gradient lead to the formation of humps or increased track-height above the substrate.

From the foregoing discussion, the optimal laser scanning speed at this power level was identified as 0.4 m/s, with an attendant LED of 250 J/m. This is supported by the optimal depth-to-width ratio of 0.5, as well as a depth of penetration greater than the layer thickness, which are expected to result in adequate bonding of preceding layers. Although top surface scans revealed spatter particles, they can be removed by using an appropriate rescanning approach during part manufacture.

## **C2. The Effects of Different Laser Scanning Speeds at a Laser Power of 150 W**

A study of the geometrical characteristics of the single tracks produced at a constant laser power of 150 W with different laser scanning speeds, shown in Figure C3, are now presented.

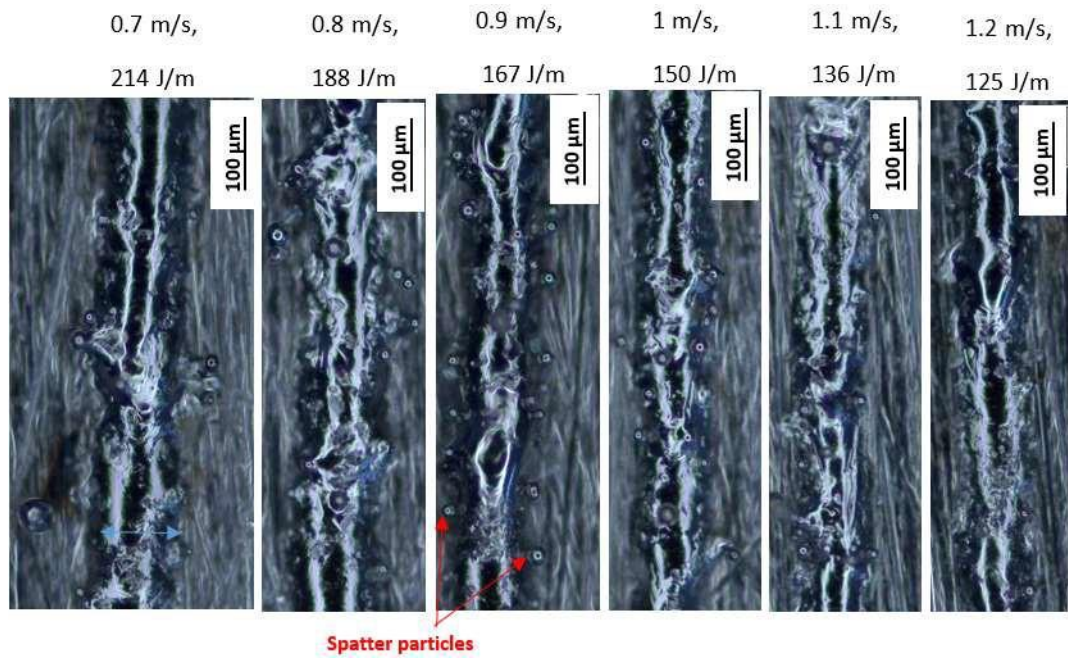


**Figure C3:** *Single tracks at a constant laser power of 150 W with different laser scanning speeds from 0.7 m/s to 1.2 m/s*

All the tracks in Figure C3 showed continuity and almost even widths. The tracks at the low laser scanning speeds of 0.7 m/s and 0.8 m/s and those at the high laser scanning speeds of 1.1 m/s and 1.2 m/s show fewer spatter particles at the edges of the tracks. A higher number of spatter particles was observed at the laser scanning speeds of 0.9 m/s and 1 m/s.

It was challenging to select the best process parameter set solely from the analysis of the top views of the tracks as, apart from the point about spatter particles, there was no clear difference between them. Therefore, their cross-sections, presented in Figure C4, were used to further study their depths of penetration, HAZ, and heights to assist in selecting the best process parameter set at this value of laser power.

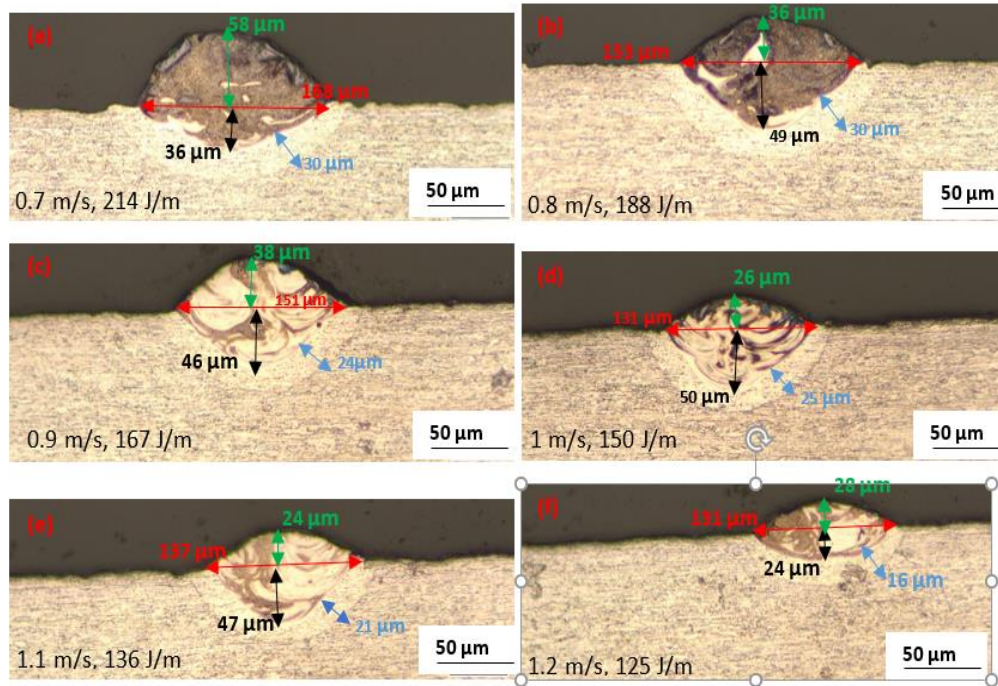


**Figure C4:** Cross-sectional views of single tracks produced at a constant laser power of 150 W, with different scanning speeds from 0.7 m/s to 1.2 m/s

It was observed that as the LED decreased with increasing laser scanning speeds, the track width increased continuously (Figure C4 (a to d)). Figure C4 (e and f) showed an inconsistency in the relationship between the laser scanning speed and width of the tracks. There was no continuous trend observed of increasing or decreasing heights of tracks and depths of penetration with increasing laser scanning speed. Bertolli et al. (2017) studied the variation of heights and widths of tracks with changing volumetric energy density (VED) and found that higher heights of tracks were due to Plateau-Rayleigh instability and poor wettability of the melt on the substrate. They mentioned that as the laser scanning speed increased, the contact angle increased due to high surface tension and poor wettability. Therefore, the tracks changed from a flat and shallow shape to a taller and narrower shape. They further observed that track heights greater than the layer thickness were undesirable as they were likely to cause jamming of the recoating device during multi-layer processes.

All the tracks in this figure exhibited cross-sectional characteristics that denoted a conduction mode of melting, with inadequate penetration and depth-to-width ratios less than the reported ideal value of 0.5. Based on this and the observed narrow tracks with spatter particles from the top surface view, it was possible to conclude that there

was no optimal set of process parameters for this value of laser power.

### C3. The Effects of Different Laser Scanning Speeds at a Laser Power of 200 W

The influence of different scanning speeds on the widths and depths of penetration of tracks at this magnitude of laser power was investigated by analysing cross-sectional views of the tracks whose surface scans are displayed in Figure C5.

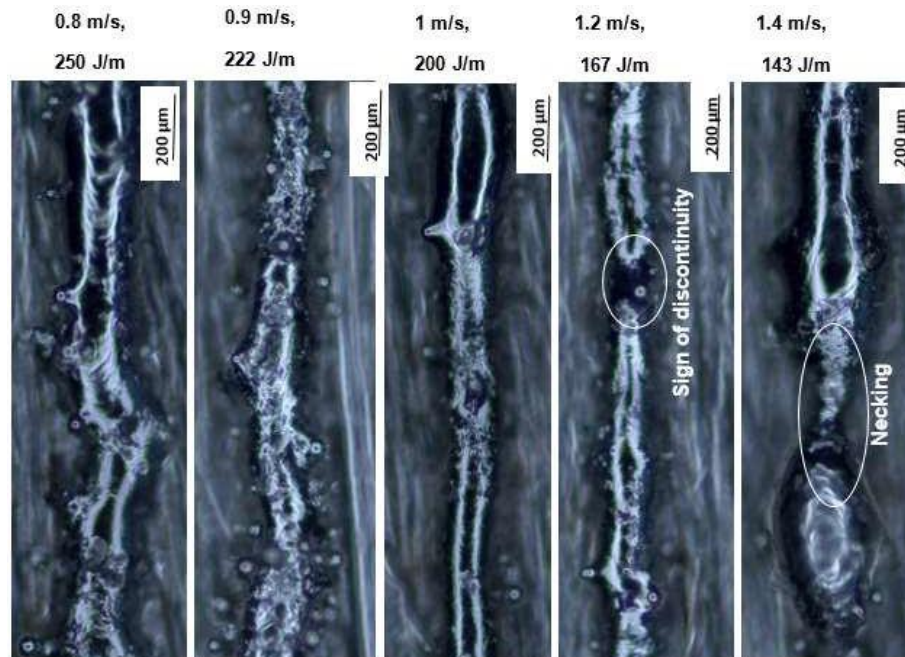


**Figure C5:** *Single tracks at a constant laser power of 200 W with different laser scanning speeds from 0.8 m/s to 1.4 m/s*

The tracks in this figure showed a high number of spatter particles at their peripheries for the lower laser scanning speeds of 0.8 m/s and 0.9 m/s, which reduced with rising laser scanning speed. At the high laser scanning speed of 1.2 m/s, the track showed a discontinuity. Further increase in the laser scanning speed to the highest value of 1.4 m/s led to necking. Necking and discontinuities are the result of insufficient energy input, which is not enough to achieve complete melting of the powder and substrate material. This leads to the formation of small melt pools that then break up into balls easily because of Rayleigh instability (Shi et al., 2017). The results shown in this figure were consistent with the findings of Wang et al., 2018, who recognised that a faster scanning speed leads to a smaller melt pool volume and shallower HAZ. The cross-sections of the tracks shown in this figure are presented in Figure C6 for further discussion.

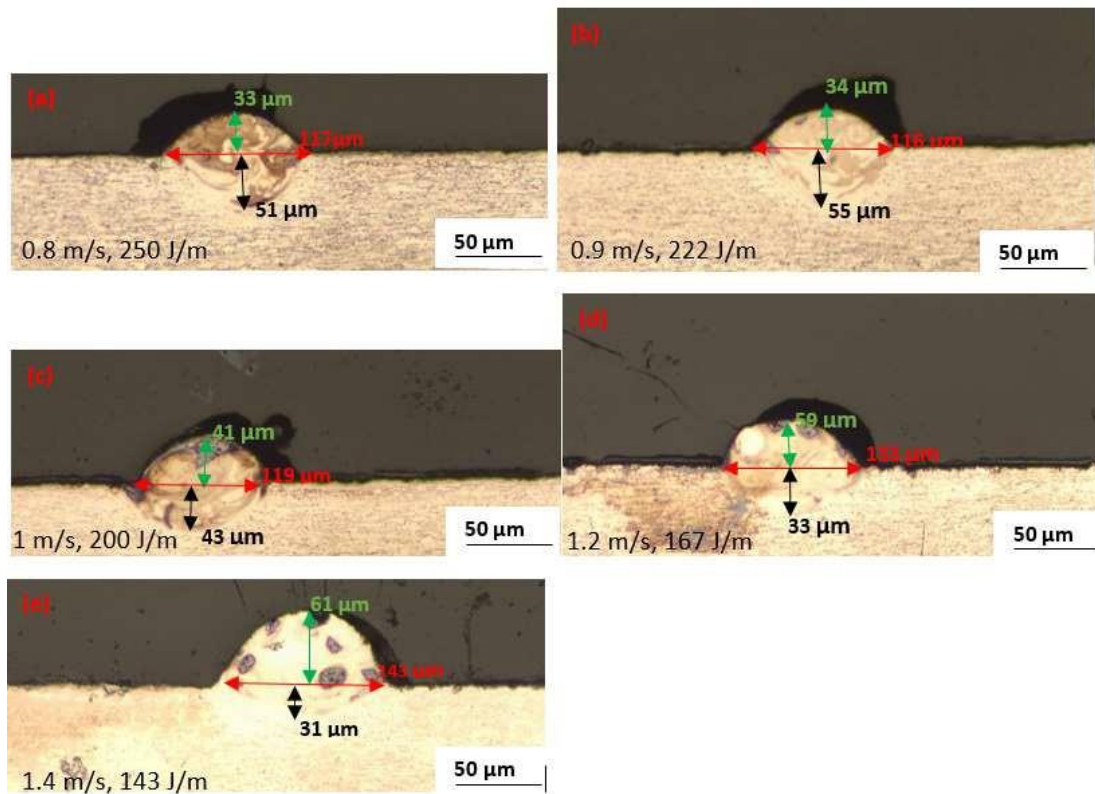


**Figure C6:** Cross-sectional views of tracks produced at a constant laser power of 200 W with different laser scanning speeds from 1 m/s to 1.6 m/s

At this magnitude of power, a trend of decreasing depth of penetration with increasing scanning speed was observed from the laser scanning speed of 0.9 m/s to 1.4 m/s. The widths of the tracks varied inconsistently with increasing laser scanning speed, while the heights of the tracks increased consistently with rising laser scanning speed. Similar results were found by Shrestha et al. (2021), who reported that the variation in width of tracks as the LED increased was limited by the laser spot diameter. They further mentioned that the increase in energy density for the same laser spot size was likely to lead to an increase in the depth of penetration rather than width of tracks after reaching a certain depth. The authors further observed that the trend of increasing track height with increasing scanning speed was due to high melt pool viscosity and surface tension that increased with decreasing temperature of the melt pool.

The abnormality of a reduction in the depth of penetration at the lowest laser scanning speed instead of a continuation in the increase of the depth was observed in Figure C6 (a). This abnormality was recognized separately by Shrestha et al. (2021) and Kusuma et al. (2016), who observed that in some cases higher LEDs led to shallower

penetration. The cross-section built at a speed of 0.9 m/s in Figure C6 had a depth-to-width ratio of 0.5, which was expected to result in sufficient bonding between layers. The ratios of depth-to width for all the other cross-sections were either higher or lower than this value. The top view of the track shown in Figure C6 (b) was one of three in the figure that were continuous, with almost even widths. Therefore, for a laser power of 200 W, the laser scanning speed of 0.9 m/s with the attendant LED of 222 J/m, was deemed the best.

#### C4. The Effects of Different Laser Scanning Speeds at a Laser Power of 250 W

Figure C7 depicts the geometrical characteristics of the top surfaces of single tracks produced at a constant laser power of 250 W and differing laser scanning speeds from 1.1 m/s to 1.9 m/s.

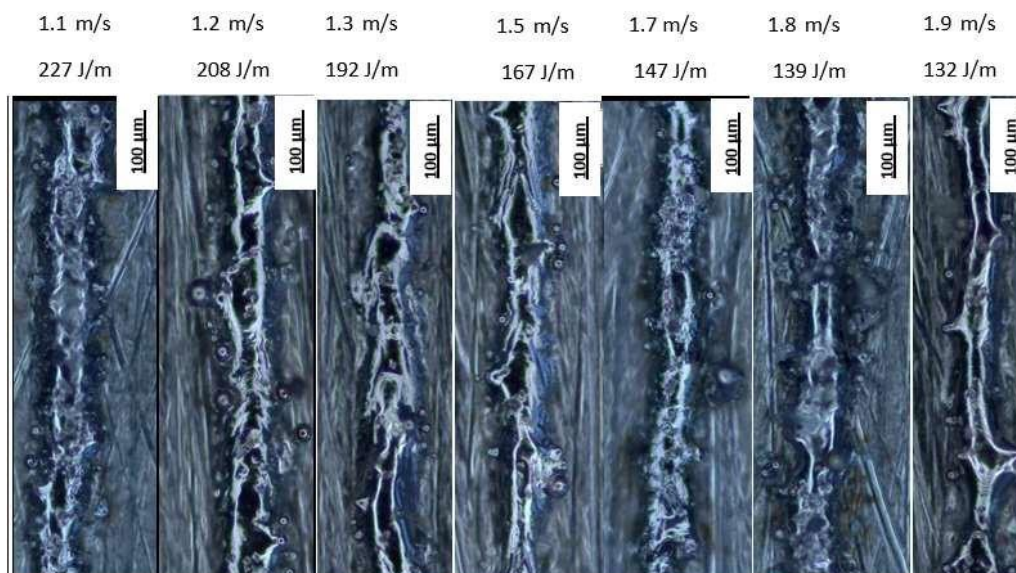


**Figure C7:** Top view of single tracks produced at a constant laser power of 250 W with different scanning speeds from 1.1 m/s to 1.9 m/s

The tracks shown in Figure C7 illustrate that the quantity of spatter particles decreases as the laser scanning speed increases. This was thought to be because at low laser scanning speeds the energy input is substantial causing some melt powder to be ejected from the melt and solidified somewhere else near the track's periphery. According to the equation for LED, decreasing the laser scanning speed at constant power increases the LED, which increases the energy input into tracks, which then leads to a higher temperature. Dzogbewu et al. (2023) reported similar findings. As it

was unclear which track to choose as the best at this stage, determining the best set of process parameters was not possible. As a result, further study of the cross-sections of these tracks was required to aid in the selection of the appropriate set of process parameters. Images of the cross-sections of these single tracks are presented in Figure C8.

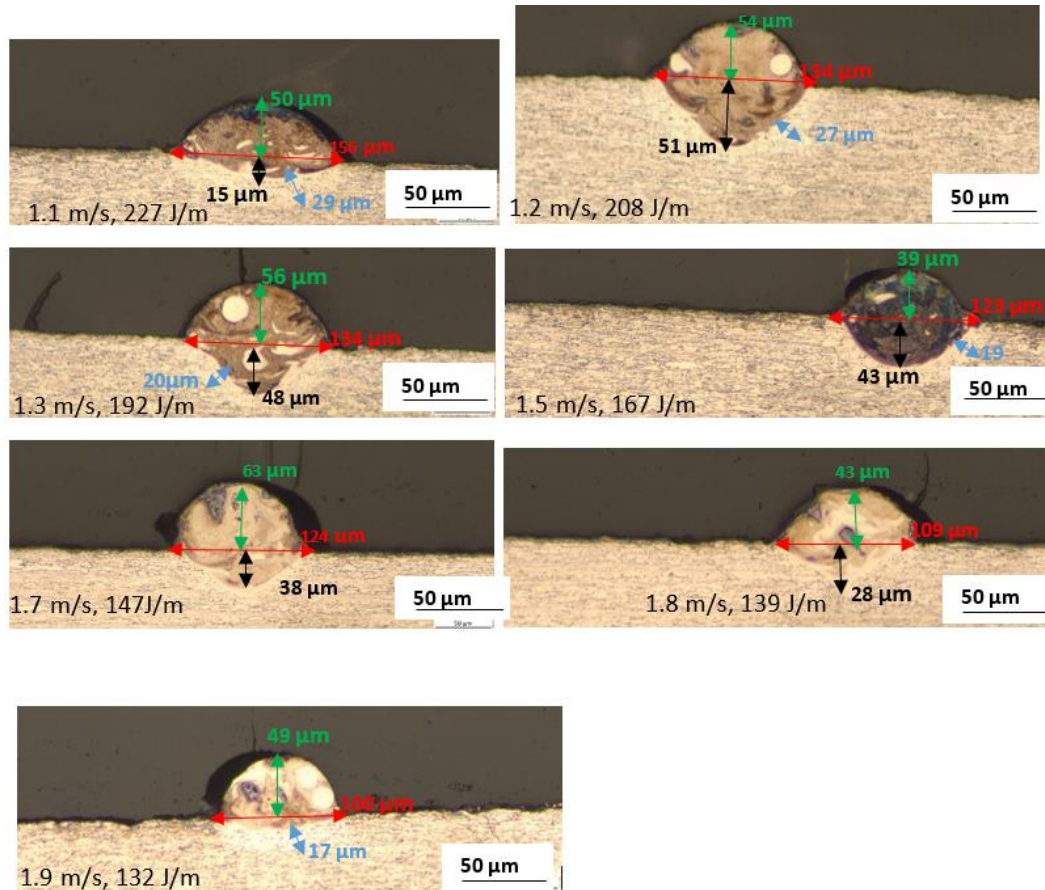


**Figure C8:** Cross-sectional views of tracks produced at a constant laser power of 250 W and different laser scanning speeds

Yadroitsava et al. (2015) investigated the peculiarities of the formation of single tracks at different laser power densities and observed that high-power laser densities could lead to very deep penetration and evaporation of the melt, or the production of shallow and wide melt pools, the latter which resulted in instability of the molten pool and a balling effect. The results found in Figure C8 showed the formation of a shallow and wide melt pool at the lowest scanning speed and highest LED of 1.1 m/s and 227 J/m, respectively, in this series of tracks. However, as the scanning speed increased from 1.2 m/s to 1.9 m/s, the depths of penetration and widths of the tracks decreased.

There was no clear trend of the heights of tracks with rising laser scanning speed. The interaction of the laser beam with powder decreases with an increasing scanning speed, with a consequent reduction in the width of the molten pool (Makoana et al., 2018). This tied in well with the results shown in Figure C8, where the widths of built tracks were seen to decrease as the laser scanning speed rose. The measured values of the widths and depths of penetration of the track cross-sections all resulted in depth-to-width ratios that were less than 0.5, which denoted poor penetration of the tracks. Insufficient penetration of tracks is expected to lead to debonding of layers during the 3D printing of parts, which is undesirable. Therefore, there was no best set of process parameters at this value of laser power that could be used for further building of 3D parts.

### C5. The Effects of Different Laser Scanning Speeds at a Laser Power of 300 W

The top surface scans of the tracks built at laser power of 300 W with different scanning speeds from 1.2 m/s to 2 m/s are shown in Figure C9 for use in studying their surface morphologies.

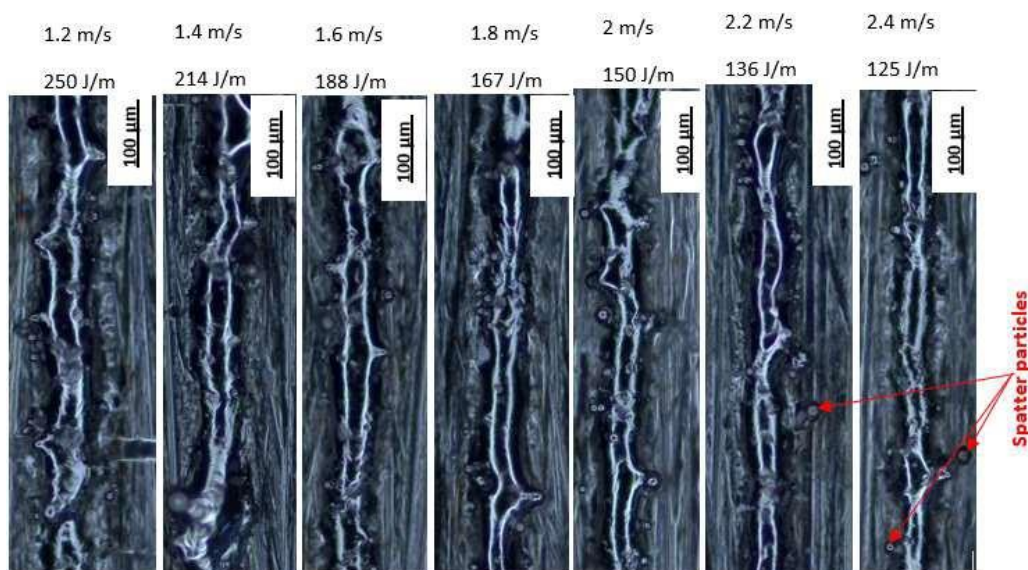


**Figure C9:** *Top surface view of the tracks built with a 300 W laser power at different scanning rates ranging from 1.2 m/s to 2.4 m/s*

In this figure, spatter particles were noticed to rise with increasing laser scanning speed. The widths of the tracks became narrower as the laser scanning speed increased from 1.8 m/s to 2.4 m/s. This is thought to have been a result of reduced values of LED available to melt powder at the higher laser scanning speeds. Previously

in this chapter it was noted that the width of the tracks was proportional to the linear energy density at the same power (Shrestha et al., 2019). Ullah et al. (2022) also observed that when the scanning speed increased, the laser energy input per unit area decreased, resulting in insufficient melting of powder.

The best tracks were found at the low laser scanning speeds ranging from 1.2 m/s to 1.6 m/s, with relatively continuous track widths. This called for more investigation of their cross-sections to aid in the identification of an optimal set of process parameters. Figure C10 depicts cross-sections of the single tracks produced at a constant laser power of 300 W and differing laser scanning speeds.

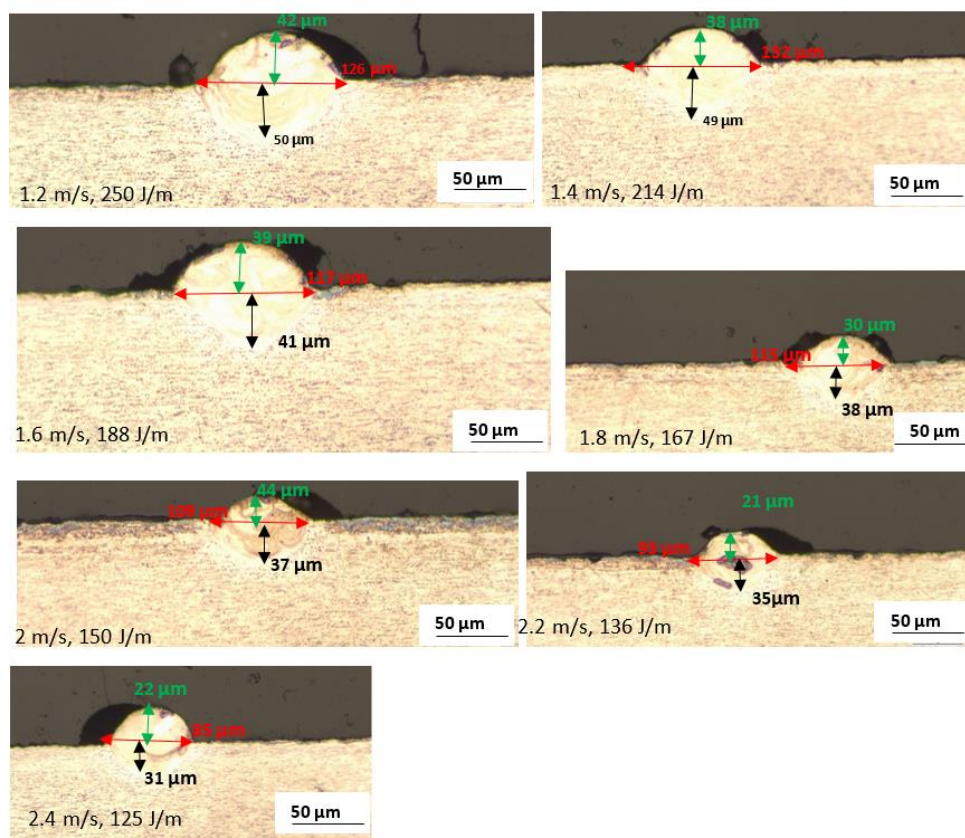


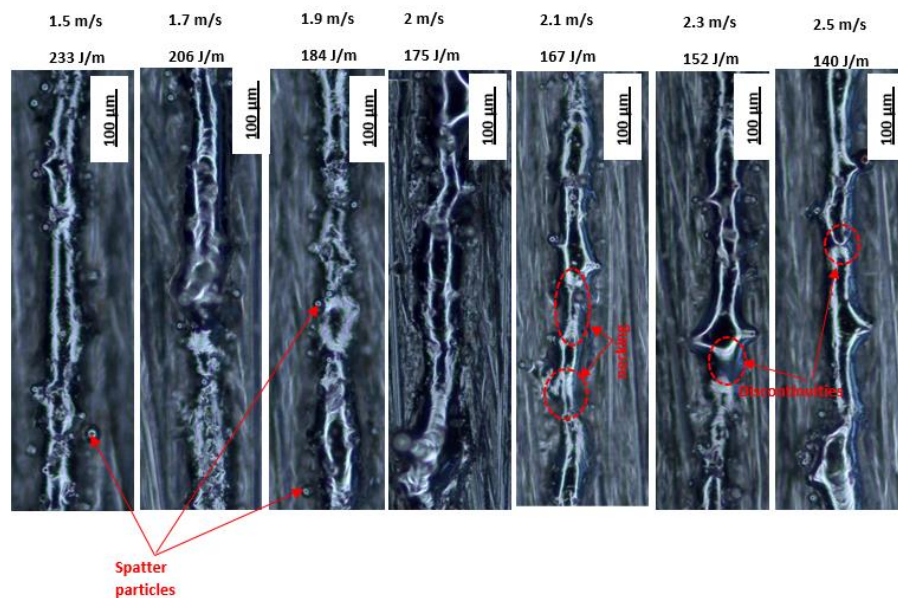
**Figure C10:** Cross-sectional views of tracks produced at a constant laser power of 300 W and different laser scanning speeds from 1.2 m/s to 2.4 m/s

At the high power of 300 W, both the depths of penetration and widths of tracks were observed to decrease with increasing laser scanning speed. This was consistent with the observations of Siao et al. (2021), that high laser scanning speeds yield short durations of heating of both the powder and substrate by the laser beam, thus leading to poor penetration. The results were also in agreement with those of Shi et al. (2017),

who reported that at a constant value of power, the increase in laser scanning speed led to a reduction in the width and depth of penetration of tracks. Furthermore, they commented that low scanning speeds allowed longer interactions of the laser with the powder and resulting melt pool that caused the development of higher temperatures and melting of more powder and lower viscosity of the melt that led to the formation of wider tracks. All the cross-sections in Figure C10 had a depth-to-width ratio of 0.4, which is less than the ideal value of 0.5. This indicates low penetration into the substrate, which is expected to result in poor bonding of layers. Based on the undesirable depth-to-width ratios of all the tracks, it was concluded that at this level of power, there was no best scanning speed in the tested range for use in creating good single tracks or 3D parts.

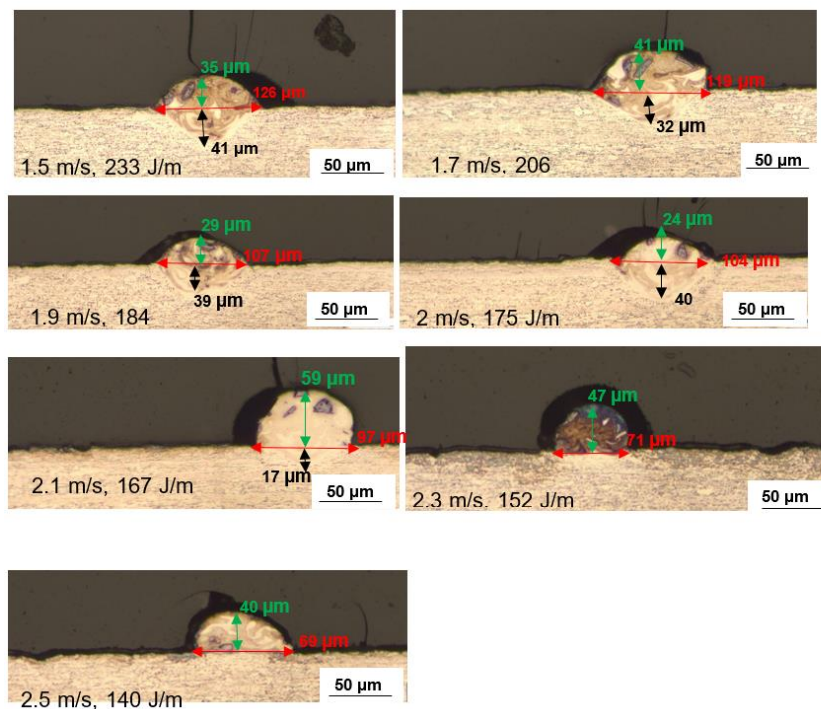
### C6. The Effects of Different Laser Scanning Speeds at a Laser Power of 350 W

Figure C11 shows the geometrical properties of the top surfaces of single tracks produced at a constant laser power of 250 W and different laser scanning speeds ranging from 1.5 m/s to 2.5 m/s.



**Figure C11:** The top view of the surface scans produced at a laser power of 350 W at different scanning speeds from 1.5 m/s to 2.5 m/s

In this figure, the widths of the tracks diminished with increasing laser scanning speed, resulting in a necking effect at laser scanning speed of 2.1 m/s. The tracks became discontinuous as the laser scanning speed was increased to 2.5 m/s. Discontinuities occur because of insufficient energy to melt the powder due to the laser beam's shorter dwell duration over the powder bed. The best tracks were identified as those that exhibited continuity and occurred at laser scanning speeds of 1.5 m/s to 2 m/s. However, a cross-sectional examination of these tracks was deemed necessary to aid in the selection of the best set of process parameters at 350 W. Figure C12 shows cross-sections of these tracks, built at a constant laser power of 350 W and scanning speeds ranging from 1.5 m/s to 2.5 m/s.



**Figure C12:** Cross-sectional views of tracks produced at a constant laser power of 350 W and different laser scanning speed from 1.5 m/s to 2.5 m/s

At the highest magnitude of laser power of 350 W used in the present work, the depth of penetration was seen here to vary inconsistently with increasing laser scanning speed from 1.5 m/s to 2 m/s. The widths of tracks on the other hand, decreased continuously with increasing laser scanning speed. Clearly, at this power the variation of laser scanning speed had a more significant effect on the widths of tracks than on the depth of penetration. At low laser scanning speeds, the laser beam has enough time to melt the powder and penetrate through the substrate, thus forming a large melt

pool area (Yadroitsava et al., 2015). The contact angles were seen to be high at the higher laser scanning speeds, from 2.1 m/s to 2.5 m/s. This was thought to be the result of poor wettability of the melt on the substrate, due to the high viscosity and surface tension of the former, that led to increased heights of the tracks.

The formation of a hump observed at high scanning speeds from 2.1 m/s to 2.5 m/s was thought to be due to the low dwell times of the laser beam on the powder, with the consequence that the viscosity and surface tensions of the formed melt were high. This resulted in the formation of narrow tracks with poor depths of penetration. Shi et al. (2017) reported that poor penetration of tracks led to insufficient bonding during the manufacturing of parts. The results obtained here agreed with the findings of Bertolli et al. (2017) discussed previously in this chapter. The measured values of the width and depth of the tracks all had depth-to-width ratios that were less than 0.5. It can be concluded from this that at this value of laser power, there was no best scanning speed.

### C7. The Effects of a Constant Scanning Speed at Different Values of Laser Power

The cross-sectional views of tracks built at a constant scanning speed of 0.8 m/s, with different magnitudes of laser power from 100 W to 200 W are shown in Figure C13.

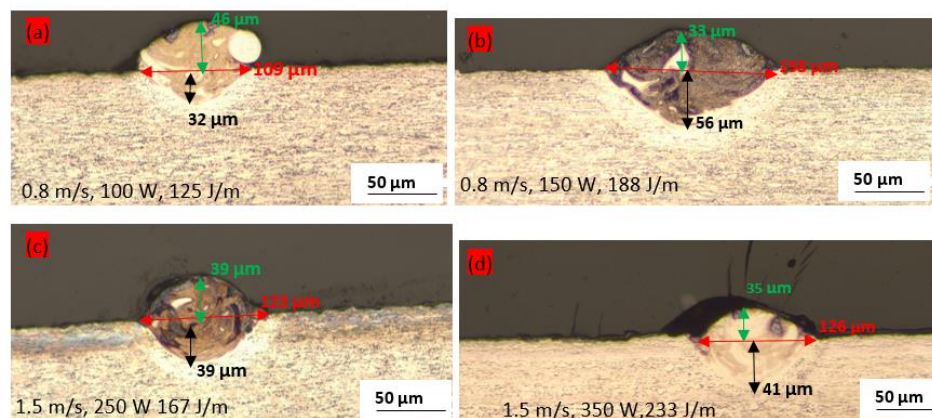


**Figure C13:** Cross-sectional views of tracks built at (a and b) a constant speed of 0.8 m/s, with different magnitudes of laser power from 100 W to 150 W, and (c and d) a constant speed of 1.5 m/s and magnitudes of laser power of 250 W and 350 W

The measured values of widths of the tracks at a constant laser scanning speed of 0.8 m/s, shown in Figure C13 (a and b), depicted increasing widths and depths of penetration of tracks with increasing laser power. The same trend was observed in Figure C13 (c and d) at a constant laser scanning speed of 1.5 m/s. The increase of power at the same laser scanning speed increases the energy input, which results in an increased temperature of the melt pool. The foregoing observations were consistent with the findings of Siao et al. (2021), who reported that the depth of the molten pool increased more significantly due to a combination of higher LED and slow scanning speed. This, they observed, yielded a longer heating duration of the powder by the laser beam, thus producing wide tracks with deeper penetration. However, the cross-sections shown in this figure yielded depth-to-width ratios that were less than 0.35, which is significantly less than the optimum value of 0.5. This indicated that at the given values of laser power, the selected speeds were all too high to cause deep penetration.

## APPENDIX D: ANALYSIS OF SINGLE TRACKS BUILT AT A 20 % VOLUME FRACTION OF SiC IN AN SiC/Ti6Al4V(ELI) COMPOSITE

### D1. The Effects of Different Laser Scanning Speeds at a Laser Power of 100 W

Images of the surface scans of single tracks produced at a constant magnitude of laser power of 100 W are presented in Figure D1.

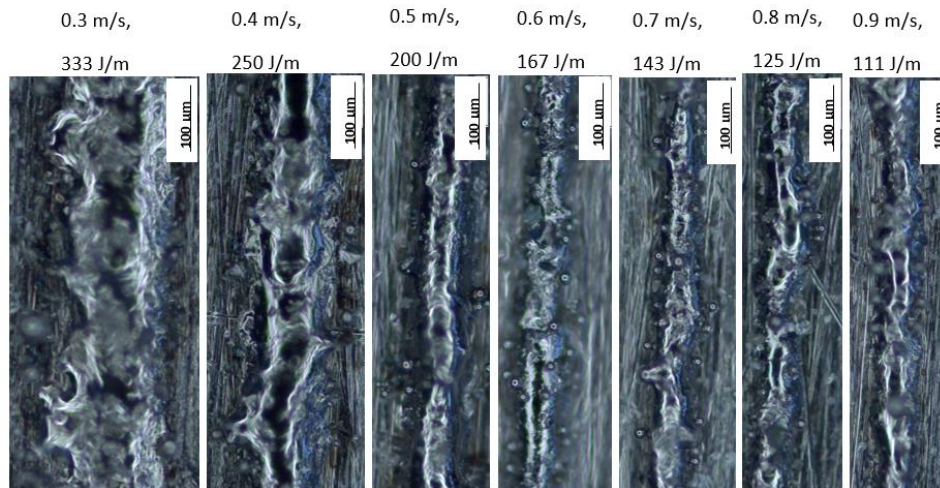


**Figure D1:** Top surface views of single tracks produced at a constant laser power of 100 W, with different laser scanning speeds from 0.3 m/s to 0.9 m/s

The tracks in Figure D1 showed fairly continuous tracks with even widths that reduced as the laser scanning speed increased. The images showed high incidences of spatter particles for scanning speeds between 0.5 m/s to 0.8 m/s and none at the highest scanning speed of 0.9 m/s and lowest scanning speeds of 0.3 m/s and 0.4 m/s. The tracks at the lowest laser scanning speeds of 0.3 m/s and 0.4 m/s appeared to have significantly wider tracks than the others, which is expected to offer the advantage of reduced time for building 3D parts. These wider tracks are thought to have occurred because of low scanning speeds that gave rise to higher LEDs, which increased the energy input and, therefore, the temperature of the melt. As surface tension is known to be temperature dependent, at high temperatures arising from energy densities, the surface tension is expected to be low at the centre of the melt and high at the edges of the melt pool as a result of the Gaussian distribution of energy in a laser beam (Krasa et al., 2013). The difference in surface tension causes the fluid to flow from areas of low surface tension to those with high surface tension (Wei et al., 2017). Low surface tension also implies that the fluid has good wettability on the surface it is on.

The wider widths of tracks at low scanning speeds seen in Figure D1 could be explained by the foregoing observations. Moreover, the wider track widths were also expected to be a result of lower melt viscosities, as viscosity decreases with increasing temperatures and causes shallower melt pools (Wei et al., 2017). A study of the cross-sectional dimensions of these tracks was then carried out based on the images shown in Figure D2.

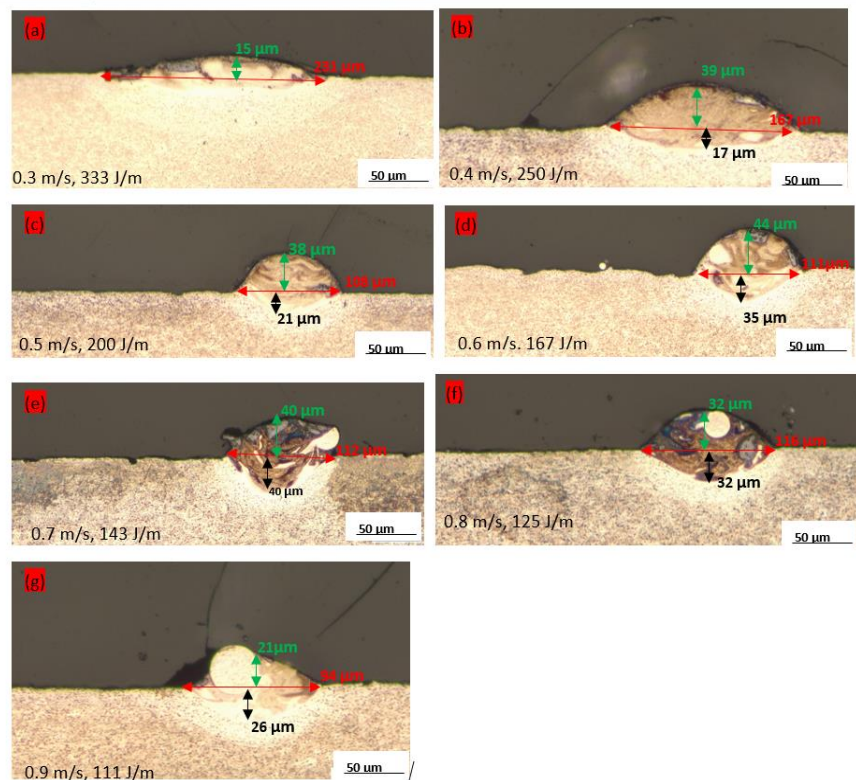


**Figure D2:** Top surface view of single tracks produced at a constant laser power of 100 W, with different laser scanning speeds from 0.3 m/s to 0.9 m/s

At the low laser scanning speeds and high LEDs of 0.3 m/s and 0.4 m/s, and 333 J/m and 250 J/m, respectively, the tracks were observed to be wider and shallower with poor penetration into the substrate than the rest. The widths of the tracks were observed to decrease from Figure D2 (a to c), and as the laser scanning speed was further increased from 0.6 m/s to 0.9 m/s, the track-widths increased. The last trend was noted to be abnormal and was taken to imply that the relationship between the process parameters and arising effects on the powder bed fusion process were nonlinear, as was reported separately by Dzogbewu et al. (2022) and Kusuma et al.

(2016). It was evident from the results in Figure D2 (a to e) that the depth of penetration increased with decreasing LED and rising laser scanning speed. At the highest laser scanning speeds of 0.8 m/s and 0.9 m/s, a decreasing trend in the depth of penetration was observed.

A study of heights of the tracks above the substrate of the cross-sections shown in Figure D2 highlighted a lack of trend for the three lowest scanning speeds and a continuous decrease for the last four scanning speeds. Calculations of the depth-to-width ratios of the tracks in this case showed all the cross-sections to have values that were much less than the optimal value of 0.5. Thus, whilst surface scans showed wide tracks without discontinuities at the lowest two scanning speeds, their low ratios of depth-to-width mitigated against them. Therefore, it was concluded that at this value of power, there was no best scanning speed amongst those used to print tracks.

## D2. The Effects of Different Varying Laser Scanning Speeds at a Laser Power of 150 W

A study of the effect of different scanning speeds on widths of tracks and their surface morphology was carried out by analysing the top views of the tracks shown in Figure D3.

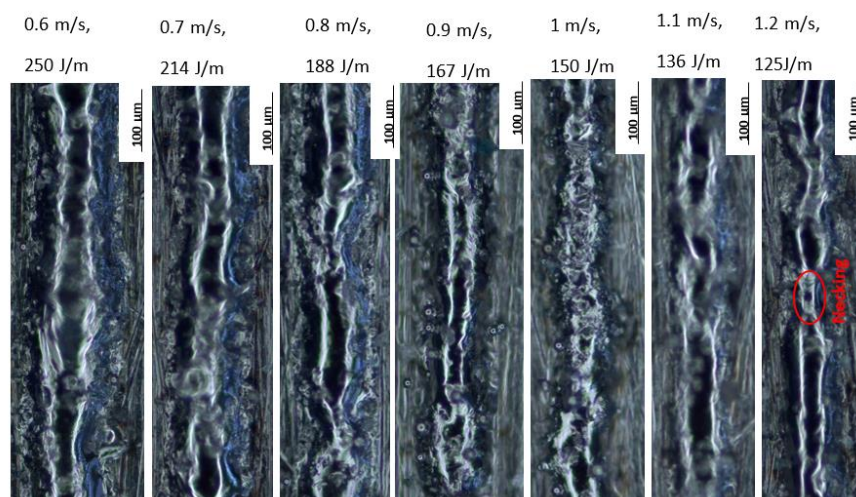


**Figure D3:** Top surface views of single tracks produced at a constant laser power of 150 W, with different laser scanning speeds from 0.6 m/s to 1.2 m/s

All the tracks shown in Figure D3 were continuous, with widths that reduced with increasing laser scanning speed. The presence of spatter Ti6Al4V(ELI) particles was

observed at laser scanning speeds of 0.9 m/s and 1 m/s. The track at the highest laser scanning speed of 1.2 m/s showed necking which is known to be a sign of imminent balling due to insufficient energy to melt the powder. The best tracks were seen at scanning speeds ranging from 0.6 m/s to 0.8 m/s, and were fairly wide and continuous, with no spatter particles. However, further information on the cross-sections was deemed necessary to help identify the best laser scanning speed. The geometrical properties of these tracks were then examined using the cross-sections shown in Figure D4, with the arising discussion presented below the figure.

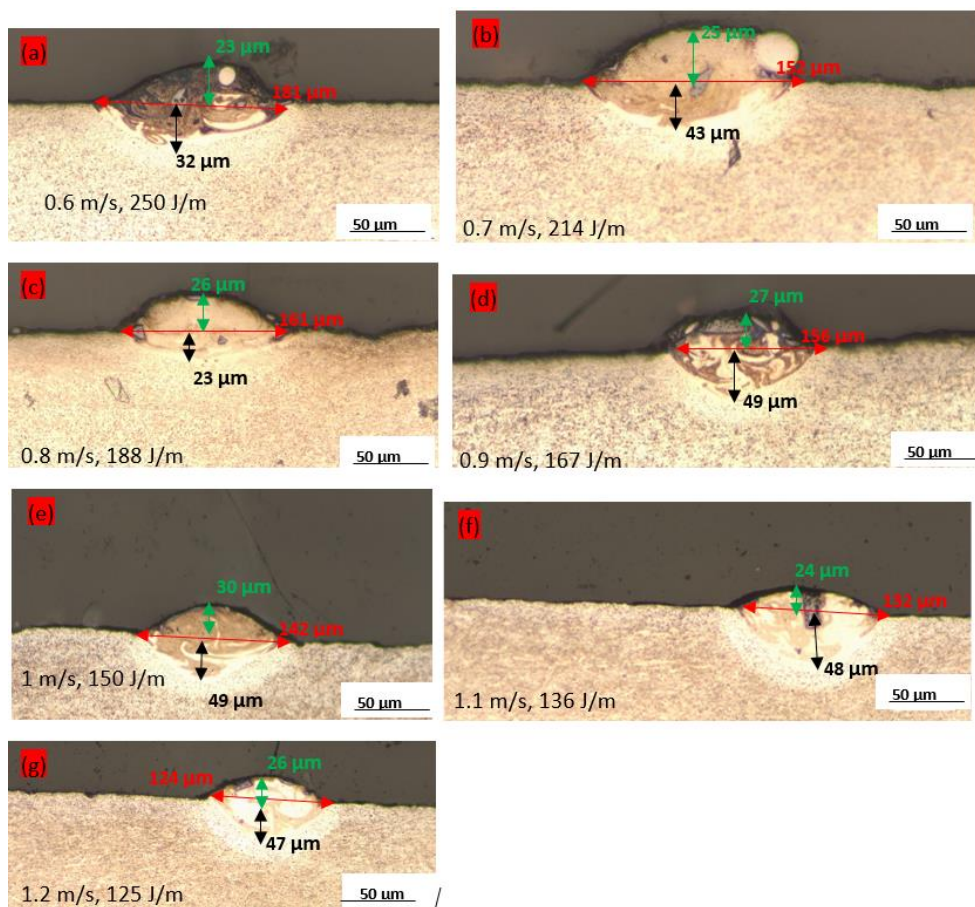


**Figure D4:** Top surface view of single tracks produced at a constant laser power of 100 W, with different laser scanning speeds from 0.3 m/s to 0.9 m/s

The track-widths of the cross-sections in this figure were noticed to decrease continuously with rising laser scanning speed from Figure D4 (a) to Figure D4 (g), with one exception. The heights of the tracks were seen to increase continuously with increasing scanning speed in Figure D4 (a to e) and to vary with no trend at higher scanning speeds. There was no consistent trend in the depth of penetration of the

tracks, with rising laser scanning speed. However, deeper penetrations were noticeable in Figure D4 (d to g). The increasing depth of penetration at higher laser scanning speeds and the attendant low LEDs was observed as an abnormal trend that pointed to the absence of a direct relationship between the scanning speed and depth of penetration.

Although the top view of the tracks from the laser scanning speeds from 0.6 m/s to 0.8 m/s revealed the best characteristics, their cross-sections in Figure D4 had depth-to-width ratios less than 0.5. This was an indication of poor depth of penetration, which was expected to lead to insufficient layer bonding. As a result, it was concluded that there was no best scanning speed among the ones used in these builds at this level of power that could be used for subsequent printing of good 3D parts.

### D3. The Effects of Different Laser Scanning Speeds at a Laser Power of 200 W

Figure D5 shows the top view of the single tracks built at a constant laser power of 200 W, with different laser scanning speeds from 0.8 m/s to 1.6 m/s for use in studying their surface morphology.

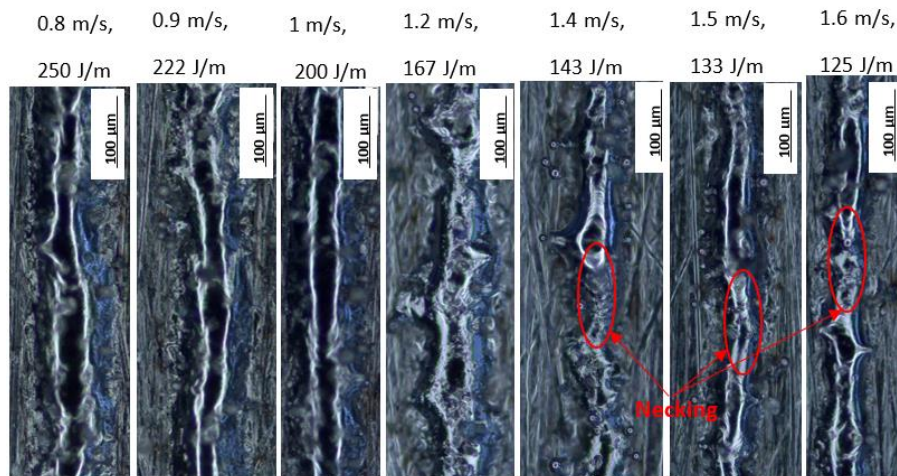


**Figure D5:** Top views of single tracks produced at a constant power of 200 W and different laser scanning speeds from 0.8 m/s to 1.6 m/s

The tracks built with laser scanning speeds of 0.8 m/s to 1.2 m/s were seen in Figure D5 to be continuous with wide and fairly constant widths. Further increase of the laser scanning speed led to decreasing widths of the tracks. The tracks built at the laser scanning speeds of 1.4 m/s to 1.6 m/s all showed minimal signs of necking, which is known to be a sign of imminent balling.

The cross-sections of these tracks are presented in Figure D6 for use to further study the effect of process parameters on their width, height, and depth of penetration.

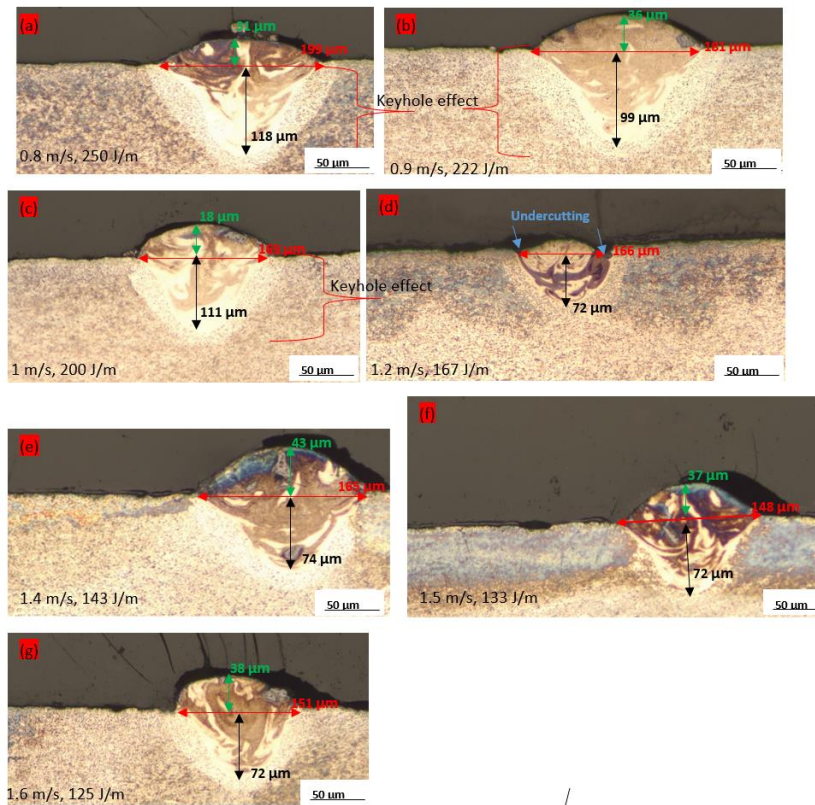


**Figure D6:** Cross-sectional views of the single tracks built at a constant laser power of 200 W, with different laser scanning speeds from 0.8 m/s to 1.6 m/s

According to Eager and Tsai (1983), the cross-section of the melt pool formed in conduction mode is approximately semi-circular. That is, the depth of penetration is about equal to half its track width (Ramosena et al., 2021). The results obtained in Figure D6 showed the occurrence of keyholes at laser scanning speeds of 0.8 m/s, 0.9 m/s, and 1 m/s, with calculated ratios of depth-to-width of the track of 0.6, 0.6, and 0.7, respectively. This was consistent with the investigation of keyhole melting of single tracks by Guo et al. (2021), in which the authors reported that keyholes occur when the recoil pressure was stronger than the surface tension force and hydrostatic pressure, which then pressed the molten fluid down to the bottom leading to the formation of a deep melt pool. With the exception of these three low values of scanning speed, the other scanning speeds, gave rise to LEDs, just sufficient enough to melt the particles of powder. Furthermore, the scanning speeds provided the laser beam

enough time to penetrate through the powder and substrate in conduction melting, creating deep melt pools, which was consistent with the observations of Wayne et al. (2014).

Increasing the laser scanning speed from 1.2 m/s to 1.6 m/s, made almost no change in the depth of penetration. The depth-to-width ratio of the tracks built at scanning speeds in this range was determined as 0.4 at the speed of 1.2 m/s and 0.5 for all the other scanning speeds in this range. Of the three tracks whose cross-sections are shown in Figure D6 (e to g), the first one had the highest values of width, height and depth of penetration, which was taken to imply shorter building times and intertrack bonding. Therefore, though a study of the cross-sections showed the best track built at the laser power of 200 W to be the one obtained at a scanning speed of 1.4 m/s with a laser energy density of 143 J/m, the surface scans showed it to have necking. Therefore, there was no best scanning speed amongst those used in this work, at this value of laser power.

#### **D4. The Effect of Different Laser Scanning Speeds at a Laser Power of 250 W**

The images of single tracks produced at a constant laser power of 250 W, with different laser scanning speeds from 1.2 m/s to 1.9 m/s, are shown in Figure D6 and were used here to study and discuss the morphology of their top surfaces.

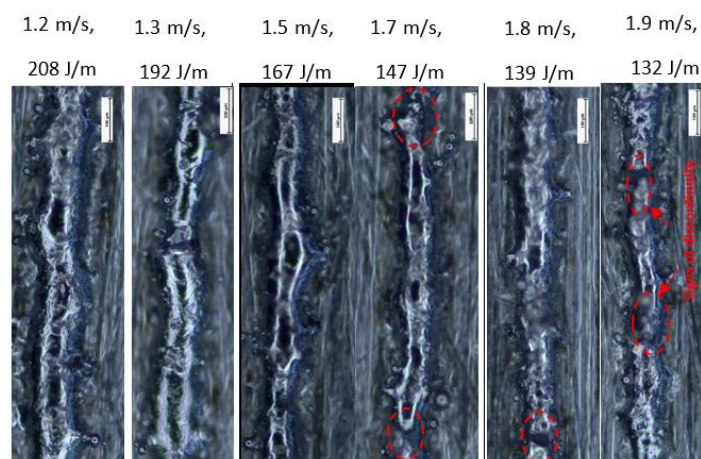


**Figure D7:** Top view images of tracks built at a laser power of 250 W with different laser scan speeds from 1.2 m/s to 1.9 m/s

It was evident from Figure D7 that only the track built at the low scanning speed of 1.2 m/s was continuous with an even width. As the laser scanning speed increased

from 1.3 m/s to 1.9 m/s, the widths of the tracks reduced, and the tracks became discontinuous. This was consistent with the known fact that, at constant power, an increase in laser scanning speed leads to a decrease in the LED, which results in insufficient energy input to fully melt the powder, thus forming discontinuities (Fotovvati et al., 2018; Kusuma et al., 2016). The effect of process parameters on the width, height, and depth of penetration of tracks produced at the constant laser power of 250 W, with different laser scanning speeds from 1.1 m/s to 1.9 m/s, was investigated by studying the cross-sectional images shown in Figure D8.

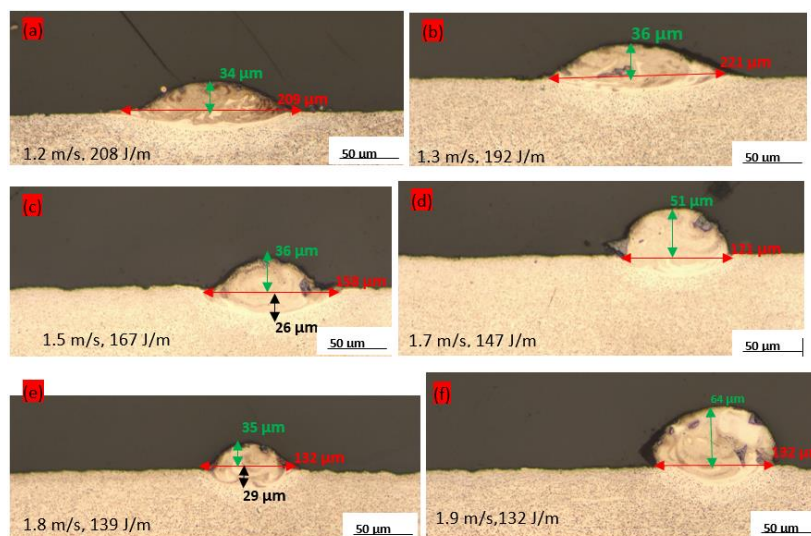


**Figure D8:** Cross-sectional views of single tracks built at a constant laser power of 250 W, with different laser scanning speeds from 1.1 m/s to 1.9 m/s.

It was evident from the images in Figure D8 that at the highest LEDs of 208 J/m and 192 J/m, the melt pools were shallow with wide tracks. The highest track in this series was attained at the highest scanning speed of 1.9 m/s. However, there was no consistent variation in the height of tracks with changes in the laser scanning speed. As has been mentioned previously, low scanning speeds increase the LED and, therefore, temperatures of the melt, which in turn leads to a reduction of viscosity and surface tension. As this effect is more at the centre of the tracks, the melt flows from the centre outwards to form wide and shallow tracks, as was also observed by Bayat et al. (2017), and a change from conduction to convection mode of heat transfer.

Comparing the cross-sections built at laser power values of 250 W and 200 W, the former showed poorer penetration than the latter, which were not only deeper but also exhibited keyholes at the lower three laser scanning speeds. This was contrary to the

expectation that at the higher values of power, the cross-sections would have deeper penetration, particularly where the LED was in the same range as at the lower values of laser power. This implied that the reduction in the depth of penetration of tracks as a result of high LED, discussed in the previous paragraph, predominated over the increase in the depth of penetration at this higher value of laser power. Therefore, the assumption made previously, that a higher LED led to a higher depth of penetration broke down at high values of laser power. The cross-sections of all the tracks produced at this value of laser power exhibited poor depths of penetration that would lead to poor interlayer bonding of 3D parts. Moreover, all but the track built at the lowest laser scanning speed showed the presence of discontinuities, which reduce the integrity of any 3D parts built with their process parameters. Therefore, there was no process parameter set used to build tracks at this value of power that was good for building good 3D parts.

#### **D5. The Effect of Different Laser Scanning Speeds at a Laser Power of 300 W**

The SEM micrographs of tracks produced at a laser power of 300 W and different laser scanning speeds are presented in Figure D9 and were used here to study their surface morphology.

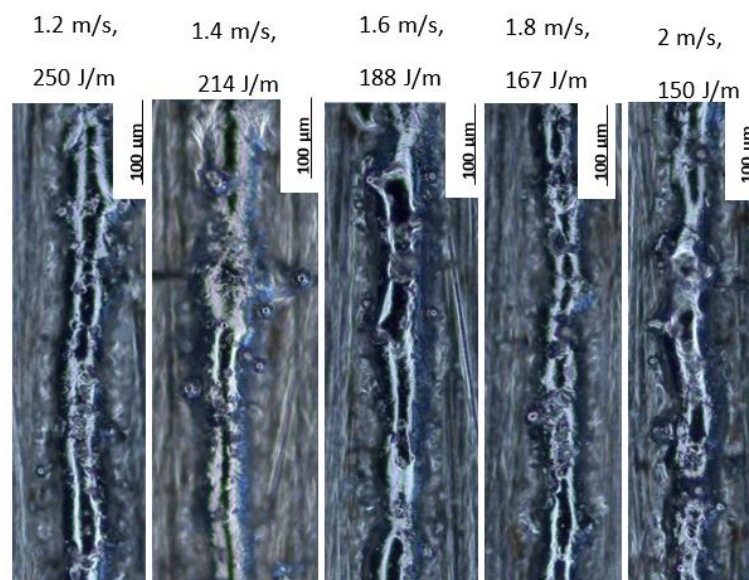


**Figure D9:** *Top view micrographs of tracks built at different laser scanning speeds and a laser power of 300 W*

The tracks shown in Figure D9 built at laser scanning speeds of 1.2 m/s to 1.6 m/s were continuous with almost even widths. Further increase in the laser scanning speed to 1.8 m/s and 2 m/s led to the tracks with some signs of discontinuity. A few spatter particles were observed at the laser scanning speed of 1.6 m/s.

An investigation of the width, height and depth of penetration of these tracks was carried out through study of the images in Figure D10.

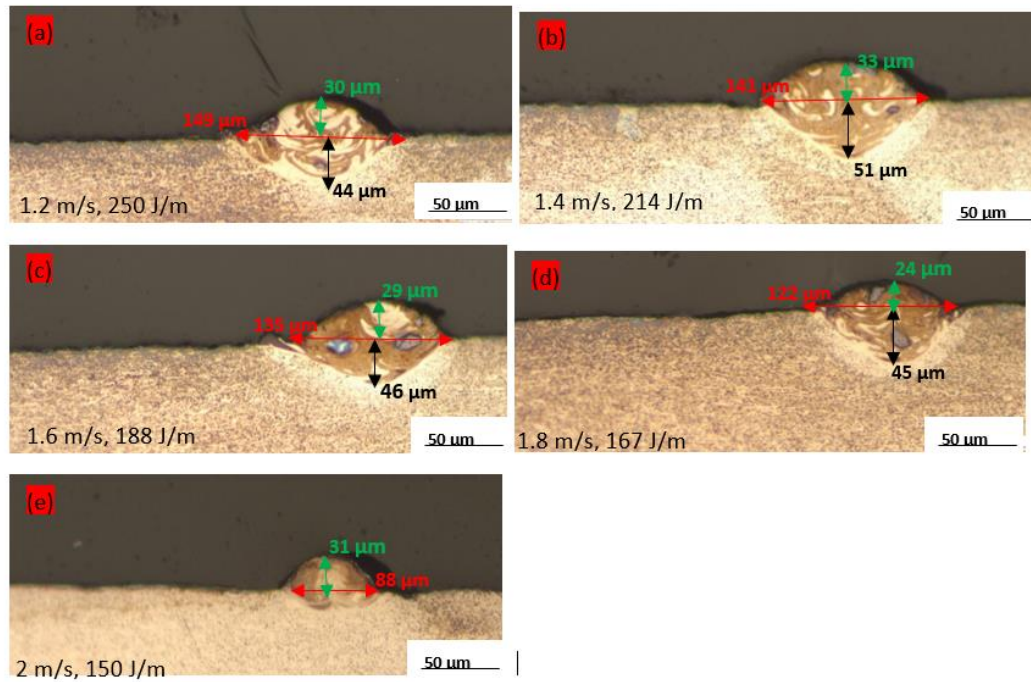


**Figure D10:** Images of the cross-sections of single tracks built at a laser power of 300 W, with different laser scanning speeds from 1.2 m/s to 2 m/s

The cross-sections in Figure D10 showed inconsistency of the depths of penetration and heights of the tracks, with rising laser scanning speeds. The depth-to-width ratios for all the tracks were all less than the optimal value of 0.5. There was a continuous decrease in the widths of the tracks with increasing scanning speed up to a scanning speed of 2 m/s. This was consistent with the observation by Yadroitsev et al. (2015) that the faster the laser beam ran over powder, the less time there was for it to fully melt and penetrate the powder bed. Furthermore, this was accompanied by a concurrent decrease in the energy available to melt the powder. As all the cross-sections in Figure D10 had depth-to-width ratios that were less than 0.5, there was no best set of process parameters amongst those used at this value of laser power.

## D6. The Effect of Different Laser Scanning Speeds at a Laser Power of 350 W

The SEM micrographs of tracks produced at a laser power of 350 W and different laser scanning speeds are presented in Figure D11 and were used here to study their surface morphology.

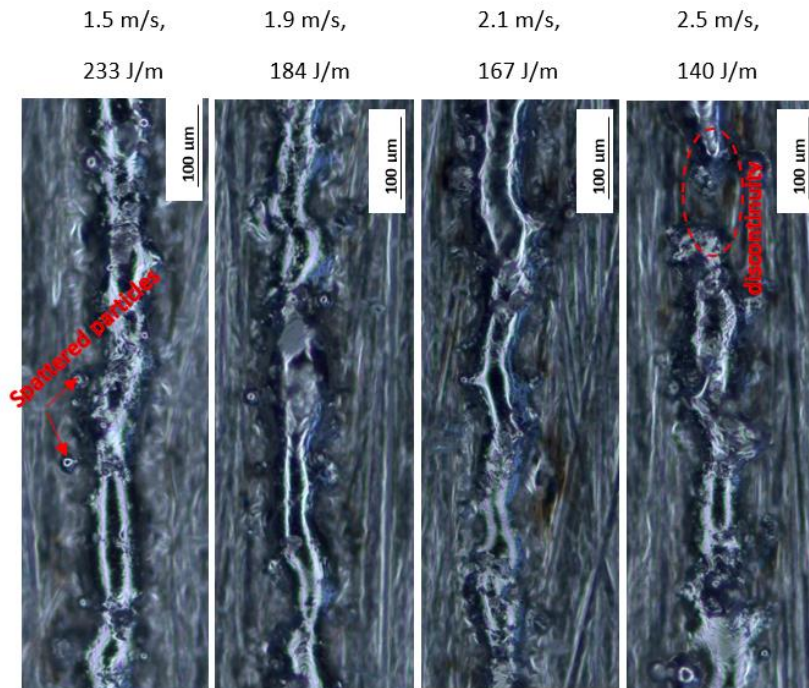


**Figure D11:** Top view images of single tracks built at a constant power of 350 W with different laser scanning speeds from 1.5 m/s to 2.5 m/s

The top surface view of the track at the lowest scanning speed of 1.5 m/s showed a continuous track with an almost even width, with a few spatter particles at the sides. Uneven widths of tracks were observed at scanning speeds of 0.9 m/s to 2.1 m/s. Increasing the laser scanning speed to the highest value of 2.5 m/s led to the formation of a discontinuous track with signs of balling that was thought due to insufficient energy availed to melt the powder.

The cross-sectional views of the tracks shown in Figure D11 are presented in Figure D12 and were used here to study their cross-sectional, geometrical characteristics.

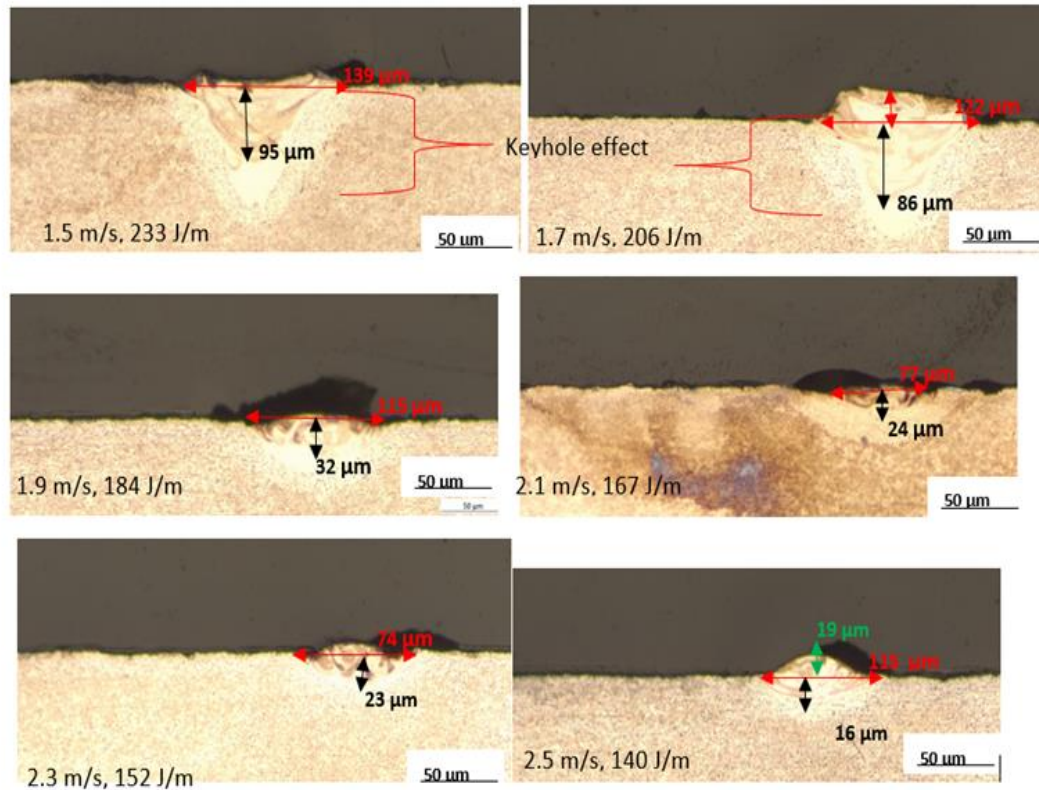


**Figure D12:** Cross-sectional view of single tracks built at a laser power of 350 W, with different laser scanning speeds from 1.5 m/s to 2.5 m/s

The tracks built at scanning speeds of 1.5 m/s and 1.7 m/s showed the keyhole effect, with depth-to-width ratios of 0.7. A ratio greater than 0.5 indicates the keyhole effect. The keyhole in this case was caused by the prevailing low scanning speeds giving rise to high LEDs, high enough time to penetrate through the powder and into the substrate. However, it was noted that higher laser scanning speeds from 1.9 m/s to 2.5 m/s led to poor depths of penetration with depth-to-width ratios less than 0.5. Poor penetration is caused by insufficient melting due to decreased energy density, as the laser scanning speed rises at the same value of power (Yadroitsev et al., 2013). Xuezhi et al. (2017) investigated the optimization of process parameters in SLM based on the geometrical characteristics of single tracks and reported that when low laser scanning speeds were used with high values of laser power, this combination led to distortion and irregularities of tracks. It is known that a high value of laser power induces high values of recoil pressure on the melt pool. Moreover, low scanning speeds, on the other hand, lead to longer dwell times of the laser beam, which results in high degrees of overheating of the melt. High values of recoil pressure acting on the surface of

molten pools are known to cause distortions such as the keyhole effect observed in the first two images of Figure D12. The measured values of depth in Figure D12 indicated a decreasing depth of penetration with rising laser scanning speed. Despite the even track with no discontinuities observed at a laser scanning speed of 1.5 m/s, none of the cross-sections of the tracks had the optimal ratio of depth-to-width ratio. Therefore, it was concluded that there was no best set of process parameters amongst those used here that could be recommended for building 3D parts.

## APPENDIX E. ANALYSIS OF SINGLE TRACKS BUILT AT A 25 % VOLUME FRACTION OF SiC IN AN SiC/Ti6Al4V(ELI) COMPOSITE

### E1. The Effect of Different Laser Scanning Speeds at a Laser Power of 100 W

Figure E1 shows the top views of the tracks built at a constant power of 100 W with different laser scanning speeds, which were used here to study their morphological characteristics.

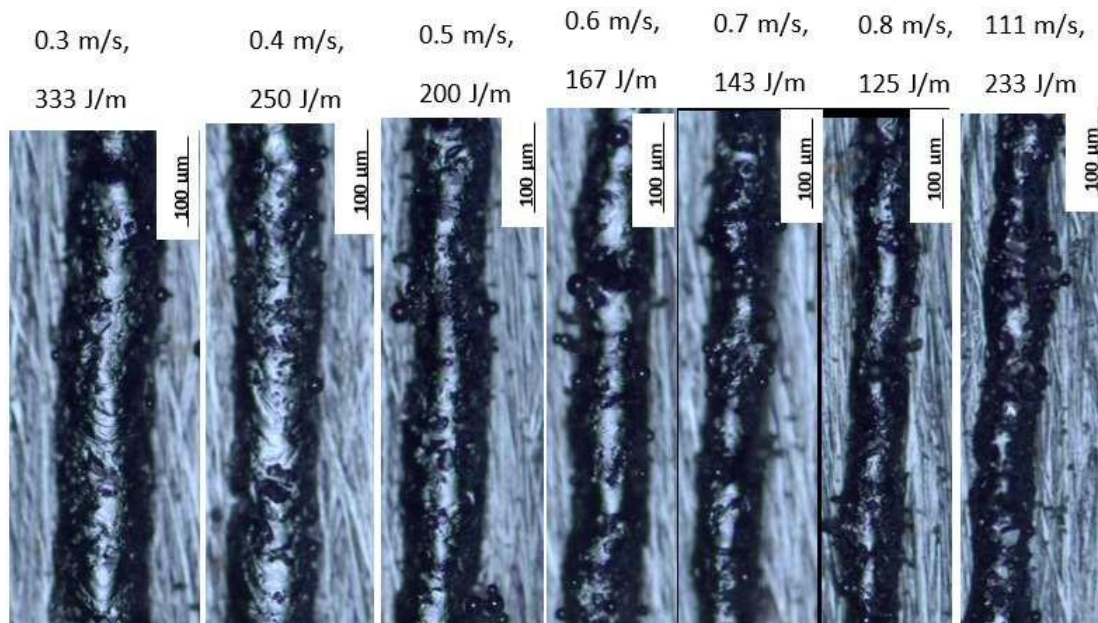


**Figure E1:** Top views of single tracks built at different laser scanning speeds from 0.3 m/s to 0.9 m/s at a constant power of 100 W

All the tracks in Figure E1 were continuous with almost constant widths that reduced as the laser scanning speed rose from 0.3 m/s to 0.9 m/s. The appearance of spatter particles on the tracks occurred from a laser scanning speed of 0.4 m/s to 0.9 m/s. There were fewer spatter particles at the lowest scanning speed of 0.3 m/s and the highest LED of 333 J/m. This was thought to be because, at this value of scanning speed, the temperature of the melt pool was very high, allowing sufficient melting of the particles towards the edges of the track through the conduction mode of melting. Similar results were also reported by Andani et al. (2018), that increasing the laser scanning speed reduced the energy density and led to reduced melt pool temperatures, which were not sufficient to fully melt all the particles at the edges of the tracks.

Further study of the depth of penetration, height, and width of the tracks shown in Figure E1 was done based on the cross-sections presented in Figure E2.

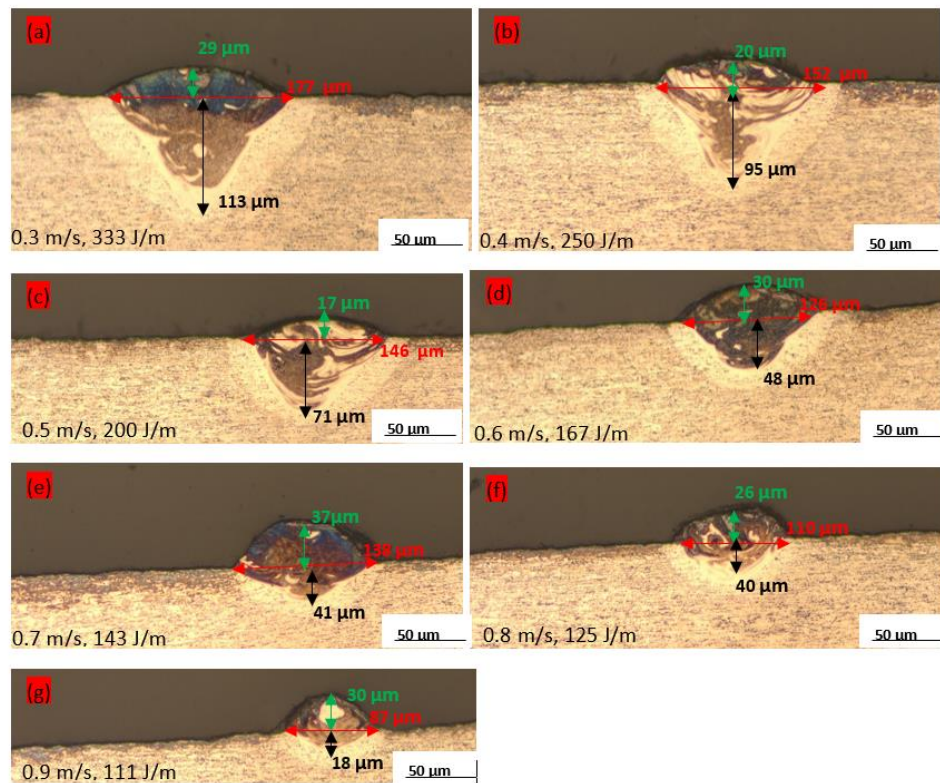


**Figure E2:** Cross-sectional views of single tracks produced at a laser power of 100 W, with different laser scanning speeds from 0.3 m/s to 0.9 m/s

At this low value of laser power of 100 W, the keyhole effect was observed in the cross-sections with the highest LEDs of 333 J/m (0.3 m/s) and 250 J/m (0.4 m/s). The keyhole effect was thought to have occurred because of the low prevailing laser scanning speeds in these two cases, which provided the laser beam enough time to penetrate through the powder to the substrate, consistent with the works of Guo et al. (2019) and Yu et al. (2016). Antony et al. (2015) and Andani et al. (2018) observed that slow scanning speeds coupled with high energy densities caused the evolution of high temperatures that led to evaporation of the molten pool and the formation of strong recoil pressures. They further noted that when the recoil pressures exceeded the surface tension forces, it caused the formation of depressions into the substrate thus forming keyholes.

It is clear from Figure E2 that increasing the laser scanning speed led to a decrease in the depth of penetration. At a scanning speed of 0.5 m/s and LED of 200 J/m, the

Page | 260

measured values of the track width, depth of penetration, and corresponding depth-to-width ratio were 146  $\mu\text{m}$ , 71  $\mu\text{m}$  and 0.5, respectively, while the tracks built at higher laser scanning speeds, from 0.6 m/s to 0.9 m/s, gave depth-to-width ratios of 0.4. These lower depth-to-width ratios denoted poor penetration into the substrate. Therefore, it was concluded that the best laser scanning speed at a laser power of 100 W was 0.5 m/s. This was because the tracks built using these two process parameters yielded the optimum depth-to-width ratio of 0.5 and a top surface with a continuous track. As a result, it is expected that their use would provide enough penetration into the previous layer or substrate to ensure good bonding between them, which would, in turn, lead to the creation of 3D parts with good mechanical properties.

## E2. The Effect of Different Laser Scanning Speeds at a Laser Power of 150 W

Figure E3 presents the top views of the single tracks built at different laser scanning speeds from 0.6 m/s to 1.2 m/s, which were used here to study their surface morphologies.

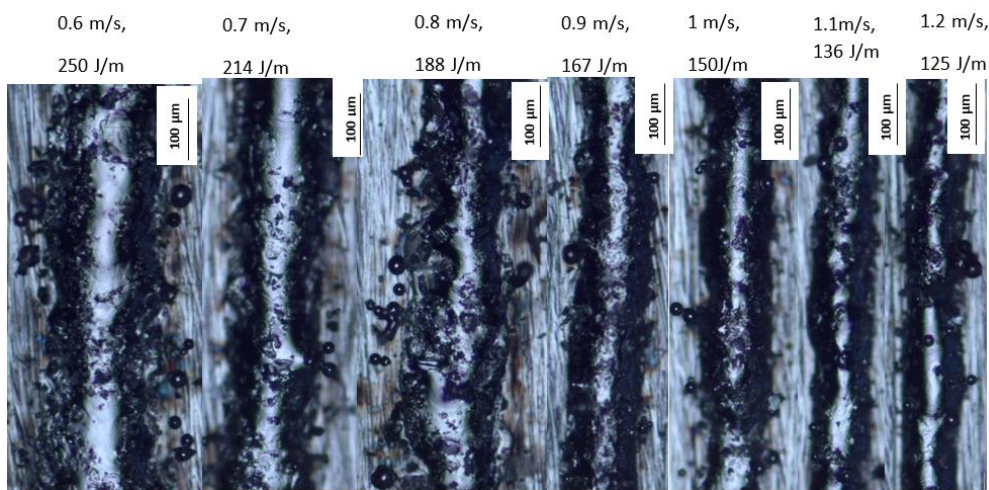


**Figure E3:** *Single tracks built at a constant laser power of 150 W with different laser scanning speeds from 0.6 m/s to 1.2 m/s*

Figure E3 shows tracks that were continuous with almost constant widths that decreased with rising laser scanning speed. The tracks at the lower scanning speeds, from 0.6 m/s to 0.8 m/s, were noticeably wider than those at the higher speeds, from 0.9 m/s to 1.2 m/s. Moreover, the spatter particles at the peripheries of the tracks were mainly at the low scanning speeds and reduced in number as the laser scanning speed was raised from 0.9 m/s to 1.2 m/s. Andani et al. (2018), commenting on the formation

of spatter particles during SLM, reported that at low scanning speeds (high energy densities), the temperatures were high and rapidly melted and evaporated the melt creation of vapour recoil pressure that acted as a force ejecting some of the melt away from the melt pool. The ejected melt then solidified on the sides of tracks as spatter particles. Moreover, they observed that increasing the laser scanning speed reduced the number of spatter particles.

Further study of the geometrical characteristics of the tracks was done based on the cross-sections in Figure E4.

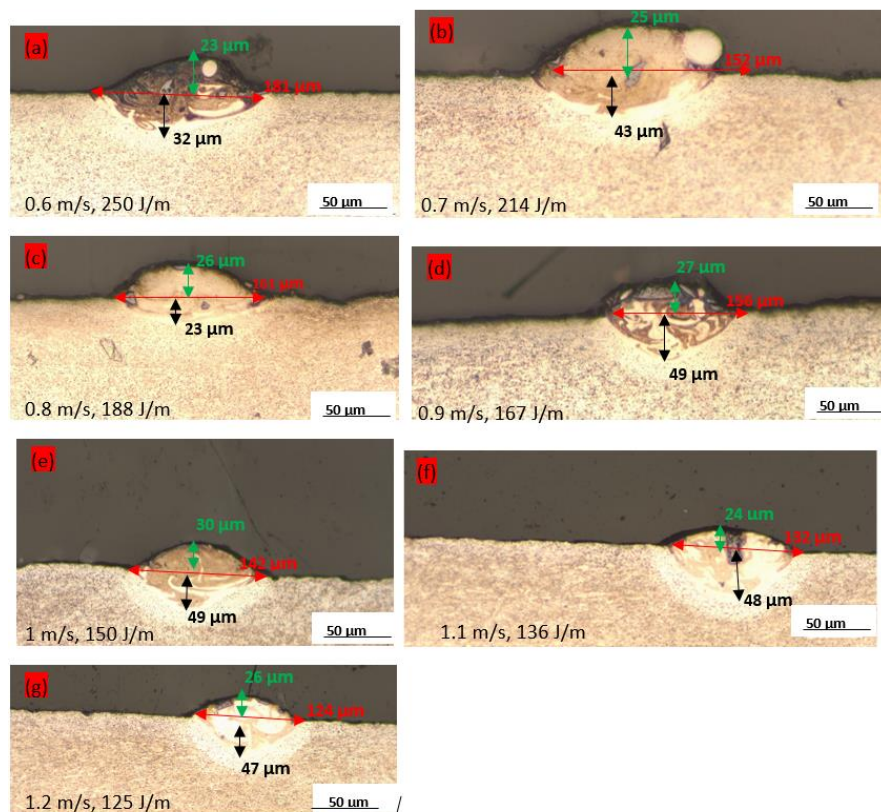


**Figure E4:** Cross-sections of tracks produced at a laser power of 150 W, with laser scanning speeds ranging from 0.6 m/s to 1.2 m/s

At this value of laser power, the depth of penetration was observed to decrease with rising laser scanning speed for all speeds, apart for the two highest and lowest scanning speeds where a reverse trend prevailed. The depth of penetration was poor for all the tracks, being largely less than the layer thickness of 45–50 µm. On the other hand, the widths of the tracks decreased with the increase of laser scanning speeds except for the lowest two speeds where the reverse trend occurred, which was consistent with the findings of Yu et al. (2016). Except for the last track with ratio of

0.4, all the tracks had depth-to-width ratios less than 0.3. Even though the surface scans of the tracks were continuous, their cross-sections had ratios less than the optimal value of 0.5, indicating inadequate penetration. As a result, none of the laser scanning speeds used at this level of power were considered suitable to produce tracks with good geometrical properties.

Comparing the tracks built at laser powers of 100 W to 150 W, for the same laser scanning speeds between 0.7 m/s to 0.9 m/s, inclusive in Table A1 shown earlier in this Chapter 6, the depths of penetration and widths of tracks were higher for the higher value of laser power. This was thought to be a consequence of the higher values of LED causing increasing penetration and melt pool temperature, the latter which led to reduced surface tension and viscosity and, therefore, facilitating better wetting of the melt. However, at the laser scanning speed of 0.6 m/s, the width of the track increased, while the depth of penetration decreased with increasing laser power.

### E3. The Effects of Different Laser Scanning Speeds at Laser Power of 200 W

The single tracks built at a constant laser power of 200 W with different laser scanning speeds are shown in Figure E5 and were used here to study their surface morphologies.

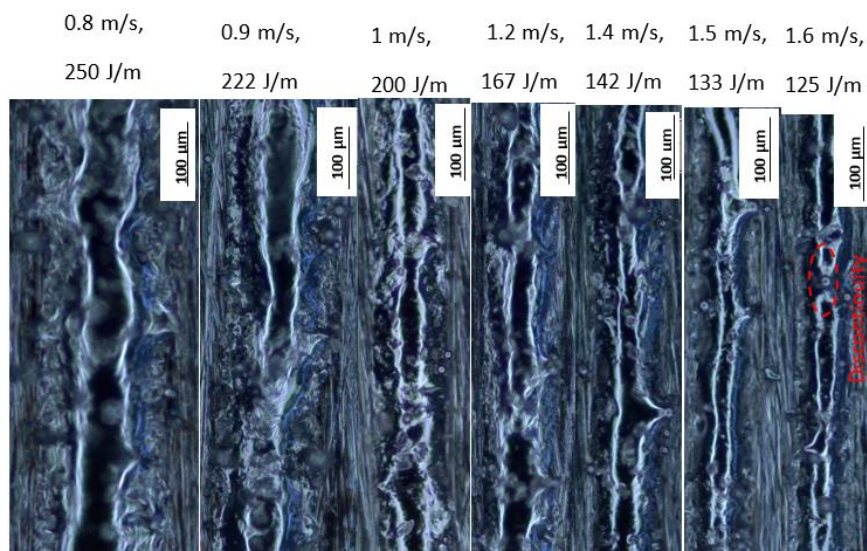


**Figure E5:** Top view of the tracks built at laser scanning speeds from 0.9 m/s to 1.6 m/s at a constant laser power of 200 W

Similar to the trend observed for tracks built at a laser power of 150 W, the widths of the tracks built at this value of laser power were seen here to decrease with increasing laser scanning speed. It is evident from Figure E5 that the wide tracks were obtained at the low speeds of 0.8 m/s and 0.9 m/s. Increasing the scanning speed above these values led to diminished widths of tracks, that also showed signs of discontinuities at the highest scanning speed of 1.6 m/s. The acceptable tracks were those built at scanning speeds of 0.8 m/s to 1.2 m/s, that were wide with fairly constant widths. Further study of the cross-sections in Figure E6 was done to investigate their geometrical characteristics to help identify the best process parameters.

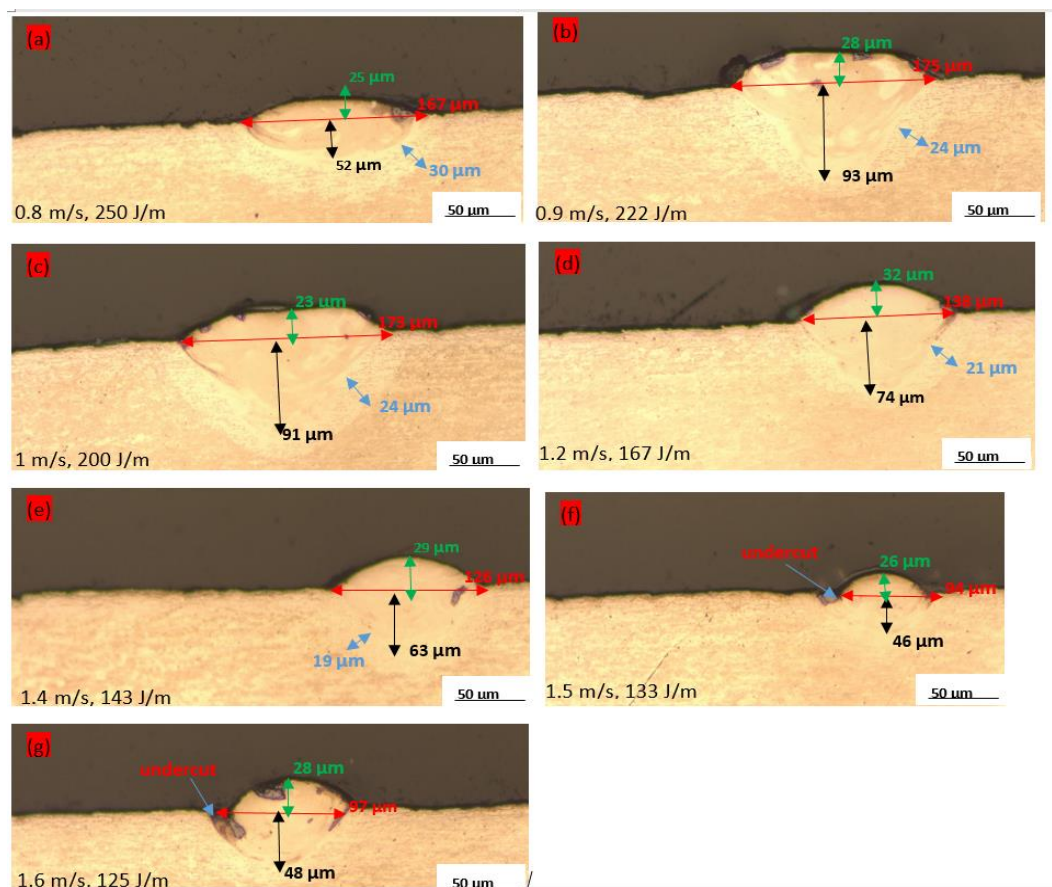


**Figure E6: Cross-sectional images of single tracks produced at a laser power of 200 W and different scanning speeds**

The cross-section of the track built at a scanning speed of 0.8 m/s at this value of laser power (a high LED of 250 J/m) showed a low penetration that is just above the upper range of the layer thickness. As previously stated in this chapter, low scanning speeds enhance energy density and thus melt temperatures, resulting in a decrease

in viscosity and surface tension. Because this effect is stronger in the centre of the tracks, melt flows outwards to generate wide and shallow tracks, as reported by Bayat et al. (2017), and the transition from conduction to convection mode of heat transport.

When the laser scanning speed was raised to 0.9 m/s, with an attendant drop of the LED to 222 J/m, the keyhole effect occurred. A transition to a keyhole effect in Figure E6 (b) showed that the vapour recoil pressures exceeded the capillary forces causing the formation of a deep depression into the substrate, as was observed by Dzogbewu et al. (2022).

While the height of tracks varied inconsistently with increasing scanning speed, the depths of penetration and widths of the tracks decreased with increasing scanning speed, except for the two lowest and highest scanning speeds where the reverse trend prevailed.

The measured values of the widths and depths of penetration of the cross-sections in Figure E6 (b to e) had depth-to-width ratios of 0.5. Though all these cross-sections had the same ratio of depth-to-width to an accuracy of one decimal place, only Figure E6 (e) had this exact value to an accuracy of two decimal places, the others being lower. The last two cross-sections also exhibited undercuts, which is known to be a sign of impending balling, as was observed by Dzogbewu et al. (2022). Though the top surface scans at the scanning speed of 1.4 m/s showed a track with a narrow width, its cross-section had a depth-to-width ratio of 0.5. Therefore, the best laser scanning speed at this value of laser power was 1.4 m/s with an LED of 143 J/m. This process parameter set led to the formation of tracks with a depth of penetration into the lower layer or substrate of 26% to 40% of the thickness of the layers of powder.

At the laser scanning speeds of 0.8 m/s and 0.9 m/s, the widths and depths of penetration of the tracks increased with increasing laser power from 100 W to 200 W. The predominance of keyholes was greater at this value of laser power than at the lower value of 150 W.

#### E4. The Effects of Different Laser Scanning Speeds at a Laser Power of 250 W

Figure E7 shows micrographs of tracks built with a laser power of 250 W, with different laser scanning speeds from 1.1 m/s to 1.9 m/s.

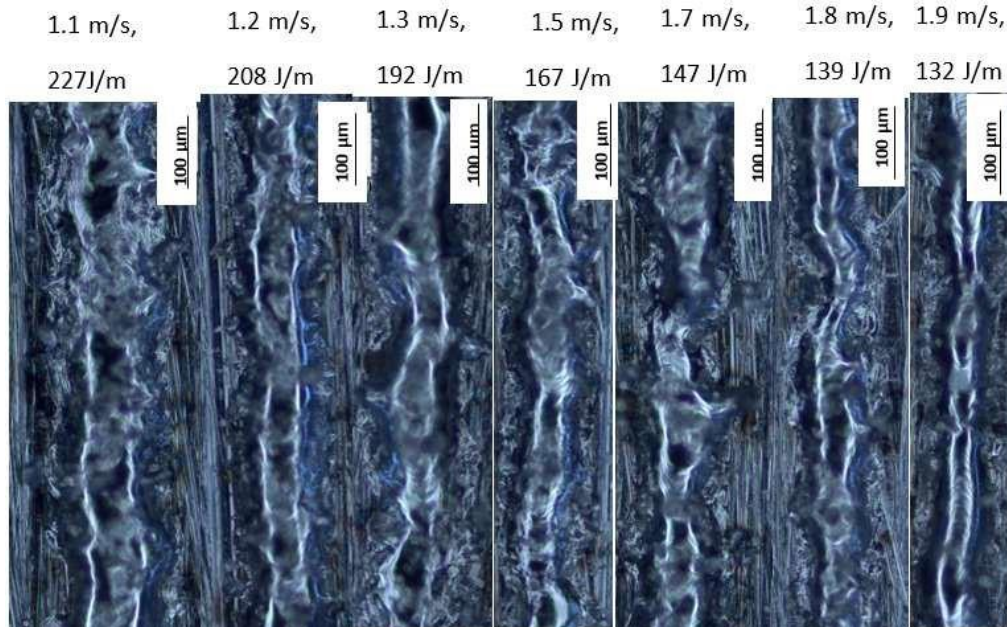


**Figure E7:** Top surface micrographs of tracks, built at a constant power of 250 W and different laser scanning speeds from 1.1 m/s to 1.9 m/s

The micrographs presented in Figure E7 showed a wide track at the lowest laser scanning speed of 1.1 and a continuous reduction of the widths of the tracks with increasing laser scanning speed. The track built at the highest laser scanning speed of 1.9 m/s was narrower than the rest of the tracks. The foregoing observations can be explained from the facts previously mentioned that the increase of laser scanning speed at the same value of laser power leads to a reduction of energy density and, therefore, temperature of the melt pool. Because surface tension and viscosity are known to be temperature dependent, as previously indicated in this work, surface tension and viscosity are expected to be greatest at the highest laser scanning speed where the energy density and, hence, temperature are the lowest. High surface tension and viscosity reduce the spreading ability of melt and adhesion onto the substrate and lead to a narrowing down of tracks (Yadroitsev et al., 2013).

The depth of penetration, height and width of the tracks shown in these micrographs were studied further based on their cross-sections shown in Figure E8.

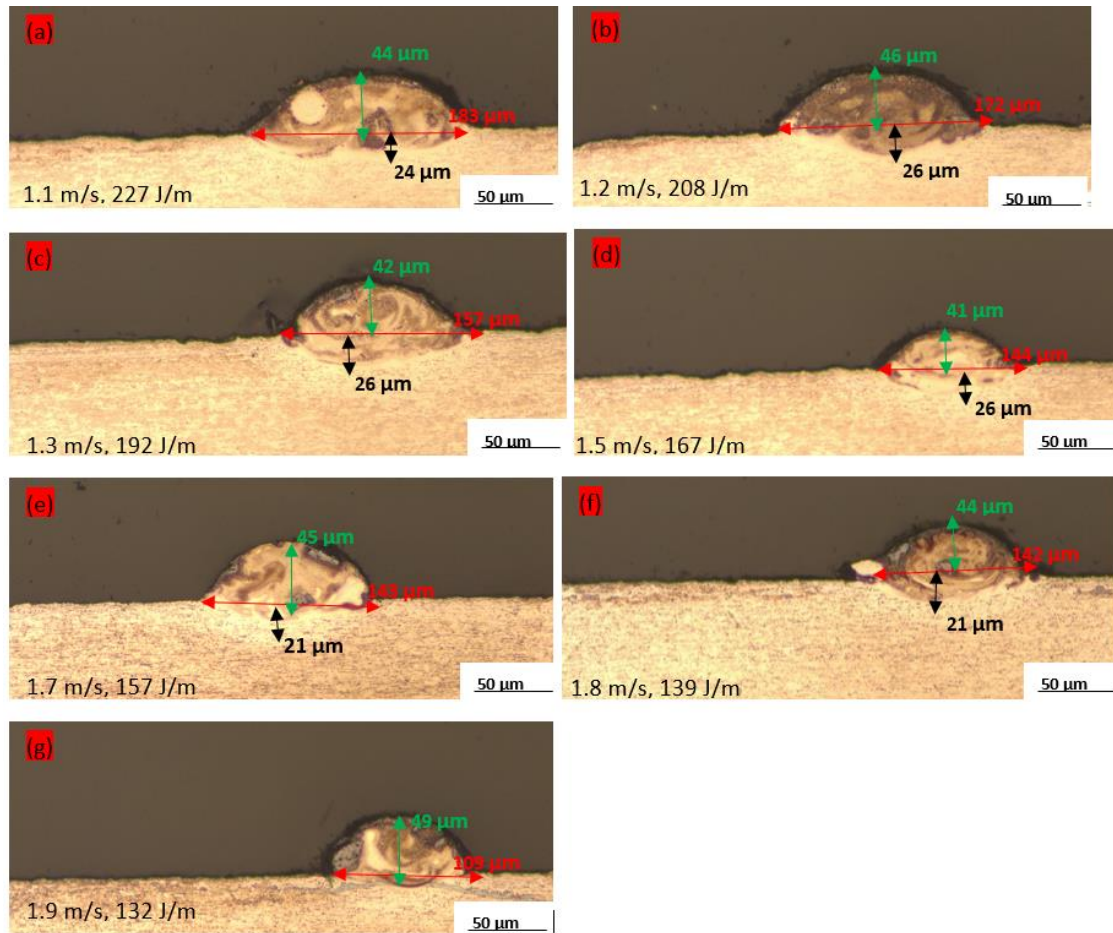


**Figure E8:** Cross-sectional views of single tracks built at a laser power of 250 W

The measured track widths of the cross-sections shown in Figure E8 indicated a reduction of width with rising laser scanning speed, for all cases apart from a scanning speed of 1.7 m/s, where a reverse trend was seen. It is reasonable to infer that decreased energy density per unit area corresponding to increasing laser scanning speed reduced the interaction time of the laser with the powder thus leading to insufficient melting of powder and an increase in unmelted particles of powder, as was observed by Yu et al. (2016). The height and depth of penetration of tracks were both observed to vary inconsistently with increasing laser scanning speed. Although the top surface scans in Figure E7 showed continuous melted tracks, their cross-sections shown in Figure E8 had depth-to-width ratios that were less than 0.2. This was indicative of poor penetration of the wide tracks in all the cross-sections. Therefore, none of the laser scanning speeds used at this value of laser power could be considered for further building of single layers and 3D parts.

At the same laser scanning speed of 1.2 m/s for values of laser power of 150 W, 200 W, and 250 W, there was a continuous increase in the widths of tracks but with no consistent trend with respect to the depth of penetration. The depth of penetration rather increased with an increase of laser power from 150 W to 200 W and then decreased when the power was increased to 250 W. These contrasting trends are an indication that there is no simple relationship between the process parameters used in laser powder-based fusion and the characteristics of the parts built and is consistent with the observations of Dzogbewu et al. (2022).

### E5. The Effect of Different Laser Scanning Speeds at a Laser Power of 300 W

The images shown in Figure E9 were of tracks produced at a constant laser power of 300 W and at different laser scanning speeds and were used here for studying the surface morphologies of the built tracks.

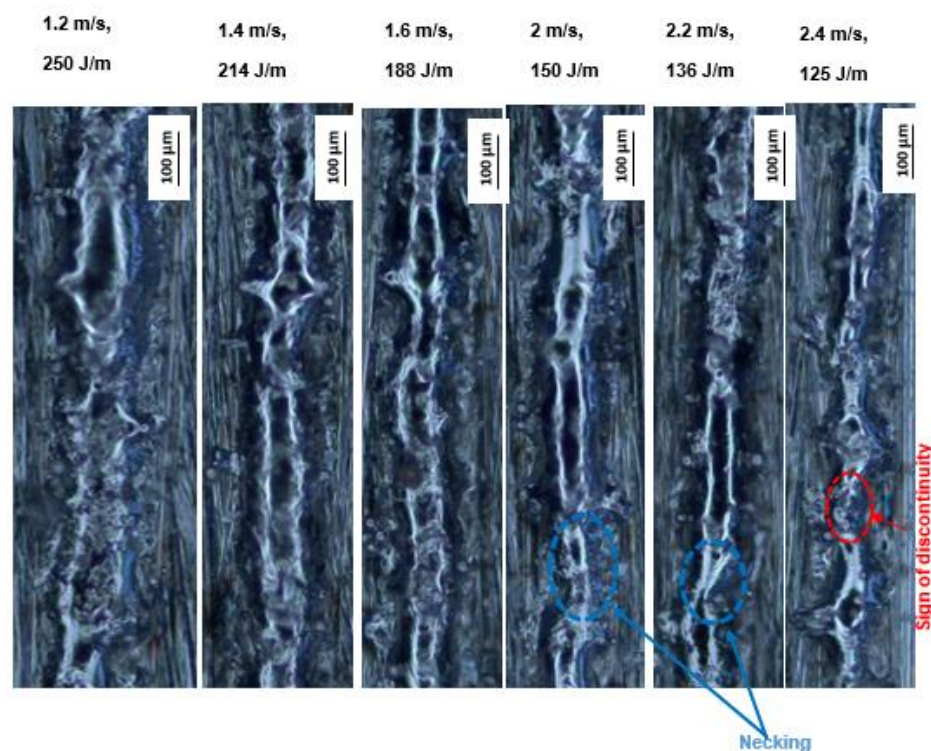


**Figure E9:** Top surface micrographs of tracks, built at a constant power of 300 W and different laser scanning speeds from 1.2. m/s to 2.4 m/s.

The tracks built with scanning speeds from 1.22 m/s to 1.6 m/s in this figure were reasonably continuous throughout their lengths. However, those that were built at scanning speeds between at 2 m/s and 2.2 m/s showed necking, which is a sign of

balling. A discontinuity occurred at the highest laser scanning speed of 2.4 m/s. It is evident that the width of the tracks decreased as the laser scanning speed increased. As previously discussed in this chapter, increasing the laser scanning speed at a constant laser power reduces the LED, resulting in insufficient melting of the powder and consistent with the work of Yu et al. (2016). Furthermore, the narrower tracks are due to the laser's shorter dwell time on the powder bed (Guo et al., 2019). Further study of the cross-sections of these top surface scans was carried out based on the images presented in Figure E10.

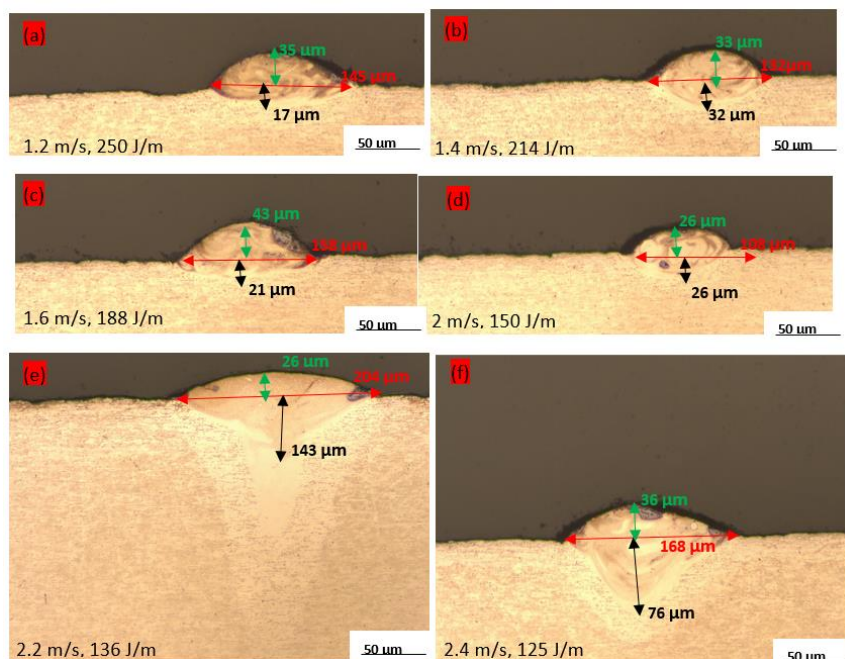


**Figure E10: Cross-sectional views of the tracks built at a laser power of 300 W**

There was an absence of trends in the variation of the depths of penetration, widths and heights of tracks with increasing laser scanning speed. The highest depths of penetration and widths were observed at the highest laser scanning speeds of 2.2 m/s and 2.4 m/s, which also showed the keyhole effect. These results were inconsistent with expectations since, as has been noted previously in this work, as the laser scanning speed rises at constant power, the energy density per unit area decreases, providing insufficient energy input to raise the temperature of the melts, as was observed by Yu et al. (2016). Moreover, it was noted by Guo et al. (2019) that high laser scanning speeds reduced the interaction time of the laser beam with the particles

of powder, leading to insufficient penetration through the powder to the substrate. The abnormality of keyholes occurring at the higher laser scanning speeds observed in this case, further point to lack of a simple relationship between the process parameters and the characteristics of builds observed separately by Dzogbewu et al. (2022) and Kusuma et al. (2016). Figure E10 (f) shows a depth-to-width ratio of 0.5 which is an indication of good depth of penetration. However, it was considered abnormal to obtain a good depth of penetration at the highest laser scanning speed given the lower ratios at lower scanning speeds.

Although the top surface scans of the tracks at laser scanning speeds ranging from 1.2 m/s to 1.6 m/s exhibited continuous tracks, which was expected to result in the best parameter sets, their cross-sections demonstrated depth-to-width ratios less than 0.5, indicating low depths of penetration. Even though the top surface scan of the track at the highest scanning speed of 2.4 m/s showed a sign of discontinuity, its cross-section had a good depth of penetration. Therefore, the best scanning speed at this value of power was identified as 2.4 m/s with the attendant LED of 12 m/s. This process parameter set was deemed sufficient to re-melt the previous layer during building of 3D parts.

#### **E6. The Effect of Different Laser Scanning Speeds at a Laser Power of 350 W**

The images shown in Figure E11 were produced at a constant laser power of 350 W and at different laser scanning speeds from 1.5 m/s to 2.7 m/s and were used here to study their surface morphologies.

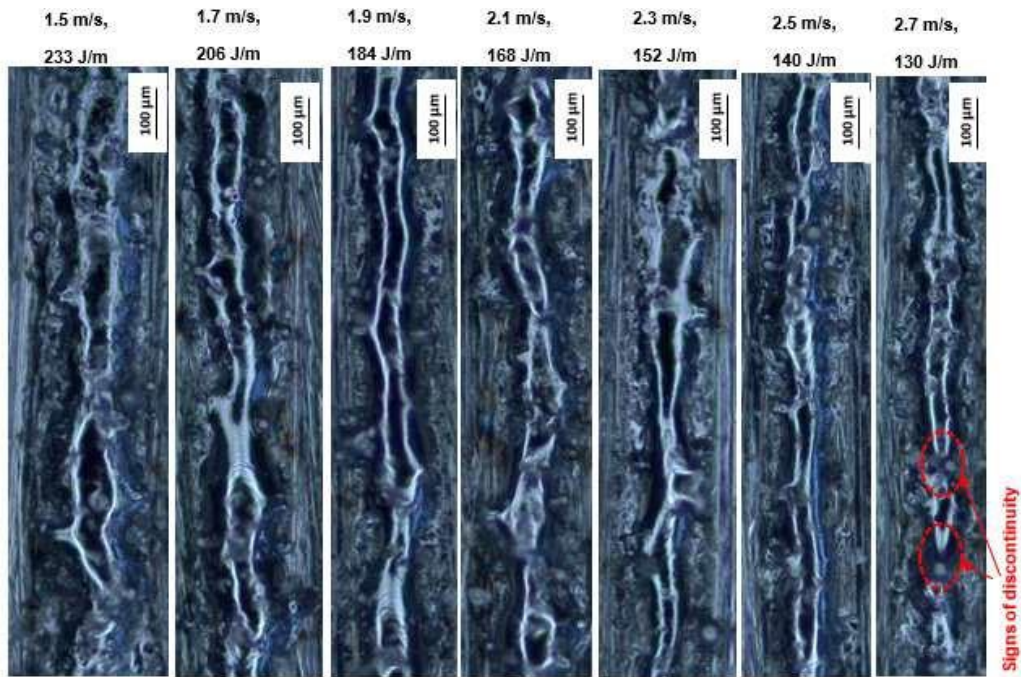


**Figure E11:** Top surface SEM micrographs of tracks, built at a constant power of 350 W and different laser scanning speeds from 1.5 m/s to 2.7 m/s

At the lowest scanning speed of 1.5 m/s, the track was wide and continuous. The increase in laser scanning speed from 1.7 m/s to 2.5 m/s resulted in a narrowing down of the tracks, which remained continuous. A discontinuity occurred when the laser scanning speed was raised to the maximum value of 2.7 m/s. Narrow track widths result from shorter dwell times of the laser beam and, therefore, failure to thoroughly melt powder (Guo et al., 2019).

The cross-sections of the top surface scans shown in Figure E11 are shown in Figure E12 and were used to investigate the geometrical characteristics of depth of penetration, width, and height of the tracks.

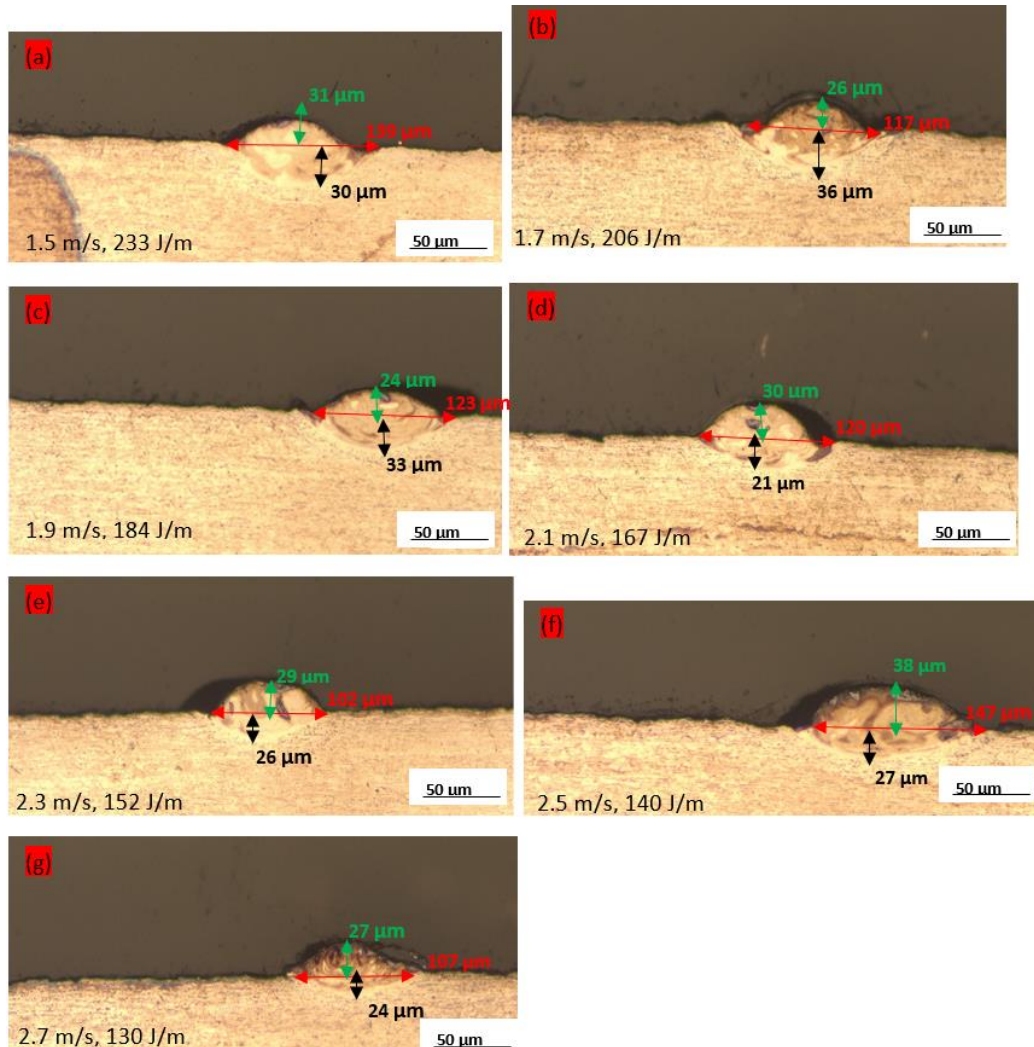


**Figure E12:** Cross-sections of tracks built at a constant laser power of 350 W and different laser scanning speeds from 1.5 m/s to 2.7 m/s

All the cross-sections in this figure indicated poor depths of penetration that showed no consistent trend with rising laser scanning speed. This inconsistency also occurred for the heights and widths of the tracks. All the cross-sections had depth-to-width ratios less than 0.3, which is less than the optimal value of 0.5, thus denoting insufficient penetration into the substrate. Though the track built at the lowest scanning speed of 1.5 m/s indicated a remarkably wide and continuous track, it also had poor depth of penetration. As a result, no optimal set of process parameters at this value of laser power could be used for building layers, since the observed inadequate penetration would result in delamination and lower mechanical properties of the built 3D parts.

## E7. The Influence of Different Values of Laser Power at a Constant Laser Scanning Speed

The cross-sections shown in Figure E13 were obtained from builds done at a laser scanning speed of 0.8 m/s and at different values of laser power of 100 W, 150 W, and 200 W. The cross-sections were used here to investigate the influence of different values of laser power on the geometrical characteristics of depth of penetration, width, and height of tracks.

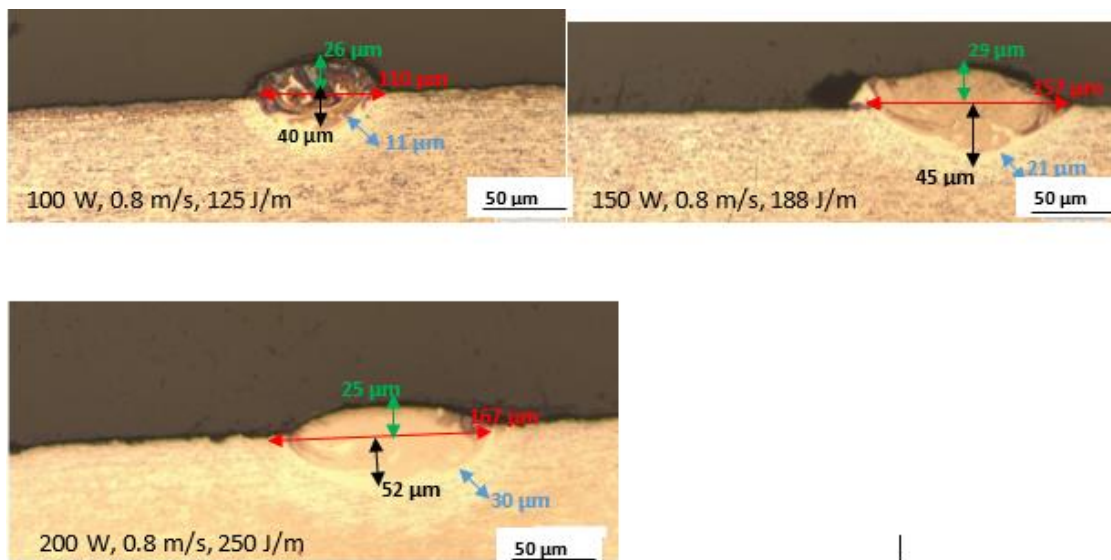


**Figure E13:** Cross-sections built at a laser scanning speed of 0.8 m/s and different values of laser power from 100 W to 200 W

It is evident from the cross-sections shown in Figure E13, that the depth of penetration, width, and HAZ of the tracks increased with increasing values of laser power. At a constant laser scanning speed, the increase of laser power leads to an increase of the LED that contributes to increased input of energy into powder per unit area. The increased input of energy and attendant increase of melt pool temperature are expected to lead to increased depth of penetration. Moreover, the depth of the HAZ is expected to increase with increasing melt pool temperatures. Similar results were observed by Dilip et al. (2017), who further reported that the laser power and scanning speed have a significant effect on the melt pool geometry.

## APPENDIX F. ANALYSIS OF SINGLE TRACKS BUILT AT A 30 % VOLUME FRACTION OF SiC IN AN SiC/Ti6Al4V(ELI) COMPOSITE

### F1. The Effect of Different Laser Scanning Speeds at a Laser Power of 100 W

Top surface views of single tracks produced at a constant laser power of 100 W and different laser scanning speeds are presented in Figure F1.

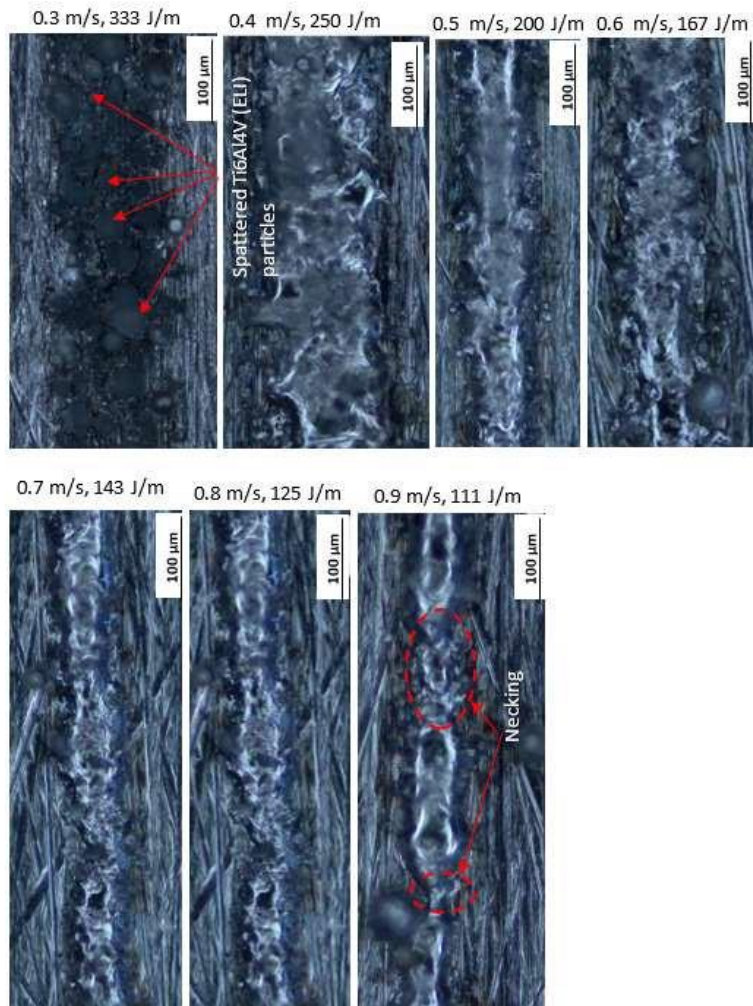


**Figure F1:** Top surface SEM images of single tracks produced at a constant laser power of 100 W with different laser scanning speeds

It has been observed and discussed previously in this chapter, for single tracks of 5% to 25% of SiC in SiC/T6Al4V(ELI) composites built at 100 W, that at the low scanning speed of 0.3 m/s and LED of 333 J/m, a broken-up track with discontinuity was formed.

As previously discussed in this chapter, a high energy density raises the temperature of the melt pool, causing the melt to evaporate. The alloy Ti6Al4V has a boiling

temperature of 2 860 °C, whereas SiC does not melt but rather sublimates over 2 700 °C. As a result, Ti6Al4V's evaporation temperature is slightly higher than SiC's sublimation temperature. Therefore, at this high energy input, it was thought that the Ti6Al4V(ELI) particles melted and evaporated, whilst the SiC particles sublimated, leading to re-solidified Ti6Al4V(ELI) particles referred to as spatter particles, as shown in the leftmost image in Figure F1. These results are consistent with the work of Shrestha et al. (2019).

The widths of the tracks were observed to decrease as the scanning speed increased. The tracks showed symptoms of necking at the high scanning speed of 0.9 m/s. Necking is caused by insufficient energy input, which is insufficient to complete the melting of the powder and substrate material (Dzogbewu et al., 2023). As previously stated, necking causes the formation of a small melt pool, which then easily breaks up into balls due to Rayleigh instability (Shi et al., 2017). The depths of penetration, widths, and heights of these tracks were investigated using their cross-sections presented in Figure F2.

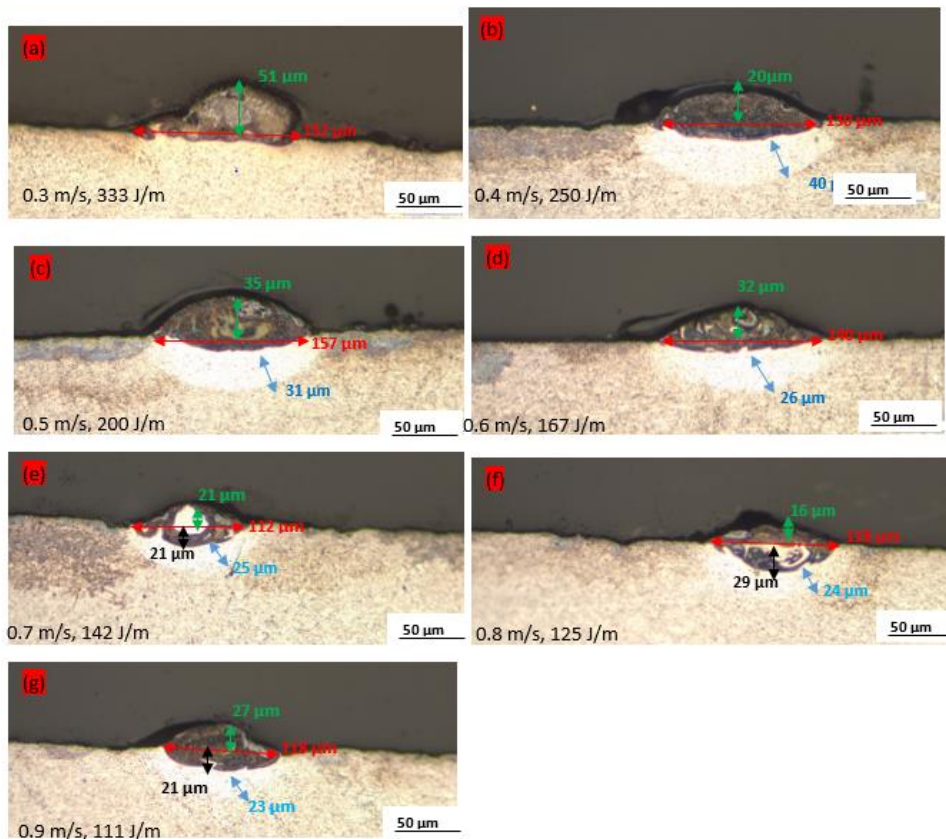


**Figure F2:** Cross-sectional views of single tracks built at a constant laser power of 100 W

At the laser power of 100 W, all the tracks had poor penetration, which implied high wettability and flowability of the melt on the substrate, as was observed in the work of Shi et al. (2016). This is enhanced by radial flow of the melt, from the centre of the melt to its outer edges (Yadroitsev et al., 2010). Since LPBF is a layer-by-layer process, shallow penetration of the tracks would lead to insufficient re-melting of the previous layer and results in delamination of layers (Dzogbewu et al., 2023). The width and height of the tracks in this figure were observed to vary inconsistently with increasing laser scanning speed. HAZ were first observed at a laser scanning speed of 0.4 m/s (Figure F2 (b)) and decreased in depth from Figure F2 (b) to Figure F2 (g) as the laser scanning speed increased.

Because SiC particles have a lower density of  $3.2 \text{ g/cm}^3$  than Ti6Al4V(ELI) at  $4.5 \text{ g/cm}^3$ , they float on top of the Ti6Al4(ELI) melt. As a result, more energy is required to heat the SiC particles and conduct them through the lower particles of Ti6Al4V(ELI) to fully melt them and penetrate through to the substrate.

Though the tracks shown in Figure F1 were all continuous, except for the last track, and with fairly constant widths, their cross-sections all showed depth-to-width ratios less than 0.2, which is far less than the optimum value of 0.5. These low ratios indicate a low depth of penetration. Therefore, it was inferred that at a laser power of 100 W, there was no best laser scanning speed that could be used to produce parts with good geometrical characteristics.

## **F2. The Effect of Different Laser Scanning Speeds at a Laser Power of 150 W**

Top surface views of single tracks produced at a laser power of 150 W, with different laser scanning speeds are presented in Figure F3.

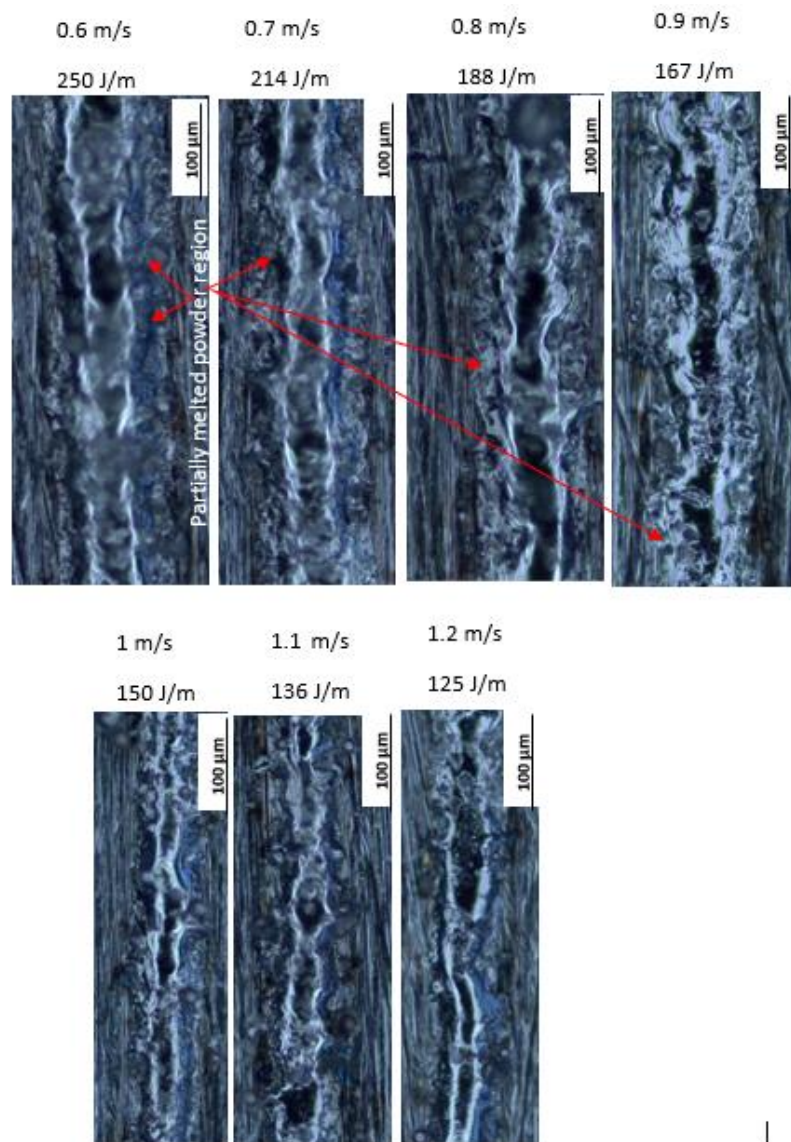


**Figure F3:** *Single tracks built at a laser power of 150 W, with different laser scanning speeds from 0.6 m/s to 1.2 m/s*

The tracks in Figure F3 all showed continuous tracks with even widths. The tracks built at low scanning speeds from 0.6 m/s to 0.9 m/s manifested large regions of partially melted powder at the sides of the tracks indicated by red arrows in the figure. It was noted that the region of partially melted powder was large at the low laser scanning speed and attendant high LED of 0.6 m/s and 240 J/m. This higher LED was thought to have created high melt temperatures that led to a widening of the track.

Moreover, due to low input of heat near the boundaries of tracks, partially melted particles were expected to occur there, since the melt pool temperature dropped towards the edges of tracks. Therefore, the wide track-widths that were wider than the

laser beam because of the high temperatures generated, reduced the viscosity and surface tension, leading to strong wettability of the melt pool. This, in turn, was expected to lead to a high incidence of partially melted particles, as was evident in this track. Increasing the laser scanning speed decreased the LED and, therefore, the temperature of the melt pool and resulted in decreased thickness of the HAZ at high scanning speeds.

The cross-sections of these tracks are presented in Figure F4 to study their widths, heights, and depths of penetration.

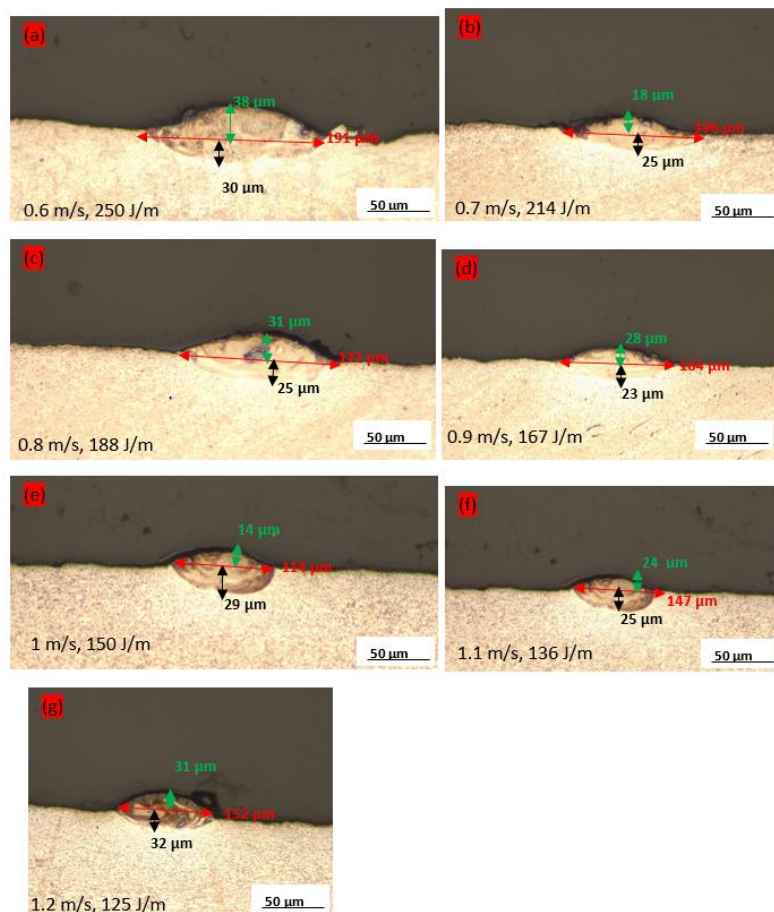


**Figure F4:** Cross-sections of tracks produced at a constant laser power of 150 W, with different laser scanning speeds from 0.6 m/s to 1.2 m/s

It is evident from an inspection of the cross-sections in Figure F4 that there was no consistent trend in the variation of the depths of penetration, widths, and heights of the tracks, with increasing laser scanning speed. All the tracks shown in the figure had low depths of penetration that were lower than the layer thickness (45–50 µm). This implied an inability to re-melt previous layers to create bonds between adjacent layers for all

scanning speeds used and at this value of laser power. This was consistent with the work of Dilip et al. (2017), who observed that poor depths of penetration would cause insufficient bonding and re-melting of layers during the building of specimens. The widths of track decreased constantly with rising laser scanning speed. The same pattern was observed and reported by Xin et al. (2021). It is known from literature that increasing laser scanning speed at a constant value of power decreases the dwell time of the laser beam over powder, decreasing the linear energy input per unit area of powder, which then causes a reduction of the melt area (Zhou et al., 2015; Dzogbewu et al., 2023).

Although the top surface scans showed tracks that were all continuous and with almost constant widths, their depth-to-width ratios were all less than 0.5, indicating low depths of penetration. As a result, the scanning speeds employed here at this value of laser power, were expected to produce layers that were likely to delaminate. Therefore, there was no scanning speed suitable for the production of 3D parts.

### F3. The Effect of Different Laser Scanning Speeds at a Laser Power of 200 W

Top images of the single tracks built at a laser power of 200 W, with different laser scanning speeds are shown in Figure F5.

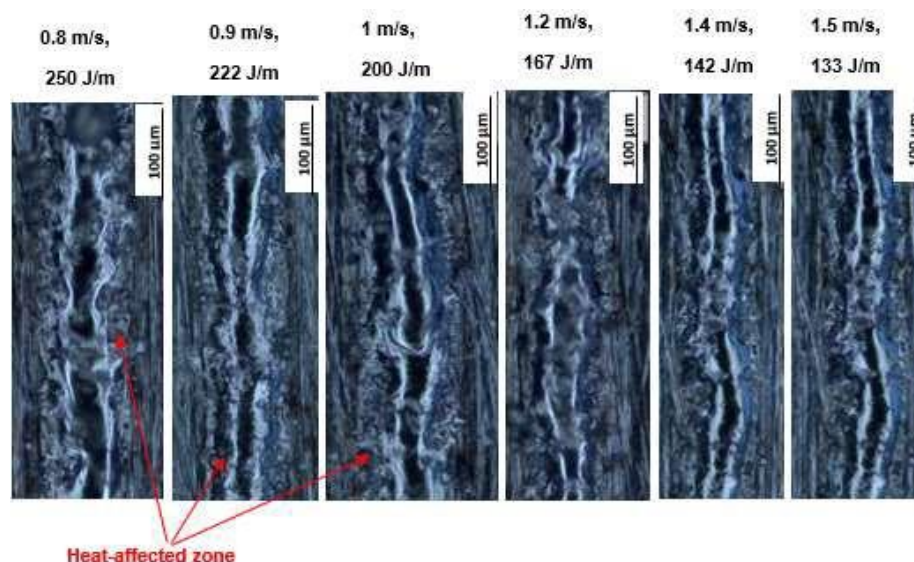


**Figure F5:** Top view images of single tracks produced at a constant laser power of 200 W and different laser scanning speeds

It is evident from the figure that all the tracks were continuous with almost even widths.

The regions with partially melted powder were largest at the low laser scanning speeds and showed diminishing multiplicity as the scanning speed rose. The former was thought to be because, at a constant value of laser power, a low laser scanning speed increases the energy input and, therefore, melt pool temperature (Yadroitsev et al., 2010; Shi et al., 2016). As has been discussed previously in this chapter, regions of partially melted powder particles at the edges of tracks result from the temperature of the melt being highest in the centre and decreases toward the edges (Shi et al., 2016). The high melt pool temperature transfers heat through conduction to the neighbouring powder particles at the edges that are not fully melted due to insufficiency of this transferred energy, as was noted by Yu et al. (2016).

A study of the depths of penetration, widths, HAZ, and heights of the built tracks was carried out based on the cross-sections of the tracks shown in Figure F6.

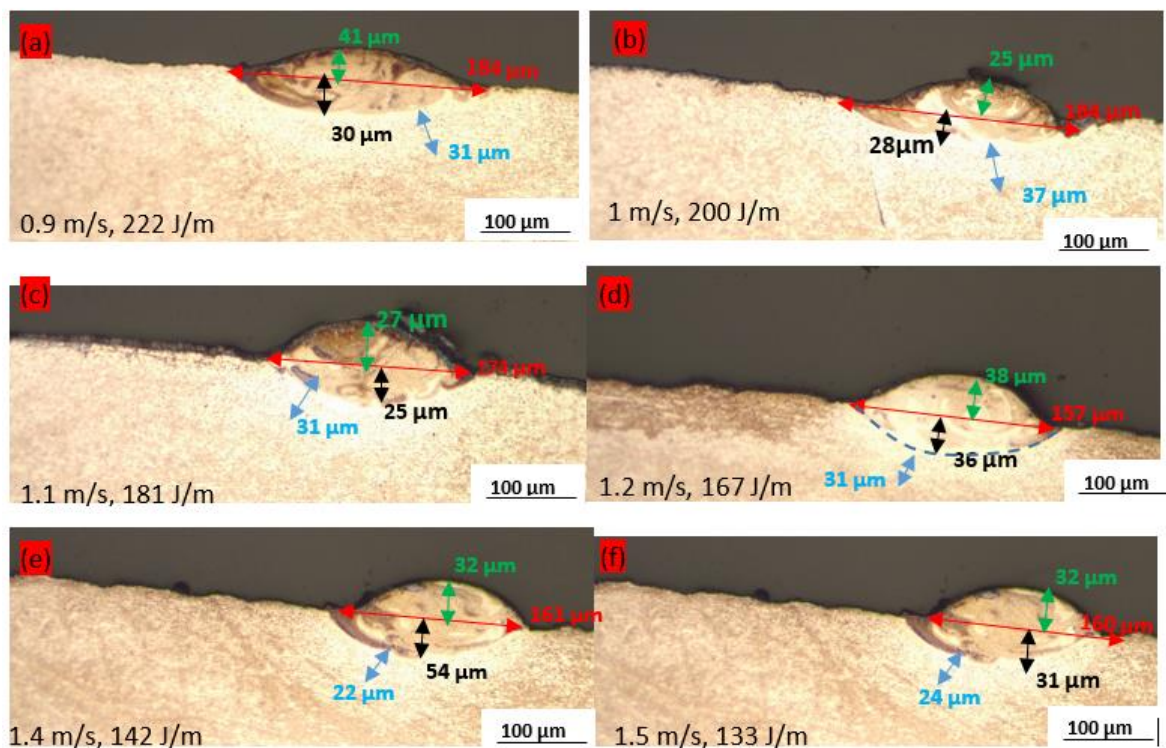


**Figure F6:** Cross-sectional images of single tracks produced at a constant laser power of 200 W

The geometrical characteristics of width, height, depth of penetration, and HAZ for these cross-sections varied inconsistently with increasing laser scanning speed. All the cross-sections showed depths of penetration that were lower than the layer

thickness (45–50  $\mu\text{m}$ ), except for Figure F6 (e). Therefore, the laser scanning speeds used at this power were not sufficient to cause re-melting of previous layers during the manufacturing of the 3D build parts.

It was concluded that, while the top surface scans of the tracks in Figure F6 showed fairly continuous tracks with even widths, their cross-sections revealed depth-to-width ratios of less than 0.3, which is less than the optimum ratio of 0.5. As a result, none of the laser scanning speeds used with this value of laser power produced suitable tracks with adequate depth of penetration to re-melt the prior layers and give strong metallurgical bonding between them and were not suitable to build 3D parts.

#### F4. The Effect of Different Laser Scanning Speeds at a Laser Power of 250 W

The top surface views of single tracks built at a constant laser power of 250 W, with different laser scanning speeds, are presented in Figure F7.

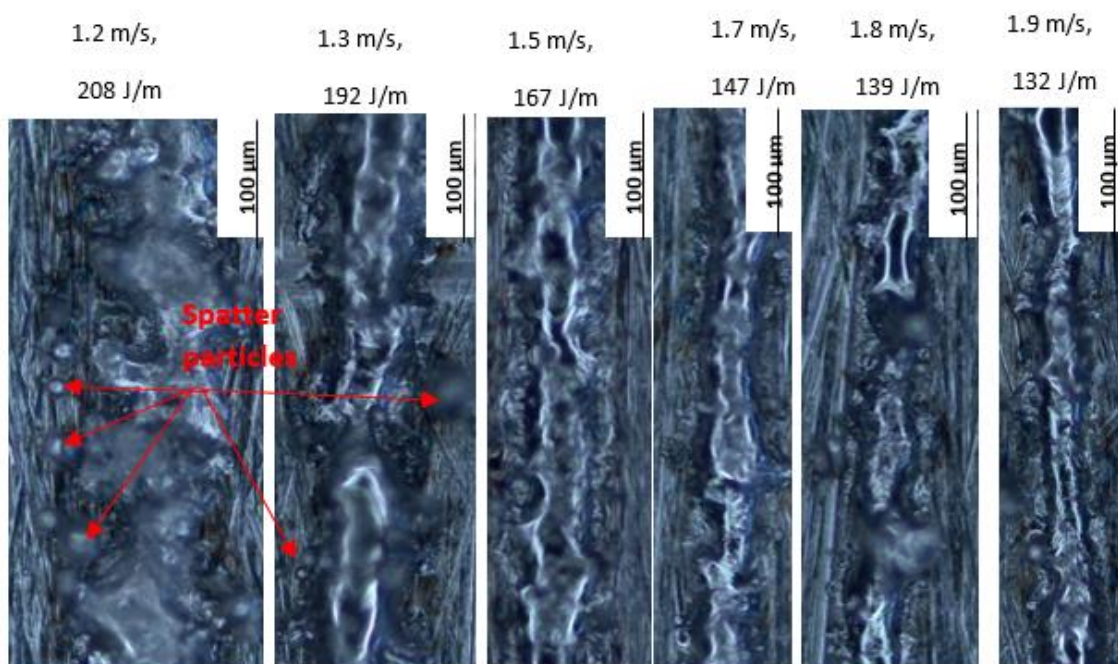


**Figure F7:** Single tracks built at a laser power of 250 W, with different laser scanning speeds

The track built at the lowest laser scanning speed of 1.2 m/s was wide due to the melt's strong wettability and ability to flow because of the effect of low surface tension and viscosity at the attendant high LED. Furthermore, the track had a lot of splatter particles around it again because of the high LED. However, as the scanning speed increased

from 1.7 m/s to 1.9 m/s, the spatter particles decreased, and the tracks were thinner. These narrow widths were caused by insufficient lateral spreading of the melt due to low wettability of the melt pool, as was observed by Wei et al. (2017). The narrow tracks in this figure implied that the range of speeds used to build them were too high, limiting the energy density per unit area. As has been observed previously in this chapter, low energy inputs decrease the melt pool temperature, causing an increase of surface tension and viscosity of the melt. Similar results were observed by Yu et al. (2016), who reported that at higher laser scanning speeds the fusion region became narrow due to insufficient liquid spreading laterally.

From the foregoing discussion, the track built at a laser scanning speed of 1.5 m/s, which showed a fairly continuous and wide track with reduced spatter particles, was considered the best in Figure F7. However, further investigation of the cross-sections of the tracks was deemed necessary to study their geometrical characteristics to help in selecting the best set of process parameters.

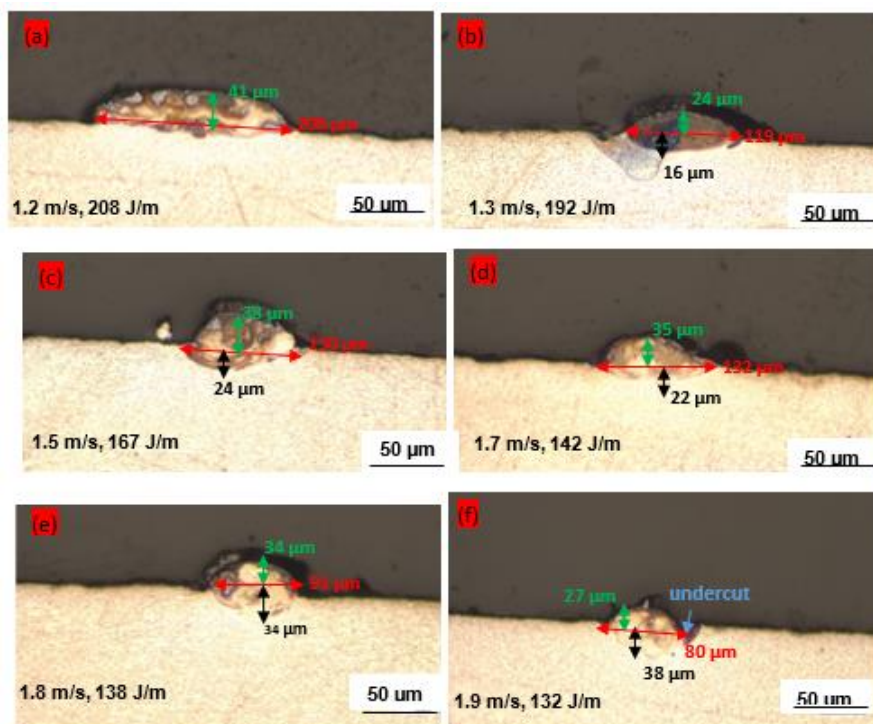


**Figure F8:** Cross-sections of single tracks built at a constant laser power of 250 W and different laser scanning speeds from 1.2 m/s to 1.9 m/s

There was inconsistency in the decrease and increase of the widths and depths of penetration of the tracks, with increasing scanning speed, respectively, except for the

Page | 282

track cross-sections shown in Figure F8 (b and d) for widths and Figure F8 (b) for the depths of penetration. All the tracks shown in the figure had poor depths of penetration into the substrate that were less than the layer thickness (45–50  $\mu\text{m}$ ). The depth-to-width ratios of the tracks were all less than 0.4, apart from the last cross-section that had a ratio of 0.5, which also exhibited undercutting. All the cross-sections indicated conduction melting because of the high scanning speeds used at this power than at low powers from 100 W to 200 W that limited the dwell time of the laser on the powder bed to sufficiently penetrate through the substrate. The highest depths of penetration were seen in these cross-sections at the highest laser scanning speeds of 1.8 m/s and 1.9 m/s, which was an unanticipated abnormality that has also been reported by Dzogbewu et al. (2023) and Kusuma et al. (2016). Because of significant reductions in surface tension, viscosity, and the accompanying rise in wetting at low laser scanning speeds and high values of laser power, no penetration occurred at the lowest laser scanning speed of 1.2 m/s, where the LED was highest. Subsequent increase of the scanning speed is thought to have led to an increase of the dwell time that allowed penetration of the laser beam, as was observed by Dzogbewu et al. (2022). The track height and width were observed to decrease consistently with increasing laser scanning speed. From the foregoing discussion it was clear that there was no best cross-section as they all showed poor depth of penetration, including the last track, which showed an optimum ratio of depth-to-width ratio of 0.5 but also exhibited undesirable undercutting.

In conclusion, none of the process parameter sets used here were considered suitable to build good 3D parts for reasons of low depth-to-width ratios and the presence of undercutting in the case where the ratio was correct.

#### **F5. The Effect of Different Laser Scanning Speeds at a Laser Power of 300 W**

The single tracks built at a constant laser power of 300 W with different laser scanning speeds are shown in Figure F9.

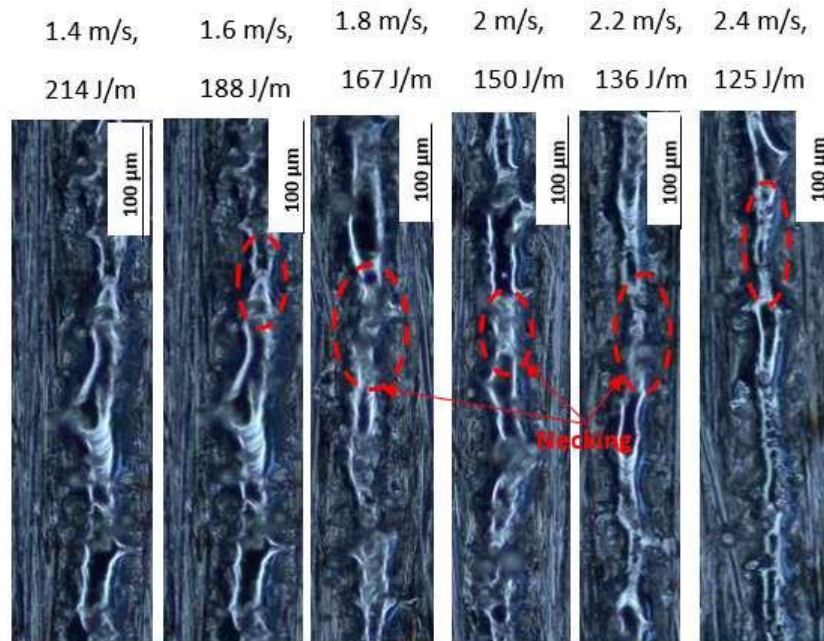


**Figure F9:** *Single tracks built at a laser power of 300 W, with different laser scanning speeds from 1.2 m/s to 2.4 m/s*

The tracks built at a laser power of 300 W were narrow with signs of necking and discontinuities, which would demand long periods for building 3D parts. These characteristics of the tracks tied in with the work of Xuezhi et al. (2017) on the optimization of process parameters in SLM based on the geometrical characteristics of single tracks. The authors reported that when low laser scanning speeds were used with high values of power, their combination led to irregularities of tracks. A high value of laser power induced strong recoil pressure on the melt pool. Meanwhile, a low scanning speed led to a longer dwell time of the laser which resulted in a high degree of overheating of the melt and vice versa. The values of scanning speeds here were on the higher end, with the lowest one being 1.4 m/s. This value was much higher than the highest values of laser scanning speed used at the low laser powers of 100 W and 150 W and was equal to the second highest value of laser scanning speed used at a laser power of 200 W, for different volume fractions of SiC in SiC/Ti6Al4V(ELI) composites. This case could thus be treated as one of high laser power and high laser scanning speeds that generated modest LEDs, and therefore the observed narrow tracks with signs of necking.

The cross-sections of these single tracks are shown in Figure F10 and were used to study their depths of penetration, heights, and widths.

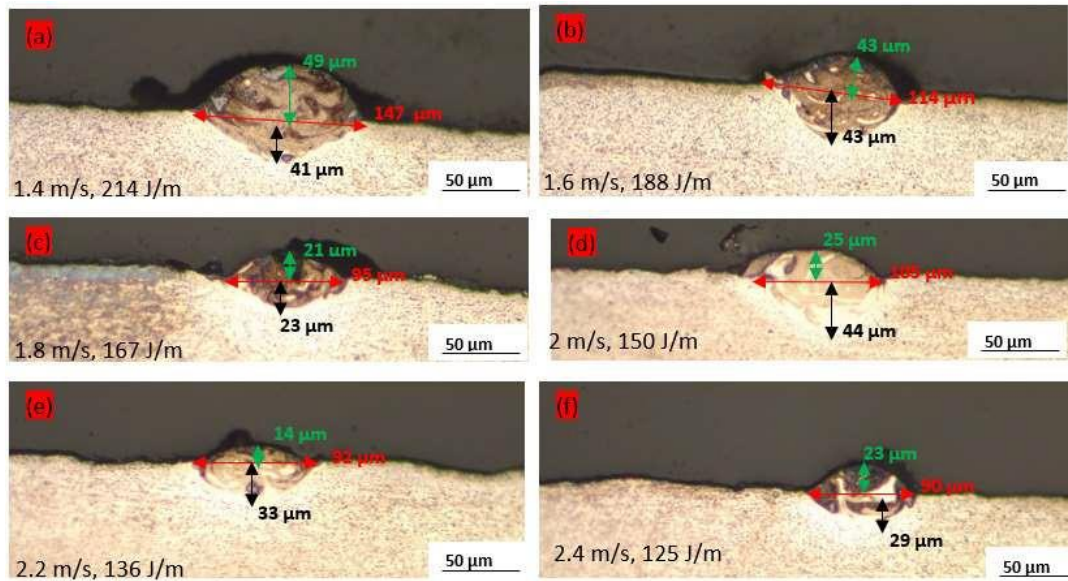


**Figure F10:** Cross-sections of single tracks built at a laser power of 300 W, with different laser scanning speeds from 1.4 m/s to 2.4 m/s

The images in Figure F10 showed a continuous decrease in the widths of tracks with increasing scanning speed, except for Figure F10 (c), and similar trends in the change of the heights and depths of penetration of tracks with increasing scanning speed with some exceptions. All the measured values of depth of penetration and width of the tracks generated ratios of depth-to-width that were less than the optimum ratio of 0.5. A ratio of less than 0.5 is indicative of poor interlayer bonding. The depths of penetration for all the tracks were lower than the layer thickness (45–50  $\mu\text{m}$ ), which implied no re-melting of previous layers was expected for these scanning speeds. These two foregoing factors in addition to the narrow tracks with signs of necking implied that the scanning speeds used at this value of laser power could not be used to build 3D parts with good characteristics.

#### **F6. The Effect of Different Laser Scanning Speeds at a Laser Power of 350 W**

The morphologies of the top surface scans of the tracks were studied using the images shown in Figure F11, built at a constant power of 350 W with different laser scanning speeds from 1.5 m/s to 2.7 m/s.

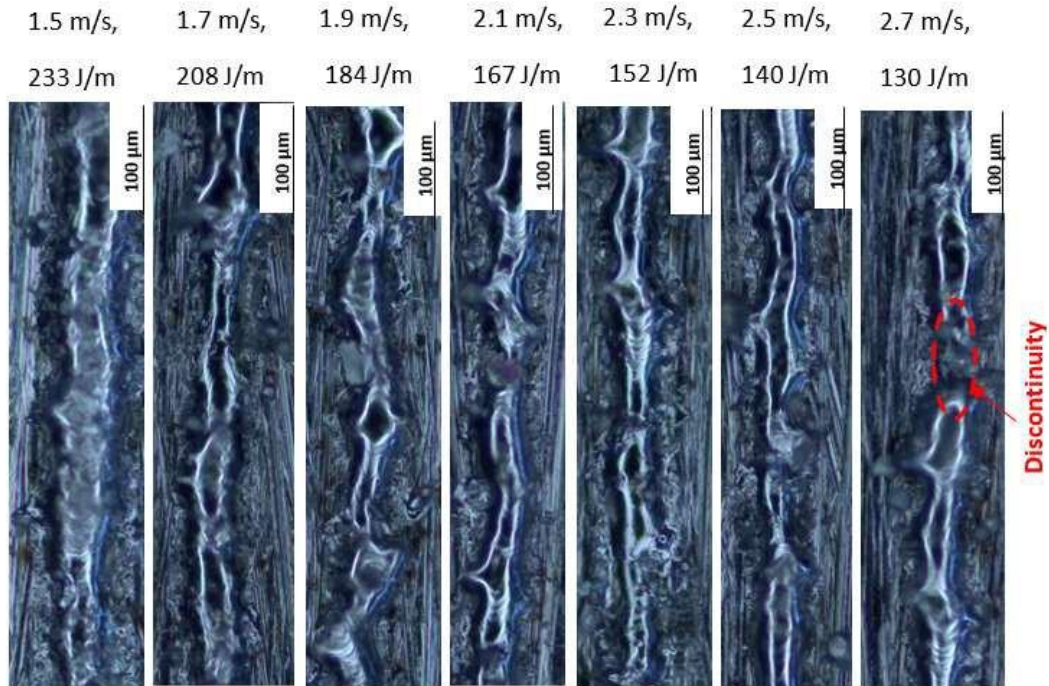


**Figure F11:** Single tracks built at a laser power of 350 W, with different laser scanning speeds from 1.5 m/s to 2.7 m/s

All the tracks shown in Figure F11 were narrow. A discontinuity was observed at the highest laser scanning speed of 2.7 m/s. The narrowing of the tracks and the presence of a discontinuity were thought to be due to high surface tension and viscosity of the melt in all the cases. Moreover, as has been discussed previously, high laser scanning speeds result in low dwell times of the laser beam and, therefore, inadequacy to melt and penetrate the powder.

Cross-sections of the single tracks shown in in Figure F11 produced at the constant laser power of 350 W and different laser scanning speeds are shown in Figure F12 and were used here to study their geometrical characteristics.

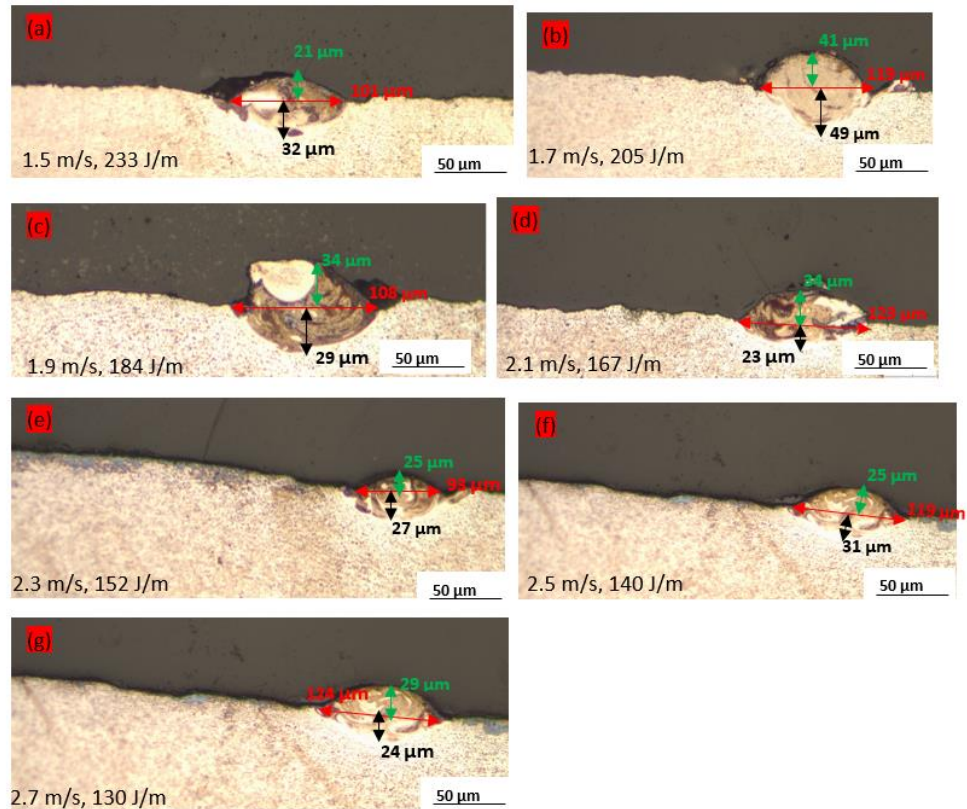


**Figure F12:** Cross-sections of single tracks produced at a constant laser power of 350 W at different scanning speeds from 1,5 m/s to 2.7 m/s

All the cross-sections shown in Figure F12 indicated poor penetration of tracks with measured values of depth of penetration that were all less than the layer thickness (45–50  $\mu\text{m}$ ). The ratios of depth-to-width for all these tracks were less than the optimum value of 0.5. The widths, depths of penetration, and heights of the tracks all showed inconsistent variations with increasing laser scanning speed. The shallow tracks observed in Figure F2 implied inability to re-melt previous layers and thus insufficient connection between adjacent layers. This was likely to lead to the formation of defects during multi-layer manufacturing processes as was observed by Xuezhai et al. (2017). It was concluded that, at this value of power, and considering the narrow tracks and the one track with a discontinuity, as well as their depth-to-width ratios that were less than 0.5, there was no best set of process parameters that could be used in the building of multiple layers.

## F7. The Effect of Different Laser Powers at a Constant Laser Scanning Speed of 0.8 m/s

The cross-sections of single tracks produced at constant laser scanning speed with different laser powers of 100 W, 150 W, and 200 W are presented in Figure F13 and were used to study the effect of power on the geometrical characteristics of single tracks.

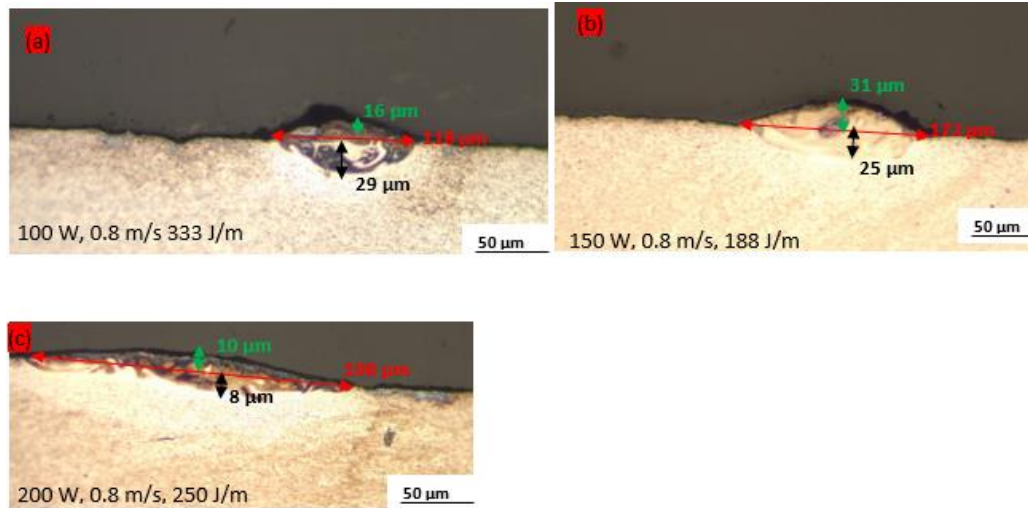


**Figure F13:** Cross-sections of single tracks produced at a constant laser scanning speed with different laser powers from 100 W to 200 W

In Figure F13 it was noted that as the power was increased the tracks became flatter and shallower. The depths of penetration decreased with rising laser power, while the widths of the tracks increased as the laser power was increased. These trends were thought to have arisen from reductions of surface tension and viscosity with the increase in power at a constant speed, causing more outward flow of the melt from the centre of the tracks to their outer edges, as was noted by Xuezhi et al. (2017).

The low density and high heat capacity of the SiC particles are likely to have been the reason for insufficient penetration of the laser beam at the high SiC volume fraction of 30%. The low density of SiC particles meant that they floated on top of the Ti6Al4V melt, while their high heat capacity allowed them to absorb and store a lot of energy within them, limiting the amount of energy transferred to the Ti6Al4V melt. This meant a reduced ability of the laser beam to penetrate sufficiently through the substrate and the noted low depths of penetration. Therefore, the process parameter sets used to build these three tracks could not be used to build good layers or 3D parts at 30 % SiC volume fraction of SiC/Ti6Al4V(ELI) composites.

## F8. REFERENCES FOR ALL APPENDICES

- [1]. Agarwala, M., Bourell, D., Beaman, J., Marcus, H., and Barlow, J., 1995. Direct selective laser sintering of metals. *Rapid Prototyping Journal*.vol.1.1, pp. 36-46.
- [2]. Andani, M.T., Dehghani, R., Karamooz-Ravari, M.R., Mirzaeifar, R., and Ni, J., 2018. A study on the effect of energy input on spatter particle creation during selective laser melting process. *Additive Manufacturing*, 20, pp. 33-43.
- [3]. Bertolia, U.S., Wolfer, M.J., Matthews, A.J., Delplanque, J.P.R., and Schoenung, J.M., 2017. On the limitations of volumetric energy density as a design parameter for Selective Laser Melting, *Materials and Design*, 113, pp. 331-340.
- [4]. Bi, J., Lei, Z., Chen, Y., Chen, X., Qin, X., and Tian, Z., 2019. Effect of process parameters on formability and surface quality of selective laser melted Al-Zn-Sc-Zr alloy from single track to block specimen. *Optics and Laser Technology*, 118, pp. 132-139.
- [5]. Dilip, J.J.S., Zhang, S., Teng, C., Zeng, K., Robinson, C., Pal, D., and Stucker, B., 2017. Influence of processing parameters on the evolution of melt pool, porosity, and microstructures in Ti-6Al-4V alloy parts fabricated by selective laser melting. *Progress in Additive Manufacturing*, 2, pp.157-167.
- [6]. Dursun, G., Ibekwe, S., Li, G., Mensah, P., Joshi, G., and Jerro, D., 2020. Influence of laser processing parameters on the surface characteristics of 316L stainless steel manufactured by selective laser melting. *Materials Today: Proceedings*, 26, pp. 387-393.
- [7]. Dzogbewu, T., Yadroitsev, I., Krakhmalev, P., Yadroitsava, I., and du Plessis, A., 2017. Optimal process parameters for in-situ alloyed Ti15Mo structures by Direct Metal Laser Sintering. In *SSF 2017-The 28th Annual International Solid Freeform Fabrication Symposium*, University of Texas, Austin, August 7–9, 2017, pp. 75-96.

- [8]. **Dzogbewu, T.C., and du Preez, W.B.**, 2022. In situ alloying of Ti10Mo fused tracks and layers via laser powder bed fusion. *Manufacturing Review*, 9, p.23.
- [9]. **Dzogbewu, T.C., and du Preez, W.B.**, 2022. Producing Ti5Mo-fused tracks and layers via laser powder bed fusion. *Metals*, 12(6), p. 950.
- [10]. **Dzogbewu, T.C., de Beer, D.J., and du Preez, W.B.**, 2023. Laser powder bed fusion of Ti15Mo fused tracks and layers. *Journal of Materials*, pp. 1-14. <http://dx.doi.org/10.1016/j.rineng.2020.100155>
- [11]. **Eagar, T.W., and Tsai, N.S.**, 1983. Temperature fields are produced by traveling distributed heat sources. *Welding Journal*, 62(12), pp. 346-355.
- [12]. **Fotovvati, B., Wayne, S.F., Lewis, G., and Asadi, E.**, 2018. A review on melt-pool characteristics in laser welding of metals. *Advances in Materials Science and Engineering*, vol.2018, pp 1-8.2018.
- [13]. **Gao, P., Wang, Z., and Zeng, X.**, 2019. Effect of process parameters on morphology, sectional characteristics and crack sensitivity of Ti-40Al-9V-0.5Y alloy single tracks produced by selective laser melting. *International Journal of Lightweight Materials and Manufacture*, 2(4), pp. 355-361.
- [14]. **Gu, D., and Shen, Y.**, 2007. Balling phenomena during direct laser sintering of multi-component Cu-based metal powder. *Journal of Alloys and Compounds*, 432(1-2), pp. 163-166.
- [15]. **Guo, C., Xu, Z., Zhou, Y., Shi, S., Li, G., Lu, H., Zhu, Q., and Ward, R.M.**, 2021. Single-track investigation of IN738LC superalloy fabricated by laser powder bed fusion: Track morphology, bead characteristics, and part quality. *Journal of Materials Processing Technology*, 290, p.117000.
- [16]. **Guo, Q., Zhao, C., Qu, M., Xiong, L., Escano, L.I., Hojjatzadeh, S.M.H., Parab, N.D., Fezzaa, K., Everhart, W., Sun, T. and Chen, L.**, 2019. In-situ characterization and quantification of melt pool variation under constant input energy density in laser powder bed fusion additive manufacturing process. *Additive Manufacturing*, 28, pp. 600-609.

- [17]. **Karimi, P., Sadeghi, E., Ålgårdh, J., and Andersson, J.**, 2019. EBM-manufactured single tracks of Alloy 718: Influence of energy input and focus offset on geometrical and microstructural characteristics. *Materials Characterization*, 148, pp. 88-99.
- [18]. **Kaserer, L., Bergmueller, S., Braun, J., and Leichtfried, G.**, 2020. Vacuum laser powder bed fusion—track consolidation, powder denudation, and future potential. *The International Journal of Advanced Manufacturing Technology*, 110, pp. 3339-3346.
- [19]. **Khairallah, S.A., Anderson, A.T., and Rubenchik, A.**, 2015. Laser powder-bed fusion additive manufacturing: Effects of main physical processes on dynamical melt flow and pore formation from mesoscopic powder simulation. arXiv 2015, arXiv:1512.02593. <https://doi.org/10.1016/j.actamat.2016.02.014>
- [20]. **Kouprianoff, D., Yadroitsava, I., du Plessis, A., Luwes, N., and Yadroitsev, I.**, 2021. Monitoring of laser powder bed fusion by acoustic emission: Investigation of single tracks and layers. *Frontiers in Mechanical Engineering*, 7, p.678076.
- [21]. **Kouprianoff, D.P.R.**, 2021. Online monitoring of laser-based powder bed fusion by acoustic emission. Doctoral dissertation, Central University of Technology, Free State, South Africa.
- [22]. **Krasa, J.**, 2013. Gaussian energy distribution of fast ions emitted by laser-produced plasmas. *Applied Surface Science*, 272, pp. 46-49.
- [23]. **Kruth, J., Thijs L., Verhaeghe, F., Craeghs, J., Van Humbeeck, J.**, 2010. A study of the microstructural evolution during selective laser melting of Ti6Al4V, *Acta Materialia*, vol. 58, no. 9, pp. 3303-3312.
- [24]. **Kusuma, C.**, 2016. The effect of laser power and scan speed on melt pool characteristics of pure titanium and Ti-6Al-4V alloy for selective laser melting. The Effect of Laser Power and Scan Speed on Melt Pool Characteristics of Pure Titanium and Ti-6Al-4V Alloy for Selective Laser Melting, master's thesis, Wright State University, 1510.

[https://corescholar.libraries.wright.edu/etd\\_all/1510](https://corescholar.libraries.wright.edu/etd_all/1510).

- [25]. **Le, T.N., and Lo, Y.L.**, 2019. Effects of sulfur concentration and Marangoni convection on melt-pool formation in transition mode of selective laser melting process. *Materials and Design*, 179, p.107866.
- [26]. **Li, Y., and Gu, D.**, 2014. Parametric analysis of thermal behavior during selective laser melting additive manufacturing of aluminum alloy powder. *Materials and Design*, 63, pp.856-867.
- [27]. **Mumtaz, K.A., and Hopkinson, N.**, 2010. Selective laser melting of thin wall parts using pulse shaping. *Journal of Materials Processing Technology*, 210(2), pp. 279-287.
- [28]. **Ramosena, L.A., Parker, B.S., Dzogbewu T.C., du Preez, W.B., and Blaine, D.C.**, 2019. Optimum process parameters for DMLS in-situ alloying of a Ti10(60Al40V) powder blend, *Proceedings of the 20th International Conference of the Rapid Product Development Association of South Africa*, Bloemfontein.
- [29]. **Shi, X., Ma, S., Liu, C., and Wu, Q.**, 2017. Parameter optimization for Ti-47Al-2Cr-2Nb in selective laser melting based on geometric characteristics of single scan tracks. *Optics and Laser Technology*, 90, pp.71-79.
- [30]. **Shrestha, S., Starr, T., and Chou, K.**, 2019. A study of keyhole porosity in selective laser melting: single-track scanning with micro-CT analysis. *Journal of Manufacturing Science and Engineering*, 141(7).
- [31]. **Ullah, A., Ur Rehman, A., Salamci, M.U., Pitir, F., and Liu, T.**, 2022. The influence of laser power and scanning speed on the microstructure and surface morphology of Cu<sub>2</sub>O parts in SLM. *Rapid Prototyping Journal*, 28(9), pp.1796-1807.
- [32]. **Vilardell, A.M., Yadroitsev, I., Yadroitsava, I., Albu, M., Takata, N., Kobashi, M., Krakhmalev, P., Koupryanoff, D., Kothleither, G., du Plessis, A.**, 2020., Manufacturing and characterization of in-situ alloyed Ti6Al4V(ELI) -3 % CU by laser powder bed fusion, *Additive*

*Manufacturing*, vol 36, pp.1-14.

- [33]. **Wang, Y., and Shi, J.**, 2018. Influence of laser scan speed on micro-segregation in selective laser melting of an iron-carbon alloy: A multi-scale simulation study. *Procedia Manufacturing*, 26, pp. 941-951.
- [34]. **Wei, P., Wei, Z., Chen, Z., Du, J., He, Y., Li, J., and Zhou, Y.**, 2017. The AlSi10Mg samples produced by selective laser melting: single track, densification, microstructure and mechanical behaviour. *Applied Surface Science*, 408, pp.38-50.
- [35]. **Wei, P., Wei, Z., Chen, Z., He, Y., and Du, J.**, 2017. Thermal behavior in single track during selective laser melting of AlSi10Mg powder. *Applied Physics A*, 123, pp.1-13.
- [36]. **Xia, M., Gu, D., Yu, G., Dai, D., Chen, H., and Shi, Q.**, 2017. Porosity evolution and its thermodynamic mechanism of randomly packed powder-bed during selective laser melting of Inconel 718 alloy. *International Journal of Machine Tools and Manufacture*, 116, pp. 96-106.
- [37]. **Xiao, X., Lu, C., Fu, Y., Ye, X., and Song, L.**, 2021. Progress on experimental study of melt pool flow dynamics in laser material processing. In *Liquid Metals*. IntechOpen.
- [38]. **Yadroitsava, I., Els, J., Booyesen, G., and Yadroitsev, I.**, 2015. Peculiarities of single-track formation from Ti6AL4V alloy at different laser power densities by selective laser melting. *South African Journal of Industrial Engineering*, 26(3), pp. 86-95.
- [39]. **Yadroitsev, I., Bertrand, P., and Smurov, I.**, 2007. Parametric analysis of the selective laser melting process. *Applied Surface Science*, 253(19), pp. 8064-8069.
- [40]. **Yadroitsev, I., Gusarov, A., Yadroitsava, I., and Smurov, I.**, 2010. Single track formation in selective laser melting of metal powders. *Journal of Materials Processing Technology*, 210(12), pp. 1624-1631.
- [41]. **Yadroitsev, I., Krakhmalev, P., Yadroitsava, I., Johansson, S., and Smurov, I.**, 2013. Energy input effect on morphology and microstructure

of selective laser melting single track from metallic powder. *Journal of Materials Processing Technology*, 213(4), pp. 606-613.

- [42]. **Yu, G., Gu, D., Dai, D., Xia, M., Ma, C., and Chang, K.**, 2016. Influence of processing parameters on laser penetration depth and melting/re-melting densification during selective laser melting of aluminum alloy. *Applied Physics A*, 122, pp. 1-12.
- [43]. **Yuan, W., Chen, H., Cheng, T., and Wei, Q.**, 2020. Effects of laser scanning speeds on different states of the molten pool during selective laser melting: Simulation and experiment. *Materials and Design*, 189, p. 108542.